

DISSERTATION IN DOPPELBETREUUNG ZUR ERLANGUNG DES  
DOKTORGRADES DER FAKULTÄT FÜR CHEMIE UND PHARMAZIE  
DER LUDWIG-MAXIMILIANS-UNIVERSITÄT (LMU) MÜNCHEN  
UND DER UNIVERSITÉ DE PAU ET DES PAYS D'ADOUR (U.P.P.A)

THÈSE EN CO-TUTELLE POUR OBTENIR LE GRADE DE DOCTEUR  
PRÉSENTÉE À L'UNIVERSITÉ DE PAU ET DES PAYS D'ADOUR  
ECOLE DOCTORALE DES SCIENCES EXACTES ET DE LEURS APPLICATIONS  
ET À LA LUDWIG-MAXIMILIANS-UNIVERSITÄT MÜNCHEN

# **Diffusion of single molecules in nanoporous mesostructured materials**

Johanna Ursula Kirstein

aus

München

2007



## **Erklärung**

Diese Dissertation wurde im Sinne von §13 Abs. 3 bzw. 4 der Promotionsordnung vom 29. Januar 1998 in deutsch-französischer Doppelbetreuung (*cotutelle de these*), gemäß der Vereinbarung vom Juli 2004, von Herrn Prof. Dr. Christoph Bräuchle und Dr. Ross Brown betreut.

## **Ehrenwörtliche Versicherung**

Diese Dissertation wurde selbständig, ohne unerlaubte Hilfe erarbeitet.

München, den 14.08.2007

Dissertation eingereicht am 14.08.2007

1. Gutachter: Prof. Dr. Christoph Bräuchle

2. Gutachter: Dr. Ross Brown

Mündliche Prüfung am 20.09.2007



Laß die Moleküle rasen,  
was sie auch zusammenknobeln!  
Laß das Tüfteln, laß das Hobeln,  
heilig halte die Ekstasen!

- CHRISTIAN MORGENSTERN

*Let the molecules career,  
leave them to their own confections.  
Never fuss about corrections  
ecstasies thou shalt revere!*

- translation by Sarah Fulford<sup>1</sup>

*Laisse les molécules faire rage,  
Quoi qu'elles en secret combinent.  
Corrections ne plus rumine,  
Pour sacrées tiens les extases!*

- traduction par Hans-Werner Kirstein

## Summary

Single-molecule methods play a growing role in materials science because they can reveal structural and dynamic features which are obscured by ensemble averaging in conventional spectroscopic techniques. In this work, such methods were used to study the dynamics of single dye molecules (guests) within different surrounding porous matrices (hosts) using wide-field microscopy and single-molecule tracking. A significant amount of tracking data was collected and sophisticated methods to analyse the data according to diffusion theory were developed. A method was established to directly correlate the diffusion information that is provided by single-molecule trajectories with the images of the porous host systems obtained by transmission electron microscopy (TEM). Furthermore, the results from single-molecule tracking experiments were compared with diffusion measurements using pulsed-field gradient NMR in the same samples. All these investigations provided detailed structural information about the porous host systems as well as a thorough understanding of the diffusional behaviour within the different environments.

Two different types of porous silica materials were investigated in this work: Sol-gel glasses and mesoporous thin films. Whereas sol-gel glasses exhibit a broad distribution of pore sizes around a mean value, mesoporous materials have pores with a distinct diameter which are arranged in well defined topologies.

Sol-gel glasses with two different mean pore diameters, 3 nm and 22 nm, were investigated using a newly synthesized streptocyanine dye for the single-molecule experiments. In the materials with the bigger pores the dye molecules were found to follow a random motion with an average diffusion coefficient of  $D_{M22}=0.72 \mu\text{m}^2 \text{s}^{-1}$ . However, in the material with smaller pores, large inhomogeneities in the diffusion behaviour were detected. A large number of molecules remained confined within regions of different diameters in the range of hundreds of nanometres. Some molecules showed changes between mobile and immobile states. Appropriate methods for the data analysis were devised in order to reveal the inhomogeneities within a single trajectory and to evaluate the changes in the diffusivity quantitatively. For comparison, pulsed-field gradient NMR measurements were done in the same sol-gel glasses and the results completed the picture obtained from the single-molecule tracking data.

Structural features on the nanometre scale cannot be directly imaged with optical methods. Therefore, a unique combination of transmission electron microscopy (TEM) and single-molecule tracking was developed to trace out the internal structure of mesoporous thin films and to establish how the diffusion dynamics depend on the underlying structure of the host. With this approach dynamical information from single

particle diffusion was directly correlated with the structural details of the porous host obtained by TEM.

Additionally, it was shown how different populations of diffusing species can be clearly distinguished in various topologies of mesoporous thin films by high resolution wide-field microscopy and single-molecule tracking. By using two different liquid-crystal templates and by varying the silica/template ratio in the synthesis recipes, pore systems with different pore-to-pore distances and pore topologies could be obtained. Brij 56 templated thin films, with a pore-to-pore distance of about 6 nm, were synthesised in hexagonal or lamellar topology or with a mixture of both. On the basis of the structure of the trajectories, the diffusivities and the orientation of the molecules, it was possible to distinguish dyes travelling on the external surface of the thin film from those travelling inside the pore system, dyes that diffuse along horizontal channels of the hexagonal phase, and those that move much more slowly in lamellar galleries of the mesoporous material. In the hexagonal phase the molecules showed very structured pathways reflecting the ordered structure of the porous host on a long range of several microns, with an average diffusion coefficient of  $D_{\text{Brij56:hex}} = 5.0 \times 10^{-3} \mu\text{m}^2 \text{s}^{-1}$ . On the contrary, doughnut-shaped diffraction patterns corresponding to molecules oriented perpendicular to the substrate were observed in the lamellar phase. These molecules diffuse randomly with a diffusion coefficient up to two orders of magnitude lower than the structured ones in the hexagonal phase ( $D_{\text{Brij56:lam}} = 5.0 \times 10^{-5} \mu\text{m}^2 \text{s}^{-1}$ ). These two populations of fast, structured trajectories and slow, randomly moving molecules, oriented perpendicular to the substrate, are observed simultaneously when a mixture of the two phases coexists in the same spin-coated film. Thin films with bigger pores (ca. 9 nm) and hexagonal or cubic arrangement of pores were synthesized using Pluronic P123 as template. In the hexagonal phase structured diffusion along the channels was observed, similar to the findings in the hexagonal Brij-templated films. However, the diffusion coefficient was one order of magnitude higher when Pluronic P123 was used as template ( $D_{\text{P123:hex}} = 4.0 \times 10^{-2} \mu\text{m}^2 \text{s}^{-1}$ ). The molecules in the cubic phase showed unstructured, random diffusion in 2D, with an even higher diffusion coefficient than in the hexagonal phase ( $D_{\text{P123:cubic}} = 3.0 \times 10^{-1} \mu\text{m}^2 \text{s}^{-1}$ ).

The data presented in this thesis thus provide for the first time a detailed picture of the real mesoporous structure and its effects on the dynamic behavior of dye molecules at the nanometre to micron scale, e.g. information about pore connectivity and accessibility. The methodology established here is expected to provide detailed insights into the dynamics of other important host-guest systems, such as bioactive molecules in porous materials for drug delivery or reactants in porous catalysts.

## Résumé

La microscopie de molécules individuelles devient de plus en plus importante pour la science des matériaux, car elle révèle des caractéristiques structurales et dynamiques qui ne sont pas accessibles si on applique des méthodes conventionnelles de la spectroscopie. Cette thèse se sert de cette méthode pour étudier les dynamiques des molécules uniques dans différents environnements poreux (les matériaux «hôtes») en utilisant la microscopie de champ-lointain et le suivi de molécules uniques. Une quantité significative de données ont été collectionnées et des méthodes sophistiquées pour l'analyse des données selon la théorie de la diffusion ont été développées. Une méthode a été mise au point pour mettre en relation directe des informations sur la diffusion, accessible par le suivi de molécules individuelles, et les images précises des structures poreuses prises par microscopie électronique en transmission (TEM). De plus, les résultats du suivi des molécules uniques ont été comparés avec les mesures de diffusion obtenues en appliquant la résonance magnétique nucléaire avec des gradients pulsés (PFG NMR) dans les mêmes échantillons. Toutes ces analyses donnent des informations détaillées sur les structures poreuses mais aussi sur les mouvements à l'intérieur des environnements différents.

Deux sortes de matériaux poreux en silice ont été étudiées dans cette thèse : des monolithes sol-gel et des films minces de mésoporeux. Les monolithes sol-gel comportent une large distribution des diamètres des pores autour d'une valeur moyenne. Les pores des matériaux mésoporeux, par contre, ont un diamètre bien défini et se présentent arrangées dans des topologies bien déterminées.

Des monolithes sol-gel de deux diamètres moyens des pores, 3 nm et 22 nm, ont été analysés par microscopie de molécules uniques en utilisant un nouveau colorant de type streptocyanine. Dans les matériaux à pores plus grands les molécules ont suivi une marche aléatoire (*random walk*) avec un coefficient de diffusion moyen de  $D_{M22}=0.72 \mu\text{m}^2 \text{s}^{-1}$ . Par contre, dans les monolithes avec les pores plus petits, des inhomogénéités de diffusion ont été détectées. La plupart des molécules ont diffusé dans des limites de quelques centaines de nanomètres. On pouvait observer d'autres molécules présentant des changements entre un état mobile et un état stationnaire. Des méthodes d'analyse des données susceptibles de dévoiler les inhomogénéités dans une trajectoire de molécule unique et d'évaluer les changements de coefficient de diffusion quantitativement ont été appliquées. À des fins de comparaison, des mesures de PFG NMR ont été exécutées avec les mêmes échantillons pour compléter les informations obtenues par le suivi de molécules uniques.

On ne peut pas voir directement les caractéristiques de la structure sur une échelle



de nanomètre par microscopie optique. C'est pourquoi une combinaison unique de la microscopie électronique en transmission et du suivi de molécules uniques a été développée, pour mettre en évidence la structure interne des ces films mésoporeux et pour découvrir la façon dont la dynamique de la diffusion dépend des structures sous-tendues des matériaux hôtes. Ainsi on pouvait mettre en relation directe l'information dynamique obtenue par le suivi des molécules individuelles avec les détails de la structure des hôtes poreux qui se dessinent dans les images de TEM.

Par ailleurs, ce travail montre comment des populations différentes de molécules diffusantes peuvent être distinguées dans les topologies variées des films minces et mésoporeux, en se servant de la microscopie de champ lointain et du suivi de molécules uniques. Des structures avec des distances différentes entre les pores et des topologies variées ont été synthétisées en utilisant deux tensioactifs différents en tant qu'agent structurant et en faisant varier le rapport silice/tensioactif dans la solution de synthèse. Des films minces avec une distance d'à peu près 6 nm entre des pores ont été synthétisés en utilisant le Brij 56 comme tensioactif. Ces films comportent une topologie soit hexagonale soit lamellaire, ou un mélange des deux. En se fondant sur la structure des trajectoires, des diffusivités et des orientations des molécules, il a été possible de faire la distinction entre des colorants qui bougent sur la surface externe des films minces et ceux à l'intérieur des pores. De plus, les colorants qui diffusent le long des canaux horizontaux de la phase hexagonale ont été distingués de ceux qui bougent beaucoup plus lentement dans les galeries lamellaires du matériau mésoporeux. Les molécules dans la phase hexagonale ont suivi des trajectoires très structurées, reflétant la structure ordonnée de l'hôte poreux, sur une échelle de plusieurs micromètres. Le coefficient moyen de diffusion dans cette phase était de  $D_{\text{Brij56:hex}} = 5.0 \times 10^{-3} \mu\text{m}^2 \text{s}^{-1}$ . Au contraire, la tache de diffraction des molécules dans la phase lamellaire a eu une forme de «beignet», correspondant à des molécules perpendiculaires à la surface de l'échantillon et donc perpendiculaires aux lamelles de silice. Ces molécules ont suivi une marche aléatoire et leur coefficient de diffusion était de deux ordres de grandeur plus petit que celui des trajectoires structurées dans la phase hexagonale ( $D_{\text{Brij56:lam}} = 5.3 \times 10^{-5} \mu\text{m}^2 \text{s}^{-1}$ ). Ces deux populations de molécules – les unes rapides et structurées, les autres lentes et de mouvement aléatoire, orientées perpendiculaire à la surface – ont coexisté dans les échantillons composés d'une mixture d'une phase hexagonale et lamellaire. Des films minces avec des pores plus grandes (env. 9 nm) et des structures hexagonales ou cubiques ont été synthétisés en utilisant le tensioactif Pluronic P123. La diffusion dans la phase hexagonale ressemblait à la diffusion dans les films synthétisés avec le tensioactif Brij 56, mais avec un coefficient de diffusion d'un ordre de grandeur plus élevé ( $D_{\text{P123:hex}} = 4.0 \times 10^{-2} \mu\text{m}^2 \text{s}^{-1}$ ). Les molécules dans la phase cubique ont bougé aléatoirement en deux dimensions, avec un coefficient de diffusion encore plus grand ( $D_{\text{P123:cubic}} = 3.0 \times 10^{-1} \mu\text{m}^2 \text{s}^{-1}$ ).

Les données et analyses présentés dans cette thèse donnent pour la première fois une image détaillée de la vraie structure mésoporeuse et de ses effets sur la dynamique des colorants sur une échelle de quelques nanomètres à quelques microns. Elles donnent des éclaircissements sur l'accessibilité et la connectivité des pores du matériau hôte. La méthodologie qui à été établie ici peut apporter une nouvelle vision détaillée de la dynamique dans d'autres systèmes hôtes, comme les molécules bio-actives incorporées dans des matériaux poreux servant à des thérapies ciblées par vectorisation des remèdes (*drug delivery systems*) ou comme des réactions dans des catalyseurs poreux.

## Zusammenfassung

Einzelmolekülmethoden spielen in den Materialwissenschaften eine immer wichtigere Rolle, da sie strukturelle und dynamische Eigenschaften aufzeigen können, die durch konventionelle Spektroskopie-Techniken nicht zugänglich sind. In dieser Arbeit wurden Einzelmolekülmethoden verwendet, um mittels Weitfeld-Mikroskopie und Einzelmolekül-*Tracking* die Dynamik einzelner Farbstoffmoleküle, der Gäste, in verschiedenen porösen Wirt-Systemen zu untersuchen. Es wurde eine große Anzahl von *Track*-Daten aufgenommen, und dabei wurden ausgefeilte Methoden zur Datenanalyse gemäß der Diffusionstheorie entwickelt. Zudem wurde eine Methode entwickelt, um die Diffusionsdaten aus Einzelmolekültrajektorien mit den elektronenmikroskopischen Abbildungen der Porenstruktur der Wirt-Systeme zu überlagern. Außerdem wurden die Resultate der Einzelmolekül-Datenanalyse mit Diffusionsmessungen an den gleichen Proben verglichen, die durch kernmagnetische Resonanz mittels gepulster Feldgradienten (PFG NMR) ermittelt wurden. Alle hier durchgeführten Untersuchungen gaben nicht nur ein detailliertes Bild der Porenstruktur der Wirt-Systeme, sondern auch einen tiefen Einblick in das Diffusionsverhalten der Gäste innerhalb der unterschiedlichen Umgebungen.

Zwei verschiedene Arten von porösen Silikamaterialien wurden in dieser Arbeit untersucht: Sol-Gel-Gläser und dünne, mesoporöse Filme. Sol-Gel-Gläser weisen eine sehr breite Verteilung unterschiedlicher Porenweiten um einen Mittelwert auf. Mesoporöse Materialien hingegen haben einen festen Porendurchmesser und die Poren sind in spezifischen Topologien angeordnet.

Sol-Gel-Gläser mit zwei unterschiedlichen mittleren Mesoporendurchmessern, 3 nm und 22 nm, wurden mittels Einzelmolekülmikroskopie untersucht. Dazu wurde ein neu synthetisierter Streptocyanin-Farbstoff verwendet. Es ergab sich, dass in den gröÙerporigen Materialien die Farbstoffmoleküle einer Zufallsbewegung folgten (*random walk*), mit einem mittleren Diffusionskoeffizienten von  $D_{M22}=0.72 \mu\text{m}^2 \text{s}^{-1}$ . Die Diffusion in den kleinerporigen Materialien wies hingegen Inhomogenitäten auf. Die Mehrzahl der Moleküle bewegte sich in Regionen mit unterschiedlichen Durchmessern, die auf einige hundert Nanometer beschränkt waren. Einige Moleküle wechselten zwischen mobilen und immobilen Zuständen. In diesen Fällen wurden geeignete Methoden zur Datenanalyse angewendet, die derartige Inhomogenitäten im Diffusionsverhalten eines einzelnen Moleküls aufdecken können und mit denen die Änderungen der Diffusionskoeffizienten quantitativ erfasst werden können. Zum Vergleich wurden in den gleichen Sol-Gel Gläsern PFG NMR Untersuchungen durchgeführt, welche die Einzelmolekülmessungen ergänzen.

Da die Porenstrukturen im Nanometerbereich nicht direkt durch optische Methoden abgebildet werden können, wurde eine einzigartige Kombination von Transmissionselektronenmikroskopie (TEM) und Einzelmolekül-*Tracking* entwickelt. So konnte die Porenstruktur der dünnen mesoporösen Filme direkt abgebildet werden und es konnte festgestellt werden, wie die zugrundeliegende Wirt-Gast-Struktur die Diffusionsdynamik der einzelnen Moleküle beeinflusst. Diese Methode ermöglichte also eine direkte Korrelation der dynamischen Information aus der Einzelmoleküldiffusion mit strukturellen Eigenheiten des porösen Wirt-Materials, die mit TEM abgebildet wurden.

Des Weiteren wurde in dieser Arbeit gezeigt, wie mittels hochauflösender Weitfeld-Mikroskopie und Analyse der Einzelmolekültrajektorien verschiedene Populationen von diffundierenden Teilchen in den unterschiedlichen Porentopologien der dünnen, mesoporösen Filme deutlich voneinander unterschieden werden können. Porensysteme mit unterschiedlichen Porenabständen und Porentopologien konnten durch Verwendung zweier Flüssigkristall-Template und durch Variation des Silica/Templat-Verhältnisses in den Syntheserezepten hergestellt werden. Mittels des Templates Brij 56 wurden dünne Filme mit einem Porenabstand von etwa 6 nm synthetisiert, die entweder eine hexagonale oder eine lamellare Porenanordnung aufwiesen oder auch ein Gemisch dieser beiden Topologien. Anhand der Struktur der Einzelmolekültrajektorien, der Diffusionskoeffizienten und der Orientierung der Moleküle konnten Farbstoffe, die sich an der Oberfläche der dünnen Filme bewegten, von solchen im Inneren der Porenstruktur unterschieden werden. Farbstoffe, die sich in waagrecht verlaufenden Röhren der hexagonalen Phase bewegten, konnten von Farbstoffen, die sich deutlich langsamer zwischen den Platten der lamellaren Struktur bewegten, abge-

grenzt werden. In der hexagonalen Phase diffundierten die Moleküle über mehrere Mikrometer hinweg entlang ausgestreckter Pfade, welche die Struktur des porösen Wirt-Systems widerspiegelten. Ihr durchschnittlicher Diffusionskoeffizient betrug dabei  $D_{\text{Brij56:hex}} = 5.0 \times 10^{-3} \mu\text{m}^2 \text{s}^{-1}$ . Im Gegensatz dazu wurden in der lamellaren Phase *Donut*-förmige Beugungsbilder beobachtet, die zeigen, dass die Moleküle hier senkrecht zum Probenstück und damit senkrecht zu den Schichten der lamellaren Phase ausgerichtet waren. Diese Moleküle folgten einer Zufallsbewegung, wobei ihr Diffusionskoeffizient zwei Größenordnungen kleiner war als der der strukturierten Moleküle in der hexagonalen Phase ( $D_{\text{Brij56:lam}} = 5.0 \times 10^{-5} \mu\text{m}^2 \text{s}^{-1}$ ). Diese zwei Populationen von Molekülen – die einen schnell und strukturiert, die anderen senkrecht ausgerichtet, sich langsam und ungeordnet bewegend – lagen in einer Probe mit einem Gemisch beider Porennetzwerke gemeinsam vor. Dünne Filme mit größeren Porenabständen (ca. 9 nm) und hexagonaler oder kubischer Porenanordnung konnten unter Verwendung des Templats Pluronic P123 synthetisiert werden. Die Diffusion in der hexagonalen Struktur war ähnlich der, die in den mittels Brij 56 hergestellten hexagonalen Filmen gefunden wurde. Mit Pluronic P123 als Templat war der Diffusionskoeffizient allerdings eine Größenordnung höher ( $D_{\text{P123:hex}} = 4.0 \times 10^{-2} \mu\text{m}^2 \text{s}^{-1}$ ). In der kubischen Phase diffundierten die Moleküle unstrukturiert, gemäß einer Zufallsbewegung in zwei Dimensionen, mit einem noch etwas größeren Diffusionskoeffizienten als in der hexagonalen Phase ( $D_{\text{P123:cubic}} = 3.0 \times 10^{-1} \mu\text{m}^2 \text{s}^{-1}$ ).

Insgesamt bieten die in dieser Doktorarbeit dargestellten Ergebnisse zum ersten Mal ein detailliertes Bild der mesoporösen Porenstrukturen und sowie ihres Einflusses auf die Dynamik der Farbstoffmoleküle auf der Nanometer- und Mikrometerskala. Zum Beispiel vermitteln sie Informationen über Verbindungen der Poren miteinander und über die Zugänglichkeit der Poren. Es wird erwartet, dass die hier vorgestellte Methodik Aufschluss über die Dynamik in anderen bedeutenden Wirt-Gast-Systemen geben kann. Mögliche Anwendungen sind beim Einschluss von bioaktiven Molekülen in porösen Materialien in der Pharmakotherapie (*drug delivery systems*) oder bei Reaktionen in porösen Katalysatoren zu sehen.

# Contents

<b>1</b>	<b>Introduction</b>	<b>1</b>
<b>2</b>	<b>Porous Materials</b>	<b>5</b>
2.1	Sol-Gel Glasses . . . . .	5
2.2	Mesoporous Thin Films . . . . .	7
2.3	Techniques for Investigation of Porous Matter . . . . .	10
2.3.1	X-ray Diffraction . . . . .	11
2.3.2	Electron Microscopy . . . . .	12
2.3.3	Atomic Force Microscopy (AFM): Surface Imaging . . . . .	14
2.3.4	Sorption Isotherms . . . . .	16
2.3.5	Pulsed-Field Gradient NMR . . . . .	18
<b>3</b>	<b>Single-Molecule Microscopy</b>	<b>21</b>
3.1	Principles of Fluorescence Microscopy . . . . .	21
3.2	Fluorescence Techniques for the Observation of Single Molecules . . . . .	24
3.2.1	Wide-field Methods . . . . .	25
3.2.2	Confocal Microscopy . . . . .	28
3.2.3	Comparison of Wide-field and Confocal Microscopy Methods . . . . .	30
3.3	Wide-Field Imaging Setup . . . . .	31
3.3.1	Excitation Pathway . . . . .	31
3.3.2	Detection Pathway . . . . .	33
3.4	Single-Molecule Tracking . . . . .	34
3.4.1	Fitting Functions . . . . .	34
3.4.2	Factors Influencing the Quality of the Fit . . . . .	35
3.4.3	Automated Single-Molecule Tracking . . . . .	38
3.4.4	Experimental Positioning Accuracy . . . . .	39
<b>4</b>	<b>Diffusion: Theory and Trajectory Analysis</b>	<b>41</b>
4.1	Microscopic Theory of Diffusion . . . . .	41
4.1.1	Theory of a Random Walk . . . . .	41
4.1.2	Probability Distributions . . . . .	44
4.1.3	Cumulative Probability Distributions . . . . .	45

## Contents

4.1.4	Deviations from the Ideal Behaviour . . . . .	48
4.2	Track Analysis . . . . .	50
4.2.1	Global Analysis . . . . .	50
4.2.2	Step Length Analysis . . . . .	51
4.2.3	Angles between Successive Steps . . . . .	58
<b>5</b>	<b>Diffusion of the Streptocyanine Dye 9A1 in Porous Sol-Gel Materials</b>	<b>63</b>
5.1	Synthesis of the Sol-Gel Glasses . . . . .	64
5.1.1	Sample Preparation for Single-Molecule Microscopy . . . . .	65
5.1.2	Sample Preparation for Pulsed-Field Gradient NMR . . . . .	66
5.2	Analysis of Host and Guest . . . . .	67
5.2.1	Sorption Isotherms . . . . .	67
5.2.2	Spectra of the Fluorescent Dye <b>9A1</b> . . . . .	68
5.3	Single-Molecule Measurements . . . . .	69
5.3.1	Single-Molecule Trajectories: Overview . . . . .	69
5.3.2	Duration of the Tracks: Experiment and Simulation . . . . .	71
5.3.3	Mean-Square Displacement Analysis . . . . .	71
5.3.4	Mobile Molecules in <b>M22</b> and <b>M3</b> : Individual Trajectories . . . . .	76
5.3.5	Distribution of Angles . . . . .	78
5.4	Pulsed-Field Gradient NMR in Sol-Gel Monoliths . . . . .	79
5.4.1	Measurements of Ethylene Glycol Self-Diffusion in <b>M22</b> , <b>M3</b> and <b>M4</b> . . . . .	80
5.4.2	Temperature Dependence of the Diffusion in <b>M4</b> . . . . .	82
5.4.3	Ethylene glycol self-diffusion in <b>SG8</b> , <b>SG26</b> and <b>SG21</b> . . . . .	85
5.4.4	Ageing of the Samples <b>M3</b> and <b>M22</b> . . . . .	86
5.4.5	Diffusion of the Dye <b>9A1</b> in <b>M22</b> . . . . .	88
5.5	Summary . . . . .	90
<b>6</b>	<b>Superimposing Single-Molecule Trajectories on TEM images</b>	<b>93</b>
6.1	Synthesis . . . . .	94
6.1.1	Ultrathin Mesoporous Films . . . . .	94
6.1.2	Incorporation of the Dye Molecules . . . . .	95
6.1.3	Substrates Suitable for TEM and Optical Wide-field Microscopy . . . . .	96
6.1.4	Recipe . . . . .	97
6.1.5	Characterisation of the Host: XRD and Ellipsometry . . . . .	98
6.2	Pattern Recognition - Identification of the same Sample Region in SMT and TEM . . . . .	98
6.3	Single-Molecule Tracking . . . . .	101
6.4	Transmission Electron Microscopy at High Resolution . . . . .	102
6.5	Overlaying SMT and TEM . . . . .	104

6.6	Individual Trajectories Correlated with the Pore Structure . . . . .	106
6.6.1	U-Trajectory: Diffusion in curved segments and at a domain boundary . . . . .	107
6.6.2	S-Trajectory: Diffusion along curves, at domain boundaries and stop at a less ordered region . . . . .	110
6.6.3	Y-Trajectory: Diffusion along strongly curved segments close to the PS beads . . . . .	113
6.7	Summary . . . . .	116
<b>7</b>	<b>Diffusion of TDI in Spin-coated Mesoporous Thin Films</b>	<b>119</b>
7.1	Synthesis of Thin Films with Different Topologies . . . . .	120
7.1.1	Overview of the Different Synthesis Recipes . . . . .	120
7.1.2	Substrates . . . . .	121
7.1.3	Different Fluorescent Dyes . . . . .	121
7.2	Diffusion of Single Molecules in Brij 56 Templated Films . . . . .	123
7.2.1	Analysis of the Host Structure . . . . .	123
7.2.2	Diffusion Measurements and Single-Molecule Tracking . . . . .	127
7.2.3	Mean-Square Displacement Analysis . . . . .	137
7.2.4	Distribution of Angles between Successive Steps . . . . .	141
7.2.5	Comparison with Symmetric Dyes: SW-TDI and DIP-TDI . . . . .	142
7.3	Pluronic Templated Films . . . . .	145
7.3.1	Characterisation of the Host . . . . .	145
7.3.2	Single-Molecule Trajectories in the Hexagonal Phase (P1) . . . . .	147
7.3.3	Single-Molecule Trajectories in the Cubic Phase (P2) . . . . .	155
7.3.4	Comparison of Diffusion in the Hexagonal and the Cubic Phase . . . . .	158
7.4	Summary . . . . .	159
<b>8</b>	<b>Overview: Diffusion Measurements by SMT and other Methods</b>	<b>161</b>
8.1	Diffusion Measurements by Tracking of Single Fluorescent Molecules . . . . .	161
8.2	Single-Molecule Experiments in Porous Hosts . . . . .	165
	<b>List of Abbreviations</b>	<b>171</b>
	<b>Bibliography</b>	<b>173</b>
	<b>Acknowledgements</b>	<b>187</b>
	<b>List of Publications</b>	<b>189</b>
	<b>Curriculum Vitae</b>	<b>191</b>





# 1 Introduction

The investigation and manipulation of matter on an atomic or molecular scale emerged as one of the key technologies of the 21<sup>st</sup> century. This field has become known under the title 'nanotechnology'. The prefix nano- is derived from the Greek word for dwarf (*νάννος*) and signifies a part in a billion ( $10^{-9}$ ). A nano-metre is in the range of ten atomic bonds, the size of an average organic molecule. Nanotechnology as such was born in the 1980's when new microscopy techniques were invented that allowed imaging of surfaces at the nanometre scale: Scanning tunnelling microscopy (STM)<sup>2,3</sup> in 1981 and atomic force microscopy (AFM)<sup>4</sup> in 1986, using nano-scale interactions of surface atoms with tunneling electrons or forces from sharp tips. Soon after this the first investigations of single molecules with optical microscopy were published.<sup>5,6,7,8</sup> The advantage of optical methods is that not only surface features can be investigated but also the behaviour of individual particles in the interior of a host matrix can be observed. This work is focussed on the investigation of translational diffusion of individual dye molecules incorporated into mesoporous hosts using optical single-molecule microscopy methods.

Two different types of host systems were investigated in this work: Mesoporous thin films, synthesized via a liquid-crystal template mechanism resulting in a very narrow pore size distribution, and sol-gel glasses, prepared without the use of a structure directing template and thus exhibiting a broad distribution of pore sizes. Ever since their first synthesis in the early 1990's by Beck *et al.*,<sup>9,10</sup> the field of liquid-crystal templated, mesoporous materials has undergone rapid and sustained development. The tunability of their structural order, pore size, pore topology and the composition of the framework material has attracted much attention, resulting in a variety of periodic materials: e.g. materials with very large pore sizes (over 10 nm),<sup>11</sup> different cubic, hexagonal and lamellar structures, and framework compositions containing many metal oxides and even non-oxides,<sup>12,13,14,15</sup> to name just a few. These attractive pore systems have been used as hosts for numerous molecular and cluster-based catalysts,<sup>16</sup> for selective sequestration of contaminants<sup>17</sup> and chromatography, for the stabilization of conducting nanoscale wires, as a matrix for carbon casting,<sup>18</sup> and for novel drug delivery systems.<sup>19,20</sup> Though less well defined than templated mesoporous materials, amorphous, micro- and mesoporous sol-gel glasses are widely used as hosts because

they are cheap and easy to prepare by sol-gel synthesis in a variety of physical forms, including powders, cast monoliths, and spin-coated thin films. Porous sol-gel materials may also perform molecular recognition or contribute to stabilization of reactive species.

Hybrid materials in which an organic guest molecule is encapsulated in a mineral host have many and varied applications, including biological and environmental sensors,<sup>21</sup> laser media,<sup>22,23,24</sup> nonlinear optical devices,<sup>25</sup> and photocatalysis.<sup>26</sup> In most of these applications the transport or orientation of guest molecules in the pores is of paramount importance for successful preparation or for the functionality of the materials. More than 30 years ago Paul Weisz emphasized the importance of diffusion processes in mass separation and chemical conversion in microporous materials.<sup>27,28</sup> In many metal-catalyzed industrial reactions, diffusion of reactants into the porous silica used to support the metal clusters is of importance.<sup>29</sup>

In this thesis, single-molecule fluorescence microscopy has been used to characterise both types of host-guest systems, i.e. sol-gel glasses and mesoporous thin films, by tracking the diffusion of individual dye molecules inside their pores. Extremely long trajectories with high statistical quality give for the first time a detailed picture of the structure and connectivity of different pore systems. The molecular 'beacons' directly trace out in striking detail the 'landscape' of the inner pore system of the host over large areas, and a detailed view of the dynamics of the guest molecules inside the porous host is obtained. To understand the intricate interplay of guest molecule dynamics – the primary data obtained by single-molecule microscopy – and host pore structure, an independent means to determine the latter is needed. Therefore, a unique combination of electron microscopic mapping and optical single-molecule tracking experiments has been developed that provides a detailed picture of the real mesoporous defect structure and its effects on the dynamic behavior of dye molecules at the nanometre scale. The porous structures are directly correlated with the diffusion dynamics of single molecules. This approach allows to observe, in unprecedented detail, how single fluorescent dye molecules travel through linear or strongly curved sections of the hexagonal channel system in a thin film of mesoporous silica, how they decelerate in certain segments of the channel structure, and how they bounce off domain boundaries. Even lateral motions between 'leaky' channels can be observed, which allow the molecules to explore different parallel channels within well-ordered periodic structures. One of the strengths of single-molecule tracking compared to ensemble measurements is bringing out heterogeneities. However, one of the weaknesses is bias by the operator, i.e. he might select bright molecules, or those that appear to show an especially interesting behaviour. A particular strength of the work presented here is comparison of single-molecule tracking with other different techniques, like diffusion measurements

---

using pulsed-field gradient NMR and superimposing single-molecule trajectories with transmission electron micrographs.

## **This work is structured as follows:**

After this introduction, Chapter 2 describes the different sample systems that were investigated in this work. First, the sol-gel process and the synthesis of micro- and mesoporous sol-gel glasses will be described. These silica materials have a certain distribution of pores present in the sample, because no structure directing agent is used for the synthesis. If a structure directing template, like a liquid-crystal template surfactant, is added to the synthesis solution, mesoporous silica thin films<sup>30,31,32</sup> can be synthesized. The template induces the formation of pores of a given diameter. The last part of this chapter focusses on methods to investigate structural properties of such porous materials, like X-ray diffraction, transmission electron microscopy, atomic force microscopy and sorption isotherms. In addition a brief introduction to diffusion measurements using pulsed-field gradient NMR will be given.

Following this presentation of the materials, an introduction to fluorescence microscopy, single-molecule methods and single-molecule tracking is provided in Chapter 3. The technical details of the microscope setup and the tracking procedure are presented in the same chapter.

In Chapter 4, the theoretical background of diffusion on a microscopic scale is explained, and the methods used to analyse single-molecule tracking data in this work are discussed.

In Chapters 5 to 7 the results of applying the techniques described in Chapter 3 and 4 to the systems introduced in Chapter 2 are discussed. First, single-molecule diffusion in sol-gel glasses, which do not have a certain pore topology or diameter, is reported on (Chapter 5). The following two chapters focus on the more ordered mesoporous thin films, having specific arrangement of pores of a given diameter. In Chapter 6 a newly developed method to overlay single-molecule tracking data with the structural information obtained by transmission electron microscopy is described. Then, a detailed discussion of single-molecule tracking experiments in mesoporous thin films, having various pore topologies and diameters, follows (Chapter 7). At the end of each Chapter a summary of the main results is provided.

## *1. Introduction*

---

In the end the data obtained in this work are compared to and put into the context of diffusion measurements conducted elsewhere on similar systems. Special focus will be on the comparison of the findings in this thesis compared to those in the literature, e.g. the diffusion coefficients or the general information about the materials (as far as it could be found in the literature). This chapter serves – along with the abstract in the beginning of this document – as overall conclusion of this thesis.

## 2 Porous Materials

In this chapter the porous materials that were investigated in this work are introduced. Physical and chemical properties of porous matter are governed by the pore diameter. IUPAC discerns three size regimes: micropores, mesopores and macropores (Table 2.1).<sup>33</sup>

**Table 2.1: IUPAC classification with of pore width.**

<b>Pore Diameter</b>	0 – 2 nm	2 – 50 nm	> 50 nm
<b>Definition</b>	Micropores	Mesopores	Macropores

The materials used in this work have pores in the meso- and also the micro-range. As important as the pores' diameter is their degree of ordering. Two groups of materials with different degrees of pore ordering have been investigated: sol-gel glasses and mesoporous thin films. Mesoporous materials are synthesized via a liquid-crystal templating mechanism and have a very defined pore topology and pore diameter, determined by the template used in the synthesis. In contrast, no template is used for the synthesis of sol-gel glasses and thus there can be a relatively broad distribution of pore sizes in these materials.

The synthesis procedure of the sol-gel glasses is presented first. Then the synthesis of mesoporous thin films by liquid-crystal templating and evaporation induced self-assembly will be explained. Different techniques for the investigation of porous matter, such as X-ray diffraction, electron microscopy or sorption isotherms close this chapter.

### 2.1 Sol-Gel Glasses

The sol-gel process, invented more than 150 years ago by Ebelmen,<sup>34</sup> is a low-temperature technique for synthesizing solid glass slabs or thin films from a colloidal dispersion – called a sol – through gelation, i.e. flocculation of the sol, and a successive drying step.

## 2. Porous Materials

The method is based on subjecting organometallic compounds, such as silicon alkoxides, to hydrolysis and polycondensation reactions. The process of the formation of, e.g. a silica glass can be explained as follows.

The method is usually a three step process, illustrated in Figure 2.1a for a silica glass. First an organometallic precursor, here a tetra-alkoxy orthosilicate, is hydrolyzed (I). The second stage of the process is the polycondensation of the hydrolysis products, yielding a 3D crosslinked network (II). In the final drying step the solvent is removed at atmospheric pressure and elevated temperature which is most often combined with a shrinkage of the material, resulting in the final xerogel. Figure 2.1b sketches the sol-gel process, starting from the hydrolysis of the precursor via gelification of the sol and the final drying and heating to form the sol-gel glass.

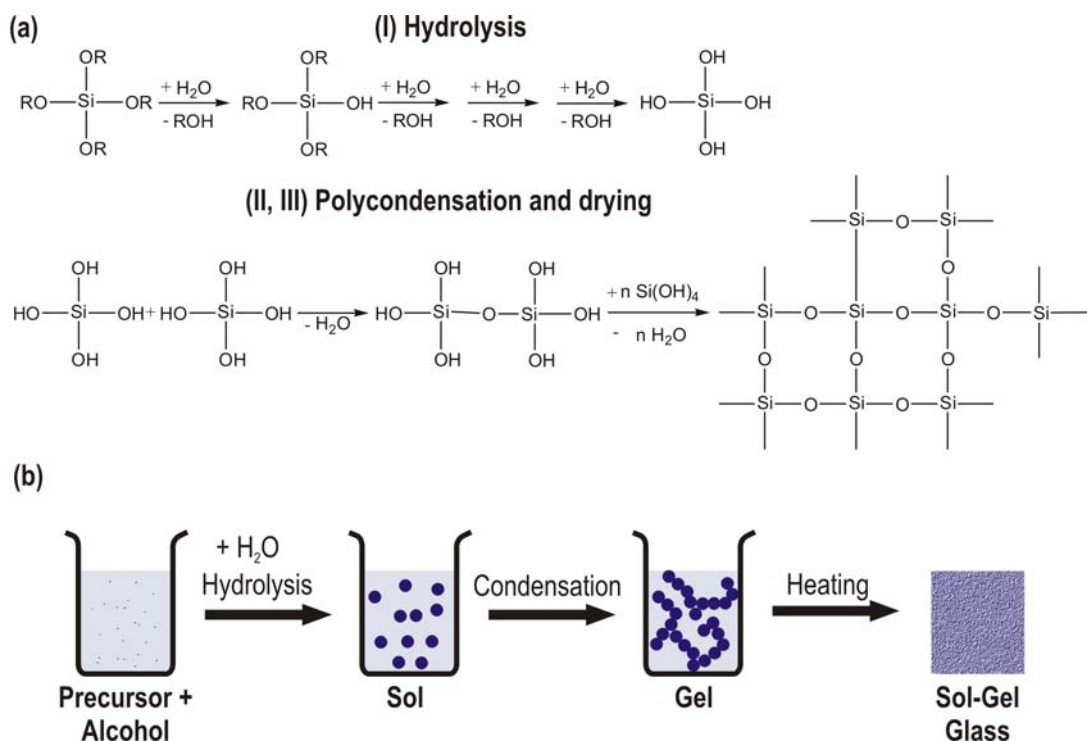


**Figure 2.1: Steps in the sol-gel synthesis process.** (a) Hydrolysis and condensation reactions of a tetra-alkoxy orthosilicate. (b) Schematic representation of the synthesis steps.

No template is used in this synthesis procedure. Therefore, the final glasses have a wide distribution of pore diameters in the micro- and mesopore range (cf. Table 2.1).

The hydrolysis can be catalyzed by an acid (most commonly by HCl or HNO<sub>3</sub>) or nucleophilic bases. The hydrolysis reaction rate is also influenced by steric conditions. For instance, it decreases with the size of the alkoxy group, as shown by the slower hydrolysis of tetraethyl orthosilicate than that of tetramethyl orthosilicate.<sup>35</sup>

Due to their high porosity sol-gel glasses can host different guests, and are used for

a wide variety of applications, such as supports for catalysis, optical filters, materials for linear and non-linear optics, or biosensors.<sup>36,37,38</sup> Porous sol-gel materials may also perform molecular recognition or contribute to stabilization of reactive species. Mild synthetic conditions allow the addition of dopants such as organic dyes, inorganic ions, and nanoparticles during the synthesis. This has been exploited, e.g. to build a solid state laser.<sup>39,40,41</sup> Sol-gel glasses are particularly important as hosts because they are cheap and easy to prepare in a variety of physical forms, including powders, cast monoliths and spin-coated thin films. However, working with sol-gel glasses is sometimes challenging. The synthesis is dependent on a number of different parameters which cannot always be controlled. Therefore the same recipe might result in different porosities of the final glasses and a lot of effort has to be made to find reproducible synthesis procedures. Furthermore, the structures are subject to ageing by further, slow polymerisation induced by residual water. Therefore porosity changes even months or years after the synthesis can occur.

Such silica glasses doped with fluorescent dyes have been studied in the present work using single-molecule fluorescence techniques and pulsed-field gradient NMR. Ageing of the samples was analysed by sorption isotherms. The experiments and results are described in Chapter 5.

## 2.2 Mesoporous Thin Films

Mesoporous materials have attracted considerable attention within the last few years as building units for nanoscale architectures like molecular sieves,<sup>17</sup> catalyst supports,<sup>16</sup> nano-reactors for a variety of chemical reactions and as hosts for nanostructured materials, e.g. for carbon casting.<sup>18</sup> They are synthesized as powders or films with pore-diameters between 2 – 50 nm from silica-containing precursor-solutions using a surfactant as structure directing agent.<sup>42</sup> According to their degree of structural order, they can be classified between the highly ordered, crystalline zeolites and the sol-gel glasses that were described in the previous section. The mesoporous materials show periodic arrangement of pores, but the mesopore walls are amorphous. Mesoporous powders can be obtained under either basic or acidic conditions, resulting, e.g. in MCM (Mobile Catalytic Material) or SBA (Santa Barbara Acidic) materials, respectively.<sup>11,10</sup> Thin films have been prepared on a variety of substrates with a thickness from a few nanometres to several microns. Compared to mesoporous powders they have the advantage of structure orientation with respect to the substrate surface and alignment of the pores over a macroscopic length scale. Mesoporous thin films can be prepared by evaporation-induced self-assembly (EISA),<sup>43,31</sup> which is based upon

the sol-gel procedure presented in the previous section. This approach employs homogeneous silica/surfactant/alcohol/water coating-solutions, containing silica precursors obtained by acid-catalyzed hydrolysis of silica monomers, such as tetraethyl orthosilicate (TEOS). Initially the surfactant concentration is below the critical micelle concentration (CMC), which means that no micelles, i.e. small units of self-assembled surfactant molecules, are present. The synthesis solutions are spin- or dip-coated to give preferential evaporation of the volatile co-solvent. The rapid solvent evaporation drives the self-assembly process towards the CMC, the formation of the liquid-crystal mesophase and simultaneously the silica condensation.<sup>44</sup> This process is illustrated in Figure 2.2.

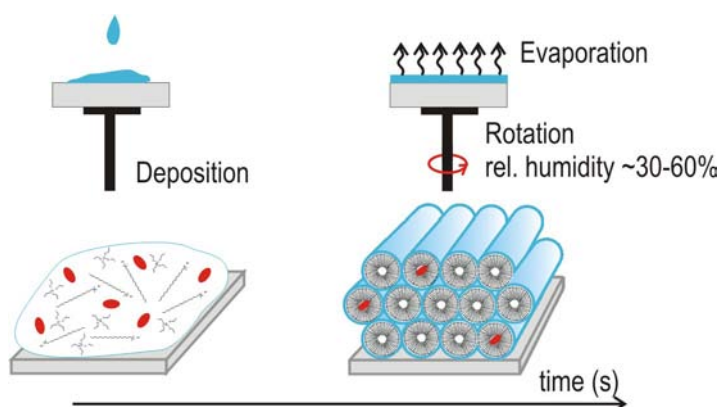


**Figure 2.2: Evaporation induced self-assembly (EISA).** The precursor solution is deposited on a substrate and rotated at about 3000 rpm. The solvent evaporates and after reaching the critical micelle concentration, the template molecules and the silica oligomer self-assemble. Finally, the silica condensates and the mesoporous film is formed.

In general, the synthesis mechanism can be explained either by a two-step process, where the liquid-crystal phase is built first and the silica is cast around it, or by a cooperative one-step mechanism, in which addition of the silicate to the surfactant molecules pre-assembles the subsequent silicate-encased surfactant micelles. The latter mechanism appears to be more likely,<sup>45,46</sup> as the formation of the mesopore phases often takes place at much lower surfactant concentrations than the critical micelle concentration of the pure liquid-crystal template. In this mechanism the multidentate charge density matching between soluble inorganic species and surfactant molecules determines the initial interaction between them.<sup>47,48</sup> In addition, <sup>14</sup>N-NMR in-situ measurements have shown, that no pure hexagonal surfactant liquid-crystal phase is formed.<sup>49</sup>

Different mesopore phases can be synthesized by varying the molar ratio between the surfactant and the silica oligomers of the precursor solution.<sup>32,50,51</sup> An important aspect of mesophase formation is how the hydrophobic tails of the surfactant self-organise within the material. To describe the packing quantitatively an effective surfactant pack-



ing parameter  $g$ , like it is used for lyotropic liquid-crystal phases,<sup>52,53</sup> is defined as

$$g = \frac{V}{a_0 l} \quad (2.2.1)$$

where  $V$  is the complete volume of the surfactant,  $a_0$  the effective head group area at the micelle surface and  $l$  the length of the surfactant tail. The  $g$ -parameter can be used to predict in first approximation the geometry of the micellar aggregates. The curvature of the micellar surface decreases with increasing  $g$ , i.e. with increasing  $V$  and decreasing  $a_0$  and  $l$ . In aqueous solution the hydrophobic heads are on the outside of the micelles. Thus a high head surface area and length of the hydrophobic tails favors the formation of spherical micelles, like in a cubic phase. Increasing the overall volume while decreasing the head surface area, reduces the volume in the interior of a sphere and thus cylindrical micelles, like in the hexagonal phase, or planar bilayers as in a lamellar phase are formed.

**Table 2.2: Surfactant packing parameter and mesophase topology.**

<b>g-factor</b>	$1/3$	$1/2$	$1/2 - 2/3$	1
<b>Topology</b>	cubic	hexagonal	cubic	lamellar
<b>Space group</b>	$(Pm3n)$	$(P6m)$	$(Ia3d)$	

The most frequently obtained 2D-mesophase consists of hexagonally ordered arrays of tubular pores oriented with the long axis parallel to the substrate surface. Lamellar structures, 3D cubic phases, and 3D hexagonal mesophases have been reported as well. Three of these topologies are sketched in Figure 2.2.

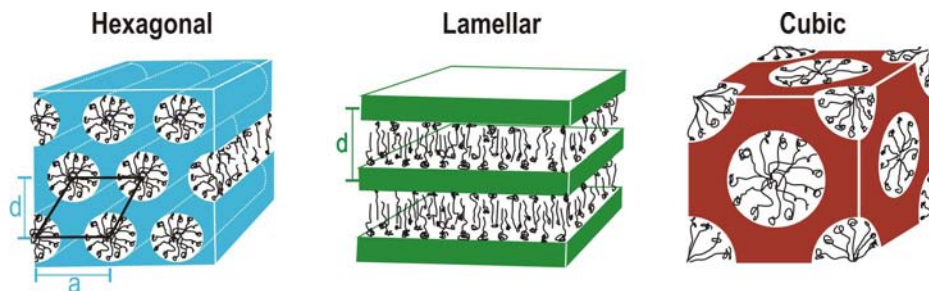


**Figure 2.3: Mesopore topologies.** Through different recipes, i.e. surfactant/silica concentration, mesopore structures with (a) hexagonal 2D- $P6m$ , (b) lamellar or (c) cubic ( $Pm3n$ ) arrangement of pores can be synthesized.

All structures have a preferred orientation, e.g. through alignment of the tubular pores parallel to the substrate surface in the 2D-hexagonal mesophase. However, on a long range the pores can be curved and they are organised in domains with different pore

orientation.<sup>54</sup> Not much is known about the size of the domains or factors influencing the domain growth. Transmission electron microscopy (TEM) measurements presented later in this work, yield domain sizes from a few hundred nanometres up to several microns.

After synthesis the liquid-crystal template usually remains inside the silica pores. This is essential for the experiments in this work, as the diffusion of dyes in as-synthesized materials was investigated, i.e. the hydrophobic dyes were diffusing in the interior of the surfactant filled pores. The template can be removed in an additional step, the so-called calcination, to increase the free pore volume and to make the mesoporous materials more robust. The sample is heated to about 500°C, in order to decompose the organic surfactants. Most importantly however, calcination does not only destroy the surfactant but also organic dyes that are incorporated into the pores during the synthesis. Therefore the materials used in this work were used as-synthesised and not calcined. It is known that the calcination process might introduce defects into the thin films,<sup>55</sup> and decreases both the pore-to-pore distance and the pore diameter. However, such mesoporous materials become more robust after calcination.

### 2.3 Techniques for Investigation of Porous Matter

In this section an overview over the variety of standard techniques to investigate the properties of the porous host materials is given. X-ray diffraction (XRD) is used to distinguish between different pore topologies and to determine the average pore-to-pore distances in a periodically ordered phase. The pore structure on the nanometre scale can be analysed via transmission electron microscopy (TEM). With this technique only small areas of the sample ( $< 1 \mu\text{m} \times 1 \mu\text{m}$ ) can be analysed in one image. In the ensemble regime the adsorption behaviour of small molecules, usually  $\text{N}_2$ , provides information about the internal surface area, the porous volume, the distribution of pore diameters and some extent the shape of the pores. However, nitrogen sorption isotherms on thin films are very difficult to obtain. Surface features of the samples can be investigated using atomic force microscopy (AFM) or scanning electron microscopy (SEM). To obtain a thorough characterisation of the material, the different methods presented here have to be used on the same sample. Furthermore, for most of the applications of such materials the behaviour of guest molecules inside the pores is important. One method to investigate diffusion of small species inside the porous system is the pulsed-field gradient NMR spectroscopy, which will be introduced at the end of this chapter. However, the above mentioned techniques are not sufficient for a complete characterisation of mesoporous materials. Further methods are needed to obtain

a better understanding of silica host structures and in addition the behaviour of guest molecules incorporated into the pores. Single-molecule diffusion measurements, like they were established in this work, provide such information, using fluorescent dye molecules as guests. The dynamics and photophysical properties of such guests within a porous host matrix are followed using fluorescence microscopy methods. Such investigations were the main topic of this work, thus fluorescence methods and diffusion theory will be covered in two individual chapters.

### 2.3.1 X-ray Diffraction

Since it was discovered that X-rays travelling through a crystalline or partly crystalline medium are scattered in distinct directions,<sup>56</sup> X-ray diffraction (XRD) has become the method of choice for structure analysis of crystalline materials. As the inter-atomic distances in a crystal are on the order of the wavelength of X-rays, the bound electrons act as a diffraction grating. XRD gives the distance of regions with highest electron density, that is the distance from one crystal plane to the next. This distance is called the *d*-spacing. The unit cell parameter *a* can be calculated from that. The mesoporous materials investigated in this work do not exhibit a crystalline structure on the atomic scale. Nevertheless, through the liquid-crystal template synthesis, they contain pores with a fixed diameter and periodic arrangement of these pores. However, owing to the low degree of order in mesoporous materials compared to single crystals often only few Bragg peaks are observed.

According to the Bragg law (Equation 2.3.1) the incident X-rays of wavelength  $\lambda$  are scattered elastically on the sets of planes of the porous system with a distance *d* under the Bragg angle  $\theta$ ; *n* being here the order of diffraction:

$$n\lambda = 2d \sin \theta \quad (2.3.1)$$

Whereas in crystalline materials the scattering occurs at each of the atom layers of the crystal, resulting in characteristic sets of sharp lines, X-ray diffractograms of mesoporous thin films show only very few and broad peaks corresponding to the layers defined by the pore topology (see Figure 2.4a). Broadening of the peaks is due to variations in the pore diameter or variations of the interplane distances, e.g. parallel and normal to the substrate. As these distances are in the nanometre range, the scattering occurs at very low angles of the incident beam. The wavelength of a Cu  $K_{\alpha}$  source, which is commonly used in XRD, is  $\lambda=1.5418 \cdot 10^{-10}$  m. Therefore, the first order reflection ( $n=1$ ) for typical pore-to-pore distances of 3 – 10 nm is located at angles of 1.47 °or

## 2. Porous Materials

$0.44^\circ$ , with  $n\lambda/2d = \sin \theta$  equals  $2.6 \cdot 10^{-2}$  or  $7.7 \cdot 10^{-2}$ . The geometry of the measurement is depicted in Figure 2.4b.

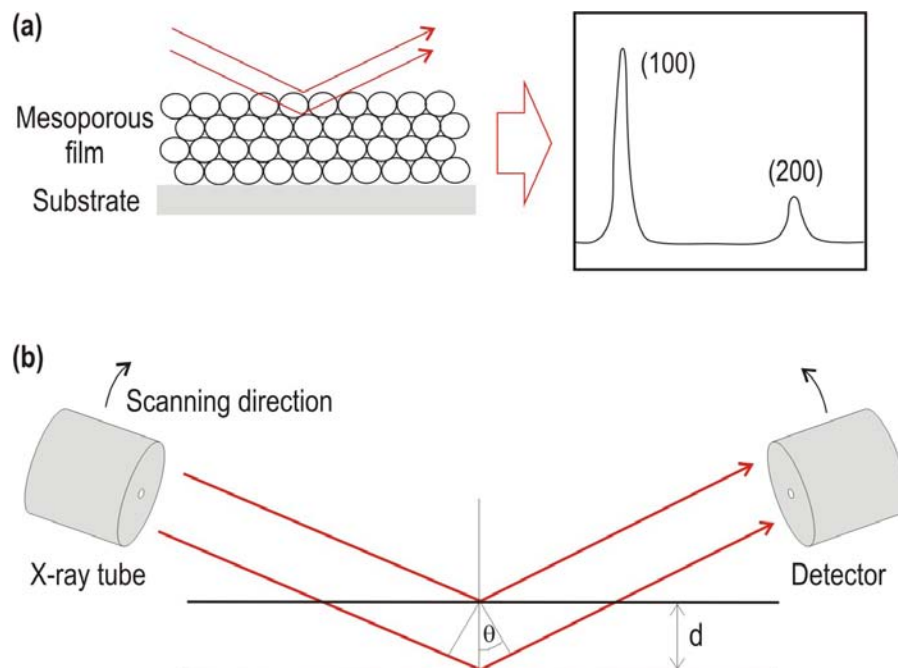


**Figure 2.4: 1D X-ray scattering.** (a) The incident X-rays are scattered on the planes of pores and collected under the same angle ( $\theta - \theta$  geometry), resulting in characteristic diffractograms. (b)  $\theta - \theta$  geometry in a XRD measurement [Adapted from<sup>57</sup>].

The measurements in this work were carried out on a Scintag XDS 2000 reflection ( $\theta - \theta$ ) diffractometer with  $\text{Cu K}_\alpha$  source. This method is fairly quick and non-destructive. However, as discussed above, the amount of information to be gained from 1D XRD is limited. Additional information, like the pore ordering with respect to the substrate, can be gained for example by electron microscopy techniques.

### 2.3.2 Electron Microscopy

Structures that are much smaller than the wavelength of visible light, like the pores of mesostructured silica materials, cannot be imaged by optical microscopy due to the diffraction limit (see below in the next chapter, Equation 3.4.8). In order to observe nanometre-scale topologies directly, electron microscopy techniques are used.<sup>58,59</sup> In a transmission electron microscope (TEM) the electrons are emitted from a filament and accelerated by a high voltage. The resulting electron beam is focussed onto the sample by electromagnetic fields, and the diffracted electrons are detected on a photographic film or a fluorescent screen. Figure 2.5 shows a schematic representation of a TEM setup.

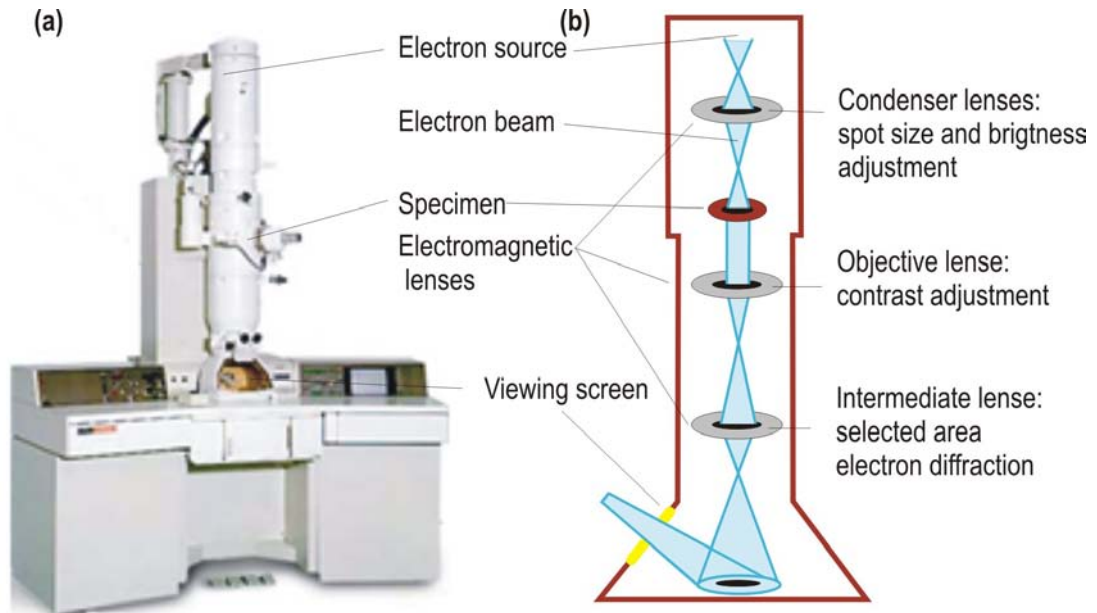


**Figure 2.5: Transmission electron microscope.** (a) Jeol JEM-2011 (b) Scheme of the beam path through the microscope [Adapted from<sup>57</sup>].

The de Broglie wavelength of electrons can be much smaller than the wavelength of visible light, and by tuning the applied electric fields a large range of magnifications can be obtained. Equation 2.3.2 describes the dependence of the wavelength  $\lambda$  on the accelerating voltage  $V$ , with Planck's constant  $h$  and  $m$ ,  $e$  the mass and charge of the electron, respectively:<sup>57</sup>

$$\lambda = \frac{h}{\sqrt{2meV}} \quad (2.3.2)$$

As we can see from this equation, the diffraction-limited resolution of the TEM is given by the ability to accelerate electrons. The higher the accelerating voltage the greater the theoretical resolving power. However, the imperfections of the electromagnetic lenses limit the resolution in practice. The electron beam primarily interacts with the bound electrons of the investigated material, thus the contrast and with it the practically achievable resolution also depends on the number of electrons per atom of the material. Carbon compounds, like organic materials, are difficult to image, and heavy elements like gold are very good electron scatterers and allow resolution down to 0.1 nm. For silica materials resolution in the nanometre range can be achieved, which suffices to see the main structural features of the materials investigated in this work.

One of the limitations of electron microscopy is that in a single high resolution image the area that can be observed is very small. An image that resolves the pore structure

of a mesoporous solid like the ones investigated in this work typically covers no more than about  $300\text{ nm} \times 300\text{ nm}$  of the sample. Larger areas can in principle be observed by mapping hundreds of such images together. This tedious and time-consuming procedure is practically limited to areas of about  $4\text{ }\mu\text{m} \times 4\text{ }\mu\text{m}$ . Moreover, it demands extremely high-quality samples that are thin enough for electron transmission over large areas. Since this is often not the case, invasive preparation, such as scratching, grinding and ion milling must be used.

In this work TEM images were obtained with a JEOL 2011 transmission electron microscope operated at 200 kV. Cross-sections were prepared by dimple grinding followed by argon ion polishing, with a dimple grinder and a precision ion polishing system (Gatan, Inc.). Alternatively, small pieces of the mesoporous film were scratched off the substrate using a razor blade. The resulting mesophase powder was transferred onto a copper grid for investigation with TEM. In addition, ultra-thin films were synthesized, which could be mapped over larger areas without additional preparation, as presented in detail in Chapter 6.

A complementary electron microscopy technique is scanning electron microscopy (SEM), where the reflected electron beam is rastered across the surface of the sample and the image is formed by counting backscattered electrons. To obtain good interactions of the beam with the surface, a thin layer of gold is sputtered onto the surface of the investigated material. Using SEM much larger areas ranging from micrometres to millimetres can be observed, but the resolution is not high enough to resolve, e.g. the pore system of a mesoporous thin film. The SEM images presented in Chapter 6 were obtained with a Phillips XL40ESEM scanning electron microscope.

### 2.3.3 Atomic Force Microscopy (AFM): Surface Imaging

The surface of mesoporous films can also be investigated by atomic force microscopy (AFM) with resolution down to a few nanometres. In general, the core element of an AFM is a probe consisting of a miniature cantilever and a sharp tip which is scanned over the sample, or the sample stage is moved underneath the tip using a piezo scanner. Forces between the tip and the sample surface lead to a deflection of the cantilever, when the tip is in close proximity of the surface. The deflection can be measured by focusing a laser spot onto the top of the cantilever and measuring the position of the reflected beam with an array of photodiodes. In this way, the surface structure can be imaged by the changes of the deflection of the tip when scanning. The universal character of the repulsive forces between the tip and the sample permits the examination of a practically unlimited range of materials. The general principle of AFM is sketched

in Figure 2.6a.

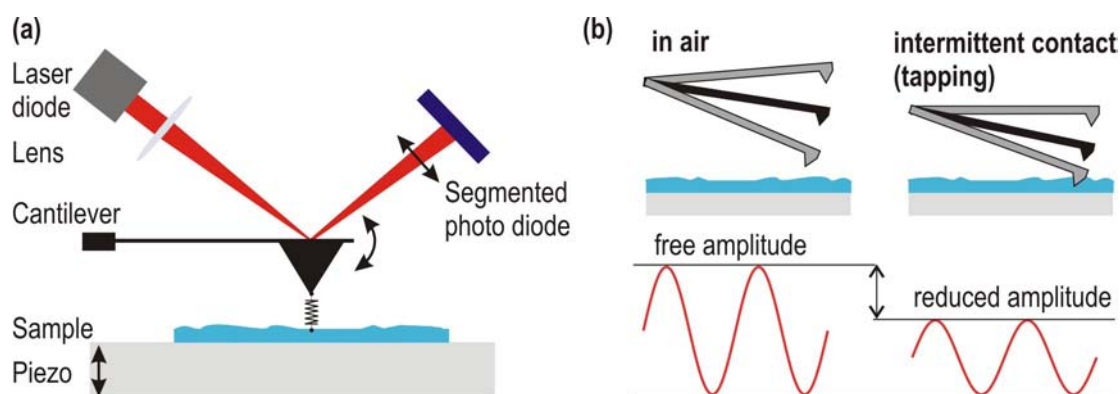


**Figure 2.6: Principle of an atomic force microscope and tapping mode AFM.** (a) While scanning the sample, the forces between tip and surface and thus the deflection of the cantilever change. The deflection of the cantilever is measured by the reflection of a laser beam, which is focussed on the top of the cantilever, on a photodiode array. (b) Tapping mode cantilever oscillation amplitude in free air and during scanning [Adapted from<sup>60</sup>].

In order to measure surface features the AFM can be operated in different modes. These modes can be distinguished via several criteria, e.g. if the tip is in contact with the surface or if frequency<sup>61</sup> or amplitude<sup>62</sup> changes of the cantilever deflection are the measured variable. In contact mode, the tip apex is in continuous contact with the surface, whereas in non-contact mode the tip does not touch the surface. An intermediate option is the tapping mode (also called intermittent mode or dynamic contact mode). The latter technique was used for the AFM images in this work, therefore it will be explained here in more detail. In this mode, the probe is driven into an oscillation at or close to its resonant frequency by a small piezoelectric element. Tip-to-sample interactions reduce the oscillation amplitude of the probe (Figure 2.6b). In practice, the oscillation amplitude is usually kept at a set-point value by adjusting tip-to-sample distance ( $z$ -position) through a feedback mechanism. The variations of the  $z$ -position during scanning are plotted as a function of the  $x,y$  position of the tip to create the height image. Additionally, material property variations can be mapped by recording the phase shift between the driving force and the tip oscillation. Amplitude modulation experiments usually involve amplitudes in the 1 – 100 nm range.

The AFM has several advantages over the SEM: First, it provides a real 3D image of the surface structure, whereas SEM can only give a 2D projection of the 3D image and no height profile. Second, no special sample treatment, such as metal coating, is needed for AFM. Third, it can be operated at ambient conditions or even in liquid, while electron microscopes work only in a high vacuum environment. Furthermore AFM can provide higher resolution than SEM; it is comparable in resolution to scanning tunneling microscopy and transmission electron microscopy. A disadvantage of

AFM compared with the SEM is the image size. The AFM can only image a maximum height on the order of micrometres and a maximum scanning area of around  $150\ \mu\text{m} \times 150\ \mu\text{m}$ .

The Surface images in this work were taken with a commercial AFM (Asylum Research MFP3D) in tapping mode. The Olympus AC160 SiN Cantilever was driven 5 % below its resonance frequency with a target amplitude of 1.2 V. In the measurements a set-point of 0.85 V was used to scan each surface with an image size of  $512\ \text{px} \times 512\ \text{px}$  and a scanning rate of 2 Hz per line.

### 2.3.4 Sorption Isotherms

In addition to the experimentally quite complex and costly techniques like XRD, TEM/SEM and AFM, sorption measurements can provide insight into the inner structure of mesoporous materials, i.e. the inner pore surface, the pore volume and the pore diameter distribution.<sup>63,64,65</sup> In a gas sorption measurement the sample is exposed to a controlled gas environment (usually dry nitrogen), and the volume  $V$  of adsorbed and desorbed gas is measured versus relative pressure  $p$  at constant temperature. An adsorption isotherm is the plot of  $V$  versus  $p/p_0$ , where  $p$  is the absolute pressure and  $p_0$  is the saturation vapor pressure. The gas adsorption proceeds via multilayer adsorption occasionally followed by capillary condensation, visible in step steps in the isotherms (e.g. Type IV, see Figure 2.7).

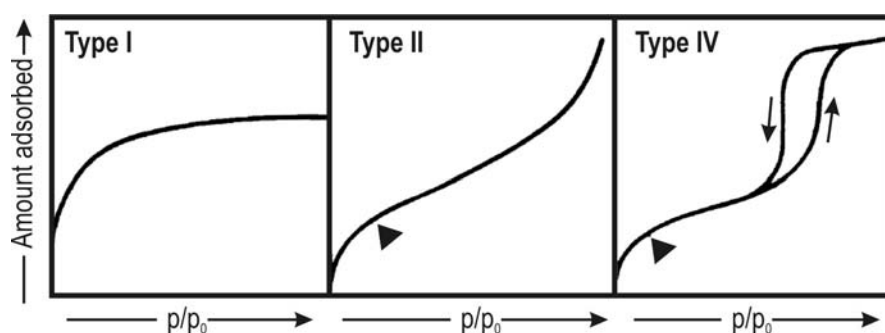


**Figure 2.7: Types of sorption isotherms.** Type I: microporous material, Type II: macroporous or non-porous material, Type IV: mesoporous material, the arrows indicate capillary condensation (up) and evaporation (down). The black triangles highlight the points at which monolayer coverage is complete and multilayer adsorption is about to begin<sup>66</sup>.

Physisorption isotherms are grouped into six types,<sup>66</sup> the most common three of which are sketched in Figure 2.7. At low surface coverage the isotherm is almost always linear. Type I isotherms are concave to the  $p/p_0$  axis and approach a limiting value as  $p/p_0 \rightarrow 1$ . Such reversible Type I isotherms are typical for microporous solids with rela-



tively small external surfaces (e.g. activated carbons, molecular sieve zeolites and certain porous oxides). The uptake is limited by the accessible micropore volume. A non-porous or macroporous material gives a reversible Type II isotherm, resulting from unrestricted monolayer-multilayer adsorption. The beginning of the almost linear middle section of the isotherm, highlighted by the black triangle, indicates the completion of monolayer coverage and the begin of multilayer adsorption. The initial part of the Type IV isotherm follows the same path as a Type II isotherm and is thus attributed to monolayer-multilayer adsorption. However, characteristic of the Type IV isotherm is hysteresis. Due to metastable 'gas' states or pore blocking,<sup>63,67</sup> capillary condensation (arrow up) and capillary evaporation (arrow down) in the mesopores occur most often not at the same relative pressures, which leads to the appearance of hysteresis loops. A steep curve in the capillary condensation regime indicates a narrow pore size distribution.

A model that allows to calculate the surface area from such multilayer adsorption isotherms was developed by Brunauer, Emmett, and Teller.<sup>68</sup> The BET model, called after its inventors, is an extension of the monolayer adsorption Langmuir theory,<sup>69</sup> to multilayer adsorption. It is based on the hypotheses that gas molecules physically adsorb on a solid in layers, that the number of layers is not limited, that there is no interaction between the layers, and that the Langmuir theory can be applied to each layer. In the case of adsorption on real solids, these assumptions often do not hold and the absolute surface areas derived from the BET model must be regarded with caution. Nonetheless, the BET model has become a standard method for the interpretation of sorption isotherms, and relative comparisons provide valuable information.

For the evaluation of the pore size distribution, the BJH model (named after Barrett, Joyner and Halenda) is commonly used.<sup>70</sup> It is based on the Kelvin equation (Equation 2.3.3). Assuming that the vapor side of the meniscus formed in a pore behaves as an ideal gas at constant temperature, this equation can be used to calculate the radius of the meniscus  $R_k$ , more precisely, the mean radius of curvature of the meniscus at which capillary condensation occurs:

$$\ln \frac{p}{p_0} = -\frac{2\sigma V_L}{R_k R T} \quad (2.3.3)$$

Here,  $V_L$  and  $\sigma$  are the molar volume and the surface tension of the sorbent,  $p/p_0$  is the relative pressure,  $T$  the absolute temperature and  $R$  the gas constant. Alternatively, for the calculation of pore sizes and volumes a nonlocal density functional theory (NLDFT) equilibrium model of  $N_2$  on silica can be used.<sup>71</sup>

### 2.3.5 Pulsed-Field Gradient NMR

All methods introduced in this chapter so far aim to characterise the host material. In contrast, pulsed-field gradient nuclear magnetic resonance (PFG NMR) is used to investigate the ensemble diffusion of a certain species within a porous host.<sup>72,73,74,75</sup> In classical nuclear magnetic resonance (NMR),<sup>72</sup> the individual nuclei, or more precisely their mechanical and magnetic moments, i.e. their 'spins', rotate about the direction of a constant externally applied magnetic field with the magnetic flux density  $B$ . Together with the spins, also the macroscopic magnetization performs this rotation and induces a voltage in the surrounding receiver coil of the spectrometer, the NMR signal. The resonance frequency of the NMR signal is proportional to the magnetic field strength, and the gyromagnetic ratio  $\gamma$  of the nucleus under study is the factor of proportionality. If an inhomogeneous magnetic field is applied, the frequency of the signal, i.e. the position in the NMR spectrum, can be used directly to determine the positions of the nuclei contributing to this signal. In PFG NMR, an inhomogeneous gradient field is applied over two short time intervals  $\delta$ , as shown in Figure 2.8.

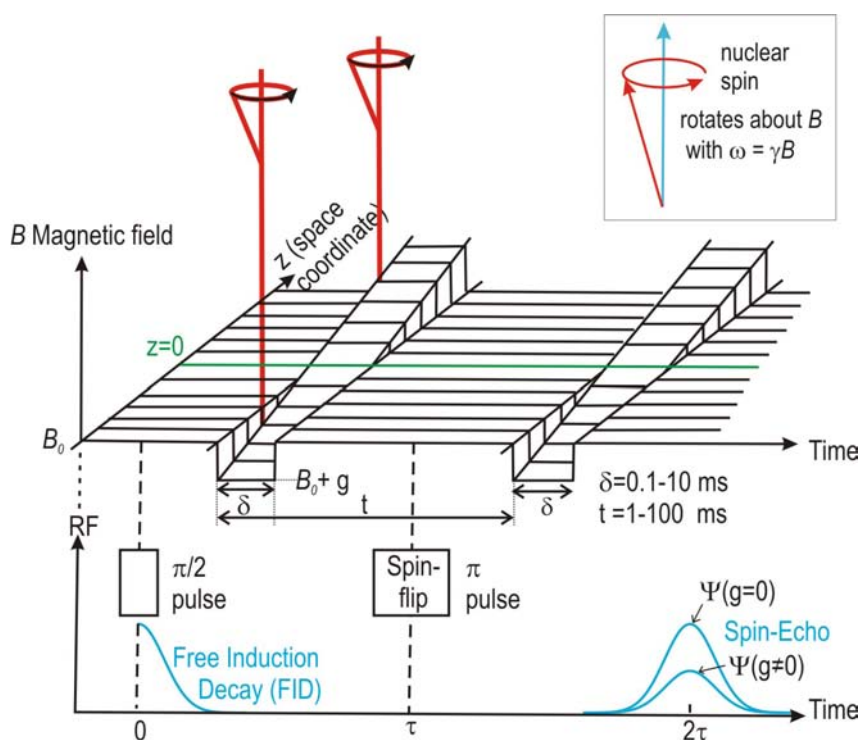


**Figure 2.8: Principle of pulsed-field gradient (PFG) NMR.** An inhomogeneous field is applied over two short time intervals  $\delta$  and leads to an attenuation of the NMR signal which, in the given example, is generated by the Hahn echo sequence (two rf pulses referred to as  $\pi/2$  and  $\pi$  pulses, respectively)<sup>73</sup>.

The NMR signal becomes thus sensitive to the positions of the spins during the two gradient pulses (indicated in the Figure in red for two different positions). Differences

in the positions of the individual nuclei and thus the molecules to which they belong, can be detected through the decay of the NMR signal. The decay of the NMR signal is described by the following equation, where  $\delta$ ,  $g$  and  $t$  are the duration, the amplitude and the separation of the two field gradient pulses;  $z$  is the coordinate along the direction of the applied field gradient:

$$\frac{\Psi(t, \gamma \delta g)}{\Psi_0} = \int p(z, t) \cos(\gamma \delta g z) dz \quad (2.3.4)$$

Here,  $p(z, t)$  denotes the probability density that a nucleus contributing to the signal is displaced by the distance  $z$  in gradient (i.e.  $z$ -) direction during the time  $t$ . The mean-square displacement  $\langle z(t)^2 \rangle$  during the time interval  $t$  between the two field gradient pulses and with it the isotropic diffusion coefficient  $D$  can be extracted from  $\Psi/\Psi_0$  as follows: Diffusion theory, as explained in Chapter 4 and in the literature (e.g. by Kärger in<sup>76</sup>), yields the propagator  $p(z, t)$ :

$$p(z, t) = \frac{1}{\sqrt{4\pi Dt}} \exp\left(-\frac{z^2}{4Dt}\right) \quad (2.3.5)$$

Insertion of Equation 2.3.5 into Equation 2.3.4 yields:

$$\frac{\Psi(t, \gamma \delta g)}{\Psi_0} = \exp(-\gamma^2 \delta^2 g^2 Dt) \stackrel{\langle z(t)^2 \rangle = 2Dt}{=} \exp\left(-\frac{1}{2} \gamma^2 \delta^2 g^2 \langle z(t)^2 \rangle\right) \quad (2.3.6)$$

The last term is calculated using the Einstein-Smoluchowski relation ( $\langle r(t)^2 \rangle = 2Dt$ , Equation 4.1.9), which is derived in the later chapter about diffusion theory.

Using PFG NMR intracrystalline diffusion and long-range diffusion in porous matter can be recorded, depending on the relation between the mean displacements covered in the experiments and the diameters of the crystallites under study. The mean-square displacement must be much smaller than the mean diameter of the crystallites to exclude an influence of the finite crystal size on the measurements. The lower limit for displacement measurements is 100 nm. A typical maximum value for the observation time  $t$  is a few 100 ms, thus minimal diffusion coefficients of  $D_{\min} = 10^{-2} \mu\text{m}^2 \text{s}^{-1}$  are observable using PFG NMR.<sup>77,78</sup> The detection limit of this technique is a minimum concentration of the measured nuclei (usually protons) of one per cubic nanometre.

Owing to the large gyromagnetic ratio  $\gamma$  of the hydrogen nucleus, hydrogen-containing molecules offer the best conditions for diffusion measurements by NMR. In addition

## 2. Porous Materials

---

measurements with zeolites have been carried out with a large number of further nuclei, including  $^2\text{H}$ ,  $^{13}\text{C}$ ,  $^{15}\text{N}$ ,  $^{19}\text{F}$ , and  $^{129}\text{Xe}$ . The possibility of simultaneously monitoring different nuclei makes PFG NMR particularly valuable for selective diffusion studies in multicomponent systems.<sup>74</sup>

## 3 Single-Molecule Microscopy

Single-molecule detection provides access to information not accessible by ensemble methods, as it gives the real distribution of a certain measurement parameter rather than the average value. This is why it has become a widely used method<sup>79,80,81</sup> in various fields, ranging from biology<sup>82,83,84,85,86,87,88</sup> to material science.<sup>89,90,91,92,93,94,95</sup>

In single-molecule microscopy the laser induced fluorescence signal of single dye molecules is recorded in a microscope setup. By tracking the successive positions of an individual molecule (single-molecule tracking, SMT) it is possible to resolve molecular trajectories and learn about translational diffusion in the sample under study.<sup>96,97,98,99,100,101</sup> In this chapter, the basics of fluorescence microscopy and the most important characteristics of dyes used for single-molecule experiments will be presented. This is followed by an overview of different techniques for the observation of single molecules and the experimental details of the wide-field setup used throughout this work. The last part of this chapter is devoted to single-molecule tracking, including the fitting procedure that allows to pinpoint a molecule with 5 nm precision. Furthermore, modern CCD technology will be introduced, which makes a very high temporal resolution down to 10 ms per image possible.

### 3.1 Principles of Fluorescence Microscopy

In order to describe the photophysics of the most common fluorescent dyes used in single-molecule microscopy a simple three-level energy diagram is sufficient.<sup>102</sup> Figure 3.1 shows such a scheme.

The molecule has an electric dipole-allowed singlet-singlet optical transition  $S_1 \leftarrow S_0$ , pumped by radiation at energy  $h\nu$  from a laser or a lamp, with  $h$  the Planck constant and  $\nu$  the optical frequency of the excitation light. The energy has to be sufficient to pump the lowest electronic excited state. After the absorption of the photon, the excited molecule quickly relaxes via vibrational modes of the molecule (internal conversion IC) and of the host (phonons) to the lowest electronic excited state, from which

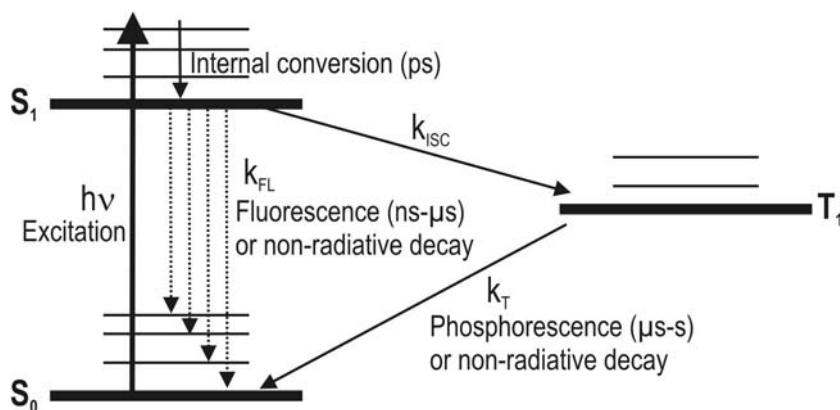


**Figure 3.1: Jablonski Diagram.** Typical energy level scheme for single-molecule spectroscopy.  $S_0$ , ground singlet state,  $S_1$ , first excited singlet,  $T_1$ , lowest triplet state or other intermediate state. For each electronic state, several levels in the vibrational progression are shown. Photons at energy  $h\nu$  excite the dipole-allowed singlet-singlet transition. The intersystem crossing rate is  $k_{ISC}$ , and the triplet decay rate is  $k_T$ . Fluorescence emission at rate  $k_{FL}$  shown as dotted lines originates from  $S_1$  and terminates on various vibrationally excited levels of  $S_0$  or  $S_0$  itself.

the excited molecule can return to the electronic ground state by emitting a fluorescence photon (dashed lines). Fluorescence lifetimes of allowed transitions (suitable for single-molecule detection) are of the order of 1 – 10 ns. After the emission, the molecule is brought back to the vibrational ground state by phonon relaxation. In general, the relaxation steps represent energy losses which cause a spectral redshift between absorption and emission bands, called the Stokes shift. Additionally there is also a certain probability for intersystem crossing (ISC) into the triplet state. From there the excited molecule can return to the electronic ground state via another radiationless ISC or by emission of a phosphorescence photon. The latter process takes place on a slower timescale than the fluorescence, it occurs within microseconds and ranges up to seconds after the excitation. A molecule 'trapped' in the triplet state therefore becomes invisible for a certain time (triplet blinking).

An absorption spectrum of the terrylene diimide derivative, which was used most frequently throughout this work<sup>103,104,105</sup> (**AS-TDI**, structure depicted in the inset), is shown in Figure 3.2 (blue line). It was measured using chloroform as a solvent with a Perkin Elmer 330 dual-beam absorption spectrometer. For fluorescent molecules the intensity of the fluorescence at a fixed wavelength can be measured as a function of the excitation wavelength. This results in an so-called fluorescence excitation spectrum, which resembles the absorption spectrum and is therefore not shown here. The fluorescence emission spectrum of **AS-TDI** is shown in red in Figure 3.2. It was measured on a F900 spectrofluorimeter (Edinburgh instruments).

For the observation of a single-molecule, the fluorescence emission rate has to be max-

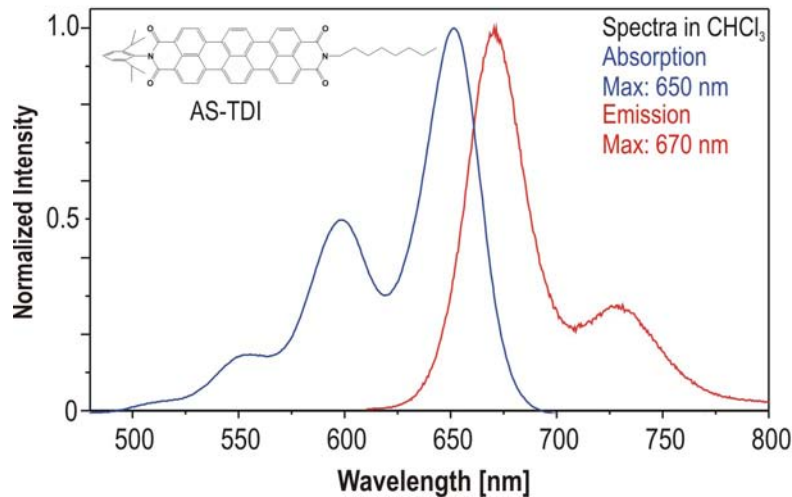


**Figure 3.2: Terrylene diimide Spectra.** Absorption and fluorescence spectrum of the asymmetric TDI derivative (AS-TDI, structure shown in the upper left corner).

imized. Therefore the molecule must be pumped with high probability and it needs to have a very high fluorescence quantum yield  $\Phi_F$  close to unity. The latter gives the efficiency of the fluorescence process and is defined as the ratio of the number of photons emitted to the number of photons absorbed. The maximum fluorescence quantum yield is 1.0 (100 %), i.e. every absorbed photon results in an emitted photon. Another way to define the quantum yield of fluorescence is by the ratio of the radiative decay rate and the sum of all, i.e. radiative and non-radiative, rates of excited state decay.

$$\Phi_F = \frac{\# \text{ emitted photons}}{\# \text{ absorbed photons}} = \frac{k_{\text{rad}}}{(k_{\text{rad}} + k_{\text{nonrad}})} \quad (3.1.1)$$

In addition to a high fluorescence quantum yield, single molecule dyes need to have a high absorption cross section  $\sigma$ , which may be interpreted as the effective area per molecule which is able to capture photons from the incident laser beam. High  $\sigma$  means that the photons of the incident light are efficiently absorbed and therefore higher signal-to-background ratios can be achieved than in the case of weak absorbers.

Processes that limit the integrated signal of single molecules are photoblinking and photobleaching, i.e. the reversible or irreversible transition to a non-radiative state. Photoblinking can be induced by transitions to the triplet state (triplet blinking, see above), taking place on a timescale of microseconds, or by other effects.<sup>106,107</sup> Photobleaching occurs for fluorescent dyes after a certain number of excitation-emission cycles. In many cases photobleaching is photo-oxidation of the fluorophore. Reducing the amount of oxygen in the surrounding atmosphere can help minimizing this effect.

## 3.2 Fluorescence Techniques for the Observation of Single Molecules

Since the first observation of a single dye molecule via its absorption<sup>5</sup> or its fluorescence excitation spectrum<sup>6</sup> a wide range of single-molecule techniques has been developed. The first single-molecule publications were based on spectral selection of narrow zero-phonon line absorption and were therefore performed at very low temperatures. Because the absorption cross section of a molecule is at least two orders of magnitude smaller than the area illuminated by a focussed laser beam, this absorption is very difficult to detect against the shot noise of unabsorbed photons.<sup>81</sup> Today, modern interference filters allow to separate the red-shifted fluorescence efficiently from scattered or reflected light of the excitation laser, and high numerical aperture objectives (up to N.A.=1.49) are used to collect high amounts of the light emitted by a single molecule. Therefore most of the single-molecule techniques nowadays are based on the detection of fluorescence light, which provides a much better signal-to-background and signal-to-noise ratio than absorption measurements.

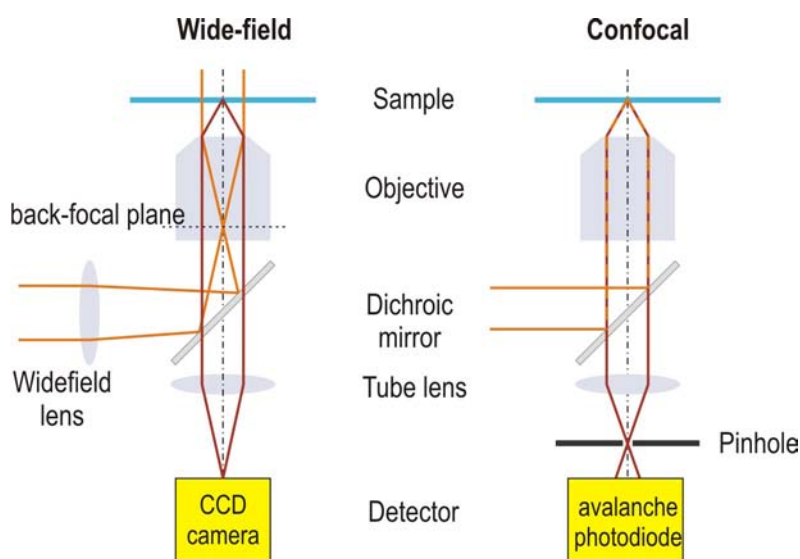


**Figure 3.3: Single-molecule fluorescence microscopy methods.** Orange: Illumination light. Red: Fluorescence light. (a) Wide-field: The molecules in a certain area, up to  $50\ \mu\text{m} \times 50\ \mu\text{m}$  in size, are excited by a widened laser beam. Fluorescence from this area is projected onto an array detector. (b) Confocal: The excitation laser beam is focussed in the diffraction limited focal volume. Fluorescence light is detected through a pinhole, to exclude out-of-focus emission, with a highly sensitive point detector.

Two different types of microscope configurations, distinguished by the detection geometry are used for single-molecule microscopy. Wide-field methods use an array detector like a CCD camera to image sample regions of several tens of micrometres in diameter at the same time (Figure 3.3a and Section 3.2.1). Confocal microscopy tech-



niques detect fluorescence from a small diffraction limited focal volume in the sample, as shown in Figure 3.3b, and images are obtained by scanning the sample or the focal spot. In this work mostly wide-field microscopy was used to investigate the diffusion of single molecules because it allows a much higher temporal resolution. This technique will be presented first, and scanning confocal microscopy will be briefly introduced afterwards.

### 3.2.1 Wide-field Methods

In wide-field microscopy an area of the sample is illuminated by a laser beam or an arc lamp, similar to a conventional white-light microscope. Fluorescence light of the excited single molecules in this area is separated by a set of optical filters and focussed onto an array detector, which is in most cases an intensified charged coupled device (CCD) chip. The implementation of this method in the wide-field setup used in this work will be explained in detail below in Section 3.3 and Figure 3.5. This method has two major advantages: by illuminating a micron-sized area of the sample the behaviour of many individual molecules can be observed simultaneously; in addition, modern CCD technology allows to collect up to several thousands of images at very high frame rates. Read-out rates of 30 frames per second are easily realized in full chip mode and rates up to 100 frames per second are possible by decreasing the size of the observed area on the chip.

In order to illuminate a micron-sized area on the sample, two different methods can be used. Standard wide-field microscopes, as the one used throughout this thesis, work in epi-fluorescence, i.e. the excitation beam is passed through the same objective that is used to collect the fluorescence light (see Figures 3.3a and 3.5). This arrangement minimizes the amount of background coming from excitation laser light, which is leaking through the optical filters in the detection pathway. A drawback of this technique is that the widened beam passes through the entire thickness of the sample and excites molecules outside the focal plane, which contribute to background fluorescence. A possibility to overcome this problem is total internal reflection microscopy (TIRF).<sup>108,109</sup> This technique makes use of the fact that light is totally reflected when it hits an interface with a medium having a smaller index of refraction  $n$  under large angles (from the normal to the interface). From the area of reflection an evanescent field reaches about 100 nm into the lower  $n$  material and can be used to excite specifically the molecules in this thin layer. The necessary refraction index change is for example formed by the glass/water interface between the cover-slip (cover-slip:  $n_D=1.52$ ) and a sample in aqueous solution (water:  $n_D=1.33$ ). In addition to this so-called objective type TIRF, which is also an epifluorescence technique, an alternative method, the

prism-type TIRF can be used. Here, the incident laser is guided through a glass prism, which is placed on top of the sample and the evanescent field penetrates into the sample at the prism-sample interface. Fluorescence from this region is then collected using a high numerical aperture objective placed below the sample. However, the TIRF technique is restricted to probes with a strong refractive index change between the objective/cover-slip or the prism and the sample, as it is the case for many biological samples in aqueous buffer solution. It is not suited for the kind of measurements presented in this work because very little refractive index change occurs between the thin silica films with the incorporated dye molecules and the cover-slips on which the films are spin-coated. However, the problem of out-of-focus background addressed by TIRF does not arise for the thin films investigated here because they are thinner than the focal depth of the microscope ( $> 1 \mu\text{m}$ ). Therefore no out-of-focus molecules can be excited by the incident laser beam and contribute to background fluorescence.

For all wide-field techniques the detected signals of the single molecules are diffraction-limited. In each frame single molecules show up as bright spots on a dark background. Since they are much smaller than the wavelength  $\lambda$ , the single molecules can be considered as point like emitters, and the response of the imaging system consisting of the objective and the lenses in the detection pathway is described by the point spread function (PSF). The radial intensity distribution is described by a first order Bessel function, which can be fitted to good approximation by a 2D Gaussian function.<sup>110</sup> Using a high numerical aperture (N.A.) objective and excitation light in the red part of the visible spectrum the single molecules will be imaged as spots of ca. 300 nm diameter (full width at half maximum) on the detector. However, the positions of these spots can be determined with a much higher accuracy by fitting a suitable peak function such as a 2D Gaussian to the signal. The accuracy of the fit is determined only by the signal-to-background and the signal-to-noise ratio. If a CCD detector with a chip consisting of a pixel array is used, the magnification and thus the number of pixels on which the single-molecule signal is imaged has to be taken into account for the accuracy of the fit. Before tackling this question in Section 3.4 a brief overview of modern CCD technology is given in the following section.

#### CCD Technology for single-molecule microscopy

The area detector represents the heart of every wide-field imaging setup. Its read out rate and the gain and noise of the amplifier strongly influence the quality of the data. Therefore this paragraph gives a short introduction into the mode of operation of CCD cameras that are used for single-molecule microscopy.

A CCD detector consists of an array of silicon diode photosensors, the pixels (= picture elements), which is coupled to a charge storage region that is, in turn, connected to an amplifier that reads out the quantity of accumulated charge. Incident photons with energy larger than the semiconductor band gap create an electron-hole pair and thus an electronic charge. The quantum efficiency and spectral response of the detector is thus defined by the transmission and absorption properties of the silicon. The minimal time  $T_{\text{image}}$  between two images and thus the temporal resolution of the measurement is determined by the exposure time  $T_{\text{exp}}$  and the readout time  $T_{\text{readout}}$  of the chip. The inverse of  $T_{\text{image}}$  is denoted the frame rate FR (typically given in units of fps = frames per second).

$$T_{\text{image}} = T_{\text{exp}} + T_{\text{readout}} = \text{FR}^{-1} \quad (3.2.1)$$

The readout time  $T_{\text{readout}}$  of one complete image depends on instrumental parameters, like the time needed to read out a single pixel and the complete number of pixels per image. Modern CCD cameras can work in frame transfer mode to decrease the readout time. In this mode only half of the pixels on the chip are exposed during  $T_{\text{exp}}$  (Image Section), the other half is shielded from light (Store Section), see Figure 3.4a. After  $T_{\text{exp}}$  the charges from the image section are transferred to the store section, so that the image section can be again exposed while the charges from the store section are read out line by line in the readout register. In that way,  $T_{\text{readout}}$  is reduced to the shift time from the image to the store section as long as  $T_{\text{exp}}$  exceeds the time needed to readout the store section. The readout time can be decreased further by using subregions of the full chip. For most cameras the shifting of the lines into the readout register limits  $T_{\text{readout}}$ . Thus a decrease of the height of the illuminated region can improve the frame rate, whereas a decrease in the width will not provide any improvement.

In general the sensitivity of a camera is governed by its readout noise, as signals below the readout noise cannot be detected regardless of the subsequent amplifying stages. Therefore, to gather comparably weak signals, like single-molecule fluorescence, additional on-chip signal amplification is needed. Different technologies exist to perform this, like intensified (ICCD) or electron multiplying CCD cameras (EMCCD). Both types have been used for the measurements in this work. The structure of an EMCCD is essentially the same as of a conventional CCD, with an additional multiplication register after the serial readout register. Thus the electronic signal is amplified prior to being read at the output node, and hence the sensitivity of the device is increased. Alternatively, the photonic signal can be increased before the CCD chip through a microchannel plate (MCP). This MCP is similar to a photomultiplier tube. The incident photons release electrons from a photocathode in front of the MCP. The electrons

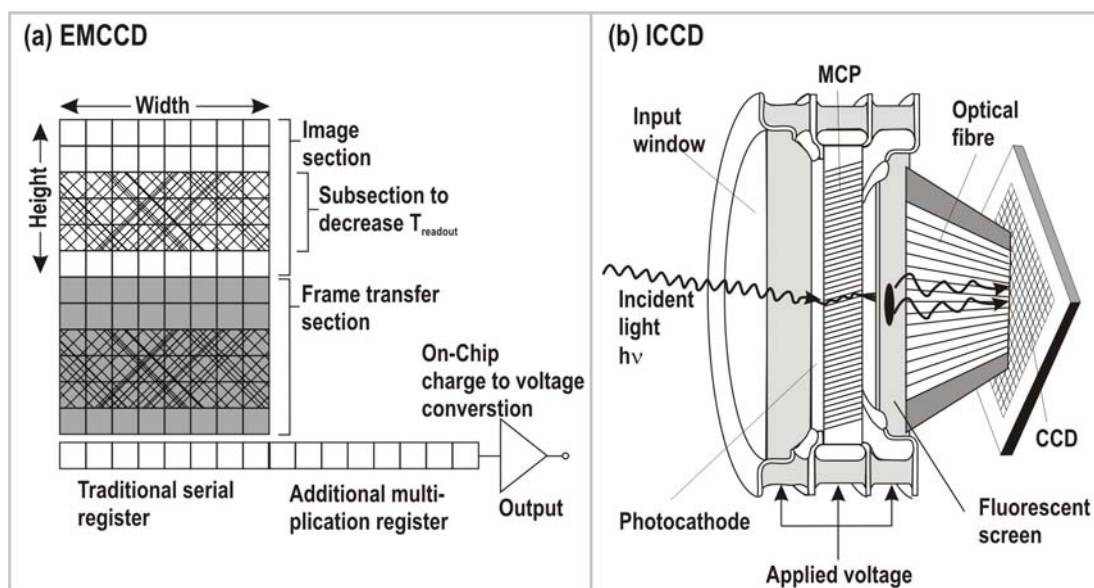


**Figure 3.4: Different CCD structures.** (a) EMCCD (electron multiplying). (b) ICCD (Intensified). Adapted from<sup>111</sup>.

are then accelerated through the multiplier, consisting of a series of angled tubes, like sketched in Figure 3.4b. In the accelerating field they gain sufficient energy to knock off additional electrons along the tubes of the MCP. The multiplied electrons are then either detected directly by a special electron bombardment CCD or indirectly by using a fluorescent screen coupled with an optical fibre array to a conventional CCD. By using a pulsed gate voltage, an ICCD can achieve very short exposure times. However, for single-molecule experiments EMCCD cameras are better suited, because they provide a higher sensitivity than ICCD devices and sufficiently high frame rates.

The quantum efficiency of a CCD can be increased by exposing the sensitive region of the chip, its 'back'-side. In conventional CCD cameras the incoming light has to pass first the region with the gate electrodes attached to the 'front'-side of the chip that are used to shift the charge through the CCD. In a back-illuminated CCD the bulk silicon substrate of the chip has been thinned by etching until it is transparent and therefore the chip can be exposed at the substrate side. Through this quite expensive process the quantum efficiency can be as high as 90% for light in the visible region.

### 3.2.2 Confocal Microscopy

Alternatively to the large-area excitation of wide-field imaging, the sample can also be illuminated with the smallest diffraction limited spot possible and the fluorescence from this spot can be collected with a point detector. Such point detectors are simple

photo-multiplier tubes or more sensitive avalanche photo diodes (APDs). In order to excite the molecules within and detect the signal from the diffraction limited confocal volume, the collimated excitation laser beam is focussed onto the sample plane, and the emitted fluorescence is then re-collected and re-collimated by the same microscope objective. Residual laser light is filtered with high quality interference filters, like in wide-field imaging. A pinhole in the detection pathway, as shown in Figure 3.3b, blocks out of focus light in the detection pathway to increase the resolution along the optical  $z$ -axis. The diameter of the pinhole determines the absolute depth of field for the confocal image, so that the overall size of the focal spot is in the range of 300 nm in diameter in the observation plane and about 900 nm along the optical axis. It has a volume of about one femtoliter. In order to obtain images of larger areas on the sample, the excitation focus or the sample have to be scanned point by point. Therefore confocal techniques are also referred to as scanning methods. In addition to the molecules' position, confocal microscopy can provide further useful information about the single emitters. By introducing a polarizer into the excitation and detection pathway the orientation of the molecule in the observation plane can be determined.<sup>94,112,113</sup> The point signal from immobile single-molecules can be split into the spectral components by a prism or grating and imaged onto a CCD camera.<sup>112</sup> In this way the spectral dynamics of a dye can be followed at video rate, i.e. 24 frames per second. However, even though one point can be observed with high temporal resolution, the scanning time per point is the limiting factor for fast accumulation of larger images. In a conventional laser scanning microscope like the Zeiss LSM 410 used for the confocal measurements in Chapter 7, the fastest scanning time for a 256 px  $\times$  256 px region of the sample is about one second. To obtain high resolution images with a signal-to-noise ratio suitable for tracking with high positioning accuracy, much slower scanning times have to be chosen (e.g. 64 s for one 256 px  $\times$  256 px image). Therefore, real-time observation of the molecular motion is only possible for very slowly diffusing species.

A confocal technique that can be used to measure faster diffusion is fluorescence correlation spectroscopy (FCS).<sup>114,115,116</sup> Here, the signal of individual dye molecules diffusing through the focal volume is recorded against time. The diffusion coefficient and the concentration of the dye in solution can be calculated from the autocorrelation function  $g^{(2)}(\tau)$  of the fluorescence intensity  $I(t)$  in the focal volume:

$$g^{(2)}(\tau) = \frac{\langle I(t) \cdot I(t + \tau) \rangle}{\langle I(t)^2 \rangle}, \quad (3.2.2)$$

A disadvantage of FCS is that it requires a model to extract the diffusion coefficient from the intensity correlation function. This is not a serious drawback for diffusion in liquids, but a substantial limitation for the complicated motions within the intricate

porous structures investigated in this work. In Chapter 8, a few studies from the literature using FCS in mesoporous silica are discussed. However, even though average diffusion coefficients can be calculated and models with several diffusion components are applied, FCS measurements cannot provide the detailed structural and dynamical information accessible by single-molecule tracking.

The range of diffusion coefficients that are accessible by FCS measurements depends, among other factors, on the size and shape of the confocal volume of the given setup. The diffusion times through the focus should be long enough that antibunching effects, i.e. blinking on a timescale of 1 – 10 ns, are averaged out. Moreover, the upper limit is correlated with the concentration of molecules in the focus and thus also the size of the molecules: If too few molecules are in the focus, the number of fluctuations is too low for a good auto- or crosscorrelation of the signal intensities; on the other hand if too many molecules are in the focus, the fluctuations due to diffusion of the molecules are averaged out and statistical fluctuations dominate the signal. In general, the optimum concentration of molecules is slightly higher than that for single particle measurements, ideally between  $10^{-12}$  and  $10^{-9}$  mol L<sup>-1</sup>.<sup>117</sup> At these concentrations typically more than one molecule is in the focus at the same time, thus one might argue that this technique is not a 'real' single-molecule technique.

#### 3.2.3 Comparison of Wide-field and Confocal Microscopy Methods

Wide-field and confocal microscopy methods both have their advantages and disadvantages and for each individual problem the best-suited method has to be determined. Therefore, a short summary of the differences between the two methods and their respective assets and drawbacks will be given.

As mentioned above, the methods differ experimentally in the way the single-molecule signal is excited and detected. In wide-field microscopy a whole area of the sample is excited and the light from this area is imaged onto an array detector (Figure 3.3a). In confocal microscopy the excitation laser is focussed to a diffraction limited volume, and fluorescence light is detected from this volume with a point detector. Out of focus fluorescence is excluded by an additional pinhole in the detection pathway (Figure 3.3b).

Table 3.1 summarizes the main specifications and the advantages and disadvantages of the individual methods.

Table 3.1: Single-molecule fluorescence methods.

Wide-field		Confocal
<b>Temporal Resolution</b>		
1D		1 $\mu$ s
2D	Full chip 512 px $\times$ 512 px: 30 fps <sup>a</sup> 128 px $\times$ 512 px: 125 fps	200 px $\times$ 200 px: > 1 s per frame
3D		20 s
<b>Focal dimensions</b>		
x-y-plane	300 nm	300 nm
z-direction	Standard: 1 – 2 $\mu$ m TIRF: 100 – 200 nm	900 nm
<b>Advantages</b>	<ul style="list-style-type: none"> <li>• high temporal and spatial resolution for imaging</li> <li>• large area with many molecules observed simultaneously</li> <li>• TIRF: high z-resolution</li> </ul>	<ul style="list-style-type: none"> <li>• spot scan with high temporal resolution</li> <li>• orientation and spectra measured simultaneously</li> <li>• high z-resolution</li> </ul>
<b>Limitations</b>	<ul style="list-style-type: none"> <li>• no detailed spectral or orientational information accessible</li> <li>• Standard wide-field: out-of-focus blur</li> <li>• TIRF: index of refraction change needed</li> </ul>	<ul style="list-style-type: none"> <li>• slow acquisition of images</li> <li>• Standard confocal: only one molecule in the focal volume</li> <li>• FCS: no information on the direction of motion</li> </ul>

<sup>a</sup>fps=frames per second

### 3.3 Wide-Field Imaging Setup

The wide-field imaging setup used in this work is sketched in Figure 3.5. In the following the excitation pathway of the incident laser light and the detection pathway of the emitted single-molecule fluorescence will be described in detail.

#### 3.3.1 Excitation Pathway

For excitation of both types of dye (**9A1** and **TDI**, see Chapters 5 and 6, 7) a Helium-Neon-Gaslaser was used with a maximum power of 75 mW at 632.8 nm (Coherent, Inc.). The light is guided through a laser line filter (Laser Components GmbH,  $\lambda = 632.8$  nm) to obtain a narrow-band excitation, and an optical density (OD) filter wheel (continuous change of OD 0 - 2, Thorlabs) to adjust the laser intensity for the different measurements. Initially, the laser beam was magnified five times by a telescope (Thor-

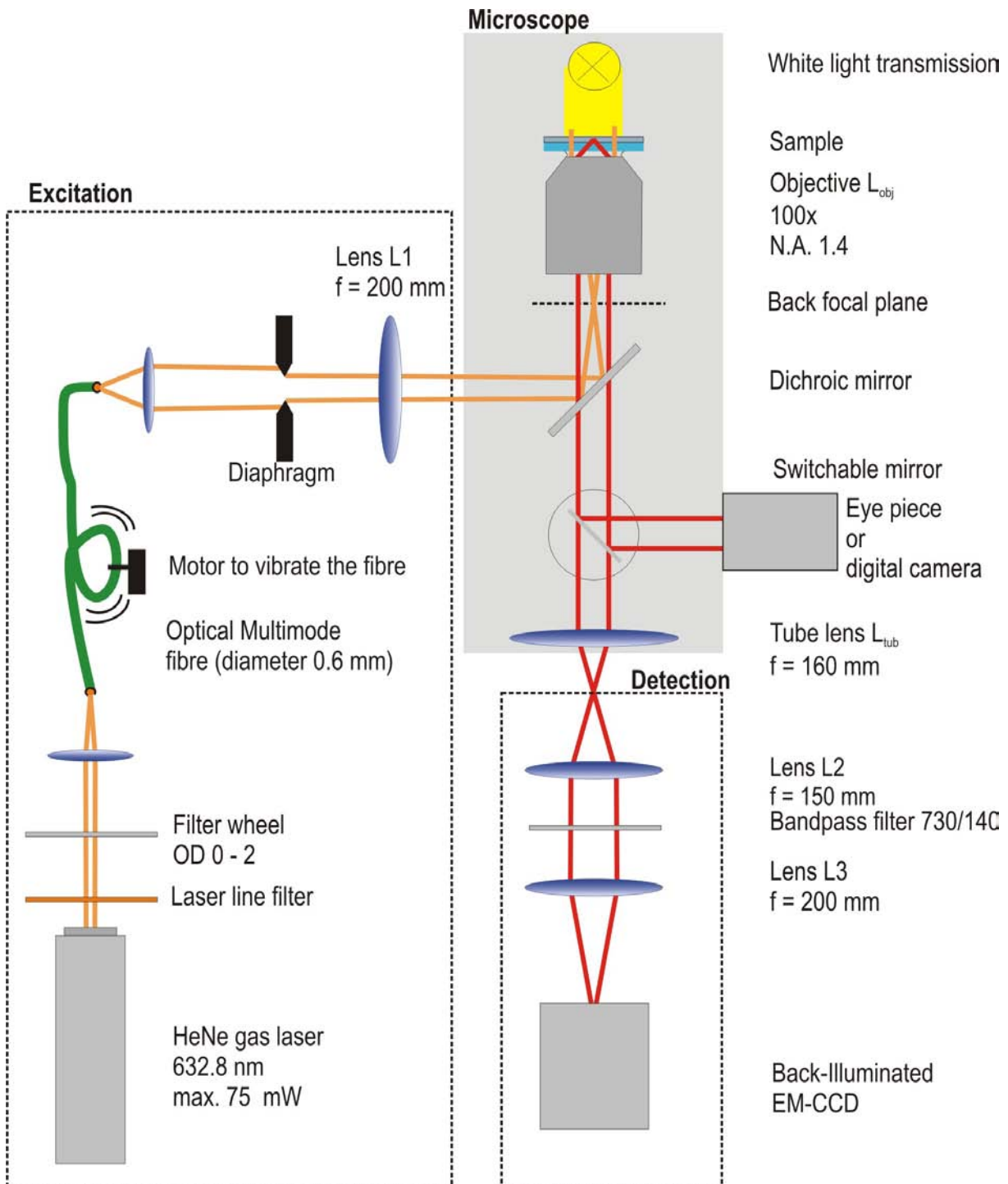


**Figure 3.5: Wide-field Imaging Setup.** The magnified image of the laser in the diaphragm is projected onto the back-focal plane of the microscope. In the detection pathway, emission of the single-molecules is separated by filters from excitation light and focussed onto the CCD camera after additional magnification.



labs) and guided with a periscope through the diaphragm that serves to adjust the beam diameter and the wide-field lens into the microscope (Nikon Eclipse TE 200).<sup>118</sup> To obtain a more homogeneous illumination of the sample, the setup was rebuilt and instead of the telescope and the two mirrors an optical multimode fibre ( $\varnothing$  0.6 mm, Optronis GmbH) was integrated that acts as a spatial mode-filter. The laser is coupled into the fibre by an achromatic lens (50 mm, Thorlabs), and another identical lens is used to parallelize the light at the fibre exit. An additional advantage of this new setup is that different excitation lasers can be easily overlaid with each other. To get rid of interference patterns at the fibre exit, the fibre is constantly shaken by a motor. Furthermore, the round diaphragm was exchanged with a home-built rectangular one to avoid photobleaching in sample regions that are not in the rectangular region of interest imaged on the CCD chip. The image of the diaphragm is focussed by the wide-field lens (200 mm achromat, Thorlabs) in the back focal plane of the objective. Thus, a parallel beam leaves the objective, and the molecules are excited in a rectangular area of about  $30 \mu\text{m} \times 30 \mu\text{m}$ , that corresponds to the image of the illuminated diaphragm on the sample. The laser power is adjusted individually for each measurement, depending on the frame rate and the dye used in the measurement (see above, Section 3.2.1). In most experiments an excitation intensity of  $I_{\text{exc}} = 0.1 - 1 \text{ kW cm}^{-2}$  is used. An oil-immersion objective with a high numerical aperture (Nikon, CFI Plan Apochromat 100 $\times$  Oil, N.A. 1.4) allows to obtain a high excitation and detection efficiency.

### 3.3.2 Detection Pathway

The individual molecules can be considered as point like emitters. Their fluorescence is collected by the microscope objective  $L_{\text{obj}}$  and passes a dichroic mirror (Dual Line Beamsplitter 532/633, AHF Analysentechnik, Tübingen) and the tube lens  $L_{\text{tub}}$  (160 mm). The fluorescence light is guided to the side exit of the microscope by a switchable mirror. By a telescope consisting of the lenses  $L_2$  ( $f_2 = 150 \text{ mm}$ ), and  $L_3$  ( $f_3 = 200 \text{ mm}$ ), the fluorescence signal is magnified by a factor of 1.33 and focussed onto the CCD camera. Using a 100 $\times$  objective, the overall magnification is  $1.33 \cdot 100 \times = 133 \times$ . It was adjusted to this value in order to obtain an optimal image of the single molecules on the CCD chip (see below, Figure 3.6). In the parallel beam path between  $L_2$  and  $L_3$  a bandpass filter (730/140, AHF) eliminates scattered excitation light. The microscope also has a white light unit that is adjusted for Köhler illumination in transmission. The transmitted light can either be guided to the CCD camera, to the eyepiece of the microscope or to a digital camera for alignment purposes (Nikon, Coolpix).

The initial setup was equipped with a microchannel plate (MCP) intensified CCD camera (Princeton Instruments, PentaMAX) with frame-transfer-CCD chip (EEV, 512 px  $\times$

512 px). The pixels on the MCP chip with a size of 22.5  $\mu\text{m}$  were projected onto the pixels of the CCD chip with a size of 15  $\mu\text{m}$ . One pixel on the chip corresponds to 169 nm on the sample, calculated in the following way:

$$\frac{\text{size of one pixel on the MCP}}{\text{overall magnification}} = \frac{22.5 \mu\text{m}}{133} = 169 \text{ nm} \quad (3.3.1)$$

To improve the detection efficiency of the setup, the ICCD was replaced by a back-illuminated electron multiplying CCD camera (iXon DV887, 512  $\times$  512 Pixel). Here, one pixel had the size of 16  $\mu\text{m}$  corresponding to a theoretical value of 120 nm on the sample, calculated as in Equation 3.3.1. Evaluation of measurements with the USAF test target (Melles Griot) gave a value of 122 nm/pixel, which fits well with the theoretical value. The higher detection efficiency of the new EMCCD camera and the smaller area per pixel<sup>119</sup> greatly improve the positioning accuracy.

## 3.4 Single-Molecule Tracking

Observing diffusion in porous host-guest systems serves not only to visualize the structure of the materials, but also to establish the diffusion dynamics of individual guest molecules inside the pores. Tracking individual fluorescing molecules in the pores thus provides important insight into mesoporous hybrid systems.<sup>120,93,91</sup>

The signal of a single molecule appears as a diffraction limited spot on the detector. For conventional wide-field optics and light in the red part of the visible spectrum, these spots have a full width at half maximum of about 300 nm. The accuracy with which the position of the molecule can be determined depends on the signal-to-noise ratio (SNR) and on the distribution of the signal over the image pixel, as explained in the following paragraphs.

### 3.4.1 Fitting Functions

The far-field image of an individual molecule with its transition dipole moment oriented within the observation plane or of freely rotating molecules can be described by a Bessel function,<sup>110,121</sup> which can be approximated by a 2D gaussian function (Equa-

tion 3.4.1).<sup>122,98,123</sup>

$$f(x,y,A,w) = A \cdot \exp\left(-\frac{(x-x_0)^2 + (y-y_0)^2}{w^2}\right) \quad (3.4.1)$$

Here  $x_0$  and  $y_0$  designate the centre coordinates of the Gaussian, i.e. the position of the tracked molecule,  $A$  the amplitude of the signal and  $w$  the width of the gaussian curve. The width  $w$  is linked to the full width at half maximum  $w_{\text{FWHM}}$  in the following way:

$$w_{\text{FWHM}} = w \cdot \sqrt{\ln(4)} = 1.177 \cdot w \quad (3.4.2)$$

Furthermore,

$$w^2 = 2\sigma_{xy}^2, \quad (3.4.3)$$

where  $\sigma_{xy}^2$  is the radial variance of the 2D Gaussian.

The emission pattern of molecules oriented with their transition dipole moment perpendicular to the observation plane and thus with the optical z-axis, exhibit the shape of a 'doughnut'.<sup>124,125,126,127,128,129</sup> This is fitted with a product of the above described gaussian and a sine squared function:

$$f(x,y,A,w,r) = A \cdot \exp\left(-\frac{(x-x_0)^2 + (y-y_0)^2}{w^2}\right) \cdot \sin^2\left(\frac{\pi \sqrt{(x-x_0)^2 + (y-y_0)^2}}{2r}\right) \quad (3.4.4)$$

### 3.4.2 Factors Influencing the Quality of the Fit

The object centre  $(x_0, y_0)$  that is found by fitting a single-molecule pattern according to Equation 3.4.1 or 3.4.4 using a  $\chi^2$  minimization is only an estimate for the true object centre. The positioning accuracy is defined as the region in which the true object centre can be found with a probability of 68%, which corresponds to the standard deviation of the fit of the  $x_0$  and  $y_0$  - position. Usually this accuracy is at least ten times smaller than the  $w_{\text{FWHM}}$  of the single-molecule pattern. It depends on specific instrument and measurement parameters, e.g. detector pixel size, read-out rate, quantum efficiency of the detector, laser power, instrument shot noise or fluorescent background signal. All

### 3. Single-Molecule Microscopy

---

these factors contribute to the signal-to-noise ratio (SNR) of the image. The SNR is defined as follows:<sup>130,121</sup>

$$\text{SNR} = \frac{I_0}{\sqrt{\sigma_{\text{bg}}^2 + \sigma_{I_0}^2}} \quad (3.4.5)$$

where  $I_0$  designates the maximum signal intensity above background,  $\sigma_{\text{bg}}$  the variance of the background intensity values and  $\sigma_{I_0}^2$  the true variance of the maximum signal intensity above the background. As stated above all these parameters depend on the image acquisition parameters. Kubitscheck *et al.* deduce the following expression for the localization accuracy:<sup>121,130,131</sup>

$$\sigma(r) = \sqrt{3.53 \left[ \sum_{i=-N_x}^{N_x} \sum_{j=-N_y}^{N_y} \frac{(I_0^2 x_i^2 / \sigma_{xy}^4) \exp[-(x_i^2 + y_j^2) / 2\sigma_{xy}^2]}{\sigma_{\text{bg}}^2 + \sigma^2(I(x_i, y_j))} \right]^{-1}} \quad (3.4.6)$$

Here,  $I_0$  is the maximum intensity in the region of interest (size of  $(2N_x + 1) \times (2N_y + 1)$ ),  $x_i$  and  $y_j$  are the coordinates on the detector and  $\sigma_{xy}$  the width of the Gaussian (see Equation 3.4.3).  $\sigma_{\text{bg}}^2$  and  $\sigma^2(I(x_i, y_j))$  are the variance of the background intensity and local variance of the signal intensity at the position  $(x_i, y_j)$ , respectively. With the definition of the SNR in Equation 3.4.5,  $\sigma(r)$  is approximately:<sup>131</sup>

$$\sigma(r) \approx \frac{q}{\text{SNR}} \quad (3.4.7)$$

where the parameter  $q$  depends only on the size of a discrete interval on the sample that corresponds to one pixel on the detector in relation to the width of the gaussian function  $\sigma_{xy}$ . It has the dimension of a length. Equation 3.4.7 shows that the positioning accuracy is approximately proportional to the SNR for a given setup. The size of the discrete intervals on the sample that correspond to one pixel on the detector can be adjusted correctly by changing the magnification factor in the detection pathway and adapting it to the size of a pixel on the camera chip. In an EMCCD the signal intensity can be well adjusted by the gain, i.e. the on-chip multiplication factor. Ideally the full dynamic range of the detector, i.e. the full range between minimum and maximum signal intensity that can be detected, is used, while saturation of the pixels is avoided. Figure 3.6 exemplifies the problem of adjusting the size of a pixel correctly to the width and amplitude of the gaussian curve in order to get the minimum  $\sigma(r)$ . The area under the gaussian curve is proportional to the overall number of photons of the signal and

remains unchanged in (a)-(c); only the number of pixels over which the signal is spread varies. In (a) the magnification is too low, nearly all the signal intensity is collected in one pixel. This pixel is over-saturated, whereas the neighbouring ones are very little illuminated. Along one dimension (top images in the Figure) only three pixels contribute to the signal, therefore the accuracy of the fit is low. The middle image, (b), illustrates the ideal case, where the signal is spread over a sufficiently high number of pixels while taking advantage of the full dynamic range of the detector. On the right the magnification is too high, so that the signal spreads too much, thus the contrast and the SNR is low.

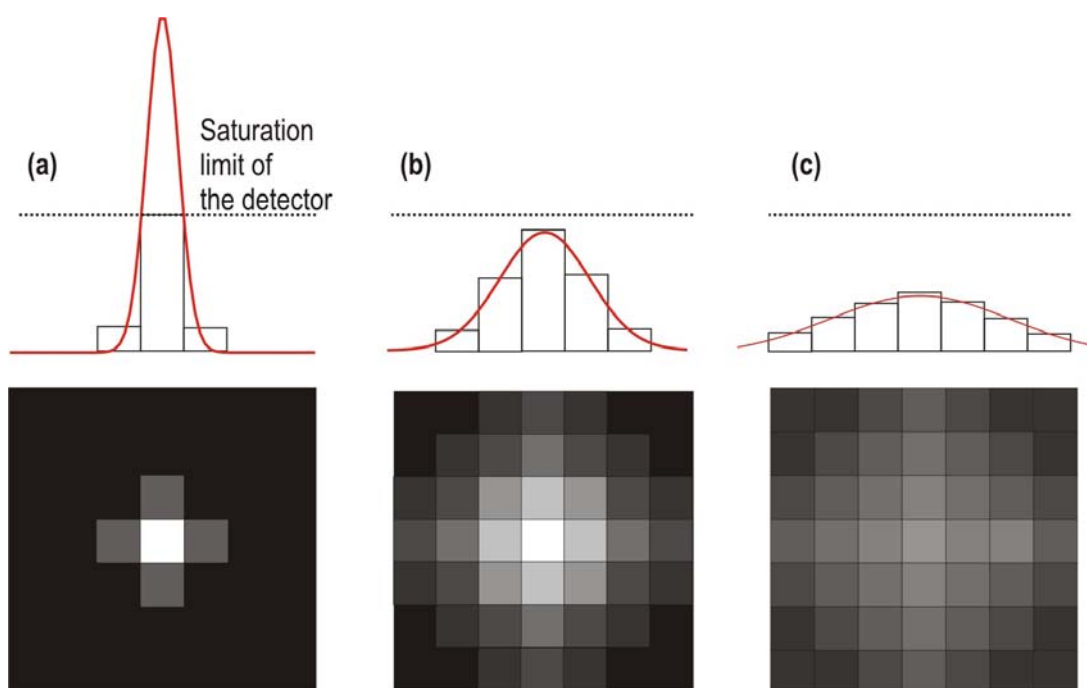


**Figure 3.6: Influence of size of the pixels on the detector and the width of the gaussian function  $\sigma_{xy}$  on the accuracy fit.** Top: Signal along one direction and corresponding gaussian fit. Bottom: Distribution of the signal on the pixels of the array detector. (a) Low optical magnification in the detection pathway yields a too small signal width, where the centre pixel is over-saturated. (b) Ideal case: The full dynamic range of the detector is used and a sufficiently high number of pixels is covered to obtain a high fitting accuracy. (c) The signal spreads too much, when the magnification is too high. The signal intensity is not much higher than the background.

An additional aspect has to be taken into account, when the molecules are diffusing during the integration time of the individual images. In this case the spots are not perfectly gaussian-shaped but can be elongated in the direction of the diffusion. These elongated patterns can also be used to determine the diffusion coefficient of the molecules in each individual frame using the spot-size-analysis method.<sup>132</sup> In this work, the exposure times for the individual frames are adapted such that the elongation of the spots is negligible.

The positioning accuracy is not to be confused with the resolution of a setup. The latter designates the minimum distance of two particles that allows to determine the position of each particle separately. This distance is roughly equal to the full width at half maximum of the signal and is given by the Rayleigh criterion:

$$\Delta_{\text{Rayleigh}} = \frac{0.61\lambda}{\text{N.A.}} \quad \text{with} \quad \text{N.A.} = n \cdot \sin \alpha \quad (3.4.8)$$

N.A. is the numerical aperture of the objective, which is given by the index of refraction of the medium in which the sample is incorporated and the maximum angle  $\alpha$  from which light can be collected by the objective. It follows that the higher the N.A. the higher the light collection efficiency of the objective and also the shorter the minimum distance of two objects that can be resolved. However, the measurements in this thesis were performed at concentrations so low that the probability that two molecules come close to each other is very low. If two molecules come closer than their mean step length their trajectories cannot be unambiguously assigned afterwards.

#### 3.4.3 Automated Single-Molecule Tracking

In order to investigate the diffusion behaviour of single molecules incorporated into porous hosts, movies of up to 1000 images are collected with the setup described in the previous section. From the collected movies the positions of the molecules in each individual frame have to be determined. The fitting is done frame by frame for each individual molecule with a dedicated program developed in-house. Initially the signal of an individual molecule is selected with the mouse in the first frame where the molecule appears. The program fits one of the above stated gaussian functions to the single-molecule signal within a given region of interest of the pixel image around the cursor, taking the coordinates of the mouse-click as an initial guess for the fit. The size of the region can be adjusted manually and must be adapted to the concentration of molecules, their diffusion coefficients and the width of the signal; it is typically set to values between  $5 \text{ px} \times 5 \text{ px}$  and  $15 \text{ px} \times 15 \text{ px}$ . As soon as the gaussian fit is done in an individual frame the program writes all the parameters of the fit including their respective errors into a new line of the output file and proceeds to the next frame. The fitted  $(x, y)$ -position of the previous frame is taken as an initial guess and the centre of the fitting region for the new fit. Hence, for fast moving molecules the region of interest has to be chosen larger than for slow moving ones. The number of iterations can be given manually in the program. Ideally the tracking algorithm follows a molecule during all frames of a movie or until the molecule photobleaches. A stop condition is

implemented in the program, that interrupts the tracking as soon as a good fit cannot be obtained.

If the molecules are blinking a lot or if the concentration is so high that the tracking routine might 'jump over' to a neighbouring molecule, the maximum number of frames for automated tracking can be limited. This makes it possible to follow the process by eye and correct for possibly occurring tracking errors immediately.

The output file contains 10 or 12 columns, which are frame and molecule number,  $(x, y)$ -coordinates, Amplitude  $A$ , width  $w$  and the corresponding fitting errors, all in units of pixels on the CCD chip. When a doughnut function is used to fit the image of the molecules, two additional lines are added containing the doughnut radius  $r$  and its error (cf. Equation 3.4.4). These output files are then read and analysed by a *FORTRAN90* program and visualized using *gnuplot* (by Thomas Williams, Colin Kelley),<sup>133</sup> as described in Chapter 4.

#### 3.4.4 Experimental Positioning Accuracy

As discussed in the previous sections, the positioning accuracy depends on different image acquisition parameters, e.g. the exposure time of one image, the excitation intensity or the camera gain. These parameters have to be adapted for each measurement to the specific experimental conditions.

The exposure time has to be adjusted to the diffusion coefficient of the dye within the given system and also to the photostability of the dye. It can range from a few milliseconds to several seconds per image. The maximum temporal resolution of the setup is limited by the detection speed of the CCD camera in frame transfer mode for a given number of pixels and by the brightness of the molecules; the maximum observation time is limited by drift of the microscope stage and bleaching of the molecules. If the dye is diffusing slowly long exposure times can be used, and the power of the excitation beam must be reduced to prevent photobleaching during the acquisition time of the movie. At room temperature almost all molecules in aqueous solution photobleach after the emission of maximum  $10^6$  photons.<sup>102,134</sup> However, even without photobleaching the signal count rate can not be increased infinitely by increasing the laser intensity, due to saturation of the dye. If the product of the absorption cross-section and the laser intensity divided by the photon energy  $h\nu$  becomes comparable to the fluorescence rate, the molecule will be in the excited state a significant fraction of the time. Thus, the rate of photons emitted cannot exceed the fluorescence rate ( $k_{\text{FL}}$  in Figure 3.1). In addition, at the saturation limit the dye can be excited easier to higher

excited states, from where it can be easier photochemically degraded into non fluorescent forms (photobleaching). Therefore the laser intensity should be adapted to stay well below the saturation limit.

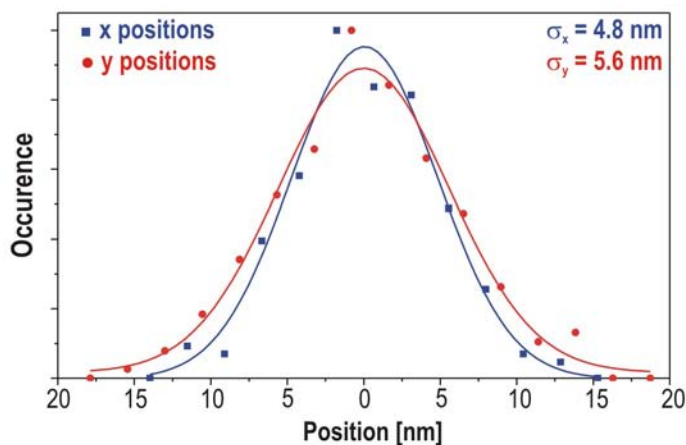


**Figure 3.7: Distribution of  $x$  and  $y$  positions as a measure for the accuracy fit.** Data from an immobilized AS-TDI molecule in a PMMA polymer matrix.

In order to determine the positioning accuracy experimentally, the positions of immobilized molecules were determined. For this purpose thin films of AS-TDI in polymethyl methacrylate (PMMA) were spin-coated on clean cover-slips. PMMA forms a solid polymer matrix in which the TDI molecules cannot move. The positioning accuracy was then determined from the variance of results of a time trace of one immobilized molecule. Figure 3.7 shows the distribution of  $x$  and  $y$  values of a molecule that was tracked in 200 frames. The movie was measured with 50 ms per frame and the gain was set to 200 in the camera software of the Andor EMCCD. The distributions were fitted with a gaussian function, resulting in  $\sigma_x = 4.8$  nm and  $\sigma_y = 5.6$  nm. The average value of the standard deviation of the fitted  $x$  and  $y$  positions, calculated by the tracking program, is  $\sigma_{av} = 5.8$  nm, which is slightly higher than the standard deviation of the gaussian distribution. The latter values for the standard deviations of the fitted positions were used to draw the error bars in the trajectories. For higher exposure times even better positioning accuracy could be achieved for bright molecules.



# 4 Diffusion: Theory and Trajectory Analysis

This chapter is devoted to the theory of diffusion. First, the microscopic model of a random walk is described and deviations from random behaviour are discussed. In the second part, it will be shown how this theory can be applied to data obtained from wide-field microscopy and single-molecule tracking.

## 4.1 Microscopic Theory of Diffusion

The macroscopic phenomenon of diffusion processes is caused by the random motion of microscopic particles (i.e. here dye molecules) relative to their surrounding matrix. Here some useful relations describing the motion of single molecules are briefly re-derived – first, in one and then in two and three dimensions. Most importantly, it is shown how the diffusion coefficient  $D$  can be related to the mean-square displacement (MSD) of single molecules.

The simple model developed by Einstein in 1905<sup>135</sup> and presented here works well in many cases. Deviations can, e.g. arise from constrained geometries at not too long times (normal diffusion only as long as  $r^2$  is smaller than the characteristic scale of the pore system), or convection.

### 4.1.1 Theory of a Random Walk

The motion of a molecule will consist of periods of undisturbed motion interrupted by sudden changes of direction when it collides with another molecule. The collisions will in general affect the speed of the molecule but its average speed remains constant as long as the temperature is fixed.

The model of the random walk idealizes this behaviour as follows: The time between collisions is a constant  $\tau$ . The direction of motion is completely randomized by a collision, the molecule has no inkling of the past, and the molecule speed  $v$  remains constant. Therefore the distance  $d$  between two collisions is also constant and given by  $d = v_x\tau$ ;  $d$  is also called the step length. The complete time  $t$  of a walk can be expressed as the number of steps  $n$  since  $t$  is given by  $n = t/\tau$ .

In one dimension the molecule has just one degree of freedom  $x$ , and can only move forward or backward. After  $n$  steps the molecule has the position:<sup>136</sup>

$$x(n) = x(n - 1) \pm d \quad (4.1.1)$$

Steps forward ( $+d$ ) have the same probability as steps backward ( $-d$ ) and all individual steps are independent. Considering an ensemble of identical molecules starting at  $x=0$  at  $t=0$ , their average  $x$  will be zero at all times:  $\langle x \rangle = 0$ . With time, i.e. with increasing number of steps, however, a spread of the ensemble occurs. This spread can be described by the standard deviation  $\sigma$  of  $x$ :

$$\sigma = \sqrt{\langle x^2 \rangle - \langle x \rangle^2} \quad (4.1.2)$$

Because  $\langle x \rangle = 0$  is known, only  $\langle x^2 \rangle$ , the mean-square displacement (MSD), remains to be determined. According to Equation 4.1.1, the square of the distance is:

$$x(n)^2 = x(n - 1)^2 \pm 2x(n - 1)d + d^2 \quad (4.1.3)$$

The ensemble average after  $n$  steps thus gives for the MSD:

$$\begin{aligned} \langle x(n)^2 \rangle &= \langle x(n - 1)^2 \rangle + \langle \pm 2x(n - 1)d \rangle + \langle d^2 \rangle = \\ &= \langle x(n - 1)^2 \rangle \pm d^2 \end{aligned} \quad (4.1.4)$$

The term  $\langle \pm 2x(n - 1)d \rangle$  is zero, as there is an equal probability for forward and backward steps. From  $x(0) = 0$  for all molecules, it follows that

$$\langle x(0)^2 \rangle = 0, \langle x(1)^2 \rangle = d^2, \langle x(2)^2 \rangle = 2d^2, \dots, \langle x(n)^2 \rangle = nd^2 \quad (4.1.5)$$

Thus the mean-square displacement  $\langle x(t)^2 \rangle$  increases linearly with the number of steps  $n$ , and therefore with time  $t$ .

$$\langle x(t)^2 \rangle = \frac{t}{\tau} d^2 = \frac{d^2}{\tau} t \quad (4.1.6)$$

The step length  $d$  and the time for one step  $\tau$  can be replaced by the diffusion coefficient  $D$ , which is defined as:

$$D := \frac{d^2}{2\tau} \quad (4.1.7)$$

The additional factor  $1/2$  is introduced to achieve consistency with the macroscopically defined Fick's second law, with  $c(x,t)$  the concentration at position  $x$  at time  $t$ :

$$\frac{\partial c(x,t)}{\partial t} = D \frac{\partial^2 c(x,t)}{\partial x^2} \quad (4.1.8)$$

Inserting Equation 4.1.7 into 4.1.6 gives:

$$\langle x(t)^2 \rangle = 2Dt \quad (4.1.9)$$

and

$$\sqrt{\langle x(t)^2 \rangle} = \sqrt{2Dt} \quad (4.1.10)$$

The diffusion coefficient  $D$  characterises the motion of molecules of a given kind at a given temperature within a given environment. It depends on the size of the molecules, the composition of the surrounding matrix and the temperature.

In two and three dimensions Equation 4.1.9 takes the following forms:

$$2D : \quad r^2 = x^2 + y^2 \quad \Rightarrow \quad \langle r(t)^2 \rangle = 4Dt \quad (4.1.11)$$

$$3D : \quad r^2 = x^2 + y^2 + z^2 \quad \Rightarrow \quad \langle r(t)^2 \rangle = 6Dt \quad (4.1.12)$$

If only the two dimensional projection of a three dimensional diffusion is measured, the two dimensional description is valid, because the motion along  $z$  is not taken into

account.

### 4.1.2 Probability Distributions

The signed distance  $X$  that a molecule covers in a single step can be considered as a random variable. From  $\langle x \rangle = 0$  it follows that the expectation value of  $X$  is  $\mu = 0$ . Likewise, from  $\langle x^2 \rangle = d^2$  (Equation 4.1.5) the variance of  $X$  is given as  $\sigma^2 = d^2$ . The position  $S_n$  of a molecule starting at  $x = 0$  after  $n$  steps is given by:

$$S_n = X_1 + X_2 + \dots + X_n \quad (4.1.13)$$

Each step is described by a random variable  $X_i$ , where all  $X_i$  are independent and have the same probability distribution. According to the central limit theorem, the probability to find a molecule at a distance  $x$  from the origin after  $n$  steps, i.e. the probability distribution of  $S_n$ , converges to a normal distribution  $N(\mu_n, \sigma_n)$  for high step numbers  $n$  with expectation value  $\mu_n = n\mu$  and variance  $\sigma_n^2 = n\sigma^2$ :

$$p(x, n) \xrightarrow{n \rightarrow \infty} N(\mu_n, \sigma_n) = N(n\mu, \sqrt{n}\sigma) = \frac{1}{\sqrt{n}\sigma\sqrt{2\pi}} \exp\left(-\frac{x - n\mu}{2(\sqrt{n}\sigma)^2}\right) \quad (4.1.14)$$

Since  $n = t/\tau$ ,  $\mu = 0$  and  $\sigma = d$ , it follows:

$$p(x, t) = \frac{1}{\sqrt{2\pi t d^2 \tau^{-1}}} \exp\left(-\frac{x^2}{2(\sqrt{t d^2 \tau^{-1}})^2}\right) = \stackrel{d^2/\tau=2D}{=} \frac{1}{\sqrt{4\pi D t}} \exp\left(-\frac{x^2}{4Dt}\right) \quad (4.1.15)$$

From this it is clear that the probability to find the molecule is highest at the origin and that the spread of the ensemble increases with increasing number of steps. This is also true for the spread of positions of an ensemble of molecules provided ergodicity holds good on the time scale of the measurement.<sup>97</sup>

Similar to the above treatment of a 1D random walk, we can consider a movement in 2D with  $r^2 = x^2 + y^2$  ( $x$  and  $y$  are independent variables) and again step length  $d$ . Since  $x = d \cos \phi$  and  $y = d \sin \phi$  the MSD along  $x$  and  $y$  is:

$$\langle x^2 \rangle = \frac{1}{2\pi} \int_0^{2\pi} d^2 \cos^2 \phi \, d\phi = \frac{d^2}{2} \quad (4.1.16)$$

$$\langle y^2 \rangle = \frac{1}{2\pi} \int_0^{2\pi} d^2 \sin^2 \phi \, d\phi = \frac{d^2}{2} \quad (4.1.17)$$

The standard deviation is thus  $\sigma = d/\sqrt{2}$ . It was shown above that for one step of duration  $\tau$

$$\langle r(\tau)^2 \rangle = 4\tau D_{2D} = d^2 \quad (4.1.18)$$

Thus, the diffusion coefficient for 2D diffusion  $D_{2D}$  is here

$$D_{2D} = \frac{d^2}{4\tau} \Leftrightarrow \frac{d^2}{\tau} = 4D_{2D} \quad (4.1.19)$$

Therefore the probability distribution is in two dimensions:

$$\begin{aligned} p(x,y,t) &= p(x,t) p(y,t) = \\ &= \left( \frac{1}{\sqrt{td^2\tau^{-1}2\pi}} \right)^2 \exp\left(-\frac{x^2+y^2}{td^2\tau^{-1}}\right) = \\ &\stackrel{r^2=x^2+y^2}{=} \frac{1}{4\pi Dt} \exp\left(-\frac{r^2}{4Dt}\right) = p(r,t) \end{aligned} \quad (4.1.20)$$

### 4.1.3 Cumulative Probability Distributions

Knowing the probability distribution of  $x$  and  $r$ , respectively, the cumulative probability distribution function for a given square step length  $R^2$  can be calculated. This cumulative distribution function gives the probability to obtain a value  $x^2 \leq R^2$  or  $r^2 \leq R^2$ . Here, the one-dimensional case is considered first and then extended to two dimensions.

### Diffusion in 1D

First, the probability distribution of  $x^2 := u$ , i.e.  $x = \pm\sqrt{u}$ , with  $u \in [0, \infty)$ , after a time  $t$  has to be derived.

$$q(u,t)du = [p(\sqrt{u},t) + p(-\sqrt{u},t)]\frac{dx}{du}du \quad (4.1.21)$$

With  $x = \pm\sqrt{u}$ ,  $\frac{dx}{du} = \frac{1}{2\sqrt{u}}$  and Equation 4.1.15, this gives:

$$q(u,t)du = \frac{1}{\sqrt{4\pi Dt u}} \exp\left(-\frac{u}{4Dt}\right) du \quad (4.1.22)$$

The cumulative probability  $P(R^2, t)$  to obtain a value  $x^2 \leq R^2$  at time  $t$  is the integral of the probability distribution of  $x^2 = u$ :

$$\begin{aligned} P(R^2, t) &= \int_0^{R^2} q(u,t)du = \\ &= \int_0^{R^2} \frac{1}{\sqrt{4\pi Dt u}} \exp\left(-\frac{u}{4Dt}\right) du = \\ &= \operatorname{erf}\left(\sqrt{\frac{R^2}{4Dt}}\right) \stackrel{\langle x(t)^2 \rangle = 2Dt}{=} \operatorname{erf}\left(\sqrt{\frac{R^2}{2\langle x(t)^2 \rangle}}\right) \end{aligned} \quad (4.1.23)$$

### Diffusion in 2D

In the above Equation 4.1.20 it is understood that integration of the probability distribution will be performed over the cartesian coordinates  $x$  and  $y$ . Therefore it can be rewritten more precisely as:

$$p(x,y,t)dxdy = \frac{1}{4\pi Dt} \exp\left(-\frac{x^2 + y^2}{4Dt}\right) dxdy \quad (4.1.24)$$

Since the steps in a 2D random walk are evenly distributed in all directions it is convenient to switch to spherical coordinates and to integrate then over all values of  $\phi$ . With

$r^2 = x^2 + y^2$  and  $dx dy \rightarrow r dr d\phi$  the above equation reads:

$$\begin{aligned}
 \tilde{p}(r, \phi, t) dr d\phi &= p(r, t) r dr d\phi \\
 &= \frac{1}{4\pi Dt} \exp\left(-\frac{r^2}{4Dt}\right) r dr d\phi \\
 \tilde{p}(r, t) dr &= \int_0^{2\pi} d\phi \frac{1}{4\pi Dt} \exp\left(-\frac{r^2}{4Dt}\right) r dr = \\
 &= \frac{1}{2Dt} \exp\left(-\frac{r^2}{4Dt}\right) r dr
 \end{aligned} \tag{4.1.25}$$

Again, like for the 1D random walk, the probability of square displacements  $r^2$  after a time  $t$  is derived, with  $r = \pm\sqrt{u}$  and  $\frac{dr}{du} = \frac{1}{2\sqrt{u}} = \frac{1}{2r}$ :

$$\begin{aligned}
 q(u, t) du &= \tilde{p}(\sqrt{u}, t) \frac{dr}{du} du = \\
 &= \frac{1}{4Dt} \exp\left(-\frac{u}{4Dt}\right) du
 \end{aligned} \tag{4.1.26}$$

Integration yields the cumulative probability distribution:

$$\begin{aligned}
 P(R^2, t) &= \int_0^{R^2} q(u, t) du = \\
 &= \int_0^{R^2} \frac{1}{4Dt} \exp\left(-\frac{u}{4Dt}\right) du = \\
 &= \left[-\exp\left(-\frac{u}{4Dt}\right)\right]_0^{R^2} = \\
 &= 1 - \exp\left(-\frac{R^2}{4Dt}\right) \stackrel{\langle r(t)^2 \rangle = 4Dt}{=} 1 - \exp\left(-\frac{R^2}{\langle r(t)^2 \rangle}\right)
 \end{aligned} \tag{4.1.27}$$

$P(R^2, t)$  is the probability that a molecule starting at the origin at  $t = 0$  will be found within a circle of radius  $R$  at time  $t$ .

The presented diffusion theory can be extended to allow for different components of diffusion in one single trajectory by using several diffusion coefficients:<sup>98</sup> For example

a slow and a fast component with diffusion coefficients  $D_1$  and  $D_2$  and thus MSD  $\langle r(t)_1^2 \rangle$  and  $\langle r(t)_2^2 \rangle$ , in the fractions  $\alpha$  and  $(1 - \alpha)$ . Then, Equation 4.1.27 becomes:

$$P(R^2, t) = 1 - \left[ \alpha \cdot \exp\left(-\frac{R^2}{\langle r_1(t)^2 \rangle}\right) + (1 - \alpha) \cdot \exp\left(-\frac{R^2}{\langle r_2(t)^2 \rangle}\right) \right] \quad (4.1.28)$$

and in a three-component model it would read:

$$P(R^2, t) = 1 - \left[ \alpha \cdot \exp\left(-\frac{R^2}{\langle r_1(t)^2 \rangle}\right) + \beta \cdot \exp\left(-\frac{R^2}{\langle r_2(t)^2 \rangle}\right) + (1 - \alpha - \beta) \cdot \exp\left(-\frac{R^2}{\langle r_3(t)^2 \rangle}\right) \right] \quad (4.1.29)$$

#### 4.1.4 Deviations from the Ideal Behaviour

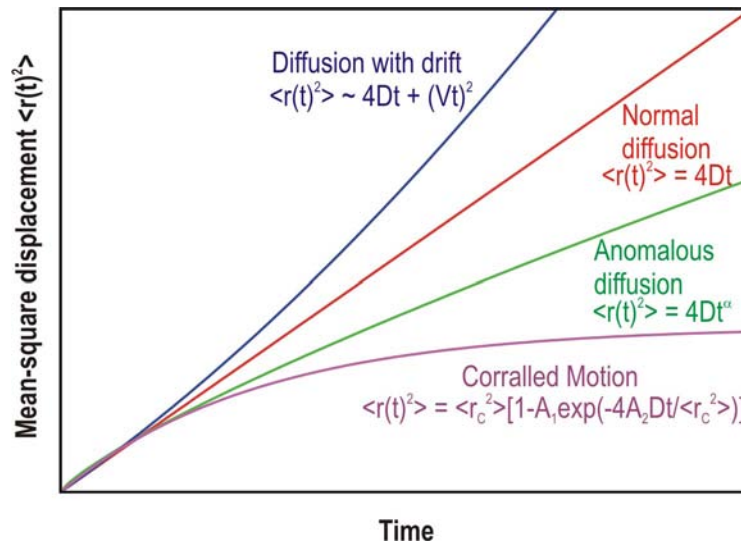


**Figure 4.1: Various modes of motion under different conditions.** The mean-square displacement  $\langle r^2 \rangle$  as a function of time  $t$  for simultaneous diffusion and flow, pure diffusion, diffusion in the presence of obstacles (anomalous diffusion), and confined motion<sup>96</sup>.

The above discussion was based on ideal behaviour of the molecules. In reality deviations from this are found, which can have various origins. Possible interactions might be: hindered diffusion in restricted geometries or between barriers, adsorption to receptors, active transport through flow or in biological systems. A major advantage of single-molecule tracking is the ability to resolve modes of motion of individual molecules, and one of its major achievements is the proof that molecular motion in a lipid bilayer<sup>137,98</sup> or within a porous host system<sup>95,93</sup> is not limited to pure diffusion. Several modes of motion have been observed: immobile, directed, confined, tethered,



normal diffusion, and anomalous diffusion.<sup>96</sup> Each of these modes of motion is characterised by a particular time evolution of the MSD  $\langle r(t)^2 \rangle$ . Plotting experimental values of  $\langle r(t)^2 \rangle$  against time, as sketched in Figure 4.1, is a powerful tool of identifying which of them dominates in a given sample. Equation 4.1.30 to 4.1.33 show the expected time dependence of  $\langle r(t)^2 \rangle$  for the most important modes of molecular motion.<sup>96</sup>

$$\text{Normal diffusion : } \langle r(t)^2 \rangle = 4Dt \quad (4.1.30)$$

$$\text{Anomalous diffusion : } \langle r(t)^2 \rangle = 4Dt^\alpha, 0 < \alpha < 1 \quad (4.1.31)$$

$$\text{Diffusion and flow : } \langle r(t)^2 \rangle = 4Dt + (Vt)^2, V \neq 0 \quad (4.1.32)$$

$$\text{Corralled motion : } \langle r(t)^2 \rangle \simeq \langle r_C^2 \rangle \left[ 1 - A_1 \exp \left( -\frac{4A_2 Dt}{\langle r_C^2 \rangle} \right) \right], \quad (4.1.33)$$

$$A_1, A_2 > 0$$

Ideal behaviour yields a linear relation, the MSD is directly proportional to the time (Equation 4.1.30). In the presence of obstacles the diffusion is hindered (Equation 4.1.31). The MSD is no longer proportional to  $t$ , but to  $t^\alpha$ . Since  $\alpha < 1$  this is, strictly speaking, anomalous subdiffusion.<sup>138,139</sup>

When the molecule remains confined to a certain region, the MSD converges to a certain value for large  $t$ . This value is given by the mean-square confinement radius  $\langle r_C^2 \rangle$ . In Equation 4.1.33  $A_1$  and  $A_2$  are constants determined by the corral geometry.<sup>140,141</sup>

In the case of directed transport (diffusion and flow, Equation 4.1.32) the drift motion  $\langle r_{\text{drift}} \rangle = Vt$  is superimposed on the diffusive motion and the curve takes a concave shape.

In small channels molecules may block each others' path such that their motion is no longer uncorrelated. This phenomenon is called single-file diffusion. However, this is not observed for the diffusion of single dye molecules in the present work, since the dye concentration in the samples is kept so low that the dye molecules never come close to each other for the reasons mentioned in Section 3.4.

## 4.2 Track Analysis

The two main goals of single-molecule tracking are to identify and characterise sub-populations of diffusing molecules and to extract spatial information about the host from the trajectories of individual particles. The statistical method is presented here that is used to investigate the differences in the diffusional behaviour of the individual molecules taking into account the structure of the host material.

The raw data obtained from tracking a single molecule are a sequence of position snapshots taken at regular time intervals. Together these form the single molecule's 2D trajectory. The visualization of this trajectory already allows a coarse by-eye classification of the molecule's diffusive behaviour – e.g. if the molecule is following a certain one-dimensional structure or if the molecule diffuses in an unstructured manner within the observation plane. However, investigation of the trajectories by eye might give misleading results, as the human eye is trained to see patterns and it might discover patterns from a purely random motion as well. In order to understand the details of the diffusion process, quantitative statistical analyses of the trajectory are needed. Analysis of the step lengths provides information about the diffusion coefficient and thus the 'speed' of the particle within the material. Investigation of the angles between successive steps can show deviations from random walk behaviour in one or two dimensions. By comparing the data obtained from many individual trajectories, different classes of diffusing molecules can be identified and the differences and similarities of the diffusion in various porous environments can be visualized. A *FORTRAN90* program was written (with the help of R. Brown) to perform the quantitative track analysis, and the results are visualized in an automated fashion using a collection of *gnuplot*<sup>133</sup> scripts.

### 4.2.1 Global Analysis

The most obvious visual analysis of a single-molecule trajectory is to plot all its points in one overview graph and to connect the points within the individual trajectories by straight lines. Such plots can be found in Figures 5.6 and 7.8, 7.10, 7.20, 7.26. One has to bear in mind that these straight lines do not represent the real pathway of the molecule because motion between the position snapshots taken with the CCD camera will in general not be linear. If the sampling rate of the positions is too low, the connecting lines represent only secants of the real curve, which the molecule followed. This is sketched in Figure 4.2a. While modern CCD cameras allow to collect videos with rates up to 100 frames per second, the resolution of the trajectories is still limited. Since the signal-to-noise ratio decreases with increasing framerates, the positioning error in-

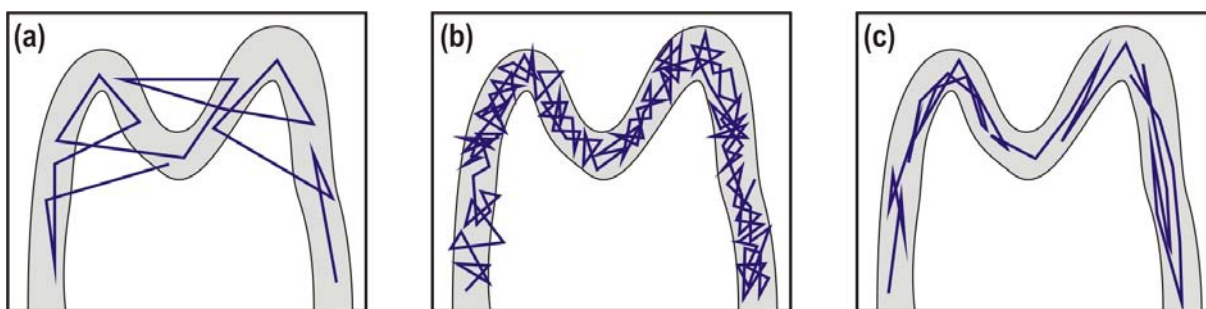


**Figure 4.2: Equilibrium of spatial and temporal resolution.** (a) Too few datapoints. (b) Positioning error bigger than average step length. (c) Good equilibrium between positioning error and step length.

creases. As soon as the positioning error exceeds the average step length in a trajectory, increasing the framerate will not help to resolve the real pathway of the molecule better (Figure 4.2b). Therefore for each system a good balance between the frame rate and the obtained positioning accuracy has to be found experimentally for each sample system, as shown in Figure 4.2c.

The overall plots of the trajectories can already provide useful information about the nature of diffusion; for example if the molecules diffuse randomly or follow 1D structures in the porous system. Different populations of diffusing molecules can be differentiated not only by the shape of the trajectories, but also by the area covered by the molecules during one movie. Molecules with a higher diffusion coefficient  $D$  do longer steps between frames. Note that, more precisely, the molecule undergoes numerous collisions and changes of direction in one sampling interval between two frames. The results of the random walk theory introduced above remain invariant, however, when the molecule position is sampled at larger time intervals than the mean time between collisions  $\tau$ , which is less than 1 ps. Therefore, in the following a step denotes the displacement of a molecule from one frame to another and the length of the connecting line constitutes thus the step length. Investigation of the step length distribution gives a detailed picture of the diffusion behaviour, as shown in the following paragraphs.

### 4.2.2 Step Length Analysis

In Section 4.1 it was shown, that a crucial parameter to describe the diffusion of individual particles on a microscopic scale is the mean-square displacement  $\langle r(t)^2 \rangle$  as a function of time. This  $\langle r(t)^2 \rangle$  can be calculated in different ways from the step length  $r$  and the square of the step length  $r^2$ . Depending on the method, inhomogeneities of the diffusion behaviour will be identified or averaged out. The different methods of

calculating the mean-square displacement are discussed here.

### Extracting step length data for different time lags

Single-molecule tracking yields a set of positions  $r(T) = [x(T), y(T)]$ , i.e. the coordinates of a particle at each time  $T$ . Particle positions are recorded as a time sequence, therefore  $x_n(T) = x(n\tau_F)$  and  $y_n(T) = y(n\tau_F)$ ,  $n = 0, 1, 2, \dots, N - 1$  with  $N$  being the total number of points in a trajectory and  $\tau_F$  the time interval between successive frames of the movie. First of all the step lengths for a given time interval  $t$  are calculated from the fitted positions. For timelags  $t$  that are multiples of the time between frames in the movies, two different methods can be used.<sup>142</sup> On the one hand, overlapping time intervals can be considered, i.e. every trajectory point is used as starting point for a step. On the other hand, independent time intervals can be regarded, this means that only every second, third, ... data point is taken into account. The latter method has the disadvantage that the number of data points  $r_i$  for a given timelag  $t$  decreases rapidly. The equation to calculate the  $i$ -th step length  $r$  from the data set for a given timelag  $t$  is thus:

$$r_i(T) = |\mathbf{r}(T_i + t) - \mathbf{r}(T_i)|$$

$$\text{overlapping intervals: } i = 0, 1, \dots, (N - 1) - t \quad (4.2.1)$$

$$\text{independent intervals: } i = n\tau, \text{ with } n = 0, 1, \dots, N/t$$

In Section 4.1 it was shown that the square of the step length  $r^2$  increases linearly with timelag  $t$  and that it has more physical importance in the analysis of diffusion than the step length  $r$  itself. Subsequently, there are different possibilities to analyse the extracted step length data. The  $r_i^2$  values for a given time interval  $t$  can be either binned into a histogram<sup>122</sup> or ranked according to their length, starting with the longest  $r_i^2$ .<sup>143</sup>

### Histogram and ranking of step lengths

Binning its values in a histogram might be the most straightforward way to visualize the distribution of  $r_i^2$ . Mathematically such a histogram can be fitted using the gaussian distribution from Equation 4.1.15 or 4.1.20. The method has the disadvantage that with the bin width a new, arbitrary parameter is introduced that affects the picture one obtains from such a plot. Especially if a trajectory consists of few data points the infor-

mation gained from this plot is limited. Another drawback of such histograms is that multiple diffusion components cannot be readily identified. Nonetheless, comparing the histograms of different individual molecules can help to separate fast molecules from slow ones. The shape and width of the histograms can be used to classify the molecules in one movie into several sub-populations.

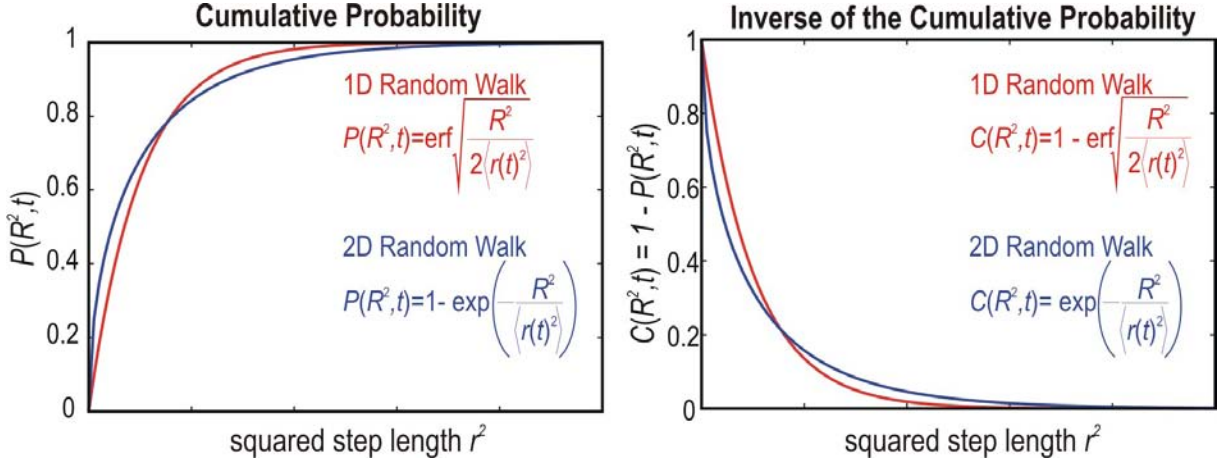


**Figure 4.3: Cumulative Probability distribution and inverse.** (a) The cumulative probability distribution  $P(R^2, t)$  is described by an error function for a 1D random walk, and by the inverse of an exponential distribution for random diffusion in 2D. (b) Plotting and fitting the data is more straightforward for the inverse distribution,  $C(R^2, t) = 1 - P(R^2, t)$ . For 2D the inverse is a simple exponential decay.

Where  $r_i^2$  histograms attempt to obtain an experimental estimate of the probability distribution  $p(r, t)$  (Equation 4.1.20) the ranking method aims to extract the cumulative probability distribution  $P(R^2, t)$  (Equations 4.1.23 and 4.1.27) from the data. Here, binning can be avoided by ordering the  $r_i^2$  values for a given time interval  $t$  and assigning then a rank  $\mathcal{R}(i)$ , starting at  $\mathcal{R}=1$  to the maximum  $r_i^2$ . For a given  $i$  the rank  $\mathcal{R}(i)$  is exactly the number of observed values of  $r^2$  that are greater than or equal to  $r_i^2$ . Therefore plotting  $\mathcal{R}(i)/\# \text{ samples}$  against  $r_i$  for each  $i$  gives an experimental estimate of the inverse cumulative distribution  $C(R^2, t)$ :

$$C(R^2, t) = P_{r \geq R^2}(t) = 1 - P_{r < R^2}(t) = 1 - P(R^2, t) \quad (4.2.2)$$

In 1D:

$$\begin{aligned} C(R^2, t) &\stackrel{4.1.23}{=} \\ &= 1 - \left[ \alpha \cdot \text{erf} \sqrt{\frac{R^2}{2\langle r_1(t)^2 \rangle}} + \beta \cdot \text{erf} \sqrt{\frac{R^2}{2\langle r_2(t)^2 \rangle}} + (1 - \alpha - \beta) \cdot \text{erf} \sqrt{\frac{R^2}{2\langle r_3(t)^2 \rangle}} \right] \end{aligned} \quad (4.2.3)$$

In 2D:

$$\begin{aligned}
 C(R^2, t) &\stackrel{4.1.27}{=} \\
 &= \alpha \cdot \exp\left(-\frac{R^2}{\langle r_1(t)^2 \rangle}\right) + \beta \cdot \exp\left(-\frac{R^2}{\langle r_2(t)^2 \rangle}\right) + (1 - \alpha - \beta) \cdot \exp\left(-\frac{R^2}{\langle r_3(t)^2 \rangle}\right)
 \end{aligned}
 \tag{4.2.4}$$

Figure 4.3a shows exemplary distributions  $P(R^2, t)$  for one component 1D and 2D random diffusion. The inverse of the distributions,  $C(R^2, t)$ , are depicted in Figure 4.3b. In 2D this is a simple exponential decay, which can be easily fitted. On a semi-logarithmic scale it can be easily seen if one or multiple components are contributing to the diffusion of an individual particle. This is illustrated in Figure 4.4, where the kink in the distributions in (b) clearly indicates the presence of several components of diffusion. In general, the experimental distributions  $C(R^2, t)$  might be fitted by a mono-, bi- or triexponential function. As a criterion to decide if multicomponent diffusion describes the data better than monomodal diffusion,  $\chi^2$  has to be significantly improved by introducing each additional component. Here, a decrease of  $\chi^2$  by a factor two<sup>144</sup> was used to justify the fit with an additional diffusion component. From these fits, mean-square displacements  $\langle r(t)_m^2 \rangle$  are obtained for each component  $i$  of the diffusion per individual time lag  $t$ , e.g. one  $\langle r(t)^2 \rangle$  in Figure 4.4a and two  $\langle r(t)_m^2 \rangle$  in (b). The diffusion coefficients of the individual molecules can then be calculated using a mean-square displacement against time analysis as discussed in the following paragraph.

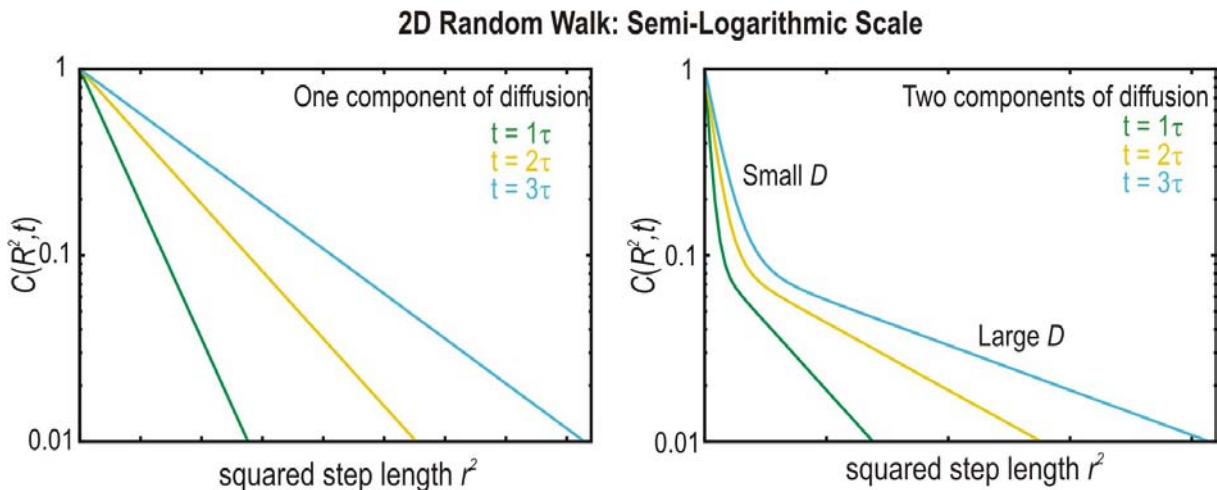


**Figure 4.4: Semi-logarithmic plots of the cumulative distribution for different time intervals. (a) Only one component of diffusion. (b) Two components of diffusion.**

### Mean-square displacement analysis and calculation of diffusion coefficients

The diffusion coefficient(s) for an individual molecule can be calculated either from the exponential decay fit parameters  $\langle r(t)_m^2 \rangle$  of  $C(R^2, t)$  or by averaging the individual squared step lengths  $r_i^2(t)$  for each given time interval  $t$ , with  $i_{max} = N$ :

$$\langle r^2(t) \rangle = \frac{\sum_{i=1}^N r_i^2(t)}{N} \quad (4.2.5)$$

The first method is denoted as the ranking method and the latter as the averaging method. The averaging method is the more straightforward and less time consuming way, as the additional fitting step for  $C(U, t)$  is replaced by a simple average, but inhomogeneities of the diffusion within a single trajectory cannot be identified.

Independently of the way  $\langle r(t)^2 \rangle$  is obtained, its values are then plotted against the time interval  $t$ . From these plots the diffusion coefficients  $D$  can be determined, as for a random walk the slope of the  $\langle r(t)^2 \rangle = \mathcal{N}Dt$ , where  $\mathcal{N} = 1, 2, 3$  is the dimension of diffusion. If different trajectories with various diffusion coefficients are shown in the same plot, it is advisable to use a double logarithmic scale for the plot. In this case different  $D$  values correspond to the distance of  $y$ -intercepts at  $x=1$ . As the 2D projection of 3D trajectories is observed, diffusion coefficients  $D$  are in most cases calculated according to the Einstein-Smoluchowski equation in 2D (Equation 4.1.11) by straight line through-zero fit. For the averaging method this yields one  $D$  value per trajectory, for the ranking method one, two or three  $D$  values, depending on the multiplicity of the exponential fit.

The ranking method allows to identify variations of the diffusion coefficient but these cannot be assigned to certain parts of the trajectory. In order to interpret variations of the diffusivity according to structural features, appropriate threshold values are defined for short, intermediate and long steps. These step lengths are plotted in the trajectory in different colours, to show if e.g. short or long steps accumulate at certain regions within the trajectory.

### Classification into different populations of molecules

In the same sample different populations of diffusing molecules can exist that differ in the shape of the trajectories and/or the diffusion coefficients. The latter can be easily distinguished in the log-log plots of  $\langle r(t)^2 \rangle$  versus time, when distinct populations of molecules show up as separated bundles of lines. An example of such a plot is given

in Figure 4.5a.

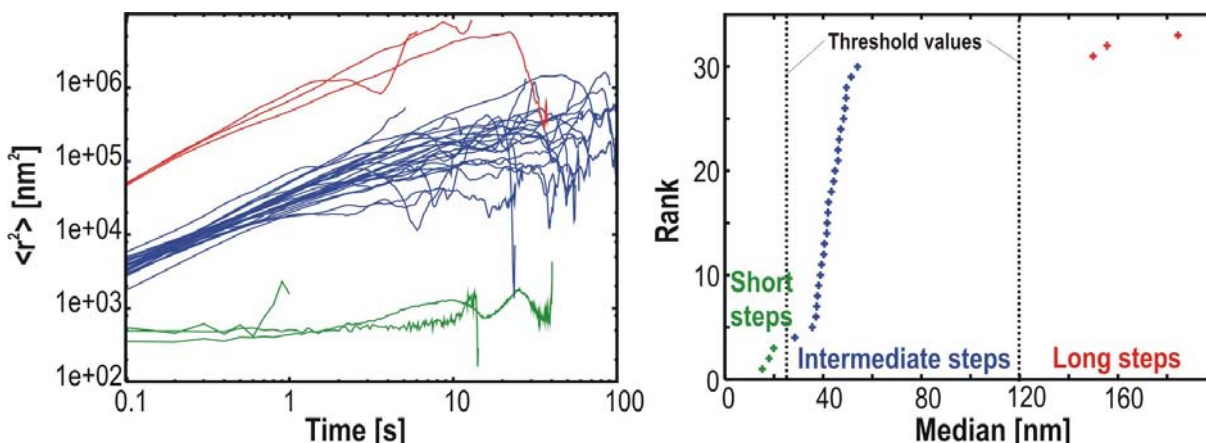


**Figure 4.5: Classification into different populations through MSD against  $t$  analysis or the median of the step length.** (a) Distinct bundles in the MSD plot reveal the presence of multiple populations of molecules with different diffusivities. (b) Ranking of the median step length of the individual trajectories shows the bundling of molecules into different populations. From this plot, threshold values can be defined to sort the molecules automatically into the different populations. These thresholds are also used to define what is a short, an intermediate and a long step.

Here, three populations of diffusing species can be distinguished by the time evolution of their MSD. One way to sort the molecules into the different populations, would thus be to calculate the diffusion coefficient for each individual trajectory and define threshold values for the calculated coefficients. A more straightforward and in practice equally reliable method is to use the median value of the individual step lengths in a trajectory. Unlike the mean value, the median is not affected by extraordinary long steps due to tracking errors. To define the threshold values the median values for all trajectories in one movie are sorted and plotted against the sorting rank, an example obtained from the data in Figure 4.5a is shown in Figure 4.5b. Values belonging to one population appear in such a plot on a nearly vertical line, the thresholds are placed in the middle of the interval separating two such step segments values. These thresholds define what is a short, an intermediate or a long jump and the trackanalysis program produces a graph where the step length populations are plotted in different colours (see above, Section 4.2.2). In this work, a maximum number of three different populations of molecules proved sufficient for all samples studied.

#### Projection on the backbone of a structured trajectory

It is known that there are bundles of tubes in the meso-porous silicas, which are arranged in domains with different orientations of pores. Even within the same domain



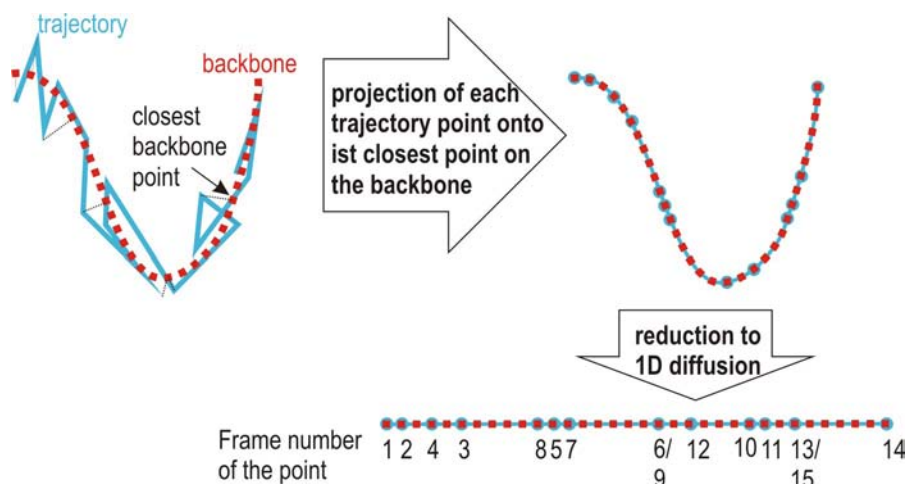


**Figure 4.6: Projection of a curved trajectory onto its backbone.** (a) Definition of the backbone. (b) Projection of each trajectory point to its closest point on the backbone. (c) Reduction to 1D diffusion and successive step length analysis.

the pores in one bundle can be strongly curved. This means, that a molecule diffusing in such a curved pore, would undergo one-dimensional diffusion, but along curved structures. Therefore it makes sense to analyse elongated trajectories in terms of progression along a bundle, i.e to project the data points distributed in 2D along a curved structure onto the backbone of the structure and analyse the diffusion along this 1D backbone. A method was developed to project such curved trajectories onto their backbone. The backbone is defined manually, by a set of points fairly regularly spaced down the middle of the trajectory, see Figure 4.6. Backbone points are not necessarily trajectory points, but represent what is considered to be closest to the tube axis. The backbone projection is done by making a .gif image of the trajectory plot and using the freeware *g3data* program (by J. Frantz), which converts pixel values in a .gif image to  $(x,y)$  pairs. Then a *FORTTRAN90* routine searches for each trajectory point the closest backbone point, i.e. each of the trajectory points is projected to the closest backbone point. To reach a high accuracy the density of points on the backbone has to be higher than the number of points in the trajectory. Diffusion is then analysed along this backbone using a 1D model.  $\langle r(t)^2 \rangle$  can again be calculated either by the averaging method or by ranking the squared step lengths. Note that in the 1D case  $C(R^2, t)$  cannot be fitted with an exponential, but with the complementary error function. Naturally, this method can only be applied to trajectories with a linear topology that are not branched.

### 4.2.3 Angles between Successive Steps

An analysis of the angles between successive steps can provide additional information. For this analysis, the angle  $\alpha \in (-180^\circ, 180^\circ]$  is calculated that every three successive data points in a trajectory enclose (Figure 4.7). For example, two steps in the same direction define an angle of  $0^\circ$  (forward), and two steps in opposite directions an angle of  $\pm 180^\circ$  (backward). Note that the angles thus obtained do not contain any information with respect to the overall orientation of the sample.

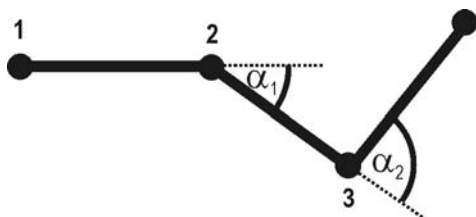


**Figure 4.7: Definition of angle between successive steps.** The angle  $\alpha_i$  that is included by every three successive trajectory points is defined as the angle between successive steps.

The angles  $\alpha_i$  can be analysed in several ways. First of all they can be plotted into a histogram. For a normal random walk in 2D this histogram should show a flat line because all angles have equal probability (Figure 4.8). A particle diffusing randomly in 1D has equal probability to do successive steps in the same or in opposite directions, therefore distinct peaks of equal height at  $\pm 180^\circ$  and  $0^\circ$  are expected. As all tracked positions have a finite positioning error in 2D, no histogram of real data, even for a perfect random walk within one linear pore, can have such a discrete distribution. However, these histograms can give information if a molecule is undergoing mainly 1D diffusion, i.e. excess of forward and backward steps, or moving randomly in 2D, i.e. flat distribution of angles. The broken lines in the figure depict exemplary distributions. In red a typical distribution for a molecule following a one-dimensional structure is shown. The blue line sketches the data for a 2D random walk with slight excess of forward diffusion, identifiable by the weak maximum around  $0^\circ$ .

Furthermore, more subtle deviations from random diffusion in one or two dimensions can be discovered from the angular distributions. For example if the molecule has a tendency to do several steps in the same direction rather than turning around, a broad peak around  $0^\circ$  and minima of the distribution around  $\pm 180^\circ$  are observed. To analyse such behaviour more accurately, the cumulative distribution of angles can be plotted using the same ranking technique as described in Section 4.2.2. As the values do not contain spatial information, only the modulus of the angles is considered in these graphs. An example for such a graph is given in Figure 4.9a. An ideal 2D random walk should result in the diagonal of the plot window (blue, solid line in the figure) and

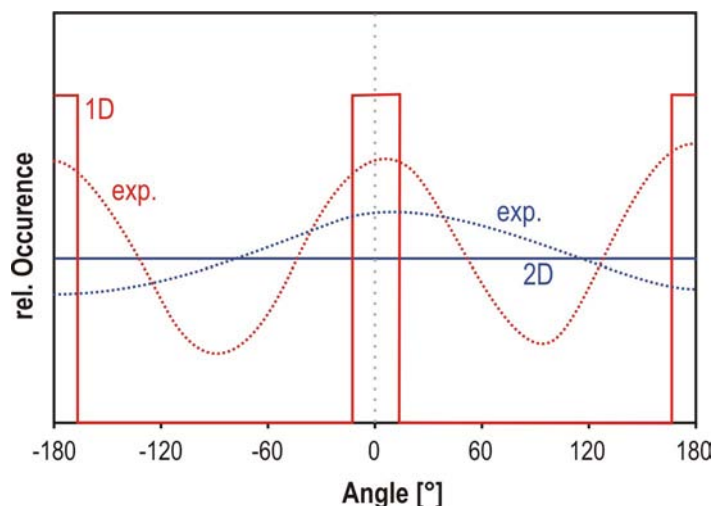


**Figure 4.8: Histogram of angles between successive steps.** Solid lines: Ideal 1D (red) and 2D (blue) random walk. Broken lines: Example distributions of real tracking data. Red: Typical distribution for a molecule following a one-dimensional structure. Blue: Random diffusion in 2D with a slight excess of steps forward.

for 1D diffusion values accumulate at  $0^\circ$  and  $180^\circ$  (red line). As said above, most of the tracked trajectories in a structured material lie in between 1D and 2D behaviour, like the dotted lines show in the figure. For any kind of random diffusion the number of angles below and above  $90^\circ$  should be equal (solid lines, black dotted line). Deviations from randomness are immediately visible from the graphs, when the curve at an angle of  $90^\circ$  is below or above 0.5. It is not known what the exact distribution - somewhere between 1D and 2D - should be. Nonetheless, independent of its precise shape, the absence of memory implicit in the model of random diffusion requires that  $P(180^\circ - \alpha) = 1 - P(\alpha)$ . That can be checked by plotting both  $(\alpha, P(\alpha))$  and  $(180^\circ - \alpha, 1 - P(\alpha))$ . The curves should be identical, but in practice deviations of the two curves are found. It has to be tested, if the deviations are significant compared to just statistical noise. This is done using a Kolmogorov-Smirnov test<sup>145</sup> is applied to test if the deviation of the two graphs is significant. This test searches the maximum distance between two data sets, here the cumulative distribution of angles and its inverse, and calculates the probability that this distance might originate from pure statistical spread of the data points for a given level of significance.

An overview of the ratio of steps forward, backward and to the side for all molecules in one movie can be plotted in a stacked column chart, like shown in Figure 4.9b. Here, angles between  $0^\circ$  and  $60^\circ$  were considered as steps forward, between  $60^\circ$  and  $120^\circ$  as sideward and  $120^\circ$  to  $180^\circ$  as steps backward. The percentage of each of the categories are plotted in one column per molecule in one movie. In order to obtain a clearer picture and to better compare the data from different movies, the columns were sorted by decreasing ratio of forward/backward steps. Note that molecules which

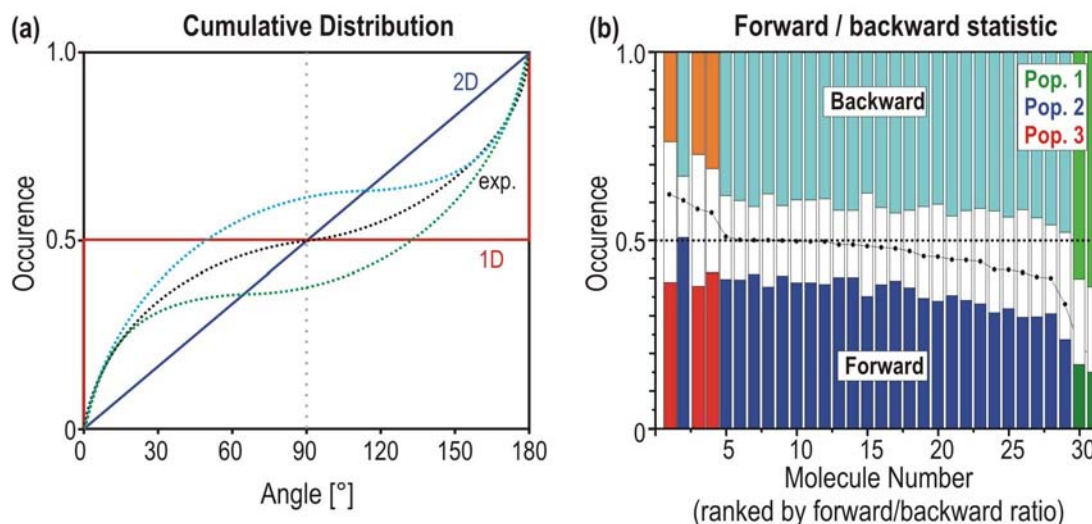


**Figure 4.9: Cumulative distribution of angles and stacked histogram of forward and backward steps.** (a) Examples for cumulative distributions of angles between successive steps for one individual molecule. Solid lines: Ideal 1D (red) and 2D (dark blue) random walk. Dotted lines: Example distributions of real tracking data. Black: Equal amount of forward and backward steps. Pale blue: Excess of forward steps. Green: Inverse of the distribution. For a random distribution of angles the original distribution and its inverse should overlap perfectly. (b) Stacked column chart of forward, intermediate and backward steps for the individual molecules tracked in one movie, sorted by decreasing forward/backward ratio (black line).

are immobile within the positioning accuracy (green columns) exhibit a large excess of 'steps' backward, due to a tracking artefact which is described above and in Ref.<sup>118</sup> The colour coding in this graph was done according to the classification of molecules into different populations described above. Interestingly, the order of molecules in the stacked histogram follows roughly the grouping into different populations.

### Angular distribution for immobile molecules

The angular histogram for the tracked data of an immobile molecule shall be discussed here in a bit more detail, as the outcome of such a plot is fairly puzzling at first sight. Figure 4.10a depicts such a graph. The U-shaped distribution is striking, implying a very large excess of 'steps' backward ( $\pm 180^\circ$ ) and hardly any 'steps' forward. Tracked data from simulated immobile trajectories, i.e. molecules with  $D = 0$  and a gaussian noise added to the position according to the positioning accuracy of experimental data, show similar distributions. Indeed, the U-shaped distribution of angles is an artefact due to the gaussian-distributed positioning error. In the following calculation the forward-backward asymmetry is derived for the 1D case.  $P(x)$  is the positioning-error gaussian distribution centred at the true molecular position. If a value of  $x_i$  is measured

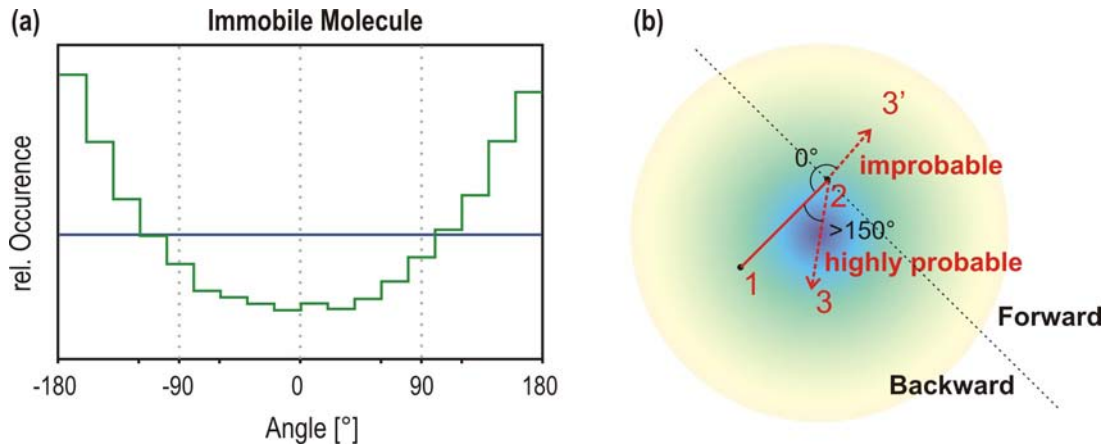


**Figure 4.10: Histogram of angles for an immobile molecule.** (a) Typical U-shaped histogram for an immobile molecule, with high excess of backward steps. (b) For the case of a gaussian distribution of points around the true centre, the probability is much higher for the subsequent 'step' to point in the direction of the centre (backward) than another step away from the centre (forward).

at step  $i$ , then

$$P_{\text{forward}} = P(x_{i-1} < x_i)P(x_{i+1} > x_i) + P(x_{i-1} > x_i)P(x_{i+1} < x_i) \quad (4.2.6)$$

$$P_{\text{backward}} = P(x_{i-1} < x_i)P(x_{i+1} < x_i) + P(x_{i-1} > x_i)P(x_{i+1} > x_i) \quad (4.2.7)$$

Since the molecule is immobile the probability distribution is the same for all  $i$ :

$$P_{\text{forward}} = 2P(x < x_i)P(x > x_i) \quad (4.2.8)$$

$$P_{\text{backward}} = 2P(x < x_i)P(x > x_i) \quad (4.2.9)$$

Setting  $p := P(x < x_i)$  leads to  $P(x > x_i) = 1 - p$ , and

$$P_{\text{forward}} = 2p(1 - p) \quad (4.2.10)$$

$$P_{\text{backward}} = p^2 + (1 - p)^2, \quad (4.2.11)$$

and the forward-backward asymmetry  $A$  is:

$$A = \frac{P_{\text{forward}}}{P_{\text{backward}}} = \frac{2p(1-p)}{p^2 + (1-p)^2} \quad (4.2.12)$$

$A \leq 1 \Leftrightarrow P_{\text{backward}} \geq P_{\text{forward}}$  holds regardless of the particular value of  $p$ , which can be seen as follows:

$$P_{\text{backward}} \geq P_{\text{forward}} \quad (4.2.13)$$

$$\Leftrightarrow P_{\text{backward}} - P_{\text{forward}} \geq 0 \quad (4.2.14)$$

$$\Leftrightarrow p^2 + 1 - 2p + p^2 - 2p + 2p^2 \geq 0 \quad (4.2.15)$$

$$\Leftrightarrow 4p^2 - 4p - 1 \geq 0 \quad (4.2.16)$$

$$\Leftrightarrow 4(p - 1/2)^2 \geq 0 \quad (4.2.17)$$

An analogous consideration holds for the 2D case (Figure 4.10b).

Now that the materials, experimental method, theoretical method and data analysis have been introduced, we are ready to discuss - in the following three chapters - the experimental results obtained by tracking the diffusion of single dye molecules in sol-gel glasses and mesoporous thin films.

# 5 Diffusion of the Streptocyanine Dye 9A1 in Porous Sol-Gel Materials

In this chapter diffusion within different types of sol-gel glasses is characterised using single-molecule microscopy and pulsed-field gradient NMR. First, the macroscopic analysis of the host matrices by adsorption measurements and ensemble fluorescence spectra of the dye used for single-molecule tracking are presented. The main section focusses on single-molecule data collected with wide-field microscopy from two different sample series **M3** and **M22**. Single-molecule techniques are especially well-suited for such heterogeneous pore systems. Tracking of single molecules yields the complete distribution of the diffusion coefficients, and, as will be shown here, single-molecule tracking can even distinguish non-Brownian behaviour of individual dye molecules, when the overall diffusion appears to be normal. In this way single molecules act as probes for spatial heterogeneities. In order to obtain a significant statistic to derive the ensemble behaviour, a high number of molecules has to be tracked. A complementary method, which provides information about the ensemble diffusion is pulsed-field gradient NMR. Therefore, the last part of this chapter reports on PFG NMR of the self-diffusion of ethylene glycol in different sol-gel systems, including those studied by SMT.

This project was done in collaboration with different groups: The synthesis of the sol-gel glasses was done by Virginie Latour, Christophe Cantau and Thierry Pigot at the University of Pau (France), sorption measurements were conducted by Pierre Mocho, University of Pau and Tina Reuther from the group of Prof. Bein at the LMU Munich. The pulsed-field gradient NMR measurements were done in cooperation with Bärbel Krause from the group of Prof. Kärger at the University of Leipzig.

## 5.1 Synthesis of the Sol-Gel Glasses

A major goal of this work was to elucidate the influence of pore size on molecular diffusion in cast silica xerogels and on spatial heterogeneities in these systems. Two types of xerogel were doped with a new streptocyanine dye: in one of the gels (**M3**) the pores are about the same size as the dye molecule, in the other (**M22**) they are much bigger. **M3** and **M22** were studied by SMT; these, and a series of similar samples with porosities in the same range were investigated by PFG NMR spectroscopy.

The porous sol-gel materials were synthesized as monoliths by the conventional method of hydrolysis and condensation of tetramethyl orthosilicate (TMOS) in the presence of methanol under neutral conditions (cf. Chapter 2.1<sup>146</sup>). Samples suitably clear and crack-free for single-molecule detection were obtained. Porosity depends on the TMOS/methanol/water molar ratio, which was 1/5/4 or 1/5/20 for the two gels investigated using single-molecule spectroscopy.<sup>93</sup> The resulting gels are called here **M22** and **M3**, respectively, after their mean mesopore sizes in nanometres, determined by the adsorption measurements described below. The initial ratio of water to TMOS (water is also produced during condensation of the silicate) is stoichiometric for **M22**, but corresponds to a large excess of water for **M3**. The solutions in methanol were added to unbuffered water (reverse osmosis, 5 – 10 S cm<sup>-1</sup>), and TMOS (Aldrich, 99%) was added in one step. This solution was stirred magnetically for two minutes. Samples of 1 mL of the sol were closed in polypropylene Eppendorf<sup>®</sup> microtubes. Gelation was achieved in 10 days in an oven at 50 °C. The microtubes were then opened for drying the gels at atmospheric pressure for 6 h at 60 °C and 60 h at 80 °C, after which the samples were kept in the closed tubes until use. Residual water and methanol are present in the dried monoliths. The loss of weight on drying under primary vacuum for four hours at 200 °C was about 15% of the dry weight, corresponding to the common micropore volume of the gels, see below in Section 5.2.

**Table 5.1: Synthesis recipes for the different sol-gel glasses (molar ratios).**

Gel	M3	M4	M22	SG8	SG26	SG21
TMOS	1	1	1	1	1	1
APTES	-	-	-	-	0.03	0.06
Methanol	5	5	5	5	5	5
Water	20	8	4	4	4	4

In order to gain a broader overview of the ensemble diffusion phenomena in such sol-gel glasses, a larger variety of samples was used for the NMR measurements. In addition to **M3** and **M22** described above, another monolithic sol-gel glass, **M4**, with



a mean mesopore diameter of about 3 – 5 nm was used. It was synthesized using the same procedure as for **M3** and **M22** with a TMOS/methanol/water molar ratio of 1/5/8. In order to obtain larger mesopore diameters and higher degrees of mesoporosity, samples were synthesized by co-condensation of TMOS and aminopropyl triethoxy silane (APTES) in two different ratios (3% APTES: **SG26** and 6% APTES: **SG21**). A summary of the different samples and their syntheses is provided in Table 5.1. The synthesis of these sol-gel glasses has been published in reference.<sup>147</sup> The purity of all materials was checked by fluorescence spectroscopy on an Edinburgh Instruments FS920 spectrofluorimeter.

### 5.1.1 Sample Preparation for Single-Molecule Microscopy

A dilution series of the streptocyanine dye **9A1**, synthesized by Corinne Payrastré and Valérie Guieu (Univ. P. Sabatier, Toulouse, France),<sup>148,149</sup> structure shown in Figure 5.1, was prepared in methanol (SDS, spectrophotometric grade), at concentrations adjusted to allow for shrinkage of the gels during drying (about 80 %). The final concentrations in the monoliths were between  $5 \times 10^{-7} \text{ mol L}^{-1}$  to  $5 \times 10^{-13} \text{ mol L}^{-1}$ . A concentration of about  $10^{-10} \text{ mol L}^{-1}$  appeared to be suited best for single-molecule tracking.

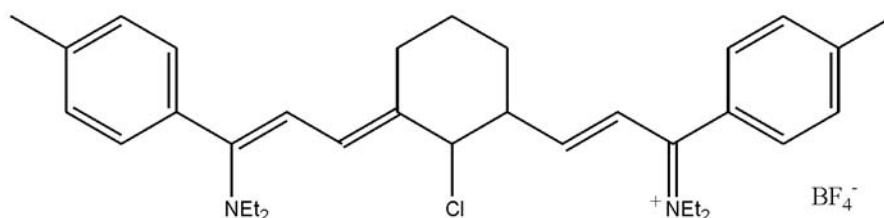


**Figure 5.1: Chemical structure of the streptocyanine dye 9A1.** 5-chloro-1,9-diethylamino-1,9-di(4-methylphenyl)-4,6-[propane]-nona-1,3,5,7-tetraenyl cation tetrafluoroborate.

Millimetre-sized chips were cut from the doped monoliths using a clean scalpel (VWR). Five to ten of these chips were deposited in a microcavity microscope slide with a few drops of ethylene glycol for index matching, covered with a cover-slip and left to equilibrate for at least half an hour before observation (Figure 5.2). From the loss of weight under vacuum drying and from the uptake of ethylene glycol by the gels, it is known that the mesopore system of both types of xerogels, **M3** and **M22**, is completely filled with ethylene glycol after 30 minutes. The sample was placed onto the microscope stage of the wide-field setup. Movies of 500 or 1000 images were collected with a temporal resolution between 50 ms and 200 ms.

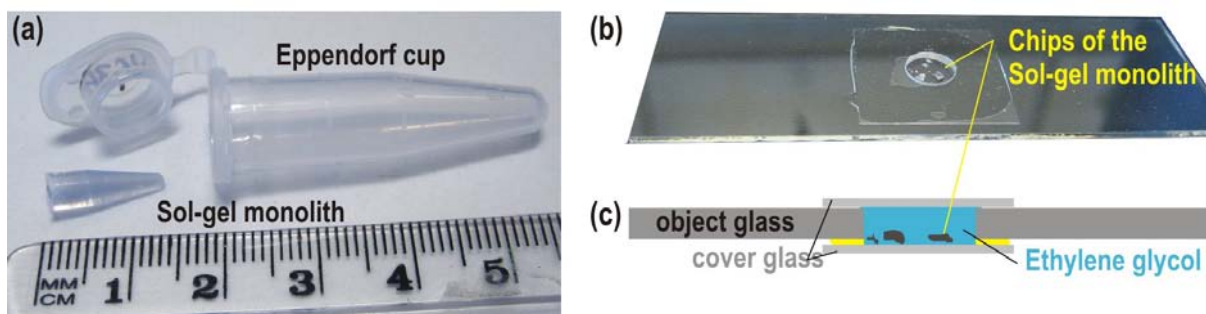


**Figure 5.2: Sol-gel samples.** (a) Sol-gel monolith in the shape of the Eppendorf® microtube in which it was synthesized. (b) Microcavity microscope slide with chips of the sol-gel material. (c) Cross-section sketch of the cavity filled with ethylene glycol and sealed with a cover-slip.

### 5.1.2 Sample Preparation for Pulsed-Field Gradient NMR

For the NMR measurements blank samples without dye were soaked with ethylene glycol. The samples were prepared on a home-built vacuum line in the following way: First the length of the monoliths was measured and if they were longer than 1 cm the tip was cut off with a scalpel because the homogeneous field in the centre of the high frequency (saddle HF) coil of the NMR spectrometer is no longer than 1 cm, thus longer samples would give rise to an undefined additional curvature in the spin-echo decay. The monolith was then placed into an NMR tube and gently evacuated to a final vacuum of about  $10^{-5}$  mbar. The pressure was decreased slowly during 2 h to prevent the formation of cracks through water evaporating too quickly from small capillaries. After that, the sample was flushed with dry Argon, and degassed ethylene glycol was added via a syringe under Argon counter current. The sample was kept in the solvent overnight, to favour a complete filling of all accessible pores with the solvent. Then the monolith was taken out of the solution, carefully wiped with a lens cleaning tissue to remove excess solvent and transferred into a dry and Argon flooded NMR tube. Mineral wool was used to fix the sample in the tube and the tube was sealed under low

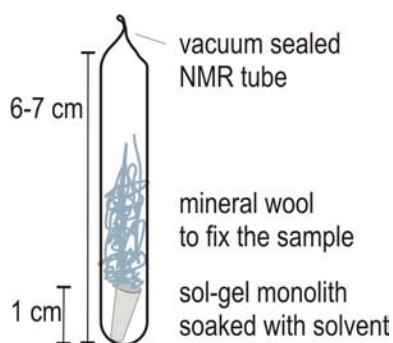


**Figure 5.3: Sample for PFG NMR.** The height of the sol-gel monolith must not exceed 1 cm, to fit into the HF coil. Mineral wool is used to fix the sample inside the tube.

vacuum using a gas burner. Figure 5.3 sketches the final NMR sample tube with the sol-gel monolith inside.

## 5.2 Analysis of Host and Guest

### 5.2.1 Sorption Isotherms

Nitrogen adsorption and desorption isotherms of the gels, depicted in Figure 5.4, were measured at 77 K on an ASAP 2010 Micropore nitrogen adsorption apparatus by our cooperation partners at the University of Pau. The isotherms of gel **M3** are of Type I (see Section 2.3).<sup>150</sup> This shows that only a single monolayer of molecules is adsorbed (Langmuir model). **M22** gels have Type IV isotherms (BET model), and thus show multi-layer adsorption (cf. Figure 2.7). The hysteresis between desorption and adsorption in **M22** is characteristic of a mesoporous material.

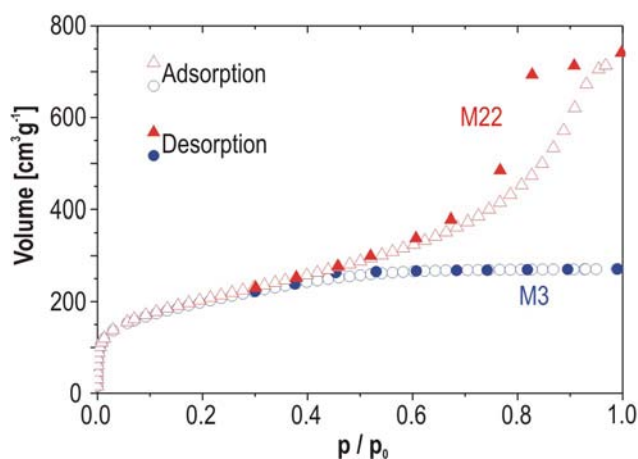


**Figure 5.4: Sorption isotherms of the xerogels.** Nitrogen adsorption (open symbols) and desorption (filled symbols) isotherms at 77 K, for the silica xerogels **M3** (blue circles) and **M22** (red triangles). The gels have very similar microporosities, but **M22** has a much larger mesoporosity, see Table 5.2.

Both materials have micro- and mesopores. The isotherms of **M3** and **M22** are very close in the range  $p/p_0 < 0.3$ , indicating a similarity of microporosities ( $p/p_0 < 0.01$ ) extending well into the mesopore range. The micropore volume is in fact the same for **M3** and **M22**. Mesoporosity in gel **M3** is limited ( $0.15 \text{ cm}^3 \text{ g}^{-1}$ ), but is much larger ( $0.9 \text{ cm}^3 \text{ g}^{-1}$ ) in **M22**. Table 5.2 summarizes the principal data deduced from the isotherms. Gel **M22**, with a wide spread of mesopore diameters (mean 22.4 nm), was less well described than **M3** by the Barrett-Joyner-Halenda (BJH) model and the figures given for its mesoporosity should be regarded as approximate.

The porosity data of the additional samples **M4**, **SG8**, **SG26** and **SG21** was measured in the same way as for **M3** and **M22**. The following table summarizes all porosity information gathered from sorption isotherms of the different samples.

Table 5.2: Porosity Data for Silica Gels **M3** and **M22**.

Gel	M3	M22	M4	SG8	SG26	SG21
BET <sup>68</sup> specific surface area (m <sup>2</sup> g <sup>-1</sup> )	715	740		726	491	467
HK <sup>151</sup> slit micropore volume (cm <sup>3</sup> g <sup>-1</sup> )	0.25	0.25		0.21	0.11	0.10
BJH <sup>70</sup> mesopore volume (cm <sup>3</sup> g <sup>-1</sup> )	0.15	0.9		0.12	0.94	0.81
BJH mesopore surface area (m <sup>2</sup> g <sup>-1</sup> )	200	160		62	142	151
HK median micropore diameter (nm)	0.8	0.8				
BJH mean mesopore diameter (nm)	3.1	22.4	3-5	8.2	26.5	21.6

### 5.2.2 Spectra of the Fluorescent Dye 9A1

The fluorescence and excitation spectra of **9A1** in methanol, water and ethylene glycol and in the monoliths were recorded with an FS920 spectrofluorimeter (Edinburgh instruments). The spectra in water and ethylene glycol are very close to those in methanol shown in Figure 5.5.

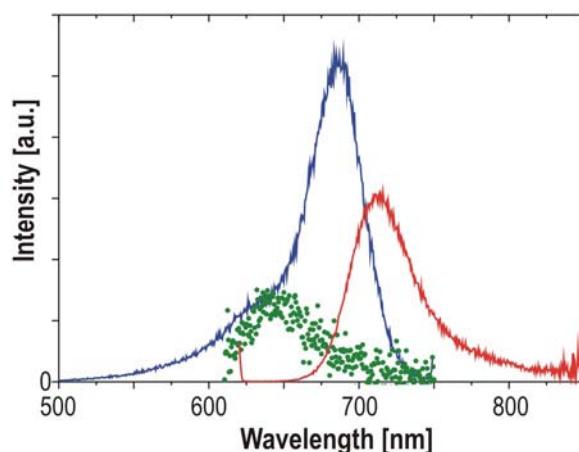


Figure 5.5: Spectra of the dye **9A1**. Fluorescence (red) and excitation spectrum (blue) of **9A1** at concentration ca.  $10^{-7}$  mol L<sup>-1</sup> in methanol and the emission spectrum in the **M22** xerogel at the same concentration (green dots, intensity scale  $100 \times$  magnified).

The fluorescence spectrum in the monoliths was substantially blue shifted compared to those in methanol solution. It was also about two orders of magnitude weaker in the monoliths than in solution. This effect was not found when similar monoliths

were doped with other dyes and must therefore reflect a reduced average fluorescence. However, single molecules could be observed with high counting rates in the single-molecule setup, therefore it is likely that the fluorescence of a majority of molecules is almost completely quenched in the xerogels whereas others are more or less undisturbed. One explanation for the weak fluorescence and the blue shift in the gel compared to the solution is a reduction of conjugation due to deformation of the molecule in the solid. It is possible that a majority of molecules are adsorbed in narrow pores, for which one would expect both stronger deformation and larger adsorption energies than for a molecule inside a wide pore. Another possible explanation is that the photophysical properties of the positively charged dye are modified by some specific and strong interaction with the pore surface, for example with surface hydroxyl groups.

## 5.3 Single-Molecule Measurements

For the single-molecule experiments the fluorescing dye molecules were excited with a HeNe Laser at 633 nm and movies of up to 1000 images were recorded to follow their diffusion. All the single-molecule measurements in this chapter were performed using the PentaMAX ICCD camera. Wide-field movies were collected from the samples loaded with a concentration of about  $10^{-10}$  mol L<sup>-1</sup> of **9A1** dye molecules. The results obtained from the different samples will be discussed in detail in this section.

### 5.3.1 Single-Molecule Trajectories: Overview

In Figure 5.6 the single particle trajectories from movies in the two different sol-gel glasses **M22** and **M3** are shown. All movies were collected with a temporal resolution of 100 ms. The focus was set to a position about 10 – 20 μm above the lower surface of the millimetre sized chips, to insure that all observed molecules are inside the bulk of the material. In order to check the homogeneity of the monoliths, about 10 movies were made in different chips of each kind of sample and at different depths within a chip. Bias of the operator is always a question when measuring and evaluating single-molecule data. Therefore, no attempt was made to look for interesting regions of the sample or to wait for an especially interesting molecule to appear. Any molecule coming into the focus was tracked. The molecular positions in each frame were determined from the fit of the two-dimensional gaussian function of Equation 3.4.1 to the fluorescence spots.

The left panel of Figure 5.6 depicts all 20 trajectories of molecules diffusing in the com-

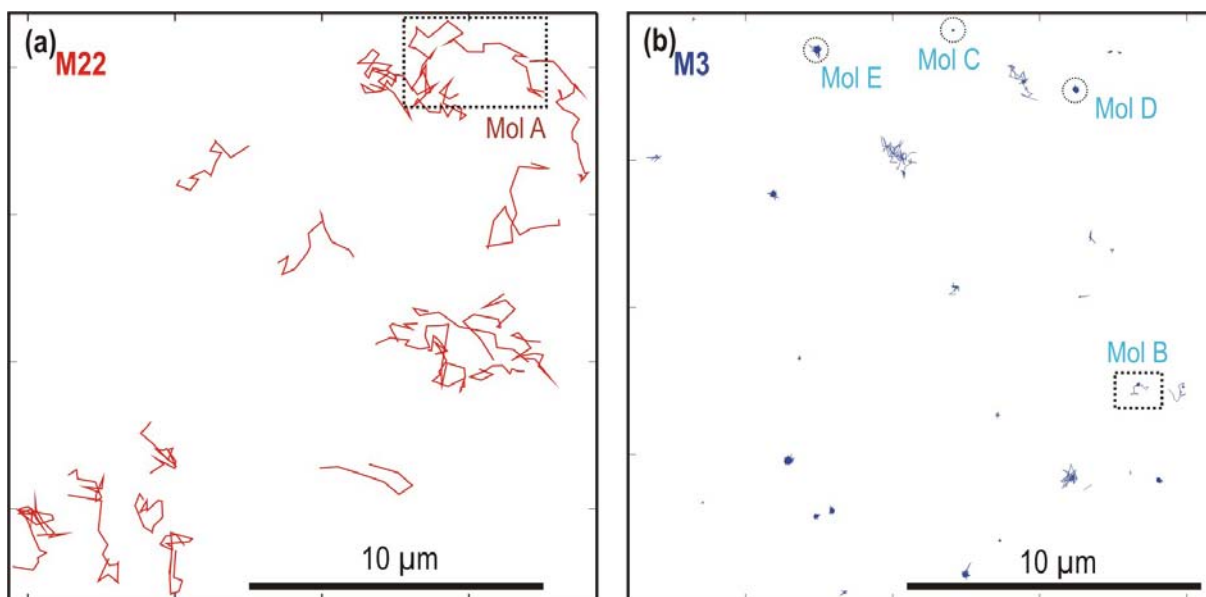


**Figure 5.6: Overview over all Single-molecule trajectories in two different sol-gel glasses.** (a) 20 unstructured trajectories covering large areas are observed in **M22**, which has mesopores of 22 nm in average. (b) In the **M3** material, with 3 nm average mesopore diameter, most molecules remain immobile or confined, or diffuse slowly in small regions. The scale is the same for both panels.

paratively wide-pored **M22** material obtained from one individual movie composed of 500 frames. Here no molecules could be observed over the complete duration of the movie, because the material extends in three dimensions, i.e. molecules can diffuse in and out of focus. Furthermore, the **9A1** dyes are less photostable than the **TDI**-derivatives used for the measurements presented later. Interactions with the substrate may alter the photophysical properties of the molecule when it is adsorbed on the pore surface, which could be an additional reason for the shortness of the trajectories. The trajectories are between four and 53 steps long, with an average track length of 18 steps. All molecules are mobile and they cover areas of up to 5  $\mu\text{m}$  while diffusing.

In contrast, on the right panel 37 trajectories of **9A1** in the comparatively narrow-pored **M3** material obtained from six different movies of 500 frames are shown. All trajectories from six different movies are plotted together, because only very few molecules could be observed in a single movie due to the low mobility of the dye in the **M3** material. However, this low mobility permits the observation of molecules during the complete duration of the movie. When comparing the two panels of the figure, which are plotted in the same scale, it is apparent that the majority of molecules of **9A1** in **M22** move several micrometres during the movie, whereas a majority of those in **M3** moves but within a very restricted area around their first sighting. Here, most of the molecules are immobile or remain confined in regions smaller than 500 nm. Very few molecules show slow diffusion or can even change between diffusion and confined

state. These first observations already indicate that diffusion of **9A1** molecules is more free in the larger pores of **M22** than in the smaller pores of **M3**. The behaviour of the individual molecules, denoted as molecules **A-E**, is discussed in more detail below.

### 5.3.2 Duration of the Tracks: Experiment and Simulation

The known geometry of the detection volume and the experimentally determined diffusion coefficients found below are used to evaluate the distribution of track durations in Monte Carlo simulations of Brownian motion. In these simulations, a molecule undergoes Brownian motion in a slab centred on the focal volume, using the distribution of step lengths between frames calculated from the diffusion coefficient. Periodic boundary conditions are applied to the motion at the slab boundaries. The distribution of times spent in the detection volume can be built up from these simulations. In the case of xerogel **M22**, diffusion alone, without photobleaching, suffices to explain the observed distribution of track durations. Tracks last significantly longer in **M3** (mean 12.3 s, standard deviation 13.6 s for trapped or immobile molecules). Single molecules of **9A1** embedded in PMMA survive  $(4.4 \pm 0.7) \times 10^6$  optical cycles, to be compared with  $(4 \pm 2) \times 10^7$  for oxazine-1, or  $(4 \pm 2) \times 10^6$  for Cy5 in the same matrix.

### 5.3.3 Mean-Square Displacement Analysis

To obtain a general picture of the overall diffusion behaviour the average mean-square displacement  $\langle r(t)^2 \rangle$  is plotted against the time lag  $t$  for the individual molecules in each of the samples. The  $\langle r(t)^2 \rangle$  values were calculated by averaging over the individual squared step lengths  $r(t)^2$  for each time lag  $t$ , as described in Chapter 4. These plots already reveal differences in the diffusivities in the two sol-gel glasses.

#### Mobile molecules in **M22** and **M3**

The MSD for all 20 molecules that were tracked in the movie of the **M22** material are plotted against the time lag on a double logarithmic scale on the left of Figure 5.7. The lines are all nearly parallel with a slope close to unity, which is typical for random diffusion. Moreover, the spread of  $y$  axis intersects shows the inhomogeneity of diffusion from one track to the other, i.e. the different molecules move all in a random manner, but with different diffusion coefficients. The average diffusion coefficient that can be calculated by fitting the lines to the Einstein-Smoluchowski equation for a 2D random

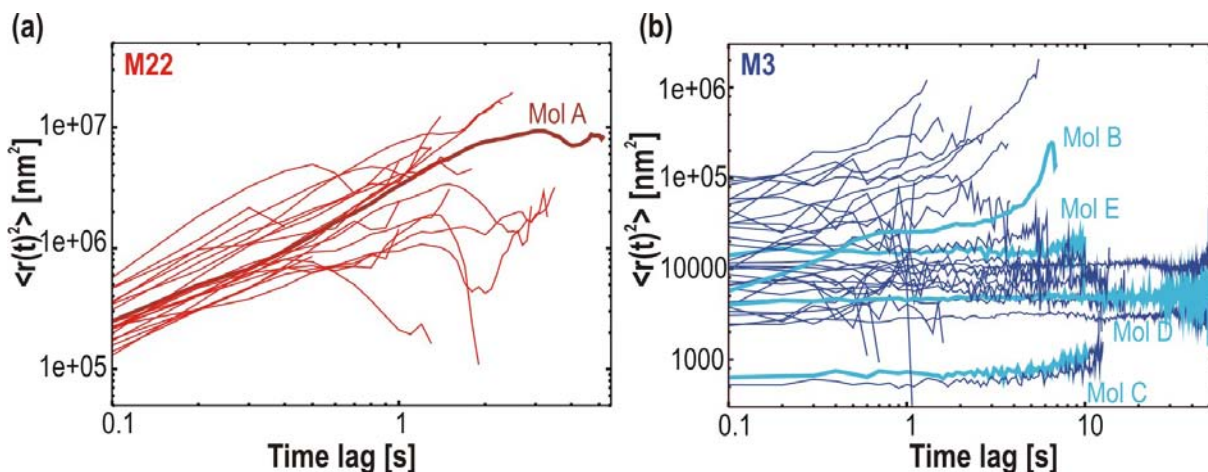


**Figure 5.7:** Plot of averaged MSD against the time lag. (a) **M22**: The bundle of lines with a slope close to unity is typical for random diffusion. (b) **M3**: A mixture of mobile molecules, where  $\langle r(t)^2 \rangle$  increases linearly with time, and confined molecules, where  $\langle r(t)^2 \rangle$  remains at a constant value. The scale is different for the two graphs, the diffusion coefficient of molecules in **M3** is about an order of magnitude lower than in **M22**.

walk (Equation 4.1.11) is  $D_{\text{M22}} = (7.2 \pm 0.1) \times 10^{-1} \mu\text{m}^2 \text{s}^{-1}$ .

On the right side of Figure 5.7 the MSD for all 42 molecules in the six **M3** movies are plotted against the time lag. Here, some of the molecules are mobile, i.e. their MSD increases linearly with the time lag. However, the majority of molecules remain immobile or confined, as becomes manifest in their flat  $\langle r(t)^2 \rangle$  curves. As will be discussed in more detail below, most of the mobile molecules do not follow a pure random walk in 2D but undergo mobile and immobile periods. Therefore, the diffusion coefficient derived by averaging over different time lags is not very precise and probably still too low to describe the true mobile fraction of the diffusion. The average value, that was calculated from nine molecules that are mobile during all or most of their trajectory is  $D_{\text{M3}(\text{mobile})} = (3.0 \pm 1.5) \times 10^{-2} \mu\text{m}^2 \text{s}^{-1}$ . It is about one order of magnitude lower than in **M22**. A detailed discussion of a molecule which is changing between mobile and immobile states will be given below. For this molecule a more accurate analysis, which allows to extract the different diffusion coefficients for one individual trajectory will be presented.

In general, a number of factors may influence the diffusion coefficient of a molecule in a material containing both micro- and mesopores. The first is whether the molecule diffuses on average while solvated in the pore fluid ('free' diffusion) or adsorbed on the pore walls ('surface' diffusion). In the first case, factors likely to influence the apparent diffusion coefficient as measured here include the rate of diffusion in the bulk of the pore fluid and the ease with which the molecule aligns its long axis with the pore axis. Both these factors depend on the viscosity, due to a preponderance of wall-fluid inter-



actions, and diffusion is slower in narrower pores where viscosity increases. Surface diffusion is also expected to be slower in the narrow pore gel because of the increase of surface area to be explored in order to make a 'step' of a given length. Another factor, which might influence the diffusion of guests inside the porous host, is the tortuosity of the channels. However, to measure the tortuosity, a detailed image of the local pore structure would be needed. This can only be provided by TEM, but on very restricted areas and with the need of invasive and time consuming sample preparation. It is not possible at the moment to distinguish the contributions of the different processes in the single-molecule tracking data, because the single-molecule tracks are too short because of photobleaching or fast diffusion and the temporal and spatial resolutions are too low. In the following, a method to test the statistical reliability of diffusion coefficients which are derived from short tracks is presented.

### Significance of distribution of diffusion coefficients

As mentioned above, single-molecule tracks are often too short to deduce reliable diffusion coefficients by fitting a straight line to  $\langle r(t)^2 \rangle$  versus  $t$ . However, in this case the distribution of jumps for just one step (timelag  $t = \tau_F$ ) can be used to determine  $D$ . Granted that the movement is pure diffusion, this choice is in fact optimal, being the maximum likelihood estimator of  $D$ , see Montiel *et al.*<sup>152</sup>

The individual diffusion coefficients can be calculated by fitting the ranked distribution of squared jumps for a timelag  $t = \tau_F$  with the inverse of the cumulative probability distribution  $C(R^2, t)$  (cf. Equation 4.2.4). In order to test the reliability of this method, values of the diffusion coefficient  $D$  for a sample of 42 molecules in **M22** (two movies) were calculated, by fitting  $C(R^2, t)$  to the experimental distributions of  $r(t)^2$  at lag  $t = \tau_F = 0.1$  s. The mean of the 42 single-molecule diffusion coefficients is  $D_{\text{mean(M22)}} = (5.6 \pm 2.7) \times 10^{-1} \mu\text{m}^2 \text{s}^{-1}$ .

The bottom panel of Figure 5.8 shows the experimental distribution of  $D$ . The histogram is skewed, with a tail of apparently fast diffusing molecules and a larger number of values comparable to the mean value. But before concluding that the material is heterogeneous, the significance of the variations in  $D$  has to be tested. The accuracy of the measurement of  $D$  cannot be better than the spread of values caused by statistical fluctuations when fitting the cumulative probability function to data sets for diffusion with a known constant value of  $D$ . Monte Carlo simulations of Fickian diffusion were done to prepare 500 synthetic data sets of 7 steps (the shortest of the 42 experimental tracks is considered, being the worst case) with a constant value of the diffusion coefficient, the mean value found above,  $D_{\text{mean(M22)}} = 5.6 \times 10^{-1} \mu\text{m}^2 \text{s}^{-1}$ . Then  $D$  was fitted

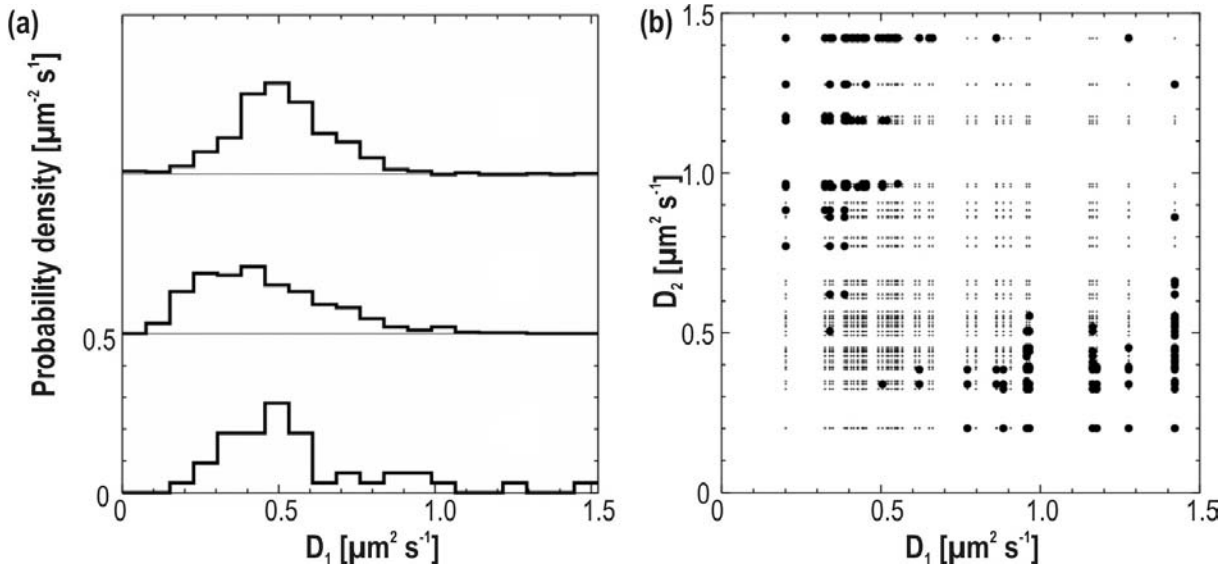


**Figure 5.8: Statistical tests for the significance of fluctuations in  $D$ : Monte-Carlo simulations and Kolmogorov-Smirnov test.** (a) Histograms of experimentally measured and synthetically produced diffusion coefficients. Bottom: Distribution of the diffusion coefficients  $D$  for 42 molecules of **9A1** in gel **M22**. Data from a fit of Equation 4.2.4 and application of Equation 4.1.11 for a single step ( $t=0.1$  s). The mean for this set of molecules is  $D_{\text{mean}} = 5.6 \times 10^{-1} \mu\text{m}^2 \text{s}^{-1}$ . Middle: Distribution calculated from mere statistical fluctuations in synthetic data with a single value of  $D = D_{\text{mean}}$ , for 500 molecules with a track length of seven steps (worst case in experimental data). Top: From synthetic data with the experimental spread of track lengths. (b) Scatter diagram of all significantly different distributions of step lengths (Kolmogorov-Smirnov test, 1% level) for pairs in a sample of 42 molecules in **M22**, represented by their diffusion coefficients  $D_1$  and  $D_2$ . Small crosses: all pairs of  $D$ ; spots: pairs of  $D$  for molecules with significantly different step lengths.

via the cumulative probabilities for  $r$  (or  $r^2$ , the result is the same) for lag 0.1 s. The middle panel of Figure 5.8a shows the histogram of the fitted values. This panel thus illustrates the spread of fitted  $D$  values that could result just from statistical fluctuations in short tracks. The same was done for a mixture of 500 track lengths in the same proportions as the experimental data. Even in the latter case, the half-width at half-maximum of the distribution is about  $\Delta D_{\text{HWHM}} = 1.5 \times 10^{-1} \mu\text{m}^2 \text{s}^{-1}$ , or 30% error. The error can be as high as 100% for short tracks. Nonetheless, when the experimental histogram is compared with the synthetic one with the same distribution of track lengths, it was found that the distributions differ at the 5% level of the Kolmogorov-Smirnov test,<sup>145</sup> adding to the confidence that the tail of fast molecules is a real effect.

Finally, the cumulative distributions of step lengths of all pairs of molecules were cross-checked. The Kolmogorov-Smirnov test showed numerous significant differences at the 1% level, for pairs of molecules with diffusion coefficients on opposite sides of the distribution of  $D$  (see Figure 5.8b). This confirms the initial impression of heterogeneity and a 5-fold range of the diffusion coefficient. Note that although molecules are

represented by their  $D$  values in Figure 5.8a, the test bears on the raw step data. This is perhaps more satisfactory than comparing  $D$ 's from a fit of  $\langle r(t)^2 \rangle$  versus  $t$  for short trajectories, where values and errors are to some extent dependent on the fitting criterion, such as the maximum or mean absolute deviation or the total squared deviation. We note in passing that the mean value of  $D$  in Figure 5.8a,  $D_{\text{mean}(\text{M22})} = 5.6 \times 10^{-1} \mu\text{m}^2 \text{s}^{-1}$ , differs from the value of  $D_{\text{M22}} = (7.2 \pm 0.1) \times 10^{-1} \mu\text{m}^2 \text{s}^{-1}$  found above from all steps of all diffusing molecules, both because those used above are a subset (from only one movie) of the data used here and because they are not used the same way.

Using the same analysis, the diffusion coefficient of the free fraction of molecules in **M3** can be estimated by excluding the trapping episodes from the cumulative probability distributions of  $r^2$  of individual molecules, as above. We find a mean value of  $D_{\text{mean}(\text{M3})} = 1.2 \times 10^{-1} \mu\text{m}^2 \text{s}^{-1}$ , or about 5 times smaller than in **M22** albeit with a much smaller sample. Although the sample is small, we note that as in **M22** there is a wide spread of the values of  $D$ , the standard deviation being  $7.1 \times 10^{-2} \mu\text{m}^2 \text{s}^{-1}$  and there are significant differences (1% level of the Kolmogorov-Smirnov test) between the smallest and largest values ( $D_{\text{min}(\text{M3})} = 3.8 \times 10^{-2} \mu\text{m}^2 \text{s}^{-1}$  and  $D_{\text{max}(\text{M3})} = 2.3 \times 10^{-1} \mu\text{m}^2 \text{s}^{-1}$ ).

### Confined and immobile molecules in M3

After the discussion of the mobile molecules in **M22** and **M3** the large majority of molecules in the **M3** monoliths which remain confined in small areas of the sample will be regarded in more detail. The question is if these molecules are really immobilized, for example by adsorption to the silica walls, or if they are trapped in small voids of the pore system. Three exemplary trajectories, highlighted in circles in Figure 5.6 (Molecules **C-E**), are magnified in Figure 5.9. Because of the high density of trajectory points they have been left unconnected in this picture.

The track points of molecule **C** depicted on the left side scatter much less than those of molecule **E** on the right side (spread over  $\varnothing$  150 – 200 nm). The diameter of the area covered by the molecule **C** on the left is  $\varnothing < 50$  nm, which is in the same range as our positioning accuracy in these movies. Therefore it can be concluded that this molecule is immobile within the accuracy of the measurements. However, molecules **D** and **E** on the right panel of the figure, move in areas which are bigger than the positioning accuracy. Molecule **D** is moving, but remains confined in a small region of the sample with a diameter of about 100 nm. An even larger area is covered by molecule **E**, which spreads over an area of about 150 – 200 nm. The confinement region appears to be a bit elongated towards the lower right corner of the trajectory plot.

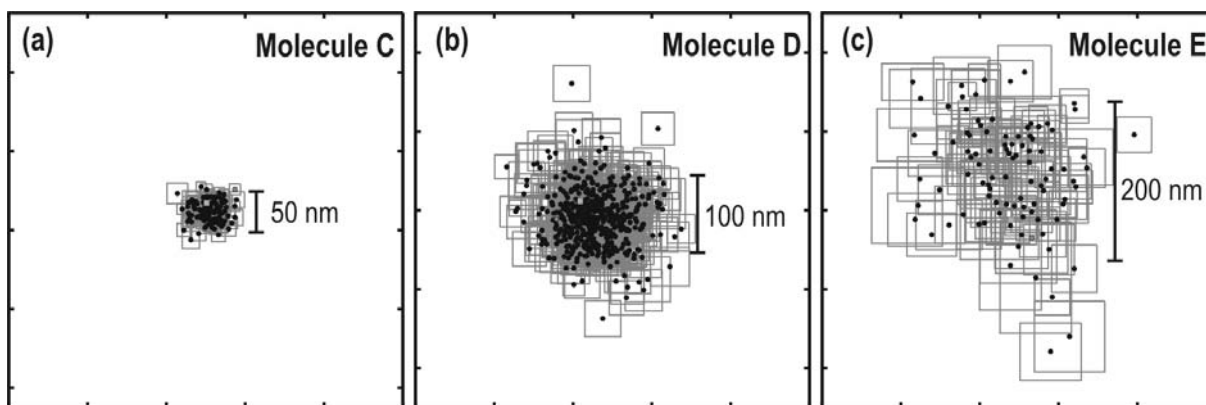


**Figure 5.9: Immobile and confined molecules in M3.** (a) Molecule C: Immobile to within the positioning accuracy ( $< 50$  nm). (b) Molecule D: confined in a region a bit smaller than 100 nm. (c) Molecule E: Confined in a region of about 150 – 200 nm in diameter. The positioning error for the individual track points is shown by the grey boxes.

A precise measure of the dimensions of the confinement is provided in the plot of the mean-square displacement against the time in Figure 5.7b. The average diameter of the confinement can be directly calculated, as it is the square root of the  $y$ -axis intercepts of the lines, according to Equation 4.1.33. Due to the limited temporal resolution, the ascending component of the curve (cf. Figure 4.1) is not visible in the plots here. In the Figure the horizontal thick light blue lines correspond to the three molecules discussed here. For molecules C-E the size of the root mean square confinement is calculated to be 26 nm, 68 nm and 126 nm in diameter, respectively, in accordance with the values extracted from the raw trajectories (Figure 5.9). From the MSD plots no spatial information about the shape of the confinement region can be obtained.

### 5.3.4 Mobile Molecules in M22 and M3: Individual Trajectories

As we have seen in the preceding sections the diffusion behaviour of the individual dye molecules depends strongly on the porosity of the silica host. Figure 5.10a and (d) show two examples of individual trajectories in the two phases. Whereas the track in M22 looks very much like Brownian motion, the molecule in M3 appears to switch between mobile and immobile states. These direct observations can be underlined by the statistical analysis of the step lengths and diffusion coefficients calculated therefrom. As described in Chapter 4 the ranked squared step lengths are plotted and fitted to mono- or bi-exponential decay functions for different time lags (Equation 4.2.2). For the trajectory of molecule A in M22 a mono-exponential decay describes the data well. This is directly visible from the straight line in the semi-logarithmic plot in (b). The plot of the  $\langle r(t)^2 \rangle$  values obtained from these fits for different time lags (Figure

5.10c) can be fitted with a straight line to the Equation 4.1.11. A diffusion coefficient of  $D = 1.0 \mu\text{m}^2 \text{s}^{-1}$  is calculated. Nearly the same  $\langle r(t)^2 \rangle$  values are obtained by simple averaging over the  $r(t)^2$  values for each given time lag, shown as open symbols in the figure with a dotted line for the fit.

By contrast, molecule **B** exhibits a more heterogeneous diffusion. Investigation by eye already gives the impression that the molecule changes between a mobile state in the beginning and at the end and an immobile period in the middle of the trajectory. Indeed, the semi-logarithmic ranked plots of  $r(t)^2$  for the molecule **B** in **M3** exhibit a distinct kink similar to the theoretical plots in Figure 4.4b. These data are fitted best with a bi-exponential for  $C(R^2, t)$ , with a decrease of  $\chi^2$  by an order of magnitude in

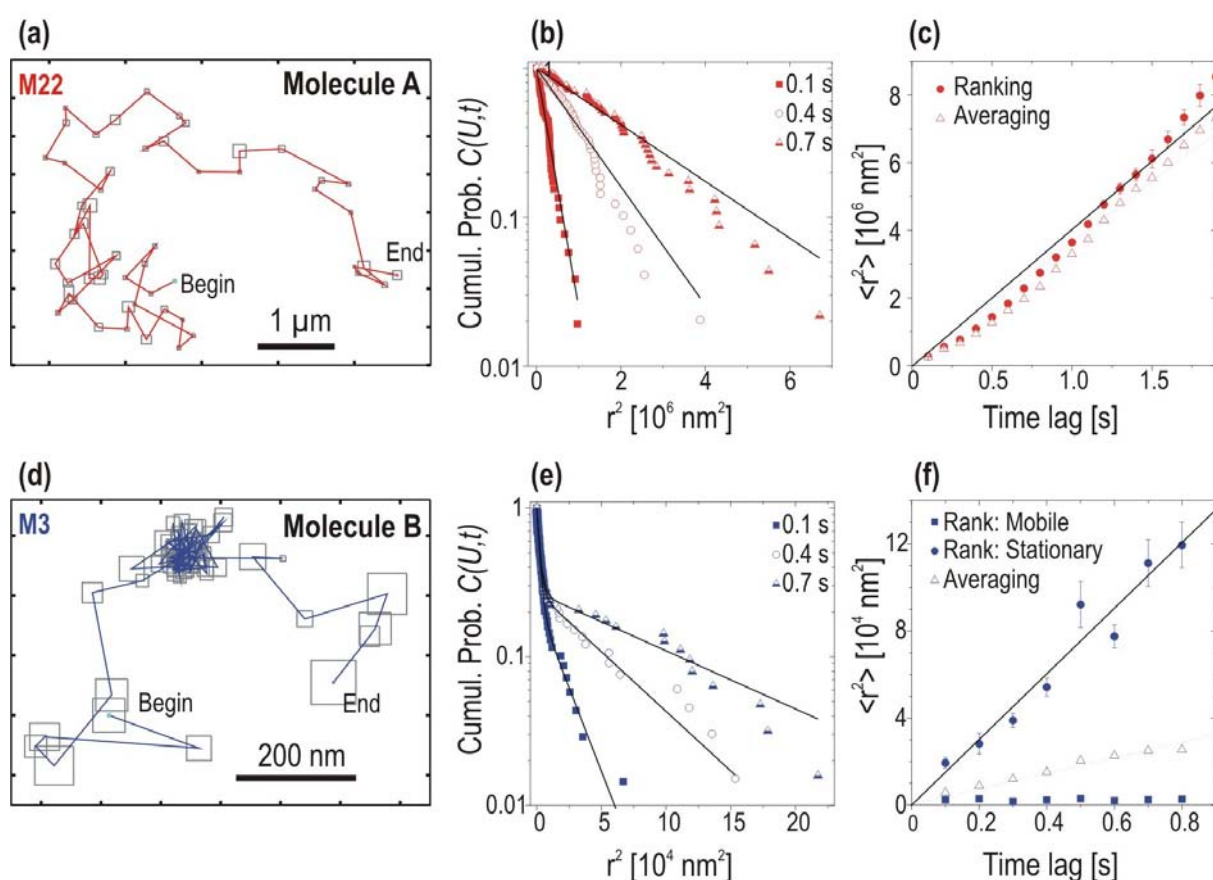


**Figure 5.10: Analysis of individual trajectories in M22 and M3.** (a) Random Diffusion in M22 material. (b) Ranked squared step lengths for three exemplary time lags and mono-exponential fit to the data. (c) The plot of  $\langle r(t)^2 \rangle$  from the ranked data against time lag and linear fit gives a diffusion coefficient of  $D = 1.0 \mu\text{m}^2 \text{s}^{-1}$ . The  $\langle r(t)^2 \rangle$  values from the averaging MSD method are plotted as open symbols for comparison. (d) Mobile-Immobile-Mobile changes are observed within the same track in M3. (e) The ranked squared step lengths and corresponding bi-exponential fits show clearly the presence of mobile and stationary parts within this track. (f) The MSD plot and corresponding fit result in  $D_1 = 3.7 \times 10^{-2} \mu\text{m}^2 \text{s}^{-1}$  for the mobile part of the track. The lower  $\langle r(t)^2 \rangle$  vary around  $2400 \text{ nm}^2$ , which is below the positioning accuracy of the tracking.

comparison to the mono-exponential fit. Thus, two characteristic  $\langle r(t)^2 \rangle$  values for each time lag are obtained. This shows that here at least two different classes of step lengths are present. The  $\langle r(t)^2 \rangle$  values are plotted against the time lag in Figure 5.10f and again fitted according to the Einstein-Smoluchowski equation for two-dimensional diffusion. The diffusion coefficient that is calculated by fitting the set of larger  $\langle r(t)^2 \rangle$  values from the bi-exponential fit is  $D_1 = 3.7 \times 10^{-2} \mu\text{m}^2 \text{s}^{-1}$ , which is about two orders of magnitude smaller than  $D$  of the molecule **A** in **M22**. The smaller  $\langle r(t)^2 \rangle$  values are distributed around  $2400 \text{ nm}^2$ , which is below the square of the positioning error of about  $50 \text{ nm}$  ( $2500 \text{ nm}^2$ ) for this molecule. Therefore the molecule is considered to be immobile to within our positioning accuracy during the 'stop' period, similar to the confined molecule **C**, which was discussed above. In contrast, the averaging method results here only in one intermediate line, corresponding to neither of the two diffusivities determined from the ranked data and can thus not be used to determine a reliable value for the diffusion coefficient of this molecule. In such a clear cut case it is actually possible to distinguish by eye where the molecule is moving and where it is immobile, so that the trajectory can be cut manually into the different intervals and the diffusion can be analysed separately, and then the averaging method yields similar values as those obtained by the ranking method. However, not all cases are as clear-cut, and the ranking method can identify variations in the diffusion behaviour, even when the different diffusivities are not directly distinguishable by eye. Such an example will be discussed in Chapter 7 for diffusion in Brij-templated mesoporous thin films.

### 5.3.5 Distribution of Angles

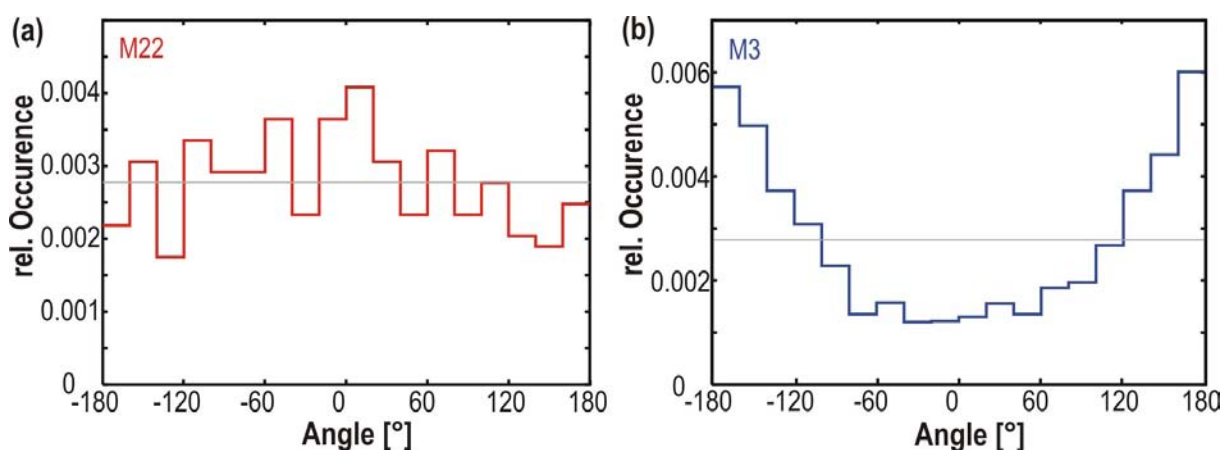


**Figure 5.11: Histogram of angles between successive steps in M22 and M3.** (a) In **M22** the angles are distributed randomly around the mean value, which is drawn as a grey line. (b) The molecules in **M3** show a high excess of steps backward and hardly any steps forward. This is a typical tracking artefact for immobile molecules, as discussed in Chapter 4, Figure 4.10 .

Finally, the distribution of angles between successive steps is analysed for **M22** and **M3** in Figure 5.11. These distributions, like all the analyses that were discussed before, disclose differences of the diffusion in both materials. The distribution of angles in **M22** is comparatively flat and random around the mean value, which agrees well with the above findings of random motion in **M22**. For **M3**, however, a U-shaped distribution is found, corresponding to a high excess of steps backward and a minimum of steps forward. Such a histogram is typical for immobile molecules and it originates from a tracking artefact, as explained in Chapter 4. This reflects the above observation of mostly immobile and confined molecules in **M3**.

## 5.4 Pulsed-Field Gradient NMR in Sol-Gel Monoliths

In order to obtain a better understanding of the single-molecule diffusion data in the two different sol-gel glasses, the self-diffusion of the pure solvent in the two materials was investigated using PFG NMR (see Section 2.3.5). This method is well suited to investigate the ensemble diffusion behaviour of small species containing several  $^1\text{H}$  nuclei, such as the ethylene glycol molecules of the solvent or the dye molecules. Additional data could be gathered from samples that were similar to **M3** and **M22**, namely **M4**, **SG8**, **SG26** and **SG21**. The synthesis recipes and porosity information of all these samples are provided in the first part of this section, Tables 5.1 and 5.2. However, the **M3**, **M4** and **M22** samples were measured about six months after the synthesis and thus after the single-molecule experiments. At that time no sorption isotherms were made. It is known that such xerogels are prone to ageing by further, slow polymerisation induced by residual water. Thus it might be possible that the pore diameter and pore volume did already decrease in comparison to the values directly after the synthesis. Here, it will be noted for each sample about how long after synthesis it was measured using PFG NMR. Unfortunately no appraisal can be made, in which time the shrinkage of the pore took place during ageing, which makes a reliable interpretation impossible.

All the measurements presented here were performed at 125 MHz or 400 MHz. It has been checked that the measurement frequency does not influence the determined parameters, like the diffusion coefficient. Unless otherwise stated, the samples were measured at room temperature ( $25^\circ\text{C} \pm 0.1^\circ\text{C}$ ), set by a temperature controller for the sample chamber. For the measurements the following relaxation times were found: The longitudinal relaxation  $T_1$  was determined by inversion recovery to be in the range of 3 – 5 s, implicating long repetition times for the measurements; the transversal relaxation time  $T_2$  in the range of 2 – 5 ms, measured by CPMG (Carr-Purcell-Meiboom-Gill

sequence<sup>153,154</sup>). These conditions were well suited for the PFG NMR experiments, even though the long  $T_1$  relaxation time required relatively long repetition times. The latter have to be set to  $5 \times T_1$  and meant thus quite protracted measurements. Either a spin-echo or 13-interval pulse repetition was used. These two pulse sequences give the same results, as long as there are no internal gradients present in the system. The  $T_2$  relaxation time remained constant for measurements of  $T_2$  using the CPMG impulse sequence and variation of the distance  $t$  between the  $\pi$ -pulses, meaning that no internal gradients were present in the samples.

### 5.4.1 Measurements of Ethylene Glycol Self-Diffusion in M22, M3 and M4

Samples of about 6 months aged **M22**, **M3**, and **M4** were measured at observation periods ranging from 5 ms to 400 ms or 800 ms. The resulting spin-echo decays and coefficients of self-diffusion are plotted in Figure 5.12. The self-diffusion coefficients  $D$  determined for each of the measurements and the according mean molecular displacements  $r$  that were calculated from  $D$  according the the Einstein-Smoluchowski equation for 3D diffusion (Equation 4.1.12), are summarized in Table 5.3.

All the spin-echo decay curves are nearly exponential and hardly any differences are visible for different observation times. The character of the confinement remains constant when varying the observation time between 5 ms and 400 ms for **M22** and **M3** or 800 ms for **M4**, corresponding to mean molecular displacements of 0.4  $\mu\text{m}$  and 3.5  $\mu\text{m}$  for **M22**, 0.6  $\mu\text{m}$  and 4.9  $\mu\text{m}$  for **M3** and 0.7  $\mu\text{m}$  7.9  $\mu\text{m}$  for **M4**. This means that for example no additional obstacles in the range between 0.4  $\mu\text{m}$  and 5.0  $\mu\text{m}$  are observed

**Table 5.3: Coefficients of self-diffusion of ethylene glycol in silica gels M22, M3 and M4.** These PFG NMR measurements were done about 6 months after synthesis of the xerogels.

	<b>M22</b>		<b>M3</b>		<b>M4</b>	
$\Delta$ [ms]	$D$ [ $\mu\text{m}^2/\text{s}$ ]	$r$ [ $\mu\text{m}$ ]	$D$ [ $\mu\text{m}^2/\text{s}$ ]	$r$ [ $\mu\text{m}$ ]	$D$ [ $\mu\text{m}^2/\text{s}$ ]	$r$ [ $\mu\text{m}$ ]
5	6.0	0.42	11	0.57	15	0.67
20	5.0	0.77	10	1.10	14	1.30
100	5.0	1.73	10	2.45	13	2.79
200	5.0	2.45	10	3.46	13	3.95
400	5.0	3.46	10	4.90	13	5.59
800					13	7.9



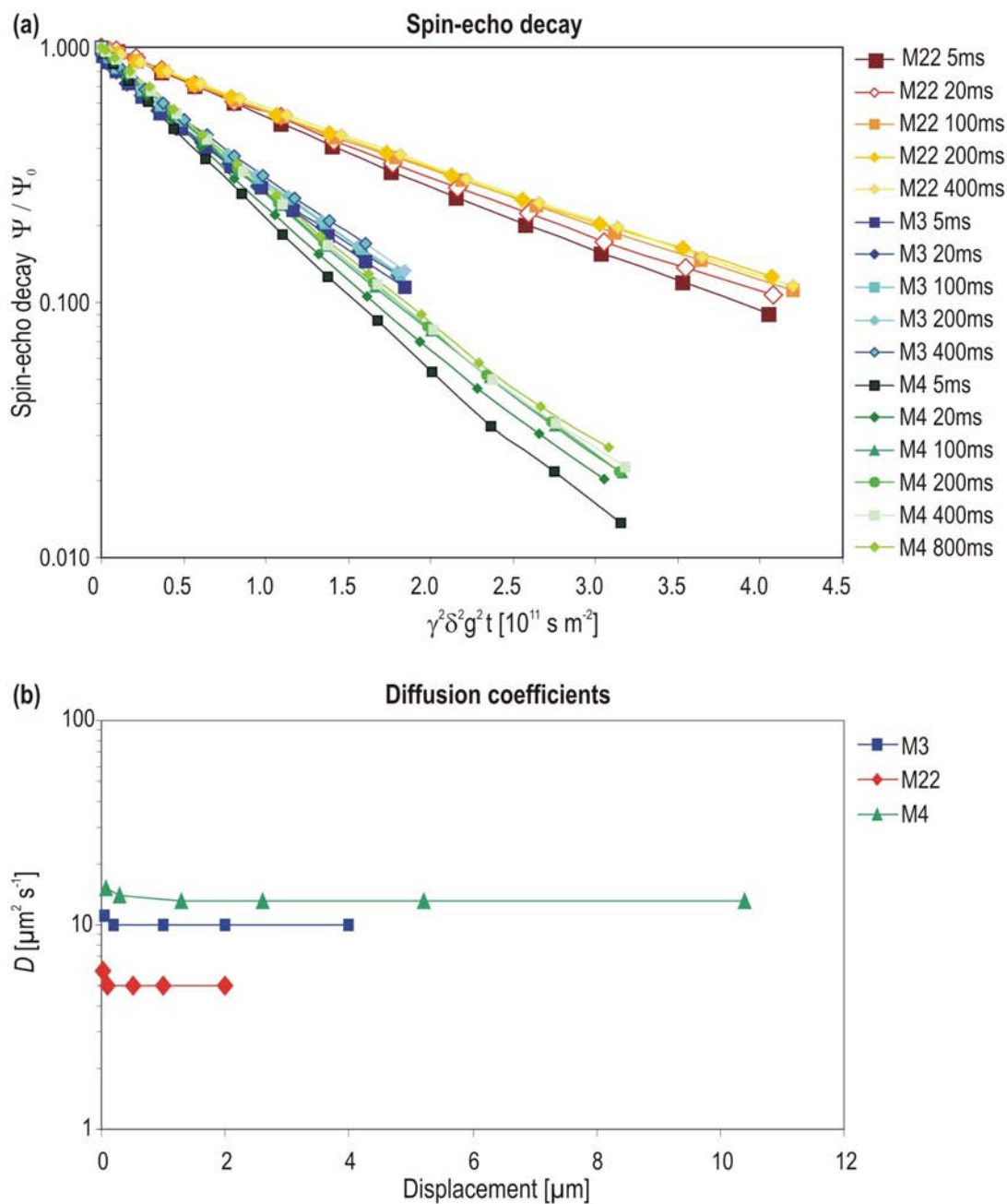


**Figure 5.12: PFG NMR of sol-gel monoliths of M3, M4 and M22.** (a) The spin-echo decay was measured for observation times of 5 ms to 400 ms or 800 ms. It is nearly exponential for **M22** and **M3** and the gradient is smaller for **M3**. (b) The coefficients of self-diffusion  $D$  for the three sol-gel glasses as a function of the displacement  $r$ , which is proportional to the square of the observation time (cf. Table 5.3). Interestingly,  $D$  is smaller for **M22** than for **M3** and **M4**, which might be explained by a different pore tortuosity rather than by the mesopore diameter. These PFG NMR measurements were done about 6 months after synthesis of the xerogels.

in the case of **M22**. In addition, the system is quasi-homogenous, which means that when averaged over a micrometre scale no differences in the diffusion coefficients are observed. This is visible from the mono-exponential decay curves.

Interestingly, the diffusion coefficient in **M22** is smaller than in **M3** and **M4**. However, as it will be shown below, after about three years of ageing the mean mesopore diameter were about the same (ca. 3.5 nm) for **M3** and **M22**. Therefore, most probably, after 6 months of ageing the difference in mesoporosity of the two materials might have been decreased already. This might be another reason for the unexpected order of the diffusivities in the two materials. Unfortunately no porosity data were collected at the time of these PFG NMR measurements. Another explanation of the smaller diffusion coefficient in **M22** than in **M3** and **M4** might be the following: Ethylene glycol is small in comparison to the pore diameter of both kinds of materials and does not experience the differences in the mean mesopore diameter. The mean micropore diameter was identical for the two sol-gel glasses. Therefore the deviations in the diffusion coefficients might be explained by a different tortuosity of the channel systems.

For comparison the coefficient of self-diffusion of pure ethylene glycol was measured as well. It amounts to  $D_{3D \text{ ethylene glycol}} = 1.3 \times 10^2 \mu\text{m}^2 \text{ s}^{-1}$  at room temperature (see Table 5.6), thus about one to two orders of magnitude higher than in the porous system. This shows that the porous systems hinders the free diffusion of the ethylene glycol molecules.

### 5.4.2 Temperature Dependence of the Diffusion in M4

**Table 5.4: Coefficients of self-diffusion of ethylene glycol in M4 at different temperatures (measured about 6 months after synthesis).**

<b>M4</b>	<b>-40°C</b>		<b>-30°C</b>		<b>-20°C</b>		<b>0°C</b>		<b>25°C</b>		<b>60°C</b>	
$\Delta$ [ms]	$D$ [ $\mu\text{m}^2/\text{s}$ ]	$r$ [ $\mu\text{m}$ ]	$D$ [ $\mu\text{m}^2/\text{s}$ ]	$r$ [ $\mu\text{m}$ ]	$D$ [ $\mu\text{m}^2/\text{s}$ ]	$r$ [ $\mu\text{m}$ ]	$D$ [ $\mu\text{m}^2/\text{s}$ ]	$r$ [ $\mu\text{m}$ ]	$D$ [ $\mu\text{m}^2/\text{s}$ ]	$r$ [ $\mu\text{m}$ ]	$D$ [ $\mu\text{m}^2/\text{s}$ ]	$r$ [ $\mu\text{m}$ ]
<b>4</b>	0.46	0.11	0.9	0.15	1.4	0.18	4.3	0.32	16	0.62		
<b>5</b>	0.36	0.10	0.7	0.14	1.2	0.19	4.2	0.35	14	0.65	62	1.36
<b>10</b>	0.2	0.11	0.55	0.18	1.2	0.27	4.1	0.50	14	0.92	60	1.90
<b>20</b>	0.16	0.14	0.53	0.25	1.1	0.36	3.8	0.68	14	1.30	59	2.66
<b>40</b>	0.16	0.20	0.48	0.34	1.0	0.49	3.7	0.94	13.5	1.80	58	3.73
<b>80</b>	0.14	0.26	0.43	0.45	1.0	0.69	3.6	1.31	13	2.50	57	5.23
<b>160</b>					0.98	0.97	3.5	1.83			56	7.33
<b>320</b>											54	10.18

In addition to the measurements at room temperature, the diffusion of ethylene glycol in **M4** monoliths was investigated at various temperatures. The results for the measurements at  $-40^{\circ}\text{C}$ ,  $-30^{\circ}\text{C}$ ,  $-20^{\circ}\text{C}$ ,  $0^{\circ}\text{C}$ ,  $25^{\circ}\text{C}$  and  $60^{\circ}\text{C}$  under variation of the observation time are presented in Figure 5.13. The determined values for the self-diffusion coefficients  $D$  of the solvent and the respective mean displacements  $r$  for the different temperatures and observation intervals are summarized in Table 5.4.

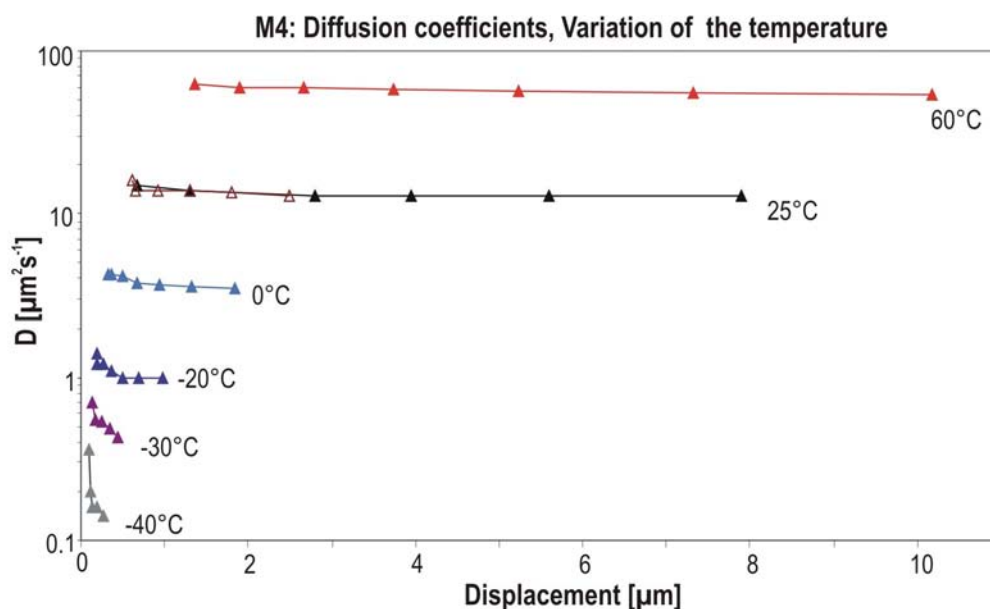


**Figure 5.13: Temperature dependent PFG NMR of M4 sol-gel monoliths.** The coefficient of self-diffusion of ethylene glycol in **M4** increases with increasing temperature. The observation times were adapted to the respective  $D$  values for the different temperatures. In the region between  $1 \mu\text{m}$  and  $10 \mu\text{m}$  no changes of  $D$  are visible, the system is quasi-homogeneous. Note that these measurements were done 6 months after the synthesis of the monoliths.

An immediate observation is that the diffusion coefficient increases with rising temperature, reflecting the increasing molecular mobility. Moreover, differences in the diffusion average out at displacements of more than  $1 \mu\text{m}$  and the  $D$  values remain fairly constant. In this region the system is quasi-homogeneous. At low temperatures also very short displacements could be observed. Here, deviations of the diffusion coefficients are visible, indicating transport barriers that only take effect at displacements of more than  $500 \text{ nm}$ . Simultaneously, one has to keep in mind that with decreasing temperature also the thermal energy of the diffusing molecules is reduced so that their ability to pass internal resistances is progressively decreasing. Exactly this behaviour has been observed in PFG NMR diffusion studies of methane and n-butane in MFI-type zeolites.<sup>155,156</sup> These observations agree well with the single-molecule trajectories inside **M3**, which is quite similar to **M4**. The individual dye molecules explored traps or confined regions of up to a few hundred nanometres in size, and at higher distances the diffusion appeared to be random. It has to be noted that the diffusion coefficients of

9A1 dissolved in ethylene glycol, obtained by SMT, are about two orders of magnitude smaller than that of pure ethylene glycol. This can be explained by the size of the dye molecules which is close to the mesopore diameter of these samples.

In addition, the activation energy for the change of the diffusion coefficient  $D$  with the temperature  $T$  can be calculated according to the Arrhenius equation:

$$D = D_0 \cdot \exp\left(-\frac{E_a}{RT}\right) \quad (5.4.1)$$

When taking the natural logarithm, this becomes:

$$\ln(D) = \ln(D_0) - \frac{E_a}{R} \left(\frac{1}{T}\right) \quad (5.4.2)$$

Here,  $D$  is the diffusion coefficient at the given temperature  $T$ ,  $D_0$  is the maximum diffusion coefficient (at infinite temperature),  $E_a$  the activation energy for diffusion (in dimensions of [energy · (amount of substance)<sup>-1</sup>]) and  $R$  is the gas constant in dimensions of [energy · temperature<sup>-1</sup> · (amount of substance)<sup>-1</sup>]. Equation 5.4.2 shows that a plot of  $\ln(D)$  against the inverse of the temperature  $1/T$  yields the activation energy divided by the gas constant  $R$ .

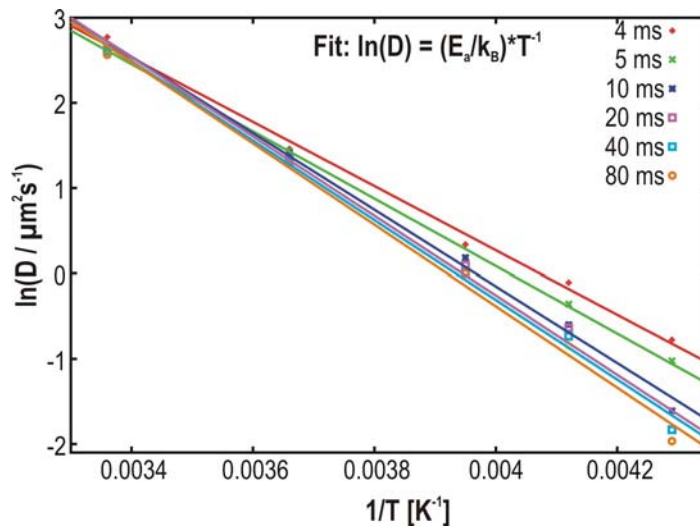


**Figure 5.14: Arrhenius plot of temperature dependent PFG NMR of M4 sol-gel monoliths.** The natural logarithm of the diffusion coefficient, taken as the rate constant of the diffusion process, is plotted against the inverse temperature for the different observation times between  $\Delta = 4$  ms and  $\Delta = 80$  ms and fitted according to Equation 5.4.2.

In Figure 5.14 the natural logarithm of the diffusion coefficient is plotted against the inverse temperature for the different observation times between  $\Delta = 4$  ms and  $\Delta = 80$  ms, including the linear fits to the different data sets. The values for 160 ms and

320 ms are not included, as only three or one data points have been measured, respectively.

The different activation energies in units of Kelvin are summarized in Table 5.5. For comparison, the enthalpy of vaporisation of ethylene glycol,  $\Delta H_{\text{vap}} = 61.9 \text{ kJ/mol}$  is added (in units of Kelvin), which can be found in the literature.<sup>157,158</sup> For a bulk liquid the activation energy of the diffusion should be order of magnitude the same as the enthalpy of vaporisation, since it requires an energy about the binding energy per molecule to make two molecules exchange their positions allowing diffusion to take place. This is indeed the case.

**Table 5.5: Activation energies derived from the linear fits in the Arrhenius plot (Figure 5.14).** The literature value was calculated from the enthalpy of vaporisation of ethylene glycol  $\Delta H_{\text{vap}} = 61.9 \text{ kJ/mol}$  found in the NIST webbook.<sup>157,158</sup>

$\Delta$ [ms]	4	5	10	20	40	80	Literature
$E_a$ [ $10^3$ K]	3.8	3.9	4.5	4.7	4.7	4.8	7.4

### 5.4.3 Ethylene glycol self-diffusion in SG8, SG26 and SG21

An additional batch of samples, namely **SG8**, **SG26** and **SG21**, was investigated to obtain a broader overview of the self-diffusion of ethylene glycol within such porous matrices. In this case the measurements were done within the first two months after the synthesis of the xerogels. Like described in the synthesis section, the synthesis recipe of **SG8** is similar to **M22**. However, in this case the mean mesopore diameter is about 8 nm and is smaller than in **M22**. Furthermore, two different ormosils were synthesized by co-condensation of TMOS and APTES. This yielded a much higher mesoporosity of the materials, and the mean mesopore diameters are 21.5 nm for **SG21** and 26.5 nm for **SG26**. The complete porosity information that was obtained by sorption measurements is summarized above in Table 5.2. Figure 5.15 and Table 5.6 summarize the diffusion coefficients of these three sol-gel glasses, together with the values obtained from **M3** and **M22** measured at the same time again, which was after more than three years of ageing after the synthesis. The latter results will be discussed in the next section.

In this case, the increase in the mesopore diameter coincides with an increasing coefficient of self-diffusion of **SG8** compared with **SG26** and **SG21**, contrary to the results from 6 months aged **M3** and **M22**. However, hardly any difference in  $D$  is visible between **SG21** and **SG26**, even though the mesopore diameter differs by 5 nm. It is

**Table 5.6: Self-diffusion coefficients of ethylene glycol in various sol-gel glasses and solution.** The subscripts indicate how much time after the synthesis of the materials the PFG-NMR measurements were done (mo=months, y=years).

<b>M4</b>	<b>SG8<sub>2 mo</sub></b>		<b>SG26<sub>2 mo</sub></b>		<b>SG21<sub>2 mo</sub></b>		<b>M3<sub>3 y</sub></b>		<b>M22<sub>3 y</sub></b>		<b>EG</b>	
$\Delta$ [ms]	$D$ [ $\mu\text{m}^2/\text{s}$ ]	$r$ [ $\mu\text{m}$ ]	$D$ [ $\mu\text{m}^2/\text{s}$ ]	$r$ [ $\mu\text{m}$ ]	$D$ [ $\mu\text{m}^2/\text{s}$ ]	$r$ [ $\mu\text{m}$ ]	$D$ [ $\mu\text{m}^2/\text{s}$ ]	$r$ [ $\mu\text{m}$ ]	$D$ [ $\mu\text{m}^2/\text{s}$ ]	$r$ [ $\mu\text{m}$ ]	$D$ [ $\mu\text{m}^2/\text{s}$ ]	$r$ [ $\mu\text{m}$ ]
5	3.7	0.33	46	1.17	42	1.12	3.5	0.32	3	0.3	130	1.97
10	3.2	0.44	45	1.64	41	1.57	3.3	0.44	–	–	–	–
20	2.9	0.59	44	2.3	40	2.19	3.2	0.62	2.5	0.55	130	3.95
100	2.7	1.27	43	5.08	40	4.9	3	1.34	2.2	1.15	130	8.83
200	2.7	1.8	42	7.1	39	6.84	2.9	1.87	2.1	1.59	130	12.49
400	–	–	–	–	–	–	2.9	2.64	2.2	2.3	130	17.66

therefore concluded that at least two different factors can influence the diffusion of the ethylene glycol molecules: the tortuosity of the channels and the pore diameter. The fact that for the **SG**-samples, measured relatively soon after synthesis, the bigger pore diameter yields also a higher diffusion coefficient, might be taken as indication that the mesopore diameters of **M3** and **M22** were already subjected to the ageing process at the time of the PFG NMR measurements.

#### 5.4.4 Ageing of the Samples M3 and M22

First of all, in order to compare the PFG NMR measurements after more than three years of ageing to those presented above (measured 6 months after the synthesis), new sorption isotherms were acquired. These measurements were performed on Quantachrome Instruments NOVA 4000e and Autosorb-1 at 77 K. Note that those isotherms were measured on a different apparatus and to determine the pore diameter and volume a DFT fit was used instead of the BJH or HK model. The surface area was calculated by a BET fit to the data as before. It was found that the mean pore diameter decreased for **M22** to a value of ca. 3.5 nm. The same value was obtained for **M3** after ageing. Similarly, the pore volume of **M22** decreased and was about equal to the volume of **M3**, which did hardly change. Table 5.7 summarizes the porosity information of the 3 years aged and the freshly synthesized samples:

The overview in Figure 5.15 depicts also the diffusion coefficients in the 3 years aged sol-gel glasses **M3** and **M22** (blue and red, closed symbols) and, for comparison, those in the 6 months aged samples (open symbols) again (Note that no porosity data is available for the time of the latter measurements). An immediate observation is that

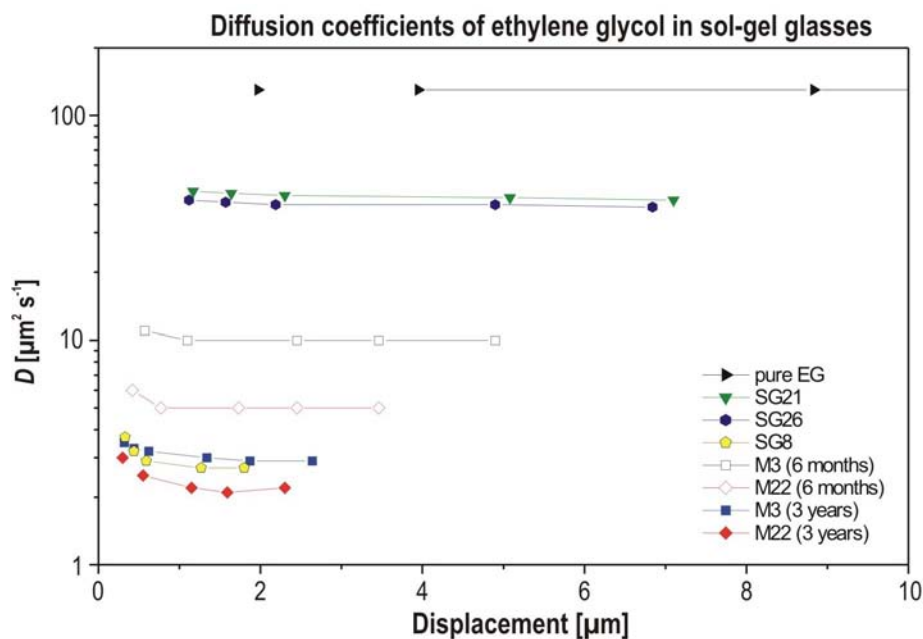


**Figure 5.15: Overview of PFG NMR of ethylene glycol in sol-gel monoliths SG8, SG26, SG21 (2 months aged) and M3, M22 after different periods of ageing (6 months and more than 3 years).** Coefficients of self-diffusion for the three additional sol-gel glasses. Here,  $D$  is smaller for SG8 than for SG26 and SG21. This might again be explained by a different tortuosity of the pores or, as  $D$  increases here with the mesopore diameter, by the increasing pore diameter. In addition, the diffusion coefficients in the aged M3 and M22 are about a factor 2-3 smaller than in the fresh samples, but similar to SG8.

after 3 years of ageing  $D$  is about a factor of two to three lower than in the 6 months aged samples. Hereby the order between M3 and M22 remains the same, but the values converge a bit, even though the pore diameter and also the pore volume are about the same for both of the long-time aged samples. These findings are taken as another indicator that for these samples the tortuosity of pores is the determinant for the differences in the diffusion coefficients. Presumably, the ageing process densifies the silica network, restricting some pores and hence lowering the average diffusion constant.

The more recently synthesized sol-gel glass SG8 shows a value in the same range as the aged M3 and M22, even though the mesopores are according to the sorption isotherms about two times bigger in diameter. Moreover, ethylene glycol in SG26 had a slightly smaller  $D$  than in SG21, even though the pores are about 5 nm bigger. From these data it might be concluded that a change in pore diameter has to be bigger than a few nanometres to show an effect on the diffusion behaviour. Nonetheless, it is quite probable that there is an effect of the pore tortuosity on the diffusion coefficient, because even for similar pore diameter and volume the diffusion was slower in M22. However, the effect might be much smaller as concluded from the first results in the different samples, because already at this stage the porosity of M22 and M3 was prob-

**Table 5.7: Porosity Data for silica gels M3 and M22.** The subscripts indicate how much time after the synthesis of the materials the PFG NMR measurements were done (y = years, mo = months).

	method	M3 <sub>3y</sub>	M22 <sub>3y</sub>	method	M3 <sub>6mo</sub>	M22 <sub>6mo</sub>
specific surface area ( $m^2g^{-1}$ )	BET	831	732	BET	715	740
pore volume ( $cm^3g^{-1}$ )	DFT	0.49	0.49	HK/BJH	0.40	1.15
mesopore diameter (nm)	DFT	~ 3.5	~ 3.5	BJH	3.1	22.4

ably much less different than it was supposed to be. For the **SG** sample series, which was as well measured about two months after the synthesis, the change of the porous systems due to ageing might not have been so strong, as still a huge difference for the diffusivity in **SG8** and **SG26/ SG21** was observed.

#### 5.4.5 Diffusion of the Dye 9A1 in M22

In addition to the self-diffusion of the pure ethylene glycol within the different pore systems, the diffusion of **9A1** in deuterated ethylene glycol should be investigated. This should enable the direct comparison with the single-molecule diffusion measurements. For this purpose **9A1** was dissolved in 99.0 % D6-ethylene glycol at a concentration of about  $10^{-4} \text{ mol L}^{-1}$  and vacuum sealed samples were prepared for PFG NMR as described above.

The first PFG NMR measurements of the dye loaded samples yielded similar values to the self-diffusion of pure ethylene glycol. An explanation for this is that the degree of deuteration of the used solvent was not high enough and a huge excess of residual protons of the ethylene glycol compared with the amount of dye molecules dissolved in the ethylene glycol was present in the samples. Unfortunately, due to the low solubility of **9A1** in this solvent and the difficulties to purchase ethylene glycol with a higher degree of deuteration, no detailed measurements of **9A1** in ethylene glycol within the porous system could be performed using PFG-NMR.

Nevertheless, one measurement could be accomplished yielding a tentative value for the diffusion of **9A1** dissolved in deuterated ethylene glycol in the pores of the aged **M22**. As mentioned in the introductory paragraph, PFG NMR can distinguish between multiple diffusing species. At low observation times the faster component outweighs the slower one, but at longer observation times the slow component becomes visible as well. The first attempt to measure the diffusion of the dye, did not extend up to



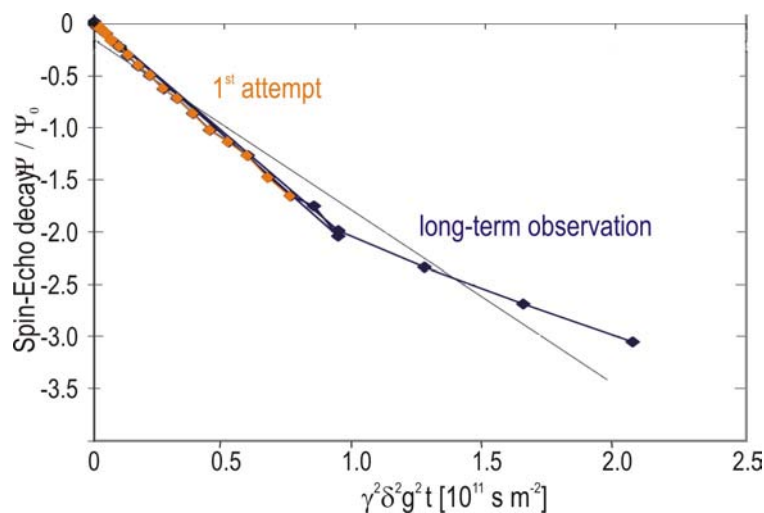


**Figure 5.16: Spin-echo decay 9A1 dissolved in ethylene glycol and incorporated in M22 (after ageing).** The decay shows a distinct kink, indicating the presence of several species with a different diffusion coefficient. The two parts can be fitted individually, yielding two diffusion coefficients  $D_{\text{fast}} = 2.2 \mu\text{m}^2 \text{s}^{-1}$  and  $D_{\text{slow}} = 0.34 \mu\text{m}^2 \text{s}^{-1}$ .  $D_{\text{fast}}$  is equal to  $D$  of the pure ethylene glycol, thus  $D_{\text{slow}}$  can be attributed to the **9A1** dye.

long enough observation times and the slower component was thus not visible (orange line in Figure 5.16). Therefore, a long-term experiment was performed to measure the spin-echo decay up to sufficiently high observation times. The resulting spin-echo decay is presented in Figure 5.16. The curve shows indeed a distinct kink. Fitting the two lines separately yielded two values for the diffusion coefficient,  $D_{\text{fast}} = 2.2 \mu\text{m}^2 \text{s}^{-1}$  and  $D_{\text{slow}} = 3.4 \times 10^{-1} \mu\text{m}^2 \text{s}^{-1}$ , respectively.  $D_{\text{fast}}$  is equal to  $D$  of the pure ethylene glycol in the aged **M22**, as shown in Figure 5.15 and Table 5.6. Therefore the  $D_{\text{slow}}$  is attributed to the second species present in the sample, the **9A1** dye. The diffusion coefficient of the dye is here about one order of magnitude smaller than  $D$  of the pure solvent. Furthermore, it is in the same range as the diffusion coefficient found for the diffusion of the single molecules measured by wide-field microscopy and SMT. Unfortunately the measurement was interrupted due to an instrument error and could not be repeated yet. Therefore these results have to be considered as preliminary. Nonetheless, they indicate that the ensemble diffusion of the dye **9A1** measured with PFG NMR is in the same range as the averaged value, which was obtained from 20 single-molecule trajectories of different length.

## 5.5 Summary

In this chapter it was shown, how single-molecule microscopy and pulsed field gradient NMR can be used to investigate the diffusion dynamics of different species within porous sol-gel glasses. Even though such silica materials do not develop crystalline structures or pore-topologies with defined pore diameters, their 'sponge-like' pore system can differ in the hierarchy of pore-diameters in the micro- and mesorange. Tracking of single molecules was applied here to two cast monolithic silica materials, **M3** and **M22**, both with micro- and mesopores, differing mainly in their mesoporosity. The mean mesopore diameters were about 3 nm and 22 nm, respectively, according to nitrogen adsorption/desorption isotherms. For these measurements a newly synthesized streptocyanine dye was found to be sufficiently photostable. The synthesis method developed here leads to transparent, crack-free monoliths in which single molecules are readily visible in the bulk of the sample.

In the sol-gel with narrower pores, the dye was found mostly confined in regions of diameter from below the positioning accuracy of the microscope, 50 nm, to about 200 nm. Since the confined molecules are much rarer in **M22** than in **M3**, it is concluded that they are probably confined due to physical traps rather than chemical bonding to the surface. Detection of such non-diffusing molecules is one of the advantages of single-molecule detection compared to fluorescence correlation spectroscopy. Other molecules diffused with a diffusion coefficient of about  $D_{\text{M3(mobile)}} = (3.0 \pm 1.5) \times 10^{-2} \mu\text{m}^2 \text{s}^{-1}$ . Interestingly, some molecules showed alternately diffusion and trapping. In the silica with wider pores (**M22**), motion of most molecules was following a random walk, over ranges of the order of 5  $\mu\text{m}$  in a few seconds, with a diffusion coefficient of the order of  $D_{\text{M22}} = 7.2 \times 10^{-1} \mu\text{m}^2 \text{s}^{-1}$ . About a 5-fold spread of the diffusion coefficients for different molecules was observed in both types of silica gels. Monte Carlo simulations were employed to prove the significance of the results and to find that for this gel most tracks were probably terminated by the molecule moving out of the detection volume, not by photobleaching.

Furthermore, PFG NMR measurements were conducted in the same sol-gel monoliths as the single-molecule tracking and also in an additional batch of similar samples. In this way a more thorough understanding of the ensemble diffusion processes in such systems could be gained. A surprising first result was, that the self-diffusion coefficient of ethylene glycol in **M22** is smaller than in **M3**. The measurements were done six months after synthesis and repeated about three years later. After the long period of ageing the mean pore diameters of **M3** and **M22** were similar, with a value of about 3.5 nm. The difference in the diffusion coefficient was still present after this period of ageing. Thus, difference in the pore tortuosity has most probably a stronger influence

on the diffusion of ethylene glycol. However, detailed information about the pore tortuosity is difficult to obtain. Nitrogen sorption isotherms do not provide such data and the positioning accuracy in the single-molecule experiments is too low to resolve curvature of the pores on a nanometre scale. Nevertheless, in a different batch of sol-gel glasses, **SG8**, **SG21** and **SG26**, the two materials with the larger pore diameter (**SG21** and **SG26**:  $\varnothing > 20$  nm) did show self-diffusion coefficients of ethanol which were about one order of magnitude higher than in the sample with the smaller pores (**SG8**). In this case, probably both factors, i.e. pore diameter and tortuosity, influence the diffusion behaviour.

Finally, even though most of the PFG NMR experiments focussed on the self-diffusion of the pure solvent, one tentative measurement to determine the ensemble diffusion coefficient of the dye **9A1** in **M22** could be performed. It showed that the ensemble diffusion coefficient determined by PFG NMR,  $D_{9A1} = 3.4 \times 10^{-1} \mu\text{m}^2 \text{s}^{-1}$ , is in the same range as the average value calculated from the single particle tracking data.

These results show that single-molecule tracking is a powerful tool to pinpoint nanoscale heterogeneities in complex systems such as sol-gel materials. In contrast, pulsed-field gradient NMR provides a detailed insight into the ensemble diffusion of different species within the porous systems. The combination of these two methods is thus ideally suited for a thorough investigation of diffusion dynamics within porous hosts.



## 6 Superimposing Single-Molecule Trajectories on TEM images

Molecular transport is at the heart of the applications of porous nanostructures as molecular sieves, catalysts and transporters of biomolecules.<sup>159,160,161,162,163</sup> Therefore, studying this transport by observing single-molecule diffusion in these systems as described in the previous chapter is of great interest in itself. However, to gain deep insight into how molecular diffusion is determined by the structure of the mesoporous host high-quality experimental diffusion data must be correlated with high-quality structural data. Where single-molecule tracking (SMT) provides the ultimate microscopic picture of molecular diffusion, the *ne plus ultra* of structural characterisation is the imaging of the host structure at the single-pore level. Since the size of a single pore is far below the diffraction limit for light microscopy only high-resolution electron microscopy (see Section 2.3) can provide this structural characterisation, with single pore resolution.

In the course of this thesis, in a cooperation with Andreas Zürner from the group of Prof. Bein, we pioneered a new technique<sup>164</sup> that combines electron microscopic imaging and single-molecule tracking. The molecular trajectory obtained by tracking a single dye molecule can be superimposed on the image of the pore structure obtained by electron microscopic mapping, in spite of the disparities of the two techniques in terms of sample requirements, measurement conditions and field of view.

The new method was used to investigate mesoporous thin films (cf. Section 2.2) with hexagonal pore ordering. In such films, the pores are lying parallel to the substrate and thus inside the observation plane of optical wide-field microscopy and transmission electron microscopy. It was a challenging task to find suitable substrates and synthesize films that the final samples were thin enough to be transparent for electron microscopy, and to ensure at the same time that it had sufficiently low fluorescent background to provide the high signal-to-noise ratio (SNR) needed for single particle tracking. Furthermore, location markers needed to be found that – when incorporated into the sample system – would be visible in both types of microscopies and thus allow to locate exactly the single-molecule trajectory in the mesopore landscape imaged by

TEM. One has to bear in mind that the two microscopy techniques work on different scales of length: A typical transmission electron micrograph that resolves mesoporous structures covers a square region of side a few hundreds of *nanometres*. On the other hand, in wide-field microscopy the illuminated area on the sample typically has a diameter of tens of *micrometres*. As mentioned above in Section 3.4, the single-molecule signals are diffraction limited with a FWHM of about the half of the wavelength. Thus, even though the position of such a single emitter can be fitted with much higher accuracy, the spread of the signal in one wide-field image has about the size of a single high resolution transmission electron micrograph. In order to overcome these differences in scale, regions of about  $3.5\ \mu\text{m} \times 3.5\ \mu\text{m}$  in size were imaged with multiple overlapping TEM images, which were mapped together.

In the following the synthesis of the very thin films ( $< 100\ \text{nm}$  thick) on special electron microscopy substrates, that are transparent for visible light and provide a relatively low fluorescence background needed for the observation of single fluorescent dye molecules, will be described. Finally, the new method to directly correlate the porous structures visible in transmission electron microscopy, but not in optical microscopy with the diffusion dynamics of single molecules, which are observable by optical microscopy but not by TEM, will be introduced. The results of applying this method to hexagonal mesoporous thin films<sup>9,11,165</sup> will be presented.

### 6.1 Synthesis

In order to apply single-molecule microscopy and transmission electron microscopy successively on the same sample, the latter must fulfill several conditions: the overall thickness of the mesoporous film and the substrate may not exceed  $150\ \text{nm}$ , to be transparent for the electron beam. In addition, the sample must contain fluorescent dye molecules, markers for the superimposition of TEM and optical images and markers for merging multiple TEM images. Furthermore the substrate has to provide a very low fluorescence background and must be free from impurities that are excited at the same wavelength as the dye. The following paragraphs describe how these stringent sample requirements can be fulfilled.

#### 6.1.1 Ultrathin Mesoporous Films

Mesostructured silica materials, as introduced in Chapter 2.2 were prepared via cooperative self-assembly of surfactant molecules with polymerizable silicate species.

The coating solution consisted of tetraethyl orthosilicate (TEOS) as silica source and the non-ionic surfactant polyoxyethylene 10 cetylother (Brij<sup>®</sup> 56, Sigma-Aldrich) as structure directing agent (see Figure 6.1), dissolved in an appropriate water/ethanol solvent mixture.

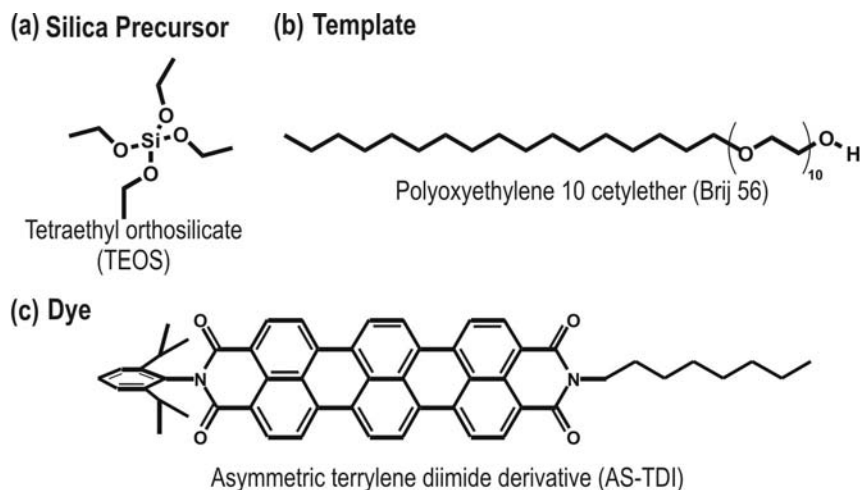


**Figure 6.1: Synthesis reagents and fluorescent dye.** (a) Silica precursor (TEOS). (b) Template Brij<sup>®</sup> 56. (c) Fluorescent terrylene diimide derivative (asymmetric **AS-TDI**), used as SMT dye and added during synthesis.

Transparent precursor silica/surfactant assemblies were prepared by a two-step process. First acid catalyzed hydrolysis-condensation of TEOS under reflux conditions was performed followed by addition of an ethanol solution of non-ionic block copolymer surfactant at room temperature. Additionally, strongly fluorescent terrylene diimide (**AS-TDI**, Figure 6.1c, synthesized in the group of K. Müllen, MPI Mainz)<sup>103,105</sup> molecules, acting as molecular reporters for SMT, polystyrene (PS) beads ( $\varnothing$  280 nm) as co-localization markers visible in both TEM and optical microscopy, and gold colloids ( $\varnothing$  5 nm) as landmarks for electron micrograph mapping were added to the synthesis solutions as described in more detail below. Ultra-thin films, transparent for TEM, were synthesized by deposition of a small volume of the coating solution onto a clean, flat substrate (see details below) and rotating it on the spin-coater. During rotation the evaporation-induced self-assembly (EISA)<sup>48,43</sup> took place and the final mesoporous structure was formed. This process resulted in silica films with a thickness between 50 – 100 nm. The EISA process is sketched in Figure 2.2 in Section 2.2.

### 6.1.2 Incorporation of the Dye Molecules

Strongly fluorescent terrylene diimide molecules (**AS-TDI**) were added at very low concentrations (final concentration ca.  $10^{-10}$  mol L<sup>-1</sup> in EtOH) to the final synthesis

solutions of the mesoporous films. They were thus incorporated into the pores during the evaporation-induced self-assembly of the material in the spin-coating process. To find the appropriate concentration for well-separated single-molecule patterns, a dilution series with various concentrations was made. The purity of the solvents and materials used was tested in blank samples without dye.

### 6.1.3 Substrates Suitable for TEM and Optical Wide-field Microscopy

In order to investigate the structure of the pore system with TEM and the diffusion of single molecules inside the pores with wide-field microscopy, the ultrathin films were synthesized on a 30 nm thick  $\text{Si}_3\text{N}_4$  membrane on 200  $\mu\text{m}$  thick Si-wafer supports (PLANO, Wetzlar) with a 500  $\mu\text{m} \times 500 \mu\text{m}$  window, as depicted in Figure 6.2a. A special sample holder was built, to mount these  $\text{Si}_3\text{N}_4$  membrane supports in the wide-field microscope (see Figure 6.2b, c). The metal sheet to hold the membrane on the microscope stage increased the distance of the sample to the objective by 100  $\mu\text{m}$ . In order to stay in the working distance of the high N.A. oil-immersion objective (max. 300  $\mu\text{m}$ ),

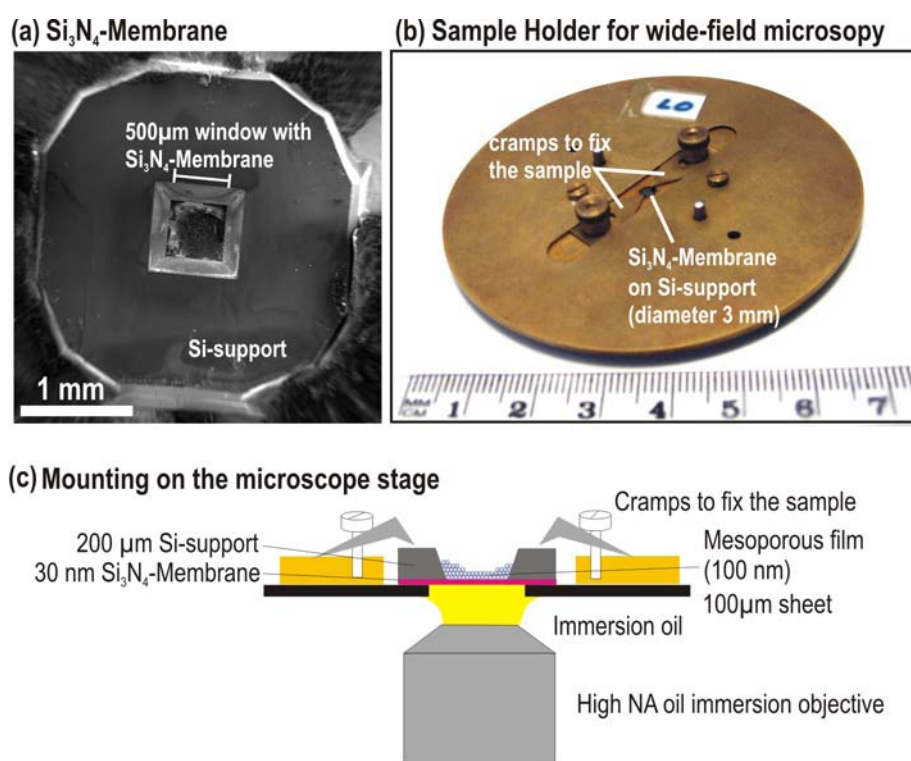


**Figure 6.2:  $\text{Si}_3\text{N}_4$  membrane supports.** (a) SEM image of the thin mesoporous film, coated on the  $\text{Si}_3\text{N}_4$  membrane on the Si-support. (b) Sample holder to mount the sample on the wide-field microscope stage. (c) Cross-section sketch of the sample mounting on the microscope. The sketch is not set to scale to show the details better.



the mesoporous film was spin-coated onto the interior of the membrane window, as sketched in Figure 6.2c. The membrane was irradiated for 1 h with  $1 \text{ W cm}^{-2}$  laser light at 633 nm prior to spin-coating, in order to photobleach all fluorescing molecules on the membrane. The membranes were not otherwise cleaned prior to spin-coating, e.g. by washing, as described below for cover-slips (Section 7.1), because they are too delicate and would be destroyed by such a procedure.

#### 6.1.4 Recipe

The recipe for the ultra-thin films was derived from the synthesis of hexagonal, Brij-templated films **B2**, presented in Chapter 7, by additional dilution of the precursor solution and by optimizing the spin-coating conditions, e.g. the humidity, in order to obtain ultra-thin films. A coating solution with molar ratios of 1 TEOS : 0.144 Brij 56 : 0.06 HCl : 61.7 EtOH : 210 H<sub>2</sub>O, resulted in ultra-thin films transmitting the electron beam of the TEM (see also recipe **B6** in Table 7.1 in the next chapter). The exact synthesis procedure for the ultrathin films was as follows: First, 2.08 g (0.01 mol) tetraethyl orthosilicate (TEOS 98%, Sigma-Aldrich) were mixed with 3 g  $0.2 \text{ mol L}^{-1}$  HCl, 1.8 g H<sub>2</sub>O and 7.9 g ethanol (spectroscopic grade, EtOH Uvasol<sup>®</sup>, Merck) and heated at 60 °C for 1 h to accomplish acid-catalyzed hydrolysis-condensation of the silica precursor. This solution was mixed with a second solution containing 600 mg Brij 56 and 12.5 g ethanol. Finally, 75  $\mu\text{L}$  of this mixture were combined with 4  $\mu\text{L}$  of a highly diluted terrylene diimide (**AS-TDI**) solution (ca.  $10^{-8} \text{ mol L}^{-1}$  in EtOH), 20  $\mu\text{L}$  of a gold colloid solution ( $\varnothing$  5 nm, concentration corresponding to 0.01% H<sub>2</sub>AuCl<sub>4</sub>, Sigma-Aldrich), 15  $\mu\text{L}$  of a polystyrene (PS) bead solution (Polybead microspheres,  $\varnothing$   $0.281 \pm 0.014 \mu\text{m}$ , 2.6% solids - latex, Polysciences, Inc., Warrington) and 40  $\mu\text{L}$  of de-ionized water. The samples were prepared in dry air by spin-coating (spin-coater: Laurell, Model WS-400B-6nPP/LITE/AS) 50  $\mu\text{L}$  of the final precursor solutions at 3000 rpm onto silicon nitride membrane window grids (PLANO, Wetzlar) or 200  $\mu\text{L}$  on silicon wafers (28 mm  $\times$  15 mm, Siltronic AG), respectively. Samples were analysed as synthesized. Here the term 'pore' that classically defines the empty space in porous materials after removal of the organic template is used to describe the template-filled effective volume in which the dye molecules can diffuse. Note that no further sample preparation, such as ion milling, was needed for electron microscopy at low and high resolution or for optical wide-field measurements. The PS beads serve as markers that are visible in both TEM and optical microscopy, and the gold colloids serve as landmarks for electron micrograph mapping are enclosed into the film.

### 6.1.5 Characterisation of the Host: XRD and Ellipsometry

For a better understanding of the structural parameters, 2D grazing incidence X-ray diffraction (GISAXS)<sup>166</sup> of samples spin-coated on Si-wafers was performed at HASY-LAB Hamburg, beamline BW4. The resulting 2D GISAXS diffraction pattern in Figure 6.3a shows a 2D-hexagonal order for the mesoporous silica. It is known that these materials show a shrinkage of the pores normal to the substrate. Thus the interplane distances parallel and tilted to the substrate differ. Here, the peaks in the 2D GISAXS correspond to  $d(10) = 5.5$  nm and  $d(01) = 5.9$  nm. The pore-to-pore distance parallel to the substrate plane is thus  $a(01) = 7.0$  nm and out-of-plane  $a(10) = 6.5$  nm. The shrinkage of the pores normal to the substrate is  $a^{(01)} - a^{(10)} / a^{(01)} = 7\%$ . The arrangement of the different lattice planes including the shrinkage of the system is sketched in Figure 6.3b. The thickness determined by ellipsometry is about 100 nm (Woollam ESM-300 Ellipsometer).

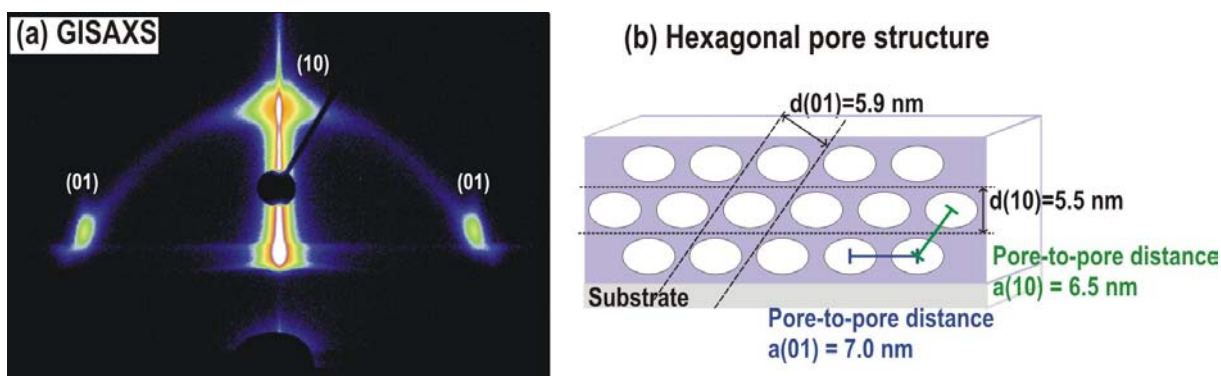


**Figure 6.3: Characterisation of the thin films.** (a) 2D grazing incidence X-ray diffractogram. Courtesy of A. Zürner, Bein group, LMU Munich. (b) Sketch of the hexagonal pore structure including shrinkage of the pores normal to the substrate, showing the arrangement of the  $d(10)$  and  $d(01)$  lattice planes and the pore-to-pore-distances  $a(01)$  and  $a(10)$  parallel to the substrate plane and out-of-plane.

## 6.2 Pattern Recognition - Identification of the same Sample Region in SMT and TEM

As mentioned above, polystyrene (PS) beads were used as markers for the co-localization of the single-molecule trajectories and TEM images. The beads must be small, to prevent a strong influence on the porous system within the thin films, but big enough to be well observable in the white light transmission images of the wide-field microscope. A size of about 280 nm was found to be optimal. Figure 6.4a shows a side-view scanning

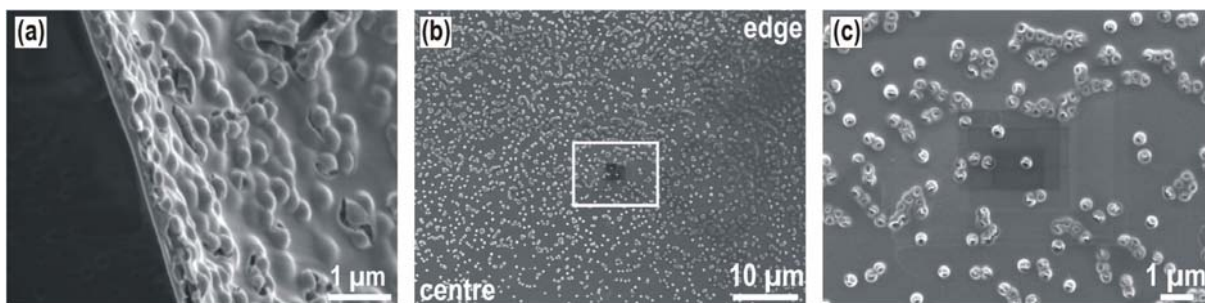


**Figure 6.4: Scanning electron micrographs (SEM) of the coated  $\text{Si}_3\text{N}_4$  membrane.** (a) Side view of the film. At this position, near the edge of the membrane, the mesoporous film is about 200 nm thick and the concentration of PS beads is too high for single-molecule tracking. (b) Plan-view of an intermediate region, close to the centre of the membrane. The concentration of PS beads is well suited for single-molecule measurements and the retrieval of identical regions in TEM and optical microscopy. (c) Plan-view at higher magnification of the region marked with a rectangle in (b). Courtesy of A. Zürner, Bein group, LMU Munich.

electron micrograph (Phillips XL40 ESEM scanning electron microscope) of the film. The polystyrene beads are embedded into the film and covered with a thin layer of mesoporous silica, i.e. that they are enclosed by the mesoporous film. At this position the mesoporous silica film on the 30 nm  $\text{Si}_3\text{N}_4$  membrane is about 200 nm thick. This image was taken in a region close to the edge of the  $\text{Si}_3\text{N}_4$  membrane window, therefore the concentration of beads is too high here for single-molecule tracking and the mesoporous film is too thick for TEM imaging. As the coating solution was deposited into the interior of the window, the solution was accumulated at the edges during spin-coating and therefore the film was thicker in this region. In the centre region of the membrane the concentration of PS was in the perfect regime for the overlay of single-molecule trajectories from optical microscopy and detailed electron microscopy pictures of the structure. Panels (b) and (c) of Figure 6.4 show images taken in this region, with around three to five particles per  $10 \mu\text{m}^2$ . In this region the film was found to be thin enough for both TEM and optical microscopy (see below).

All measurements with the optical microscope were done prior to the electron microscopy, as the ultra-high vacuum in the TEM will probably evaporate partly the solvent out of the pores and therefore change the environment in which the molecules diffuse. In order to obtain an overview of the bead concentration, and thus the correct film thickness, three edges of the membrane window and the centre region with lowest PS bead concentration were mapped in white light transmission images of  $62.5 \mu\text{m} \times 62.5 \mu\text{m}$  prior to single-molecule fluorescence imaging. These images were overlaid using automatic image cross correlation in Adobe Photoshop® (Version CS2) by the 'Photomerge' tool resulting in the map shown in Figure 6.5. The black square indicates the size of one of these images. In panel (b) an extract of the map of white-light transmission images is shown. At higher magnification a distinct pattern of

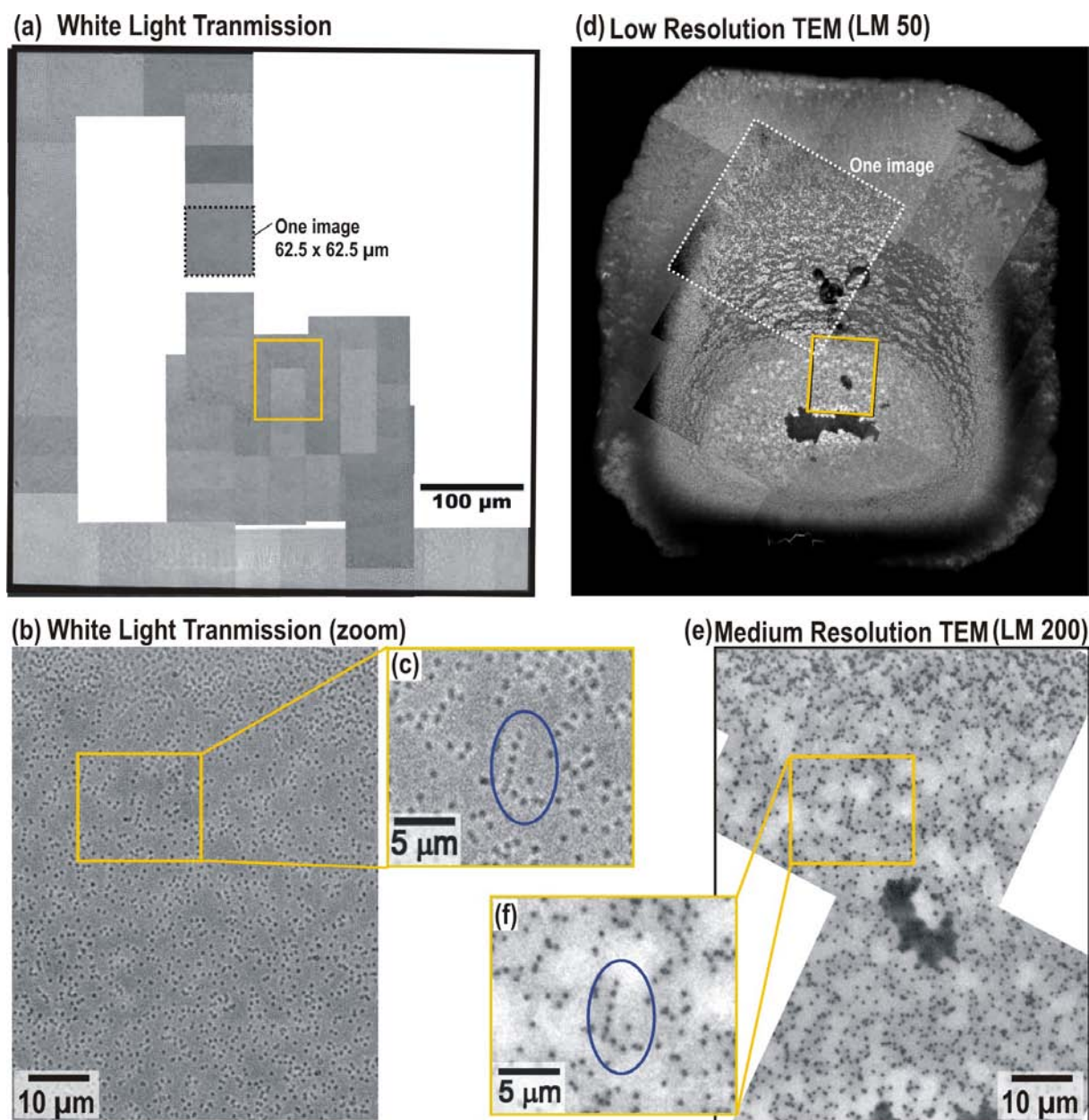


**Figure 6.5: White light transmission and TEM images of the mesoporous film, showing the embedded polystyrene beads. (a)** Map of white light transmission images of the whole membrane window ( $500\ \mu\text{m} \times 500\ \mu\text{m}$ ). The size of one white light transmission image is  $62.5\ \mu\text{m} \times 62.5\ \mu\text{m}$  (dashed square). **(b)** Zoom of the white light transmission map, showing the well separated PS beads in the region marked by the orange box in (a). **(c)** Magnification of a region with a distinct structure. **(d)** Map of TEM images at low resolution (LM 50); the size of one image is indicated by the white, dashed square. The image is rotated that the central region, with the right PS concentration and film thickness is at the same orientation as in (a). **(e)** Medium resolution TEM (LM 200) of the region highlighted with the yellow box in (d). **(f)** Magnification of the same characteristic formation of beads as in (c).

polystyrene beads can be resolved (c). Subsequent to optical microscopy, the sample was analysed with TEM. Again, the first step was mapping of the whole membrane with low resolution ( $50\times$ ), depicted in Figure 6.5d. This image was used to obtain an estimate of the orientation of the sample in the electron microscope with respect to the wide-field images. In this figure the image is already rotated such that the two pictures have the same relative orientation. The thin central region was then mapped at a magnification high enough to distinguish single PS beads ( $200\times$ ), shown in panel (e). On closer inspection of the white-light transmission image (b) and the intermediate resolution TEM (e), the identical arrangement of PS beads could be found in both. A zoom on this pattern is depicted in panels (c) and (f). Starting from this pattern, identical regions anywhere on the membrane window with suitable PS bead concentration could be recognized in wide-field and TEM images.

The whole centre region was thus investigated first by wide-field fluorescence microscopy and single-molecule tracking. The regions in which highly structured single-molecule trajectories could be found were subsequently mapped with high resolution TEM images. This procedure is described in the following paragraphs.

## 6.3 Single-Molecule Tracking

For the single-molecule experiments the fluorescent dye molecules were excited with a HeNe Laser at 633 nm, and movies of up to 1000 images were recorded to follow their diffusion. Since the films were much thinner than the focal depth of the microscope objective used ( $> 1\ \mu\text{m}$ ), images contain data from molecules at all heights inside and on the surface of the sample, and the molecules remained in focus during the complete duration of the movie. Image series were acquired with temporal resolutions of 100 ms, 200 ms or 400 ms per frame, but finally an exposure time of 200 ms was found to be most appropriate for single-molecule tracking. As the  $\text{Si}_3\text{N}_4$  membranes give a relatively high and inhomogeneous background signal, the background was subtracted frame-to-frame from the movies prior to tracking of the molecules.

One exemplary fluorescence image from a movie is shown in Figure 6.6a. The white square boxes indicate the regions that were subsequently mapped with TEM images. As described for the sol-gel samples in the previous chapter, fitting the positions of the molecules from frame to frame resulted in the single-molecule trajectories. In order to overlay these trajectories on the TEM images, the positions of the polystyrene beads had to be determined from the same movie. Therefore the laser shutter was closed after 148 s (746 frames) for the last 240 frames of the movie and the polystyrene beads were

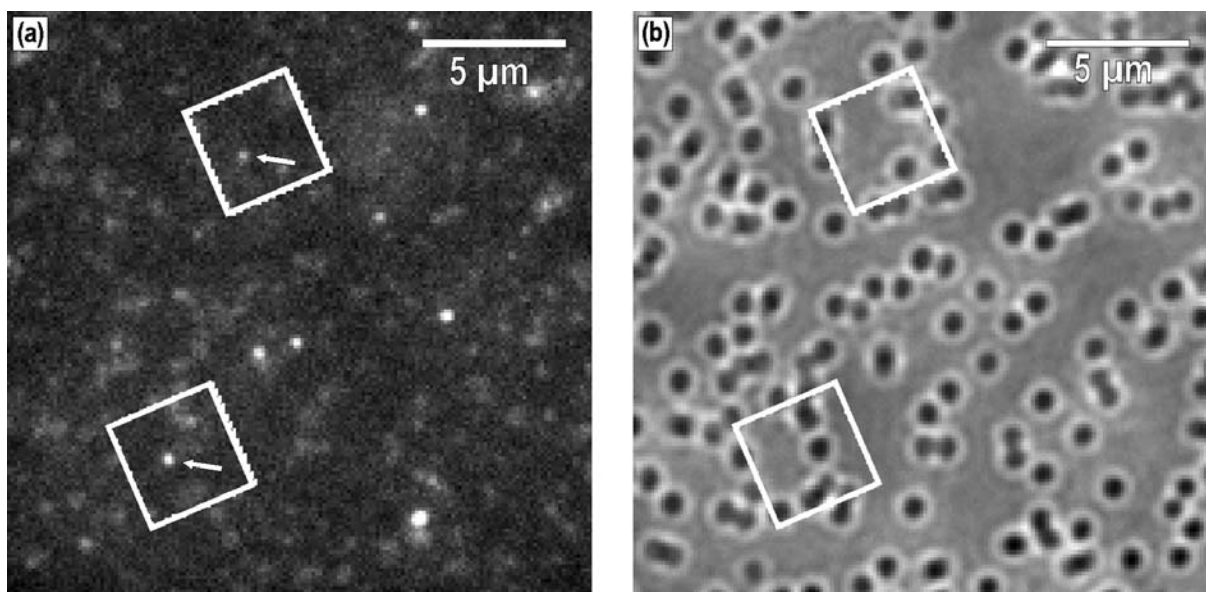


**Figure 6.6: Wide-field microscopy images.** (a) One exemplary fluorescence image of the wide-field movie, which is an extract from a complete  $30\ \mu\text{m} \times 30\ \mu\text{m}$  image. The molecules whose trajectories are depicted in Figures 6.10 and 6.12 are highlighted by an arrow. (b) Sum of the last 240 white light transmission images of the film, where the laser was shut. The PS beads are visible as black circles. The white square boxes in both images indicate the regions that were subsequently mapped with TEM. The upper square box indicates the region that was mapped with TEM images for Figure 6.10 and the lower one the region of the trajectory in Figure 6.12.

imaged in transmission under white light illumination. Their positions were fitted in inverted images with the same gaussian fit routine as the single molecules. Mean and standard deviation of the fitted PS bead positions were calculated and tabulated. Figure 6.6b shows the sum of all the white light transmission images that were recorded at the end of the movie. As there are no diffusing particles in those images, summing up all the images increases the image contrast and the PS beads can be better visualized.

## 6.4 Transmission Electron Microscopy at High Resolution

After the single-molecule tracking was done and the specific PS bead arrangement close to the trajectories was found in the TEM (Figure 6.5), 400 ( $20 \times 20$ ) TEM images of this region were taken at  $40,000\times$  magnification. The individual images of  $290\ \text{nm} \times 290\ \text{nm}$  were merged, again by image cross correlation with Adobe Photoshop<sup>®</sup>. The 5 nm gold particle markers were used as landmarks to support the merging procedure. This yielded a map of an area of about  $3.5\ \mu\text{m} \times 3.5\ \mu\text{m}$ . Such a map is shown below in Figure 6.8b. In order to better visualize the structure of the pores in the TEM images

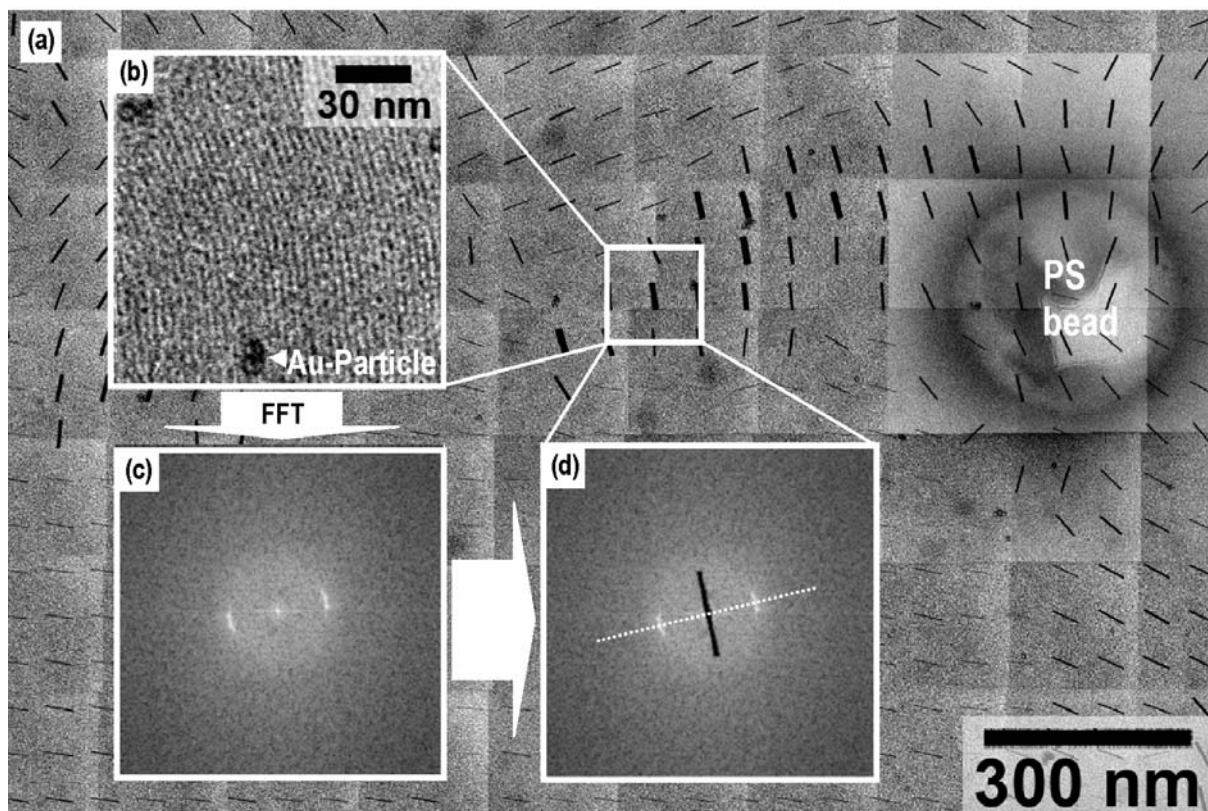


**Figure 6.7: Fast Fourier Transformation.** (a) The merged TEM map is redivided into equisized squares that are processed by Fast Fourier Transformation as shown in the insets. Moreover, on the right side of the image a PS bead embedded into the thin mesoporous film is visible. (b) Close-up of the central  $133 \text{ nm} \times 133 \text{ nm}$  square region. Here, in addition, two Au-nanoparticles that were used for merging the TEM images are visible. (c) FFT fit in this region, the maxima reflect the periodicity of the pores. (d) The direction of the channels is perpendicular to a straight line through the maxima. The thickness of the black lines, termed here 'directors', pointing along the pore direction, correlates with the structural quality.

the Fast Fourier Transform (FFT) was calculated for square regions of  $133 \text{ nm} \times 133 \text{ nm}$  each. In Figure 6.7 this process is shown in detail. The Figure shows an extract of one  $3.5 \mu\text{m} \times 3.5 \mu\text{m}$  TEM map, where the alignment of pores in different directions, i.e. different domains, is visible. The insets depict the FFT procedure. Panel (b) shows a  $133 \text{ nm} \times 133 \text{ nm}$  region with parallel alignment of pores. In addition, this image depicts two of the 5 nm Au-nanoparticles which were used for merging the images, visible as black dots. The FFT of the periodic arrangement of pores in (b) is shown in panel (c), it was calculated using the FFT tool in Digital Micrograph (Gatan, Inc.). The results of the FFT are plotted as black lines, which are perpendicular to the straight line through the maxima of the FFT and thus parallel to the periodically arranged pores, as shown in panel (d) and (a). The orientation of these 'directors' depicts the average orientation of the pores in the square region around it. The line thickness is a measure for the intensity of the maxima in the FFT fit, i.e. the line thickness scales linearly with the signal to background in the FFT image, and thus the degree of structural order in

this region. In addition to the orientation of the channels, these directors give a good overview of the domain size and domain borders.

Furthermore, on the right side of the image a polystyrene bead is visible. Also here FFT directors are visible, which is an artefact owing to a relatively low threshold value for the signal-to-background ratio (SBR=1.2) for drawing a line from the FFT signal. For the overlay of TEM images and single particle tracks, the centre positions of the PS spheres were determined by fitting a circle on the outside margin of their patterns in the TEM images by a fitting algorithm by A. Zürner, which will be described in more detail in the thesis of A. Zürner (Bein group, LMU Munich).

## 6.5 Overlaying SMT and TEM

Figure 6.8 demonstrates the spatial correlation between the single-molecule trajectories (movie of 1000 images, 200 ms per frame, Figure 6.8a) and transmission electron microscopy (Figure 6.8b). As mentioned above, the positions of the PS beads were determined by fitting a gaussian to the inverted patterns in the white light transmission images at the end of the wide-field movie and by fitting a circle to the outside margin of the image of each bead in the electron micrographs. The distances between all PS beads were calculated from the fitted positions in the wide-field movie and the transmission electron micrographs (Figure 6.8a, b). These positions are tabulated in Table 6.1.

**Table 6.1: PS bead positions in TEM images and wide-field images before and after merging and deviations of the positions after the overlay fit.**

Bead	TEM		SMT <sub>before</sub>			SMT <sub>after</sub>		Dev. [nm]
	x[nm]	y[nm]	x[px]	y[px]		x[nm]	y[nm]	
1	1680	1781	18.73	28.62	<b>Factor</b>	1698	1814	37
2	2668	2983	15.13	16.62	<b>121.3</b>	2675	2977	9
3	1660	1130	16.98	33.95	<b>Angle</b>	1637	1136	23
4	801.6	1830	25.48	31.69	<b>156.7°</b>	799.2	1796	34
<b>Average Deviation</b>								<b>26</b>

In addition, the angle that the connecting straight line of each pair of beads includes with the baseline of the image was calculated as reference frame. From the geometric relationship of the PS bead positions the scaling factor and rotating angle for overlaying the trajectories to the TEM image were fitted using a least-square algorithm. In



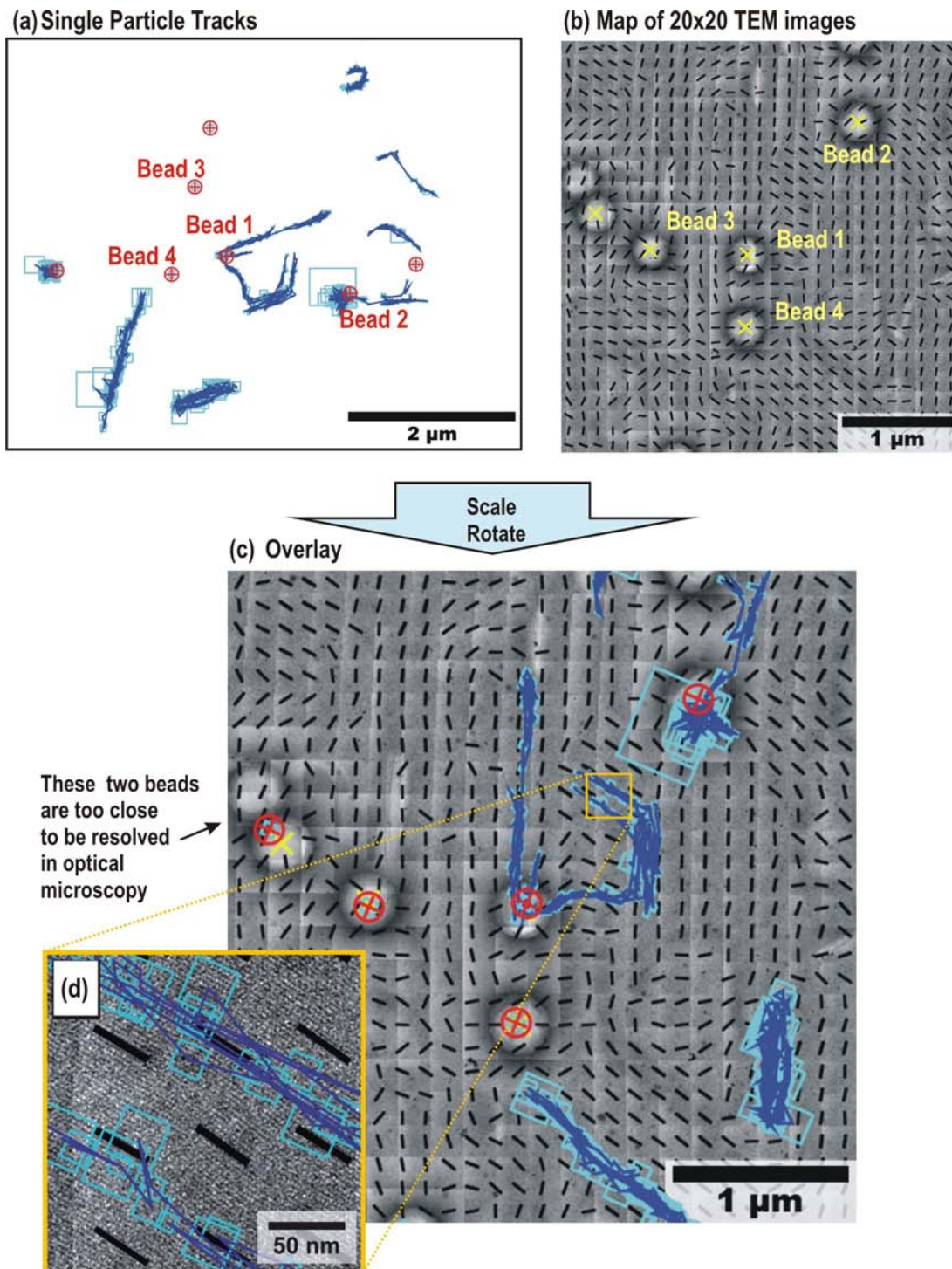


**Figure 6.8: Merging of the single-molecule trajectories and the TEM micrographs.** (a) Diffusion pathways of single molecules through the pore system (blue trajectories) and positions of the PS beads (red crosses). The bead numbers correspond to the numbers in Table 6.1. (b) Map of  $20 \times 20$  TEM images in the same region as (a), with lines indicating the direction of the channels (FFT directors) and yellow crosses marking the centre of the PS beads. (c) Final overlay of trajectories with TEM images; this was obtained by fitting to the best overlay of the PS bead positions. On the left two neighbouring beads are visible that were too close to be fitted individually in the wide-field images. (d) Enlargement of a region in (c) showing the trajectories running along the channels.

this case, a scaling Factor of 121.3 and a counterclockwise rotation by  $156.7^\circ$  gave the best fit. In addition, translation between the two images was adapted in an iterative process, which minimizes the sum of the squared distances between the beads. Column 6 and 7 in Table 6.1,  $SMT_{after}$ , give the  $x$  and  $y$  positions of the beads in the scaled and rotated wide-field image. The deviations of the bead positions in the TEM and wide-field images after the fitting procedure are tabulated in the last column.

The single particle trajectories were superimposed on the TEM image as shown in Figure 6.8c. The enlargement in Figure 6.8d shows directly the channels and the corresponding FFT directors, as well as the trajectories of the dye molecules along the channels. The accuracy with which the two images can be overlaid depends on the number of beads that can be used for the overlay and also on the positioning accuracy of each of the beads in the images. In this case four beads were used for the overlay, as tabulated above, and the average deviation for the position of the polystyrene beads in both TEM and wide-field imaging after merging was 26 nm. This value is taken as measure for the accuracy of the overlay. From the correlation of five different  $3.5 \mu\text{m} \times 3.5 \mu\text{m}$  TEM maps with the respective tracking data, a deviation of the bead positions in TEM and wide-field images was calculated to be  $29 \pm 13$  nm. Occasionally two beads are so close to each other, that they can be resolved in TEM but not in the wide-field images, where only the centre between the two beads can be fitted. An example of such a pair is visible in Figure 6.8c on the left side. They are therefore not used for the merging. However, in some cases such pairs of closely neighbouring beads had to be used for the merging to have a minimum of three anchor points for the overlay. In such cases, the individual positions of the closely neighbouring beads were determined in the TEM images. The centre position between the two beads was then correlated with the centre position of the single spot resulting from the two beads in the respective white-light transmission images, fitted by the gaussian function. For example, in Figure 6.12 two such doubled beads had to be used for correlating tracking data and TEM images, which resulted in an average deviation of 48 nm.

## 6.6 Individual Trajectories Correlated with the Pore Structure

With this approach, the influence of specific structural features of the host on the diffusion behaviour of the guest molecules can be investigated. In the following the analysis of the experimental data will show, in unprecedented detail, how a single luminescent dye molecule travels through linear or strongly curved sections of the hexagonal channel system in a thin film of mesoporous silica (as sketched in Figure 6.9a, b), how

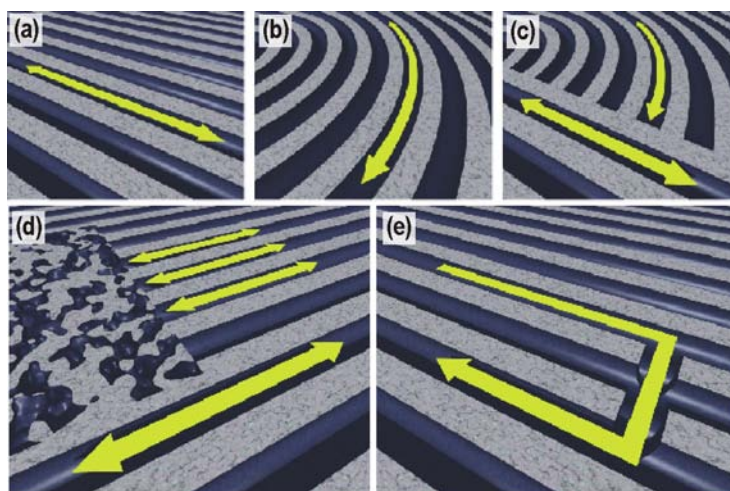


**Figure 6.9: Possible Structural elements which can be found in real 2D hexagonal mesoporous silica film.** Straight (a) and curved (b) segments. (c) Domain boundaries forcing molecules to turn back. (d) Molecular travel is stopped at less ordered regions. (e) Lateral motion between neighbouring channels.

it varies speed in the channel structure, and how it bounces off a domain boundary, where it hits walls of pores with different orientation (Figure 6.9c). Furthermore, it will be demonstrated how molecular travel is stopped at a less ordered region (Figure 6.9d), or how lateral motions between ‘leaky’ channels allow a molecule to explore different parallel channels within an otherwise well-ordered periodic structure (Figure 6.9e).

### 6.6.1 U-Trajectory: Diffusion in curved segments and at a domain boundary

Figure 6.10a depicts a trajectory of a molecule that is clearly following the porous system along different structural domains. The molecule diffuses along linear pores in the middle part of the trajectory (Figure 6.10b) and follows the curvature on the right and on the left side. In addition, it turns at a domain boundary, as shown in more detail in Figure 6.10c. The insets in the upper right corners of the Figures 6.10a, b and c show the different structural elements of this trajectory that were sketched in Figure 6.9. The positioning error for the single particle trajectories is shown by the light blue boxes. It is in the range of only 10 – 20 nm, therefore the molecular positions can be assigned to an ensemble of less than five to ten parallel channels. Thus, the width of the trajectory in the linear part in the middle, which is more than 100 nm, is real. It originates from diffusion in parallel channels and not only from a the positioning error of the fitted trajectory points (cf. Figure 6.10b).

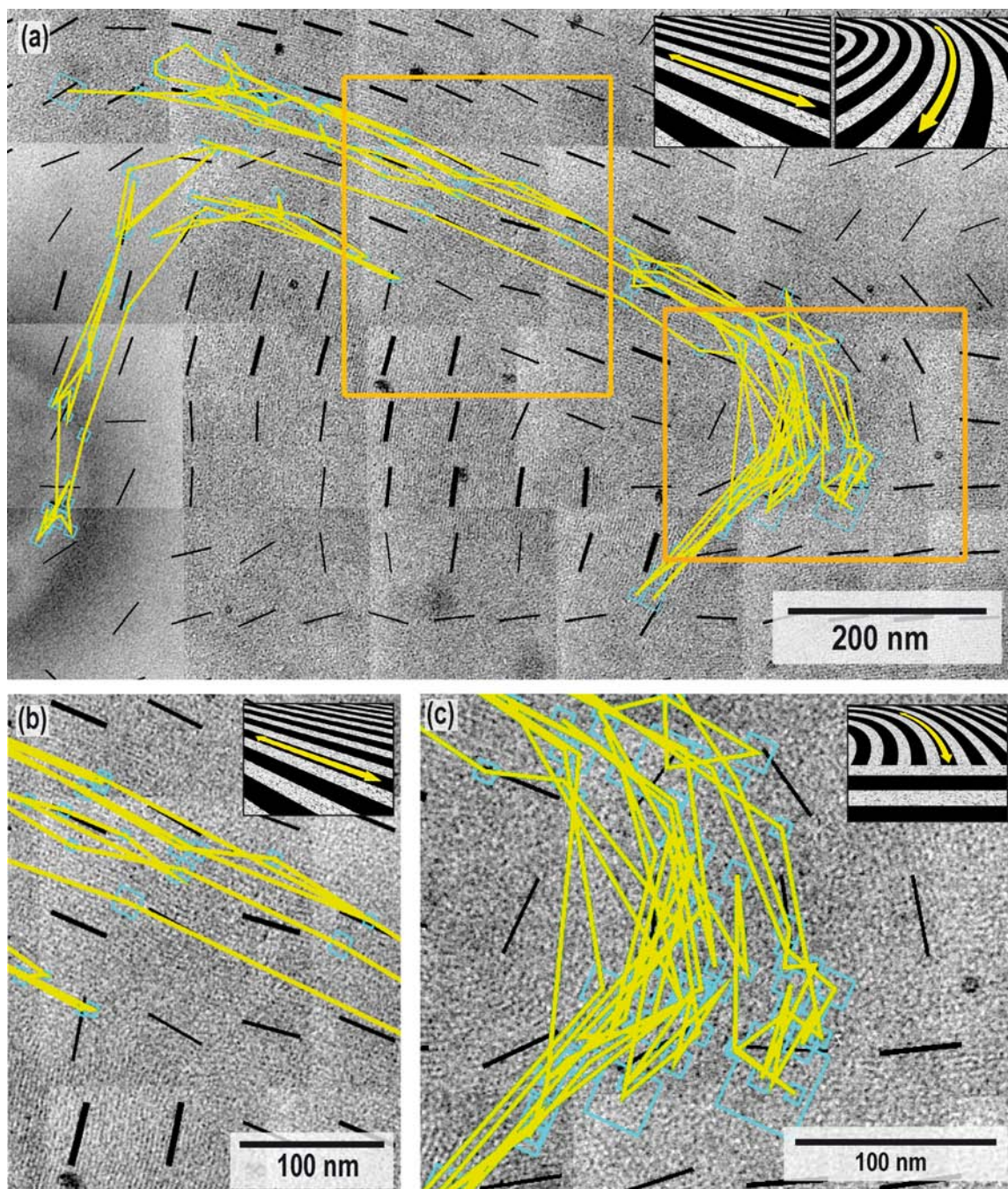


**Figure 6.10: Trajectory following linear and curved segments of the mesoporous film.** (a) The molecule diffuses along the U-shaped structure of the porous host and explores different parallel channels in the middle part of the trajectory. (b) The molecule is diffusing in different parallel channels, as the positioning error in the linear region is much smaller than the distance between the lines. (c) The curved region in (a) at higher magnification shows where the molecule turns back. The insets sketch the structural elements that were explored by this molecule. The positioning error for the single-molecule trajectory is shown by the light blue boxes.

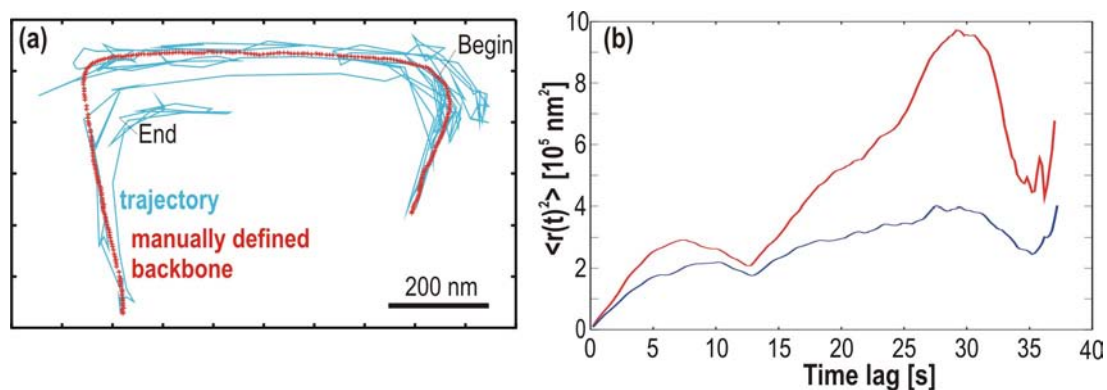


**Figure 6.11: Projection of the U-shaped trajectory onto its backbone and mean-square displacement as a function of time.** (a) The curved trajectory is shown by the blue line, and the manually defined backbone points by the red crosses. (b) MSD against time: The red line shows the result of the backbone projection, whereas the blue line corresponds to the standard averaging method of values taken from the original coordinates. The different slopes of the curves, especially for the first few data points, reflect the influence of the data analysis method on the calculated diffusion coefficients.

In order to analyse the diffusion along this trajectory the data points were projected onto a manually defined backbone of the trajectory. This procedure is described in Chapter 4. Figure 6.11a shows the trajectory in blue and the manually defined backbone points in red. The averaged mean-square displacement  $\langle r(t)^2 \rangle$  along the backbone was plotted as a function of time, as shown by the red line in Figure 6.11b. The linear relation of  $\langle r(t)^2 \rangle$  with time was fitted according to the Einstein-Smoluchowski equation for 1D diffusion (Equation 4.1.9) for the first few time lags between 0.2 s and 5 s, resulting in a one-dimensional diffusion coefficient  $D_{1D} = (3.2 \pm 0.1) \times 10^{-2} \mu\text{m}^2 \text{s}^{-1}$ . For comparison the  $\langle r(t)^2 \rangle$  values that were calculated by the standard averaging method without backbone projection are shown by the blue line in Figure 6.11b. It is important to analyse the 1D diffusion along the backbone, as the  $\langle r(t)^2 \rangle$  values are otherwise too small, especially for longer time lags, due to the curvature of the track. Note that in Figure 6.11b the MSD against time is not shown in logarithmic scale, in order not to obscure the difference in slope of the curves. An advantage of plotting this graph in linear scale is that the linear behaviour through zero for small  $\langle r(t)^2 \rangle$  and deviations from linearity for higher  $\langle r(t)^2 \rangle$  (due to insufficient statistics) are easily observed.

### 6.6.2 S-Trajectory: Diffusion along curves, at domain boundaries and stop at a less ordered region

Figure 6.12a depicts another example of a molecule faithfully following the pores and mapping out different structural units of the host structure. Here the average deviation of the overlay is 48 nm. In this case only one single bead and two pairs of closely neighbouring beads could be used for the overlay, which explains this relatively high value (see above). The molecule was blinking several times for intervals of up to 6.6 s, and the trajectory is thus divided into 11 parts, with a duration ranging from 0.6 s to 11.8 s, printed in different colours in the figure. Trajectory segments with less than 20 points are drawn in black. The perfect overlay of this S-shaped trajectory with the pore system is nicely visualized by the FFT directors.

In Figure 6.12b-d the specific regions marked with rectangular boxes in Figure 6.12a are shown, and again the insets sketch the different behavior at specific regions of the trajectory as in Figure 6.9. Although the resolution of the optical microscope is not high enough to assign the position of a molecule to one channel, it is possible to conclude that the molecule was moving in different straight parallel channels of the same domain from the width of the middle part of this trajectory (magnified in Figure 6.12b). Especially interesting is the short element at the end of the yellow trajectory part where the molecule makes an U-turn by crossing into a parallel channel, which is separated from the original channel by a distance  $> 2\sigma_{\text{positioning}}$ , as sketched in Figure 6.12b on the left. On the basis of the spatial resolution of the optical pathways, it can be concluded that the molecule is diffusing in different parallel pores. At the left end of the trajectory the molecule diffuses in a well-ordered straight structure and bounces back repeatedly from an amorphous region with no apparent pore ordering, as shown in in Figure 6.12c. On the right side in Figure 6.12a a domain boundary region is visible. This structure is shown in more detail in Figure 6.12d. Here, the molecule bounces back from the domain boundary because it hits the walls of channels with a different orientation, as sketched in Figure 6.9c and in the inset. The orange lines in Figure 6.9c are situated slightly above the region of linear channels. However, if the average deviation of the overlay of 48 nm is taken into account it is highly probable that the molecule was actually diffusing along the linear structure in the bottom region of the figure. Furthermore, one should keep in mind that we are sampling diffusion at discrete points in time and space. The connecting lines are just a method of visualizing the trajectories; they do not represent the molecules' exact path.

To analyse the diffusion along this trajectory the data points were again projected onto a manually defined backbone and the averaged  $\langle r(t)^2 \rangle$  values were fitted according to 1D diffusion for the first few timelags, with a linear relation of the mean-square

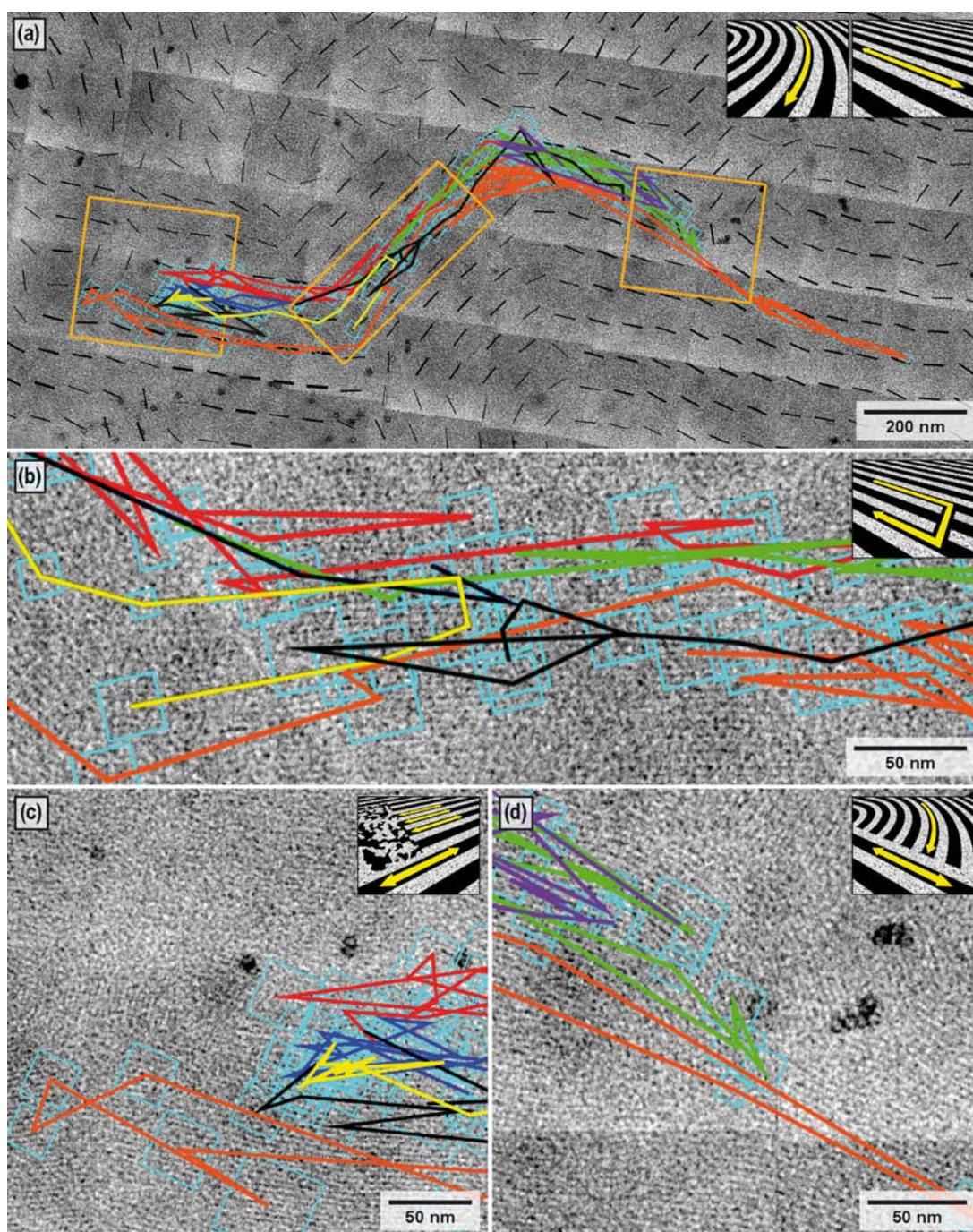


**Figure 6.12: Molecule exploring a large domain and the domain boundaries.** (a) Trajectory of a molecule, showing an S-shape corresponding to the underlying channel structure. The trajectory is divided into several sections due to blinking of the fluorescent molecule; the sections are plotted in different colours, short parts with less than 20 points are drawn in black. (b) Lateral motions between 'leaky' channels (yellow trajectory segment). (c) Area where the molecular movement is stopped at a less ordered region. (d) At a domain boundary the fluorescent molecule is forced to turn back (green pathway). The insets sketch the structural elements that were explored by this molecule. The positioning error for the single particle trajectories is shown by the light blue boxes.

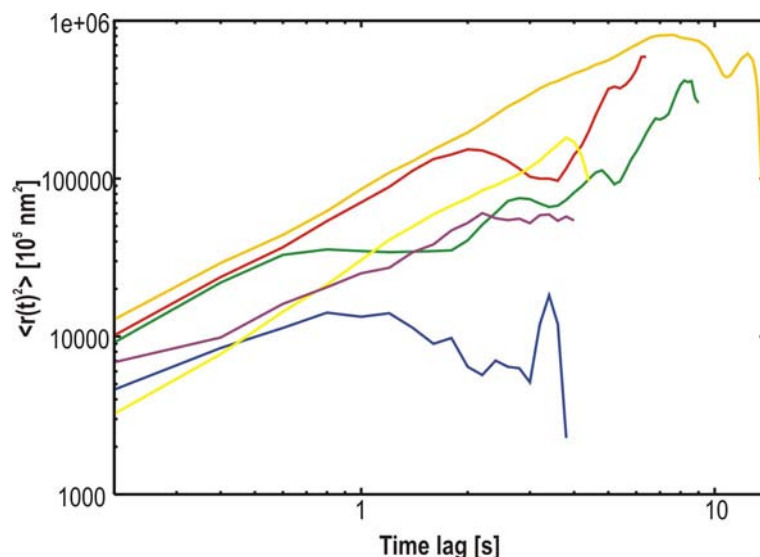


**Figure 6.13: Mean-square displacement of the different parts of the S-shaped trajectory as a function of time.** The different lines correspond to the different parts of the trajectory, the colour coding is identical to the colours of the different parts in Figure 6.12. The spread of the diffusion coefficients is directly visible from the different y-axis intersects in the double-logarithmic plot.

displacement with time. This results in an average diffusion coefficient  $D_{1D(av)} = (3.0 \pm 0.1) \times 10^{-2} \mu\text{m}^2 \text{s}^{-1}$ , which is in the same range as the diffusion coefficient for the U-shaped trajectory shown in Figure 6.10. Also here, it is important to project the trajectory on its backbone, as the  $\langle r(t)^2 \rangle$  in the curvature would otherwise bend towards smaller values for longer timelags. Figure 6.13 shows the  $\langle r(t)^2 \rangle$  against time plots for the individual trajectory parts in the same colours as in Figure 6.12. For the parts of the trajectory without blinking for at least 20 frames, the following average diffusion coefficients were calculated: red (frame 1-33)  $D_{1D(\text{red})} = (3.6 \pm 0.2) \times 10^{-2} \mu\text{m}^2 \text{s}^{-1}$ , green (frame 37-82)  $D_{1D(\text{green})} = (1.1 \pm 0.1) \times 10^{-2} \mu\text{m}^2 \text{s}^{-1}$ , blue (frame 100-119)  $D_{1D(\text{blue})} = (1.0 \pm 0.1) \times 10^{-2} \mu\text{m}^2 \text{s}^{-1}$ , yellow (frame 135-157)  $D_{1D(\text{yellow})} = (2.0 \pm 0.1) \times 10^{-2} \mu\text{m}^2 \text{s}^{-1}$ , orange (frame 176-244)  $D_{1D(\text{orange})} = (5.5 \pm 0.1) \times 10^{-2} \mu\text{m}^2 \text{s}^{-1}$  and violet (frame 308-328)  $D_{1D(\text{violet})} = (1.3 \pm 0.2) \times 10^{-2} \mu\text{m}^2 \text{s}^{-1}$ . The noticeable changes of the 'local' diffusion coefficient show that the diffusion behaviour of the molecules is strongly dependent on the surrounding pore structure. When the molecule is 'bouncing back' at an unstructured region, as in the dark blue part of the trajectory, the  $D_{1D}$  is smaller than in regions where the molecule is diffusing along the trajectory (orange, red). Besides this general observation, no further detailed assignment of diffusion coefficients to special structural units of the host was found in this study.



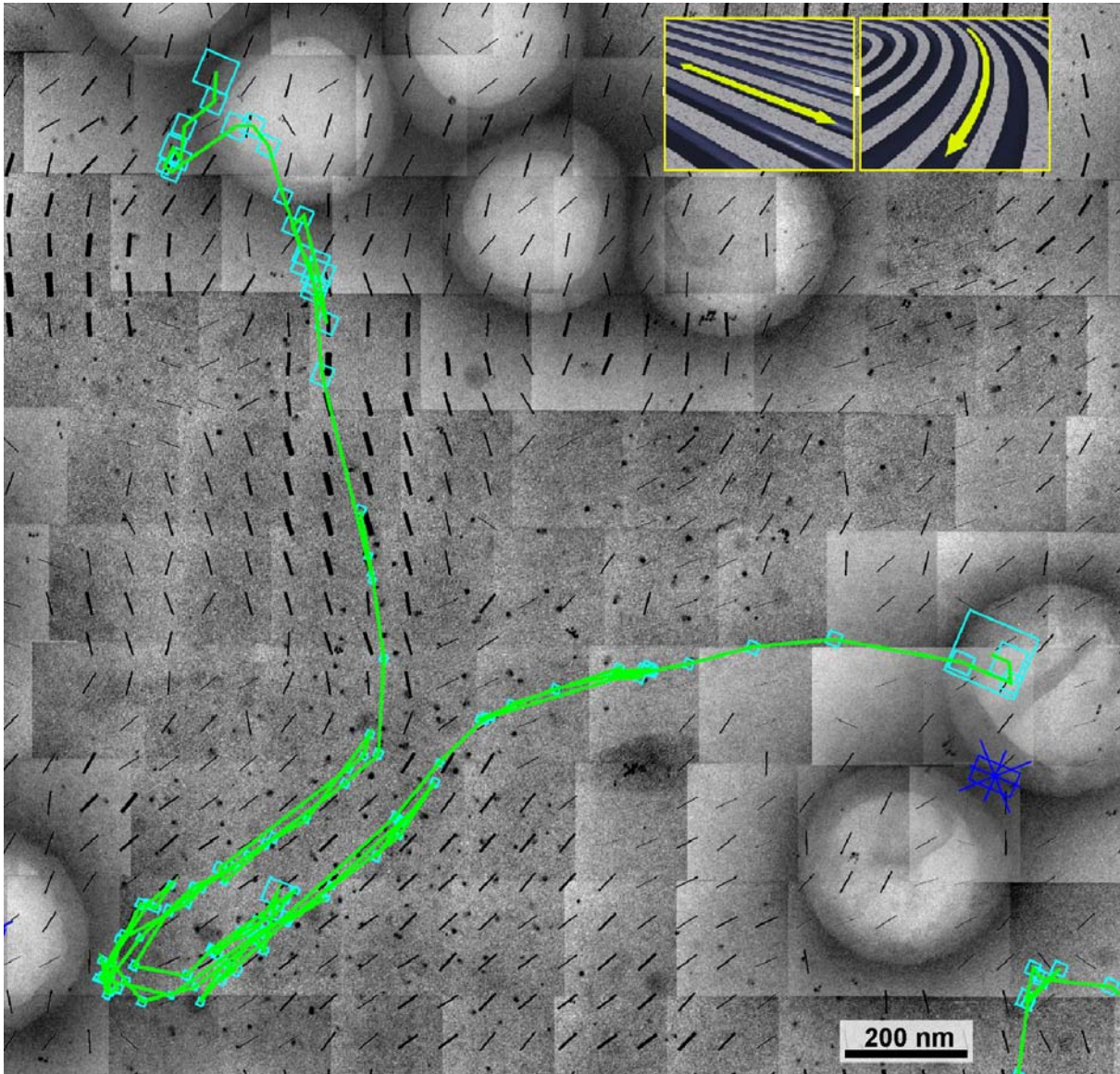
### 6.6.3 Y-Trajectory: Diffusion along strongly curved segments close to the PS beads

The trajectory in Figure 6.14 depicts a molecule diffusing through linear and curved regions of the porous structure. Again, the trajectory pathway fits perfectly well with the orientation of the FFT directors and reflects directly the underlying pore structure. This molecule was diffusing in a region with relatively high concentration of PS beads. It starts and ends close to or even on top of a PS bead and is strongly bend in the middle part in the proximity of another bead. As mentioned above, the beads are enclosed into the layer of the mesoporous film, and thus there might be a pore structure present on top. However, no structural information can be gained from the TEM images on top of the beads, the directors in this region are only artefacts. In addition, the molecule explores regions on top of the beads, which is another indicator that there is an organised pore structure. In the middle part the molecule makes a U-turn in close proximity of a bead. Possibly the influence of the bead made the structure turn around during synthesis. The FFT fits in this region are not not very precise, due to the strong change of contrast close to the bead in the TEM image.

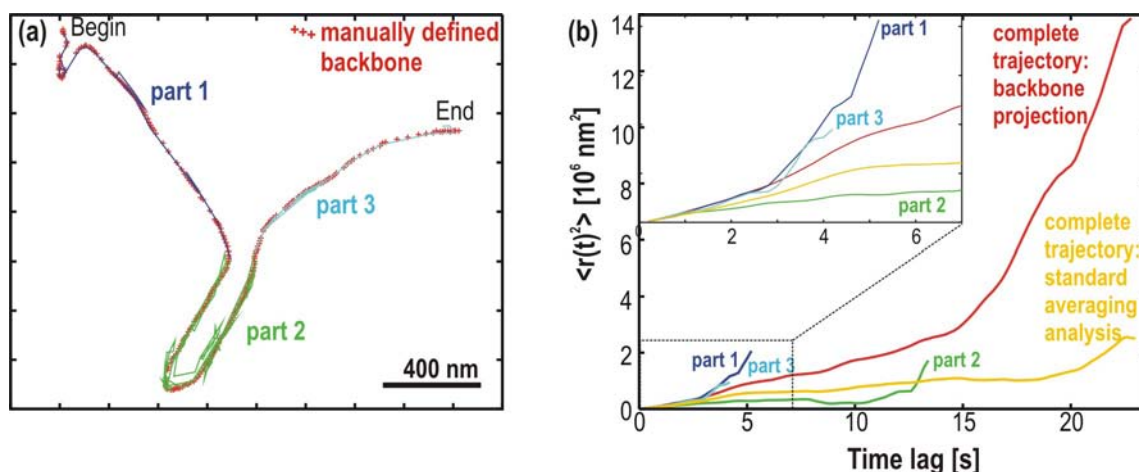
This molecule explores at least three different domains, which can be distinguished by the orientation of the FFT directors and as well by the kinks in the diffusion pathway. The latter were used to decide where to cut the trajectory manually. In the resulting three parts of the trajectory the diffusion coefficients were calculated separately.

Figure 6.15a shows the three trajectory parts in three different colours. In a trajectory having such a high curvature it is especially important to analyse the 1D diffusion along the backbone. Thus, again the points were projected onto a manually defined backbone, indicated by the red crosses in Figure 6.15a. Figure 6.15b shows the plots of the MSD against time for the individual parts of the trajectories and also for the complete trajectory.

For comparison the  $\langle r(t)^2 \rangle$  values that were calculated using the standard averaging method in 2D for the complete trajectory are plotted as well. The inset shows a close-up for the first few timelags. Here, the differences in the slope for the different trajectory parts are visible. Part 1, 3 and the overall trajectory have a similar slope. However, in the central region close to the bead the diffusion coefficient is smaller, despite the backbone projection of the data and thus despite accounting for the high curvature in this region. The averaged  $\langle r(t)^2 \rangle$  values for each of the trajectory parts and also for the complete trajectory were fitted according to the Einstein-Smoluchowski equation for one-dimensional diffusion for the first few timelags. For the complete trajectory this results in a  $D_{1D(\text{complete})} = (6.0 \pm 0.1) \times 10^{-2} \mu\text{m}^2 \text{s}^{-1}$ . In addition  $D_{1D}$  for the three intervals



**Figure 6.14: Molecule undergoing a U-turn in the neighbourhood of a PS bead.** (a) This trajectory can be separated into at least three different parts according to the orientation of the underlying pore structure, plotted in different colours in Figure 6.15. The insets depict the linear and strongly curved structural elements of this trajectory. At the strongly curved segment the molecule is in close proximity of a polystyrene bead, which probably influence the pore structure in this region and thus the diffusion pathway of the molecule.



**Figure 6.15: Projection of the Y-shaped trajectory onto its backbone and mean-square displacement as a function of time.** (a) The trajectory is divided into three parts with different pore orientation, plotted in different colours in Figure 6.15. The manually defined backbone points are indicated by the red crosses. (b) MSD against time: The different slopes correspond to the different diffusion coefficients. In the zoom in the inset it is visible that the molecule has about the same diffusion coefficient in part 1 and 3, whereas  $D$  in the middle segment (part 2) is smaller. The red line shows the result of the backbone projection of the complete track, whereas the orange line corresponds to values taken from the original coordinates. The different slopes of the curves - especially for the first few data points as shown in the inset - reflect the influence of the data analysis method on the calculated diffusion coefficients.

of the trajectory in the three domains with different pore orientation was calculated, which gave  $D_{1D(\text{part1})} = (6.2 \pm 0.2) \times 10^{-2} \mu\text{m}^2 \text{ s}^{-1}$ ,  $D_{1D(\text{part2})} = (3.6 \pm 0.1) \times 10^{-2} \mu\text{m}^2 \text{ s}^{-1}$  and  $D_{1D(\text{part3})} = (5.6 \pm 0.1) \times 10^{-2} \mu\text{m}^2 \text{ s}^{-1}$ . The diffusion coefficient in the long side-arms of the trajectory (part 1 and 3) are 1.5 to 2 times higher than in the curvature (part 2). Nonetheless, the number of trajectory points is too low to decide if this change in the diffusion coefficient is really significant or not.

When looking at the complete curves in Figure 6.15b, the increased slope of the blue lines (parts 1 and 3) and the red line (complete track) are striking. Such a curve is typical for a diffusion with drift, i.e. when the molecule is accelerated in one direction by some additional force. As discussed above in Chapter 4, the angles between successive steps can provide additional information about the diffusion of the molecule. A drift in one direction should become visible as a bias towards steps forwards. In Figure 6.16a the cumulative probability distribution of steps is plotted for this trajectory, showing a strong excess of steps forward. The blue line corresponds to the maximum distance of the cumulative distribution and its complement to which we apply the Kolmogorov-Smirnov test to check if the apparent forward bias is significant. The probability that this difference originates only from statistical noise of the data is 0.22 %. Therefore this excess of forward steps can be taken as real. However, no simple explanation for this bias can be found. The template, which remains inside the pores, or the sym-

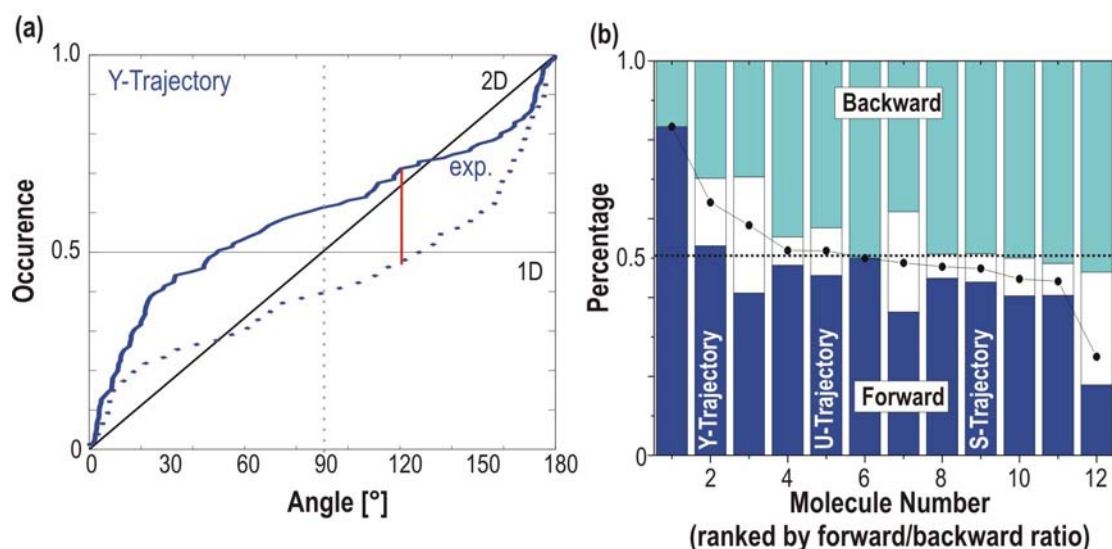


**Figure 6.16: Distribution of forward and backward steps: Cumulative distribution of angles and stacked histogram.** (a) Examples for cumulative distributions of angles between successive steps for the Y-shaped trajectory. (b) Stacked column chart of forward, intermediate and backward steps for the individual molecules tracked in the complete movie, sorted by decreasing forward/backward ratio.

metry of the molecules might have an influence. More detailed investigations of the forward/backward ratio in the angular distributions will be provided in the following chapter. For comparison, the amount of forward, intermediate and backward steps and the forward/backward ratio for all molecules that were tracked in this movie is depicted in Figure 6.16b. The distributions for the S-shaped and U-shaped trajectories that were discussed above are also marked. This graph shows that on average no excess of forward or backward steps can be found for the molecules in this movie and the Y-shaped track is one special case with high excess of forward steps. The short white bars in the centre represent the amount of intermediate steps, which is low, as expected for highly structured diffusion along one-dimensional channel systems.

## 6.7 Summary

In this chapter a novel method to overlay the single-molecule trajectories collected with optical wide-field microscopy with the electron microscopic images of a porous host system obtained from TEM measurements was presented. The combination of the two techniques provides the first direct proof that the molecular diffusion pathway through the pore system correlates with the pore orientation of the 2D hexagonal structure. It allows for the first time to directly correlate the dynamical information from the diffusion of guest molecules with the detailed structure of the porous host in regions up to

3.5  $\mu\text{m}$   $\times$  3.5  $\mu\text{m}$  in size. This approach reveals the nature of the real space porous defect structure as detected by the movement of fluorescent single molecules, containing linear or strongly curved sections of the hexagonal channel system, domain boundaries, boundaries between ordered and disordered sections, and leaky channels that permit lateral travel. The direct correlation of individual molecular trajectories with the underlying structure of the porous host opens new ways for understanding and control of the interactions of host and guest. This new methodology is expected to provide detailed insights into the dynamics of other important host-guest systems, such as bio-active molecules in porous materials for drug delivery or reactants in porous catalysts.



## 7 Diffusion of TDI in Spin-coated Mesoporous Thin Films

The experiments and results described in this chapter cover a thorough investigation of the dynamics of single TDI molecules inside the channels of different mesoporous hosts. From the experiments in Chapter 6 it is known that the single molecules follow precisely the pores of the mesostructured host and their trajectories do indeed map out domains in the heart of the material. With this knowledge, the measurements presented in the following were done on cover-slips as ideal substrates for optical microscopy, which permit to study a large number of samples with a broad range of frame rates. That way larger areas could be sampled, up to  $30\ \mu\text{m} \times 30\ \mu\text{m}$  in size, and, by measuring with high spatial and temporal resolution a detailed view of the dynamics of the guest molecules inside the porous host could be obtained. Different diffusional and orientational dynamics of molecules were observed depending on the pore topologies in different host materials that were synthesized with various amounts of the same organic template. Samples with pure phases (2D hexagonal, lamellar, cubic) were studied as well as samples exhibiting phase mixtures, where different phases coexisted in the same sample.

First, Brij 56 templated thin films with different topologies, i.e. hexagonal, lamellar or a mixture of both, are discussed here. In the second part of this chapter the diffusion in hosts with larger pores with hexagonal or cubic arrangement, which are templated by Pluronic P123, is presented.

The work was conducted in cooperation with Barbara Platschek and Nikolay Petkov from the research group of Prof. Bein at the LMU Munich. They synthesized the samples and characterised them by X-ray diffraction and transmission electron microscopy. More details about their share of the work may be found in their theses.<sup>57,166</sup> Christophe Jung from our group helped with the orientation measurements at the confocal microscope, a more detailed description of this setup and the method will be given in his thesis. The different terrylene diimide dyes were synthesized in the group of Prof. Müllen at the Max Planck Institute (MPI) for Polymer Research in Mainz.

## 7.1 Synthesis of Thin Films with Different Topologies

### 7.1.1 Overview of the Different Synthesis Recipes

A variety of mesoporous thin films with different pore diameters and pore topologies were synthesized using the non-ionic surfactants polyoxyethylene 10 cetyl ether (Brij<sup>®</sup> 56, Sigma-Aldrich) and polyethyleneoxide-polypropyleneoxide-polyethyleneoxide (PEO<sub>20</sub>-PPO<sub>70</sub>-PEO<sub>20</sub>, Pluronic<sup>®</sup> P123, BASF) as templates (see Figure 7.1). As mentioned in Chapter 2.2, the diameter of the pore is determined by the template and the pore topology by the surfactant/silica ratio. The two different templates yielded pore-to-pore distances of 6 nm for Brij 56 and 10 nm for Pluronic P123, respectively, measured by XRD (see below). Depending on the surfactant/silica ratio, hexagonal, lamellar and cubic pore systems and even mixtures of the different pore topologies were obtained.

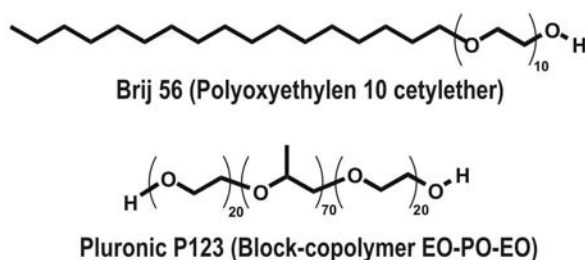


**Figure 7.1: Templates used for the synthesis of mesoporous thin films with various topologies.** Top: Polyoxyethylene 10 cetyl ether Brij<sup>®</sup> 56. Bottom: polyethyleneoxide-polypropyleneoxide-polyethyleneoxide (PEO<sub>20</sub>-PPO<sub>70</sub>-PEO<sub>20</sub>) Pluronic<sup>®</sup> P123.

The synthesis procedure was similar to the routine described in the previous chapter, but without an additional dilution step. Therefore the films presented here are thicker than those for the correlated TEM and wide-field measurements. They have a thickness of about 200 nm, again measured by ellipsometry on films synthesized on silicon wafers. The molar ratio of the final precursor solutions for the mesostructured samples that were used in this work are summarized in Table 7.1. Again, the first step was acid catalyzed hydrolysis-condensation of TEOS under reflux conditions, the composition is given in the respective columns of the table (molar ratio). Then an ethanol solution of non-ionic block copolymer surfactant was added at room temperature. The resulting solution was spin-coated on different substrates as described in the following. In the first two columns of the table it is visible that for Brij 56 the phase changes from hexagonal to lamellar with increasing surfactant/silica ratio and for Pluronic P123 from hexagonal to cubic.



**Table 7.1: Synthesis recipes (molar fractions) for mesostructured thin films.** The assignment to the different phases was done using XRD and TEM data, and will be presented later in Section 7.2.1.

Topology	TEOS	surfactant	HCl	H <sub>2</sub> O	EtOH
<b>Brij 56</b>					
<b>B1</b> Wormlike	1	0.066	0.06	27	31
<b>B2</b> Hexagonal	1	0.083	0.06	27	34
<b>B3</b> Mixture: Hex. / Lam.	1	0.13	0.06	27	44
<b>B4</b> mostly Lamellar	1	0.20	0.06	27	50
<b>B5</b> Lamellar	1	0.40	0.06	27	60
<b>B6</b> Ultrathin Hex.	1	0.090	0.056	208	44
<b>Pluronic P123</b>					
<b>P1</b> Hexagonal	1	0.013	0.06	27	60
<b>P2</b> Cubic	1	0.017	0.06	27	60

## 7.1.2 Substrates

For the experiments presented in this chapter, the mesoporous films containing dye molecules were deposited on pre-cleaned glass cover-slips that are optimal for measurements with high N.A. oil immersion objectives (20 mm × 20 mm, thickness grade 1.5 (= 170 μm), Marienfeld). For the cleaning procedure, the glasses were placed for about 30 minutes into a 0.5 % Hellmanex<sup>®</sup> II (Hellma, Müllheim) solution at 50 °C, sonicated for two minutes, and rinsed thoroughly with deionized and UV-irradiated water for five minutes. The substrates were vacuum-locked during the spin-coating process, 80 μL of the precursor solution were deposited onto them, and they were rotated with a spinning rate of 3000 rpm for 30 s (Different spin-coaters were used: CONVAC, Speedline Technologies SCS P6700 Spin coater or Laurell, Model WS-400B-6nPP / LITE / AS). Additional samples were coated onto silicon wafers (28 mm × 15 mm, Siltronic AG), to obtain a better SNR in the 1D X-ray diffractograms and for the ellipsometry measurements.

## 7.1.3 Different Fluorescent Dyes

In addition to the asymmetric dye, **AS-TDI**, that was also used for the measurements presented in the previous chapter, two symmetric terylene diimide derivatives were used for the investigations in the Brij-templated films. Figure 7.2 depicts the structures of the three molecules. The symmetric **DIP-TDI** has the same diisopropylphenyl-group that form one head-group of **AS-TDI** on both sides. In contrast, **SW-TDI** has

two double, swallow like alkyl-tails at both diimide ends, comparable to the octyl-tail of **AS-TDI**. The symmetric dye having only one octyl group on each side, which would offer an even better comparison to **AS-TDI**, could unfortunately not be synthesized due to its insufficient solubility.

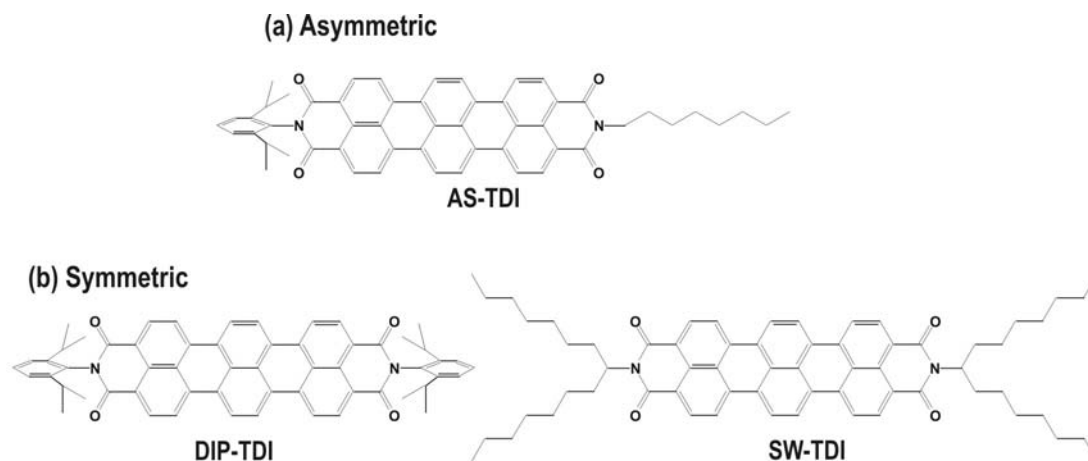


**Figure 7.2: Terrylene diimide derivatives.** Three different TDI derivatives that were used as fluorescent dyes for single-molecule tracking: (a) one asymmetric (**AS-TDI**) and (b) two symmetric dyes (**DIP-TDI**, **SW-TDI**).

It is important to know the dimensions of the dye, which is diffusing inside the mesoporous systems, to have an estimate of the size relations between the pores of the host and the extension of the guest. An molecular modelling calculation was done for **AS-TDI** using the Extensible Computational Chemistry Environment (ECCE, by Gary D. Black, Richland). The molecule is about 3.2 nm long (including head and tail), about 0.9 nm wide across the terrylene plane and about 0.8 – 0.9 nm thick, due to the alkyl chain sticking out above the terrylene plane. The molecule is thus approximately an ellipsoid of 0.9 nm in diameter and 3.2 nm in length.

As for the samples presented in the previous chapters, a dilution series with various concentrations of each of the different dye molecules was made for each of the recipes to find the optimum concentration at which the single molecules are spatially separated. In most cases it was found that around 5  $\mu\text{L}$  of highly diluted terrylene diimide solutions (ca.  $10^{-8}$  mol  $\text{L}^{-1}$  in EtOH) in 1 mL of precursor solution resulted in a concentration of dyes in the final mesoporous films, that was well suited for single-molecule microscopy and single-molecule tracking.

## 7.2 Diffusion of Single Molecules in Brij 56 Templated Films

### 7.2.1 Analysis of the Host Structure

In order to obtain a clear image of the different pore systems that can be formed using Brij 56 as template, a series of different samples was synthesized on cleaned glass cover-slips.<sup>166</sup> As mentioned above in Section 2.2, it is a well known fact that variation of the surfactant/silica ratio in the precursor solution results in different pore topologies in the mesoporous film. A broad range of different recipes with surfactant/silica ratios from low (0.03) to high (0.715) were used for the synthesis and the resulting structure was analysed using XRD and TEM (in Table 7.1 only those recipes of samples that are discussed here further are summarized).

To determine the film thickness by ellipsometry, additional samples were synthesized on silicon wafers. The measurements showed that all the films were about 170–180 nm thick.

#### X-ray diffraction

Figure 7.3a shows the different 1D X-ray diffractogrammes that were measured in Bragg-Brentano-geometry ( $\theta - \theta$ ) on fresh samples a few hours after synthesis, i.e. immediately after the wide-field measurements, using the recipes **B2**, **B3**, and **B5** from Table 7.1. Whereas sample **B1** shows only a very weak and fairly broad reflexion at  $2\theta = 1.6^\circ$  (data not shown), sample **B2** exhibits a distinct peak at about the same position. Increasing the surfactant/silica ratio further (sample **B3**) results in a diffraction pattern with two peaks at  $2\theta = 1.45^\circ$  and  $2\theta = 1.60^\circ$ , respectively. Samples with a surfactant/silica ratio  $\geq 0.27$  show only one peak at about  $2\theta = 1.45^\circ$ . The two  $d$ -values calculated for the different structures according to the Bragg equation (Equation 2.3.1) are  $d=5.5$  nm ( $2\theta = 1.60^\circ$ ) and  $d=6.2$  nm ( $2\theta = 1.45^\circ$ ), respectively. The  $d$ -spacing of the phase formed at comparatively low surfactant concentrations, **B2**, is by a factor  $\sin 120^\circ$  smaller than that of the other structure, **B5**. This is indicative of the formation of a hexagonal and a lamellar phase. The pore-to-pore distance, which is identical to the unit cell parameter  $a$  for the hexagonal phase, can be calculated from the lattice plane distance  $d = (2/\sqrt{3})a$  to  $a=6.1$  nm. For a lamellar phase the layer-to-layer distance corresponds to the spacing of the lattice planes  $d=6.2$  nm.

Furthermore, ageing effects of the samples were studied using XRD. The measure-

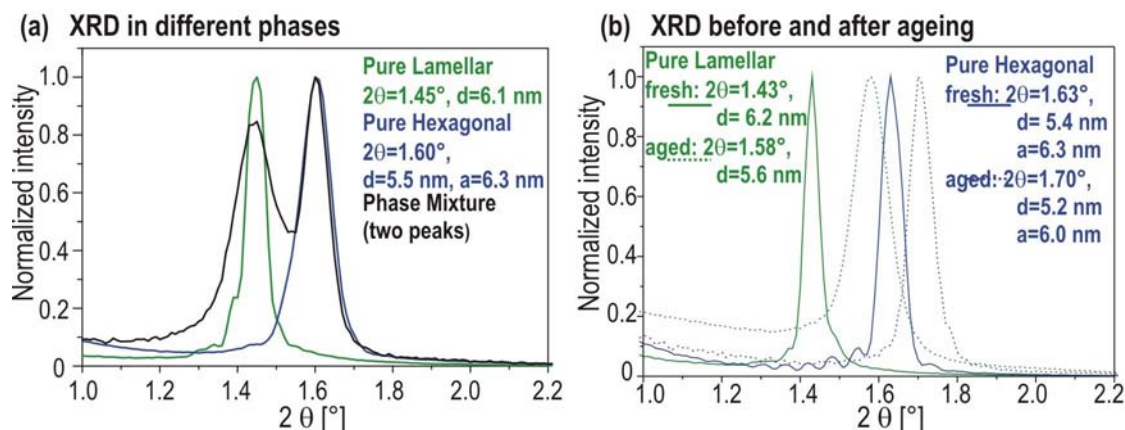


**Figure 7.3: 1D XRD of the different samples, before and after ageing.** (a) XRD of the freshly prepared samples. The left peak corresponds to the (100) reflex of the lamellar phase (**B5**, green), the right peak to the (100) hexagonal reflex (**B2**, blue). Sample **B3** (black line) shows two peaks at the same positions as **B5** and **B2**. Here a mixture of the two phases is present. (b) Shrinkage of the pore-to-pore distances for purely hexagonal (blue) and lamellar (green) phase, measured on a different sample as in (a). Solid lines: Freshly prepared samples. Dotted lines: after three weeks of aging.

ments presented above were obtained from samples a few hours up to one day after the synthesis. During this time no changes of the peak positions were observed. However, three weeks after the synthesis the peaks were shifted to higher  $2\theta$  values, which corresponds to a shrinkage of the pore-to-pore distances (see Figure 7.3b). The initial peaks at ( $2\theta = 1.43^\circ$ ) and ( $2\theta = 1.63^\circ$ ) were shifted towards ( $2\theta = 1.58^\circ$ ) and ( $2\theta = 1.70^\circ$ ), respectively. The latter values for  $2\theta$  correspond to a distance of lattice planes in the lamellar phase of  $d_{\text{lam aged}}=5.6$  nm, thus a decrease of 0.6 nm (10%). In the hexagonal phase, after ageing the lattice distance is  $d_{\text{hex aged}}=5.2$  nm and the pore-to-pore distance  $a_{\text{hex aged}}=6.0$  nm, which corresponds to a shrinkage of about 5%. The lamellar phase contracts thus about twice as much as the hexagonal phase.

This shrinkage is not necessarily caused by a shrinking of the pore diameter, and might instead result from condensation and thus contraction of the pore walls only. Diffusion measurements were done with the aged samples, and the trajectories and diffusion coefficients were similar to those of the fresh samples.

### Transmission electron microscopy

In addition, cross-sections and scratches from the different samples were analysed using TEM. Figure 7.4 shows the cross-sections that were obtained from the samples **B2**, **B3** and **B5**. On the left, the open hexagons are indicative for a hexagonal phase in sample **B2**, whereas the layered structure on the right can be assigned to a lamellar

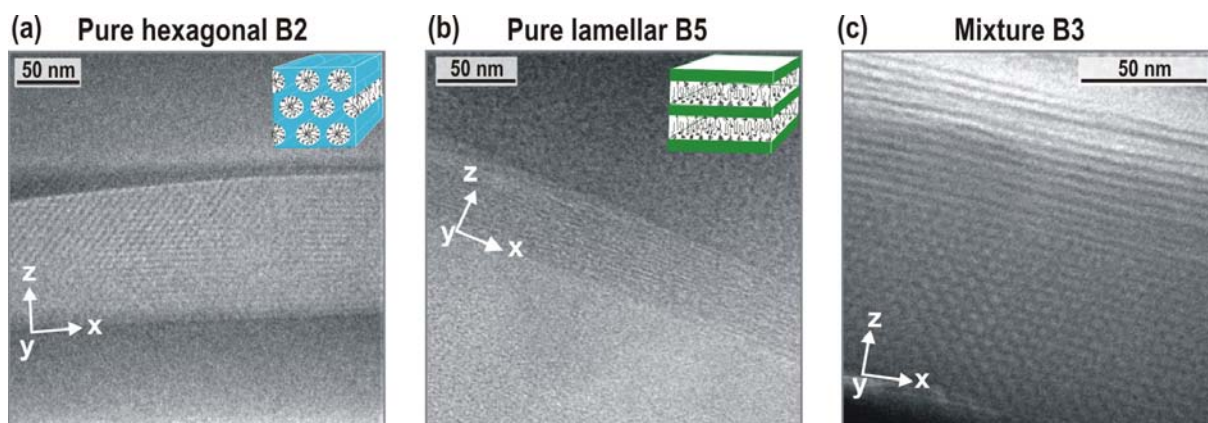


**Figure 7.4: Cross-section TEM of the different samples.** (a) The cross-section TEM clearly show the openings of the hexagonally arranged pores (**B2**) and (b) the stacking of the lamellae (**B5**). (c) For the phase mixture it displays the different mesophases stacked on top of each other. Different stacking order can be observed in other areas of this sample. In all images the glass substrate is visible at the bottom and the silica-air interface at the top, the z-arrows point along the optical axis of the widefield microscope (z-direction), x and y mark the observation plane. The insets in (a) and (b) sketch the topology of the pores as in Figure 2.2. Courtesy of B. Platschek, Bein group, LMU Munich.

phase in sample **B5**. The middle panel shows a cross-section TEM of sample **B3** which exhibits two peaks in the XRD, where the two different phases are visible in the same image, with the lamellar phase on top of the hexagonal channel system.

In addition to the cross-sections, small pieces of the samples with low surfactant/silica ratio were scratched of the substrate using a razor blade, deposited on on a copper grid for electron microscopy and analysed with TEM. In Figure 7.5a a scratch of a sample with recipe **B2** is shown. Here, the hexagonally arranged pores are seen from top. The

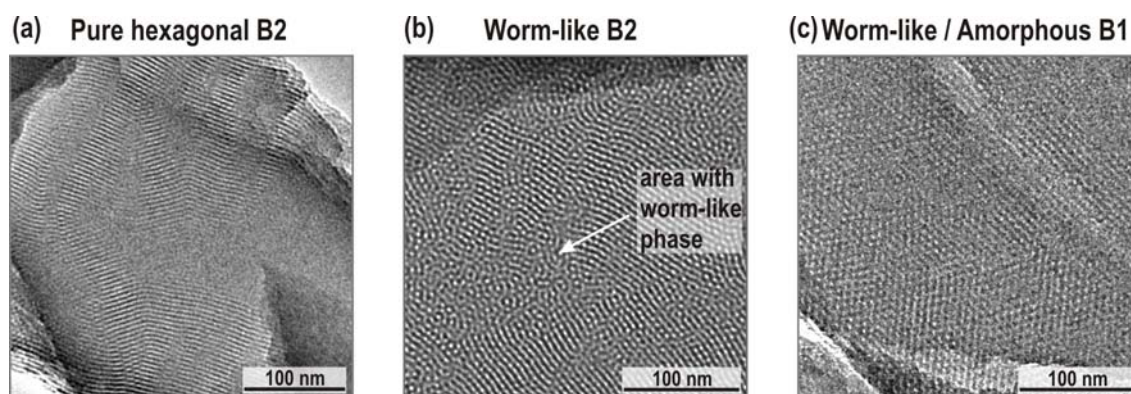


**Figure 7.5: Scratches of the different samples analysed with TEM.** (a) Hexagonal structure obtained with recipe **B2**. (b) Worm-like structure obtained with recipe **B2**. (c) Worm-like structure obtained with recipe **B1**, having a lower surfactant/silica ratio than **B2**. Courtesy of B. Platschek, Bein group, LMU Munich.

image in Figure 7.5b shows a scratch from a sample that was made using the same recipe (B2), but in this special case the structure is much less developed (worm-like). This phase can be understood as having regular  $d$ -spacing but rods too short to arrange in a hexagonal way with respect to the substrate surface. Thus, the structure results in spherical intensity maxima in reciprocal space and cannot be distinguished from a hexagonal phase by 1D XRD. No diffusion was visible in this sample, showing that the pores have no connections that would let the dye molecules move in this worm-like structure. Even though the recipe was the same as for the pure hexagonal samples, in this special case a less ordered sample was developed. In fact, the recipe for the pure hexagonal samples is at the limit towards recipes that result at all times in amorphous or worm-like structures. On the right, Figure 7.5c, a TEM image of a scratch from such a sample made with an even lower surfactant silica ratio (B1) is depicted. This sample exhibited only a very weak and broad peak at  $2\theta = 1.6^\circ$  in the XRD. The TEM also shows that the structure is not very well developed here. Note that scratching off pieces of samples with a lamellar phase will only result in images of amorphous silica, i.e. the lamellae seen from top. Therefore no such images were taken from samples with higher surfactant/silica ratio.

### Atomic force microscopy

The surface of three different samples was investigated using atomic force microscopy (AFM). The Surface Images were taken with a commercial AFM (Asylum Research

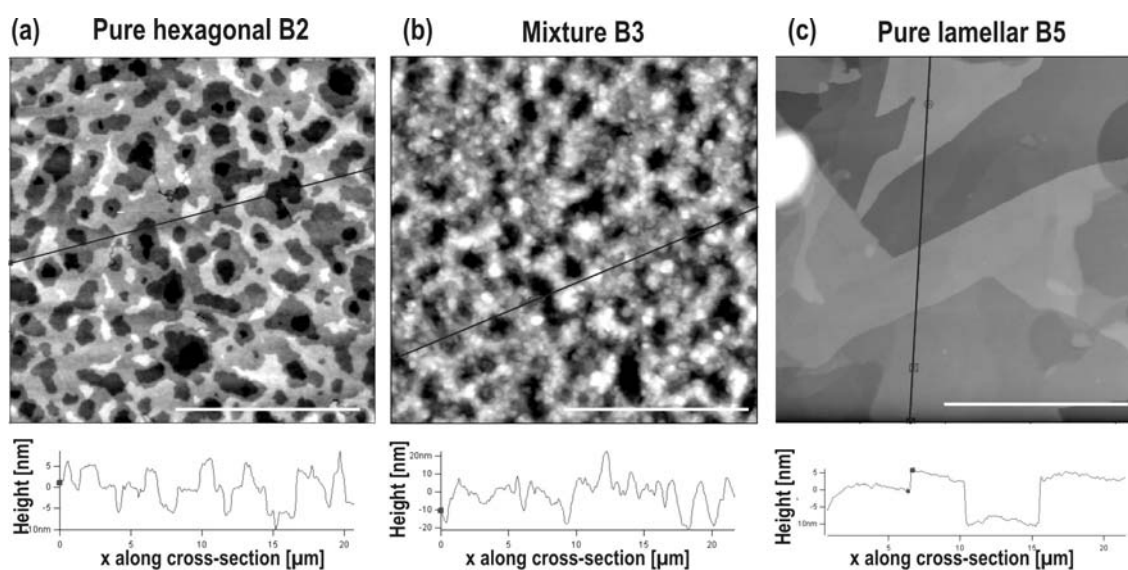


**Figure 7.6: AFM Surface scans of the different samples.** In all three images surface steps of about 6 nm are visible in the cross-section along the black line (bottom graphs). (a) B2, (b) B3, (c) B5. The scale bar in each of the images corresponds to 10  $\mu\text{m}$ .

MFP3D) in tapping mode. The Olympus AC160 SiN Cantilever was driven 5 % below its resonance frequency with a target amplitude of 1.2 V. In the measurements a set point of 0.85 V was used to scan each surface with a resolution of 512 px  $\times$  512 px and a scanning rate of 2 Hz per line. The AFM images (Figure 7.6) show the surface structure of samples from **B2**, **B3** and **B5**. In the pure hexagonal phase (**B2**) steps of about 6 nm height are visible. This corresponds to the pore-to-pore distance that was calculated from the XRD patterns (Figure 7.3). In this image four different levels can be distinguished. The lamellar phase on the right shows a more plate-like structure on the surface. Here, the height differences fit well to multiples of the d-spacing between the silica planes. The middle image, taken from the sample with the phase mixture, however, does not show very clear surface steps, but the surface roughness is in about the same range as on the surface of the two pure phases.

### 7.2.2 Diffusion Measurements and Single-Molecule Tracking

In the following it will be demonstrated that the different topologies in fact strongly influence the diffusion of the molecules inside the pores, and the diffusion in the samples **B2**, **B3** and **B5** will be discussed in detail. Here the measurements in the pure phases (**B2**, **B5**) are presented first and then a detailed discussion of the observations in the third sample (**B3**) that consists of a mixture of these two phases is given.

#### Pure phases - Samples B2 and B5

The fluorescence of the single molecules in as-synthesized films was collected using the wide-field setup described in Chapter 3.3. Like for the samples discussed in the previous section no further sample preparation was needed. Also here, the films are much thinner than the focal depth of the microscope objective used and the fluorescence images contain data from molecules at all heights inside and on the surface of the sample. Series of 1000 images were acquired with a temporal resolution of down to 50 ms per frame. Exemplary images from movies taken from the samples of **B2** and **B5** are depicted in Figure 7.7.

In the wide-field images of the hexagonal phase only gaussian-shaped diffraction patterns are observed (Figure 7.7a), whereas the single molecules in the lamellar phase appear as doughnuts (Figure 7.7b). Such doughnut diffraction patterns have previously been assigned to single molecules with their transition dipoles (here the long molecular axis of TDI) aligned along the optical axis of the microscope.<sup>124, 125, 126, 127, 128, 129</sup> In the present case this means that molecules in the lamellar phase are oriented perpendicular

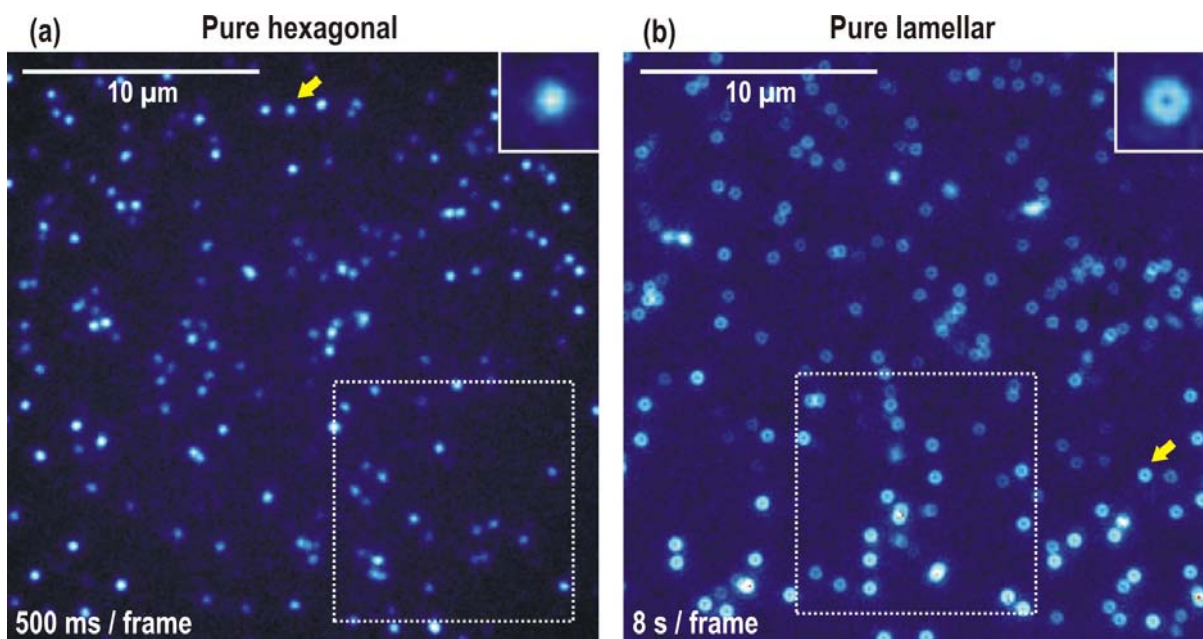


**Figure 7.7: Single-molecule images of the pure hexagonal and lamellar phases of the mesoporous hosts obtained by wide-field imaging.** The temporal resolution for the movie of the hexagonal phase was 500 ms per frame and for the lamellar phase 8 s per frame. The single-molecule images in the hexagonal phase show only gaussian-shaped diffraction patterns (a) whereas in the lamellar phase only doughnut-shaped patterns (b) are observed. The doughnuts are attributed to molecules oriented perpendicular to the substrate. Magnified images of the molecules indicated by an arrow are displayed in the top right corner of each panel. Trajectories in the regions marked with the square boxes are depicted in Figure 7.8

to the glass substrate and thus normal to the silica planes of the lamellar phase.

The exposure times for the movies in the two different phases differ by a factor of 16, as the molecules in the hexagonal phase diffuse much faster than in the lamellar phase. The strong differences in the diffusion behaviour in the two phases are illustrated in more detail in Figure 7.8a-d and below in Figure 7.13. The positions of the molecules were obtained by fitting theoretical diffraction patterns according to Equation 3.4.1 or 3.4.4 to the spots with a positioning accuracy of down to  $\pm 5$  nm.<sup>95,120</sup> Single-molecule trajectories were then built up by tracking spots from frame to frame.

In Figure 7.8 the measurements in the pure hexagonal phase on the left are set in contrast to those in the lamellar phase on the right. Molecules in the hexagonal phase travel in a highly non-random manner over distances of several microns (blue trajectories in Figure 7.8a) during the acquisition time of the movie (500 s). In contrast, the doughnut patterns in the lamellar phase show regular diffusion on a much slower timescale, and cover areas smaller than  $1 \mu\text{m}$  during the same time interval (63 frames with 8 s exposure, green trajectories in Figure 7.8b). A detailed picture of an individual trajectory in the hexagonal phase is shown in Figure 7.8c. The molecule travels first



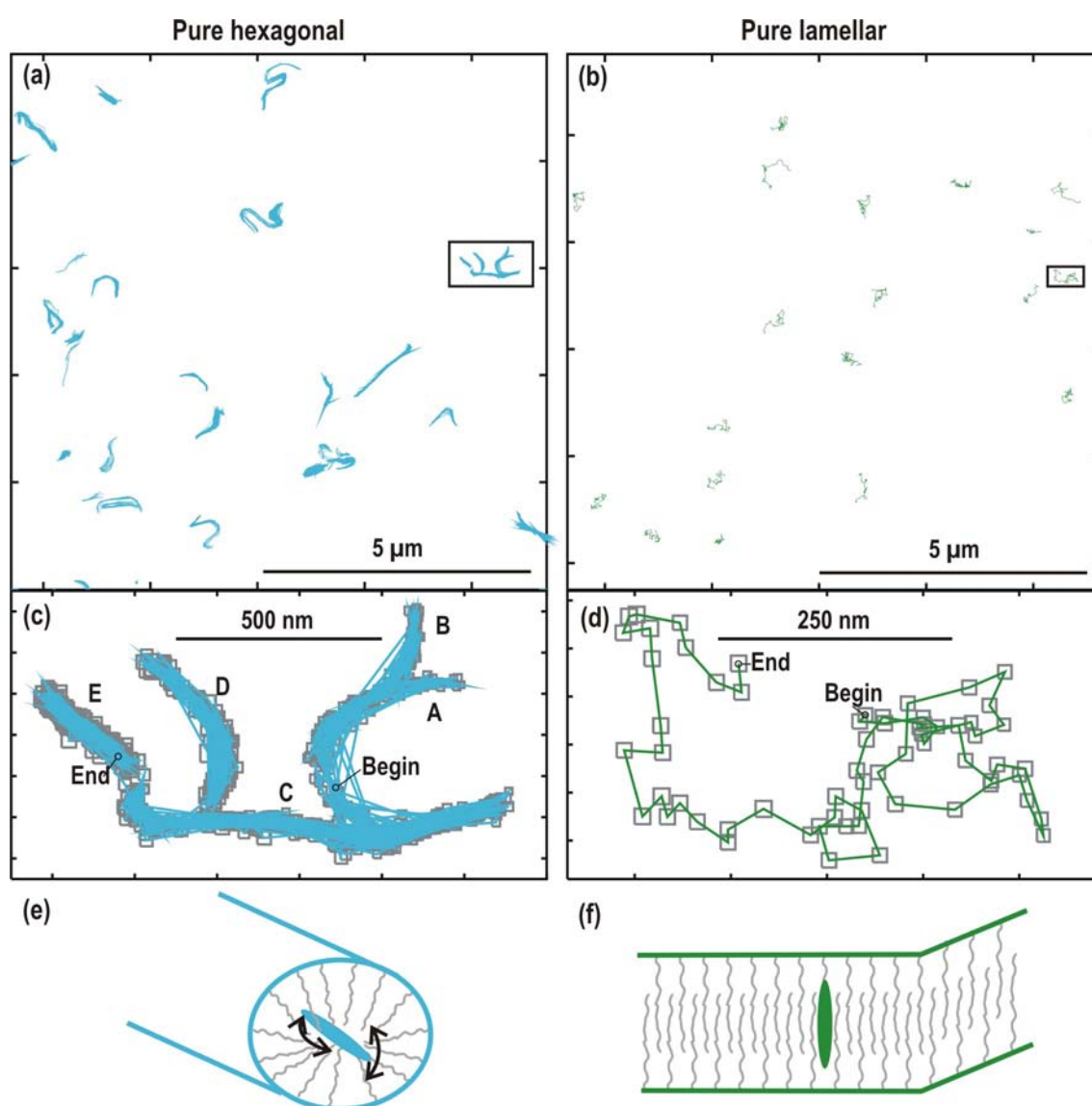


**Figure 7.8: Single particle trajectories in the pure hexagonal and pure lamellar phase.** The temporal resolution for the movie of the hexagonal phase was 500 ms per frame and for the lamellar phase 8 s per frame. The scale increases from top to bottom as we zoom into the pictures, so that we resolve more and more details of the structure. The rectangular boxes indicate the enlarged regions. (a),(b) Trajectories of the diffusion obtained by single-molecule tracking in the regions indicated by the white square in Figure 7.7a, b. Molecules showing structured diffusion in the hexagonal phase are plotted in blue (a), molecules with doughnut-shaped patterns in the lamellar phase are presented in green (b). Scale bar 5  $\mu\text{m}$ . (c),(d) Sample trajectories in the hexagonal and the lamellar phase (highlighted in the rectangular boxes in (a),(b)). The trajectory of the fast diffusing molecule in the hexagonal phase shows a pronounced structure which reflects the structure of the hexagonal channels, whereas the trajectory of a doughnut-shaped pattern in the pure lamellar phase shows random walk behaviour. The grey boxes correspond to one standard deviation of the fit to the diffraction spot. (e),(f) Schematic view of the arrangement of the guest molecules inside the hexagonal and lamellar topologies of mesoporous silica.

along the C-shaped structure on the right (**A**) and after 65 s enters side-arm **B**. Then, 100 s later, it passes into the linear structure at the bottom (**C**). After another 144 s it enters region **D** and moves around there for 69 s before coming back to region **C**. At the end it passes into region **E**, where it moves back and forth for 109 s until the end of the movie. Note that the molecule apparently probes the domain boundaries in this process, by repeatedly 'bouncing' back from dead ends of the channel regions. This is one of the many striking examples which show how a single molecule explores the structure of the host in specific way, showing the accessibility and connectivity of the channels.

The successive measurements of single-molecule trajectories and TEM images of the same region in the sample in the last chapter provided evidence that the single-molecule trajectories directly map the alignment of the channels and the domain structure. The single particle trajectories presented here underline this, since (i) TEM and XRD data show that the pores are horizontal in the focal plane; (ii) the widths of regions **A-E** exceed both the tracking error (small grey boxes around trajectory points) and the pore spacing, implying that part of the time the molecule is in different but aligned pores; (iii) surface features seen in AFM (Figure 7.6) images do not resemble in any way the structures seen by particle tracking (this excludes the movement of the molecules on distinct surface structures). Therefore the trajectories do indeed map out domains in the heart of the material. Furthermore, only the fast and randomly moving molecules were removed by washing the surface with water, demonstrates that the structured trajectories show molecules diffusing inside the hexagonal pores of the materials. In addition, the observation of the molecular motion shows the accessibility of the channels and connectivity of the domains in an unprecedented way. There is no other method that can provide this kind of structural and dynamical information in such detail.

In contrast to the highly structured motion of the molecules in the tubular surfactant micelles of the hexagonal phase, Figure 7.8d depicts an example of a molecule in the lamellar phase. It diffuses randomly in two dimensions, as would be expected for molecules trapped in the surfactant layer between the silica planes.

In addition to the translational diffusion, polarization modulation dependent confocal microscopy can provide information about the orientational dynamics of the TDI molecules inside the surfactant-filled pore systems, method described in Ref.<sup>94</sup> Details about the setup and the method will also be given in the thesis of Christophe Jung (Bräuchle group, LMU Munich). The wide-field measurements indicate already that the TDI molecules in the lamellar phase are oriented perpendicular to the substrate, showing up as doughnut patterns. Hence, a mesoporous film of pure lamellar phase was observed from the side to obtain a better excitation of the fluorophores. Details of the setup can be seen in Figure 7.9a.

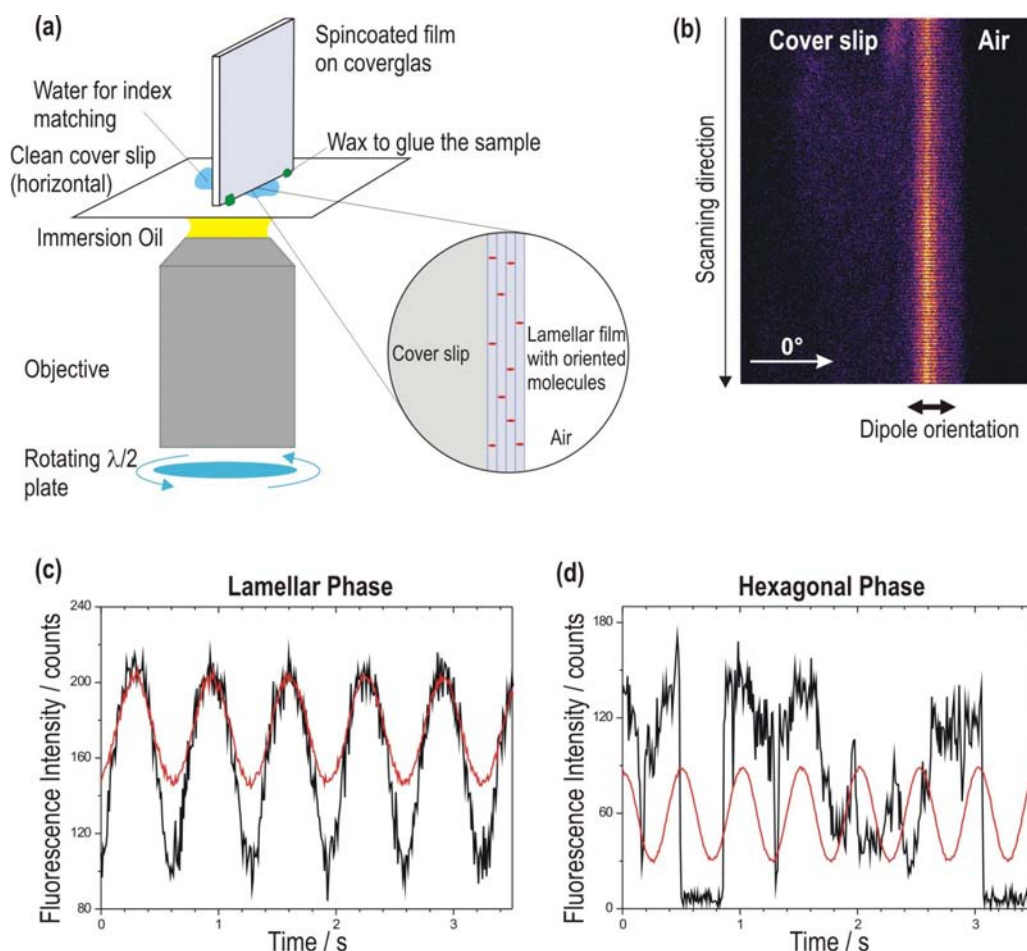


**Figure 7.9: Measurements of the orientation of the molecules in the two phases.** (a) Sketch of the alignment of the lamellar film perpendicular to the focal plane. (b) Confocal image of the ensemble fluorescence in the lamellar phase aligned like in a. The image was scanned line by line with rotation of the  $\lambda/2$  plate. (c) Fluorescence intensity trace in the lamellar phase (black), transmission reference curve in red. (d) Fluorescence intensity trace of a single molecule in the hexagonal phase and transmission reference. The fluorescence signal is not modulated according to the transmission reference, thus the molecule is rotating constantly.

The TDI molecules were embedded in the mesoporous film at ensemble concentration to provide a sufficient fluorescence signal in this geometry, and the excitation polarization was rotated continuously. Figure 7.9b shows a fluorescence image of the mesoporous film which appears as a thin striped vertical line. This reveals that the dye molecules are not randomly oriented within the lamellar phase, but all aligned in the same direction. To determine the average direction of the alignment, the confocal volume was placed some micrometres inside the mesoporous film and a fluorescence intensity trace was recorded (Figure 7.9c). The red line shows the modulation of the transmission intensity of the excitation light which is detected behind a fixed polarizer and acts as a reference for the determination of the angles (the angle of a horizontal line in Figure 7.9b is set to  $0^\circ$ ). A cosine-square modulation of the fluorescence intensity (black line) is observed. The extracted angle is  $2^\circ \pm 3^\circ$ , which is the mean angle of the

distribution of the orientations of the transition dipole moments of the dye molecules. This corresponds exactly to the direction perpendicular to the mesoporous film and thus perpendicular to the silica planes of the lamellar phase.

The orientation behaviour of TDI molecules in the hexagonal phase (recipe **B2**) was investigated with the mesoporous film placed in the focal plane of the microscope. In the wide-field movies the molecules appear as gaussian spots, and therefore do not keep a constant orientation along the  $z$ -axis of the microscope. The measurements with confocal setup were also done at ultra low concentration to gain information about the orientation dynamics of the individual emitters which are otherwise lost in ensemble averaging. First, a fluorescence image is recorded to visualize the single-molecule emission patterns. Second, the confocal volume was placed directly on the position of the molecule and the excitation polarization was rotated continuously similarly to the measurements above. Figure 7.9d shows a typical polarization fluorescence intensity trace for a single TDI molecule in the hexagonal phase. The blinking event between 0.5 s and 0.8 s, and the photobleaching step at 3.1 s are typical signatures for a single molecule. In contrast to the graph in Figure 7.9c, no periodic modulation of the fluorescence intensity (black line) is observed according to the rotation of the polarization in the excitation beam (ca. 500 ms). Moreover, strong fluctuations of the fluorescence intensity can be observed. These are most probably due to the diffusion of the molecule in and out of the focus of the confocal spot. All 26 investigated molecules exhibit a similar orientational behaviour. Thus the molecules do not keep a preferential orientation, but constantly reorient during their diffusion in the template filled pores of the hexagonal phase.

These measurements show that molecules in the lamellar phase maintain a constant orientation during diffusion, in agreement with the observed doughnut patterns, whereas molecules in the hexagonal phase constantly reorient on a timescale below 500 ms. In the lamellar phase, the inter-plane distance is estimated to be 4 – 5 nm. The pore diameter in the hexagonal phase is in the same range. For both topologies the dye (ca. 3.2 nm length) should have enough room to rotate freely. Thus, geometric hindrance from the pore walls cannot explain the dramatic differences of the diffusional behaviour of the TDI molecules between the two phases, i.e. slow diffusion with a preferential orientation of the molecules in the lamellar phase and fast diffusion with constant reorientations in the hexagonal phase. We interpret these strong differences in terms of interactions between the hydrophobic dye molecules and the amphiphilic template molecules. The very ordered state of the molecules in the lamellar phase may be explained by strong interactions of the dye molecule with the template molecules (cf. Figure 7.8f). Hence, the diffusion is hindered and therefore slow. On the contrary the continuous reorientations in the hexagonal phase indicate much weaker interac-

tions with the template than in the lamellar phase, as sketched in Figure 7.8e. These differences in the interaction strength may also explain the much faster diffusion in the hexagonal phase compared to the lamellar phase.

### Phase Mixture

Similar observations as described above for the two pure phases are made in the third sample (**B3**), consisting of a mixture of the two phases. Figure 7.10a shows the first image of a movie, collected with a time resolution of 500 ms per frame in a  $28.4 \mu\text{m} \times 25.4 \mu\text{m}$  area of this sample.

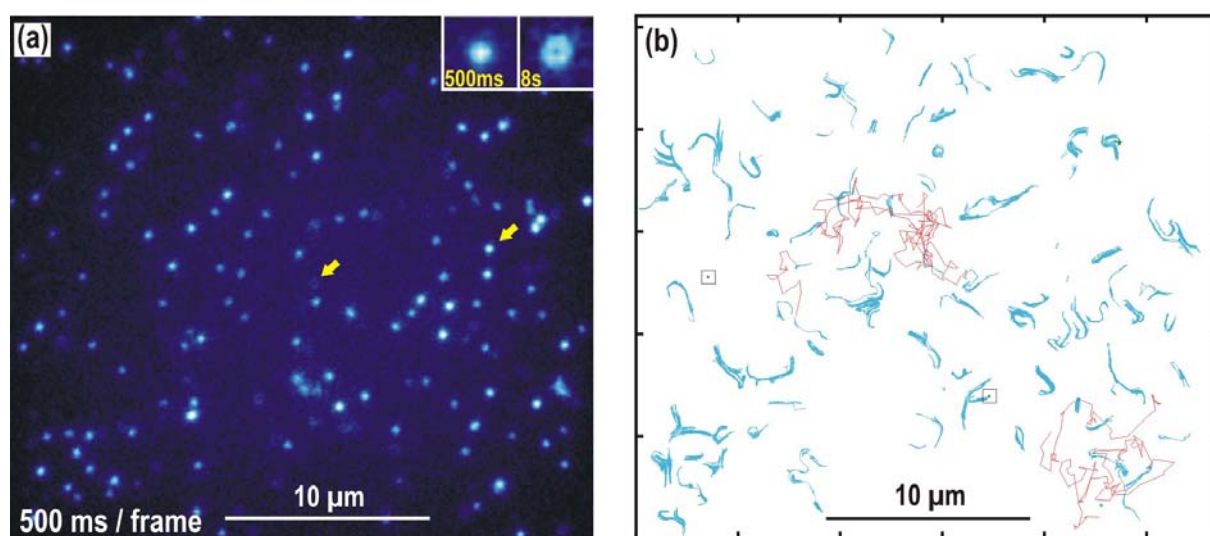


**Figure 7.10: Single-molecule microscopy and tracking in the phase mixture.** Temporal resolution: 500 ms per frame. (a) A single-molecule image of the phase mixture contains both, gaussian- and doughnut-shaped diffraction patterns. Magnified images of the molecules indicated by the arrows are shown in the upper right corner. The doughnut pattern was averaged over 16 images, so that it is presented with the same temporal resolution as in Figure 7.7b. (b) Map of all the trajectories in the wide-field movie obtained by single-molecule tracking. Structured trajectories are shown in blue, fast unstructured diffusion in red and immobile molecules in green highlighted in squared boxes.

Here, gaussian-shaped and doughnut patterns coexist within the same region. The inset depicts magnified images of the two molecules indicated by the arrows. As the doughnuts are barely visible on this short timescale, an average over 8 s, i.e. 16 frames of 500 ms each, is presented here in order to make it comparable to the exposure time of Figure 7.8b, which shows the pure lamellar phase. Single-molecule tracking from this movie results in the 117 trajectories in Figure 7.10b. Overall, we can distinguish four populations of molecules based on their different diffraction patterns and diffusive behaviour in this movie. The first type comprises molecules with gaussian-shaped spots, which are diffusing along distinct structures over a large range of one to five microns

(109 blue trajectories in Figure 7.10b). The second type has characteristic doughnut-shaped diffraction patterns, see Figure 7.10a and inset. Since their patterns are barely visible at 500 ms exposure, no tracking of such doughnuts was done in this movie. On a timescale of minutes to hours, however, these molecules show unstructured diffusion in two dimensions. Another, much smaller population consists of molecules that diffuse much faster, without showing any particular structure in their trajectories. Five examples are shown in red. An additional important observation is that multiple changes between these three types of mobility were observed for many of the molecules. Finally, we observed very few immobile molecules (to within the positioning accuracy), of which two examples are marked in square boxes in Figure 7.10b.

In accordance with the observations in the pure phases from Figure 7.8 the structured trajectories of population 1 are assigned to molecules in regions with hexagonal arrangement of pores, and the molecules with doughnut-shaped patterns of population 2 that are diffusing very slowly and randomly, to other regions with lamellar structure, present simultaneously within this sample.

The movement of the two remaining populations is not correlated with the pore topologies in the sample. In fact, the fast molecules of population 3 (red), with unstructured trajectories, could be removed by washing the surface of the sample with water, clearly indicating that the molecules were on the surface of the film. Further details about the external surface structure are provided by the AFM data shown in Figure 7.6. The immobile molecules of the small population 4 may be either captured in very small cavities inside the material or strongly adsorbed on the surface of the pore walls.

The different types of diffusing molecules are observed within the same area of the sample, implying overlaid hexagonal and lamellar phases as seen in the cross-section TEM in Figure 7.4b. The diffusion behaviour in this phase mixture fits remarkably well with that in the pure phases described above. Interestingly, some molecules can be seen migrating between the phases. This observation demonstrates clearly that the two phases are actually interconnected. A specific example is shown in Figure 7.11a. The molecule first appears with a gaussian diffraction pattern and diffuses for 5 s (10 frames) until it produces a doughnut pattern for a short period of 3.5 s. For the following 105 s it diffuses in a highly structured manner (gaussian spot). Then the spot suddenly returns to doughnut shape again for 197 s. During this time it hardly moves, due to the much lower diffusion coefficient in the lamellar phase (Figure 7.13). Structured diffusion with a gaussian spot resumes in frame 622 and lasts for 66 s. After spending another 5.5 s as a doughnut pattern, i.e. in the lamellar phase, the molecule finally diffuses back and forth inside a system of parallel channels until the end of the movie. Again, as in the pure hexagonal phase, the shape of the trajectory explored

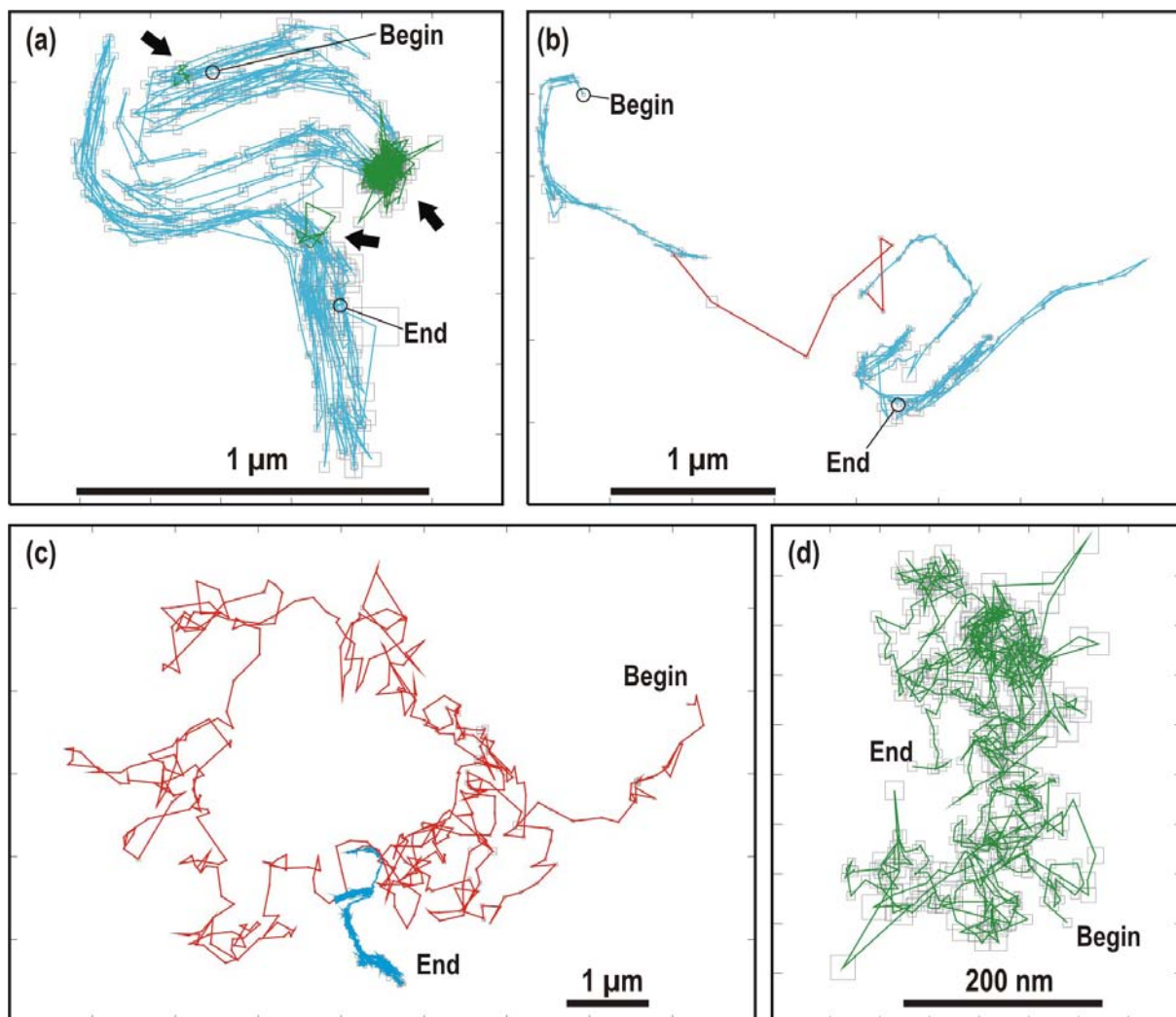


**Figure 7.11: Individual Trajectories in the phase mixture.** (a) An individual molecule undergoing several changes between the hexagonal (blue parts) and the lamellar phase (green parts, indicated by the arrows). (b) A molecule showing structured motion in the beginning for 42.5 s (blue), reaches the surface (red) and comes back into the hexagonal phase after 2.5 s. (c) The molecule diffuses on the surface in a two dimensional random walk for 48.6 s (red) and then it enters the hexagonal phase (blue) where it stays for the last 256.4 s of the movie. (d) The trajectory of a doughnut-shaped pattern that is diffusing very slowly and following a random walk in two dimensions. Temporal resolution for a,b: 500 ms per frame. c: 100 ms per frame, d: 16 s per frame.

by the gaussian pattern clearly reflects the underlying pore structure of the hexagonal phase. This molecule changed three times from a gaussian spot to a doughnut and back with different residence times in each phase. Such switching phenomena clearly show that the two phases are actually connected, probably via structural defects at the phase boundaries. Interestingly, we also observed other cases where the molecule switches several times from a gaussian to a doughnut pattern at exactly the same position, showing that molecules sometimes pass repeatedly through the same defect region between phases.

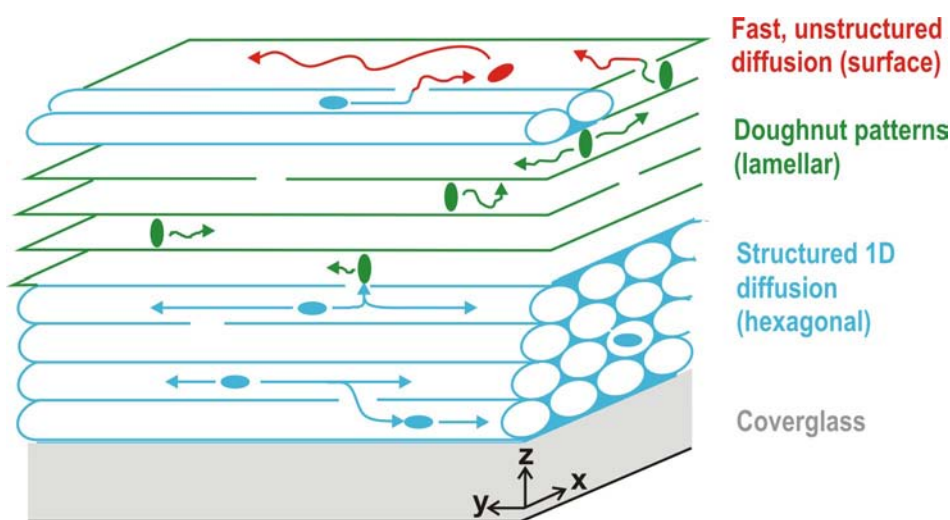


**Figure 7.12: Sketch of the diverse diffusion modes observed in the wide-field movies of the phase mixture.** Molecules diffusing randomly in the lamellar phase are oriented perpendicular to the surface (doughnuts in the wide-field movies). Structured diffusion over long distances takes place in the hexagonal phase. Molecules on the surface show fast, unstructured diffusion. Transitions between the different diffusion modes are explained by connections between the pore topologies.

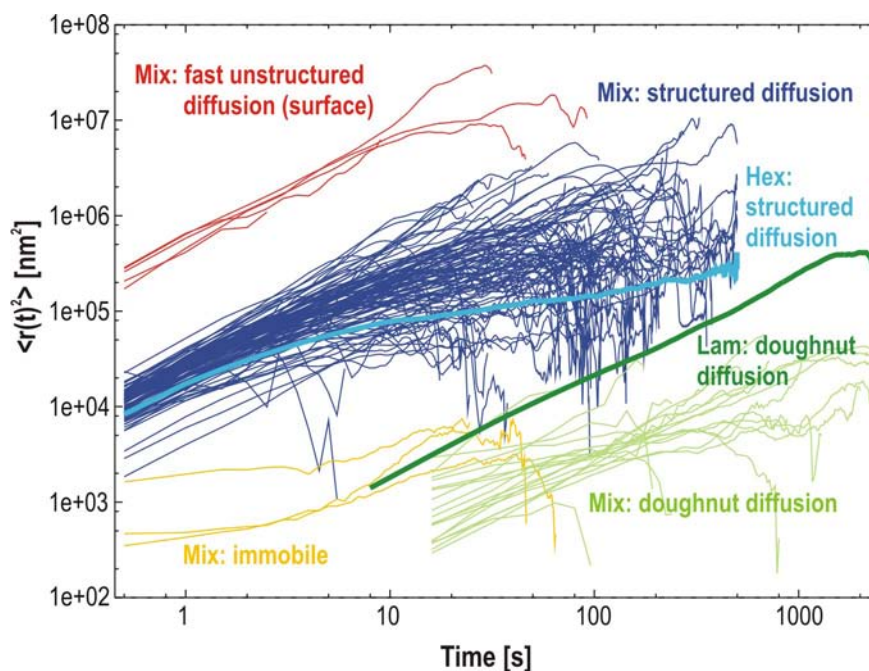
Besides migrating between phases, some molecules actually exit the film, thus showing up at the top surface. Figure 7.11b shows an example from which this is deduced. Here the molecule diffuses first in the hexagonal phase for 42 s, than exits on to the surface, where it moves very fast and randomly, and comes back into the hexagonal phase after 2.5 s, about 1  $\mu\text{m}$  away from where it appeared at the surface. A similar example that was measured with a higher temporal resolution, showing a longer period of random diffusion on the surface is presented in Figure 7.11c. A detailed trace of a doughnut in the phase mixture is provided in Figure 7.11f.

Based upon the above discussion, we can correlate the different diffusion behaviour with the structural information in Section 7.2.1 and the observations in the pure phases in Figure 7.8. A schematic general picture of the different phases present in the film and the migration within as well as between the phases is shown in Figure 7.12.



### 7.2.3 Mean-Square Displacement Analysis

The different diffusive behaviour can also be visualized by plotting the mean-square displacements  $\langle r(t)^2 \rangle$  of the individual molecules as a function of time  $t$  (Figure 7.13).<sup>96</sup> Assuming regular Brownian motion according to the Einstein-Smoluchowski relation,  $\langle r(t)^2 \rangle = 2\mathcal{N}Dt$ ,<sup>135</sup> with  $\mathcal{N} = 1, 2$ , or  $3$  according to one-, two or three-dimensional diffusion, respectively, the diffusion coefficient can be extracted from the vertical intercepts of double logarithmic plots of  $\langle r(t)^2 \rangle$  against  $t$ .



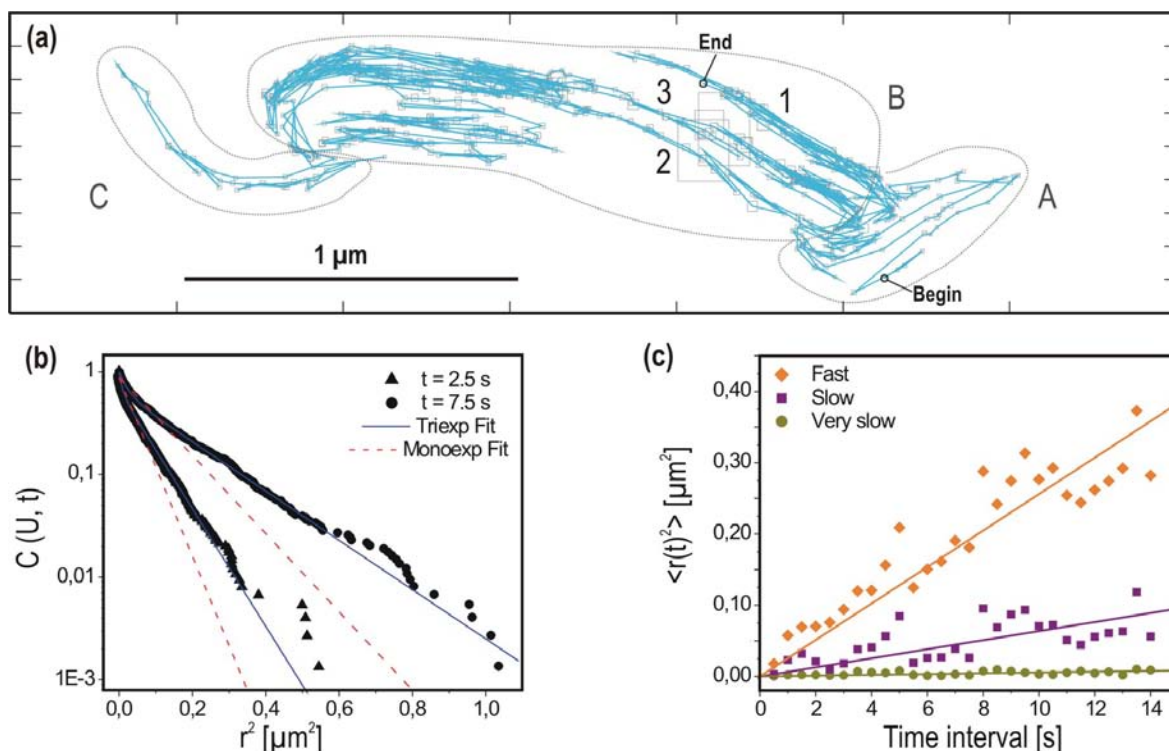
**Figure 7.13: Mean-square displacement as a function of time.** The individual molecules in the different mesoporous samples and also within the same sample can be separated according to their different diffusion coefficients. For the sake of clarity, individual trajectories are plotted only for the phase mixture, the thick lines represent the average values for the pure hexagonal (pale blue) and pure lamellar (dark green) phases. Molecules with structured trajectories in the phase mixture, population 1, are plotted dark blue, the diffusion of the doughnuts, population 2 in the phase mixture, in light green and fast and unstructured diffusion of population 3 in the phase mixture in red. The horizontal orange curves correspond to immobile molecules (population 4 in the phase mixture).

Figure 7.13 shows that (i) the molecules in the different populations in fact have distinct mobilities (bundles of roughly straight lines with a slope close to unity) and (ii) a certain spread exists for the diffusion coefficients (vertical intercepts within a bundle). This spread might be explained by the width of the peaks in the XRD patterns, indicating a certain distribution of pore sizes present in the individual phases. Such a spread of values is typical and unique for single-molecule experiments, which show the distribution of a given parameter rather than only the mean value. Such experiments have the power to resolve the heterogeneities within a sample. The diffusion coeffi-

coefficients differ by approximately two orders of magnitude both between populations 1 (hexagonal channels) and 2 (lamellar) and between populations 1 and 3 (surface). Furthermore, the dark blue lines for the molecules of population 1 can be overlaid with the thick light blue line, which corresponds to the average value for the molecules in the pure hexagonal phase ( $D_{\text{hex}} = 5.0 \times 10^{-3} \mu\text{m}^2 \text{s}^{-1}$ , fitted with  $\mathcal{N} = 1$ ). An interesting observation for the hexagonal phase is that the linear plots for short lags bend towards a horizontal asymptote for large time intervals. This is characteristic for diffusion in confined regions, which in our case are the domains explored by the molecules. The statistical information given here agrees well with the direct observation of dead ends in the individual trajectories of molecules in the pure hexagonal phase (Figure 7.8c). The domain size, extracted from the horizontal asymptote, ranges from several hundred nanometres up to one micrometre. For the dark blue lines the asymptotes are reached at higher values of  $r^2$ , indicating larger domains. This is in agreement with the direct observation of the trajectories in the mixture compared to the pure hexagonal phase in Figures 7.8a and 7.10b, respectively. The plots for the doughnut-shaped patterns in the phase mixture are in about the same range as the molecules in the lamellar phase, indicated by the thick dark green line ( $D_{\text{lam}} = 5.3 \times 10^{-5} \mu\text{m}^2 \text{s}^{-1}$ , with  $\mathcal{N} = 2$ ). For the sake of clarity only the mean values are plotted for the pure phases. The diffusivities given above thus confirm our previous assignment of the populations to the different phases. Possible explanations for the small differences of the diffusion coefficients of the doughnuts in the phase mixture and the pure lamellar phase include a slightly different amount of template in a given volume element, or a different degree of compression normal to the film surface. Especially for samples with a phase mixture, the distribution of template into the two phases can slightly differ from that in the pure phases.

The diffusion coefficients vary not only between different phases or trajectories of individual molecules within one phase, but can also change within the same trajectory of an individual molecule. Figures 7.14 and 7.15 show such cases for two individual molecules of population 1 in the phase mixture. The molecule in Figure 7.14a moves in a distinct structure and explores at least three different domains, indicated as A, B and C. The channels in A are oriented perpendicular to the channels in B, and a kink separates domains B and C. To give an impression, the channel systems 1, 2 and 3 in domain B are separated by 50 – 100 nm and each of them probably consists of several parallel channels. Similar to the molecule in the pure hexagonal phase in Figure 7.8c, this trajectory gives a lucid picture not only of the channel structure but also of the connectivity and accessibility of channels between different domains.

For the molecule moving in this structure, a detailed analysis of the diffusion behaviour was done by plotting the cumulative probability of the squared displacements



**Figure 7.14: Diffusivity changes for one individual molecule in the hexagonal part of the phase mixture B3.** (a) Trajectory of a molecule diffusing in a structured manner in parallel channel systems (1, 2, 3) and in different domains (A, B, C). (b) Plot of cumulative probability of  $r(t)^2$  for two sample time intervals ( $t=2.5$  s,  $7.5$  s). Mono-exponential fits (red dashed line) and tri-exponential fits (blue line) are given. (c) Plot of the mean-square displacement  $\langle r(t)^2 \rangle$  against the time intervals. Fits according to  $\langle r(t)^2 \rangle = 2Dt$  for the three different characteristic  $\langle r(t)^2 \rangle$  distributions.

for different time lags.<sup>93,120</sup> Regular diffusion should result in a mono-exponential decay, giving a characteristic value for the mean-square displacement  $\langle r(t)^2 \rangle$  for each lag  $t$  (Equation 4.1.27). Figure 7.14b displays these distributions for two sample time intervals ( $t = 2.5$  s and  $t = 7.5$  s). Here the data cannot be fitted with a mono-exponential decay function (red dashed lines in Figure 7.14b). Tri-exponential decay functions according to Equation 4.2.4 were found to describe the data best (blue solid lines), giving three characteristic  $r(t)^2$  values for each lag  $t$ . These values are plotted against time in Figure 7.14c. The three different sets of  $r(t)^2$  values were fitted with the Einstein-Smoluchowski equation for random diffusion in one dimension, giving values of  $D = 1.3 \times 10^{-2} \mu\text{m}^2 \text{s}^{-1}$ ,  $3.2 \times 10^{-3} \mu\text{m}^2 \text{s}^{-1}$ , and  $2.8 \times 10^{-4} \mu\text{m}^2 \text{s}^{-1}$ . These large differences imply that the molecule is diffusing in at least three kinds of environment. However, it can be shown that the three diffusion regimes are not spatially separated. The step sizes corresponding to these three diffusion modes are distributed over all parts of the trajectory, not segregated in one or other of the domains A, B or C: the mobility of the molecule does not differ significantly from one domain to the other. Instead, due to structural heterogeneities, the environment within one channel system changes

strongly along the pathway of the molecule. These heterogeneities are revealed by the molecule continuously changing its mode of motion between at least three diffusion coefficients. Therefore its diffusion cannot be described as a simple Brownian motion. An interpretation of these results could actually be a range of diffusion coefficients due to variations of local environment.

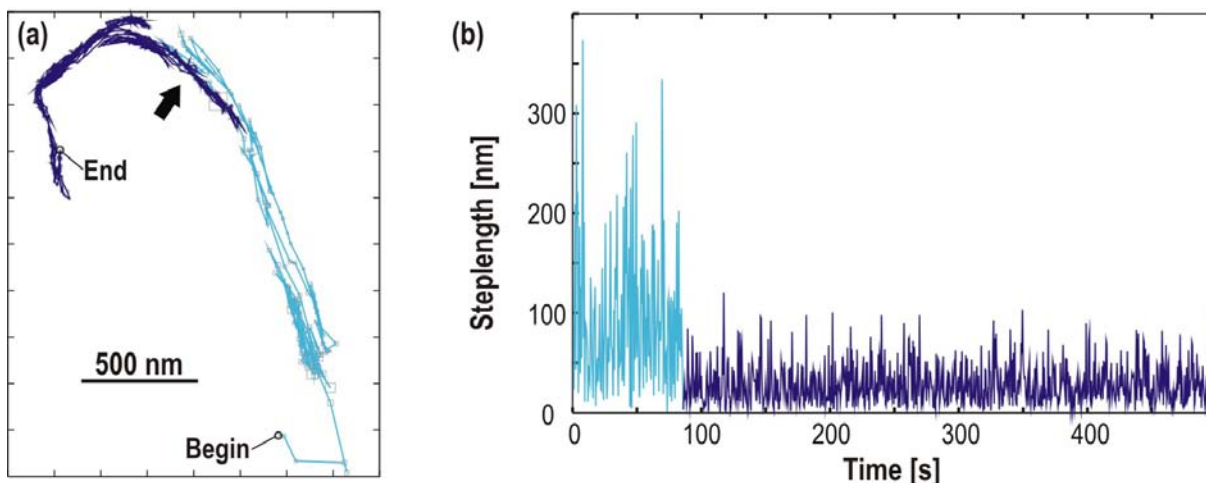


**Figure 7.15: Trajectory of a molecule in the hexagonal phase of the phase mixture B3 showing an instantaneous change of the diffusion coefficient.** (a) First, the molecule diffuses fast (pale blue), until it becomes instantaneously much brighter and also five times slower (dark blue), after 85 s (see arrow). (b) Plot of the absolute value of the step length against time for the molecule clearly showing the change in the diffusion behaviour.

Figure 7.15a shows another molecule, for which different diffusion regimes are spatially separated. It first diffuses with a diffusion coefficient within the same order of magnitude as all other molecules in the hexagonal phase (pale blue part of the trajectory), but after 85 s it becomes much brighter and diffuses more slowly, with a five times smaller effective diffusion coefficient (dark blue) for the rest of the time. This instantaneous change can be visualized by plotting the step length as absolute value against time as depicted in Figure 7.15b. This example clearly demonstrates that there are also cases where changes in the diffusivity can be correlated with spatial areas in the trajectory. Here the molecule obviously explores two different types of channels which provide different environments.

### 7.2.4 Distribution of Angles between Successive Steps

In order to gain additional information about the diffusion within the different materials, the angles between successive steps were investigated. Figure 7.16 depicts the histograms of angles between successive steps and the stacked column chart showing the ratio of forward, intermediate and backward steps for the molecules in the pure hexagonal phase.

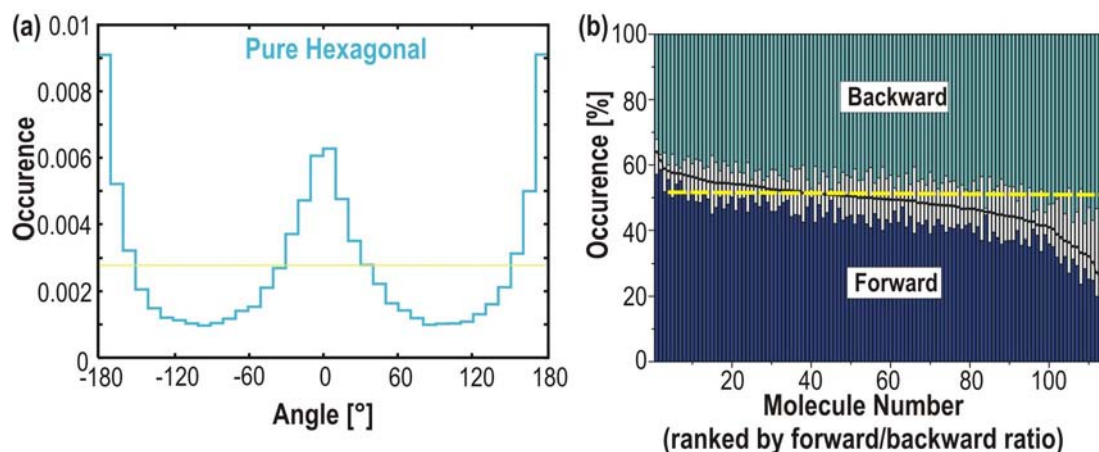


**Figure 7.16: Pure hexagonal phase B2: Angles between successive steps.** (a) Histogram: The maxima at  $\pm 180^\circ$  and  $0^\circ$  reflect the highly structured diffusion along the channels. (b) Percentage of forward, intermediate and backward steps: The black line indicates the ratio of forward/backward steps. Some molecules show an excess of forward steps, some molecules an excess of backward steps, but on average no excess of steps forward or backward is visible. The yellow line is a guide for the eye at a value of 50%.

The histogram of the left, showing the distribution of all angles between successive steps for 115 molecules tracked from the film shown above in Figure 7.7a, reflects the highly structured diffusion of the molecules along the one-dimensional channels. The molecules diffuse back and forth inside the porous system. On the right side the distribution of forward, backward and intermediate steps is shown for all 115 molecules individually, ranked by the ratio of forward/backward steps (black line). Some molecules show an excess of steps forward, others an excess of steps backward. On average no bias towards forward or backward steps is visible. A similar picture is obtained from the analogical plots of the molecules in the hexagonal phase of the phase mixture.

In contrast, the distribution of angles between successive steps in the pure lamellar phase gives a completely different picture. The histogram on the left in Figure 7.17 shows a relatively flat distribution compared with the same histogram of the hexagonal phase. However, the distribution is not completely flat as it would be expected for a purely random walk in between the planes of the lamellar phase. It shows a broad

peak around  $0^\circ$  and slight minima around  $\pm 180^\circ$ . In order to get a clearer picture, the stacked histogram of the percentage of forward, intermediate and backward steps has to be examined. In this graph the excess of forward steps is even more striking. For many molecules the amount of steps in the different directions can be sorted as follows:  $\# \text{ forward} > \# \text{ intermediate} > \# \text{ backward}$ . The structural analysis of the lamellar host by XRD or TEM provides no indications for such an irregular distribution. The arrangement of template between the planes is not known and cannot be measured, but most probably, this excess of steps forward has to be attributed to interactions of the dye molecules with the template molecules between the silica planes.

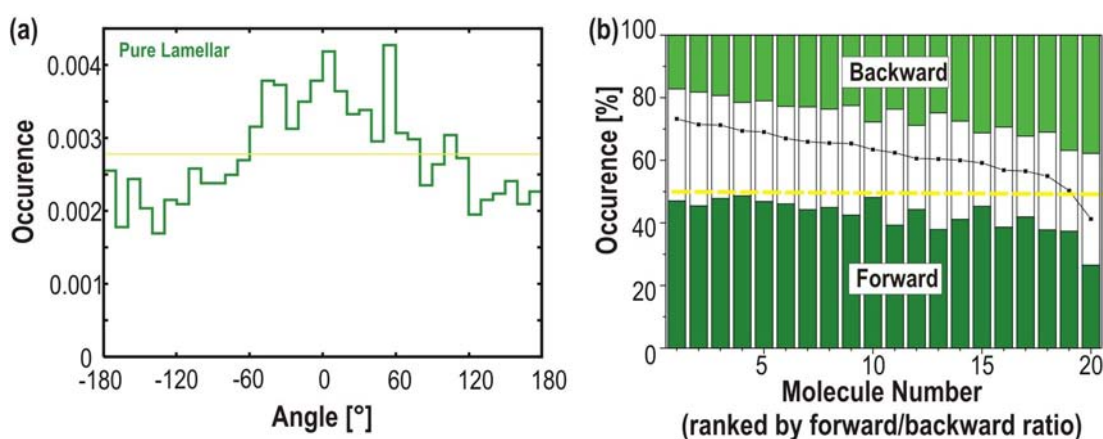


**Figure 7.17: Pure lamellar phase B5: Angles between successive steps.** (a) Histogram: The histogram shows a relatively flat distribution with a broad maximum around  $0^\circ$  and slight minima around  $\pm 180^\circ$ . (b) Percentage of forward, intermediate and backward steps: The black line indicates the ratio of forward/backward steps. Most of the molecules do more forward than intermediate steps and more intermediate than backward steps. The yellow line is a guide for the eye at a value of 50%.

### 7.2.5 Comparison with Symmetric Dyes: SW-TDI and DIP-TDI

In order to obtain a better understanding of the interactions between the dye and the surrounding host matrix, two symmetric dye molecules, **DIP-TDI** and **SW-TDI** (see Figure 7.2), were incorporated in the same way into the mesopores of thin Brij-templated films. These dyes were selected, as their terrylene diimide body is identical to the asymmetric **AS-TDI**. Both dyes are symmetrical, **DIP-TDI** has the identical head group as **AS-TDI** on both ends, and **SW-TDI** a swallow like double alkyl-tail comparable to the octyl tail of **AS-TDI**. The investigations of these dyes should elucidate if there is a correlation between the excess of forward jumps observed with **AS-TDI** and the asymmetry of the dye. Furthermore, when incorporated into the different phases of the host, single-molecule experiments on these dyes provide additional information about the interactions of the dye with its environment, e.g. which specifications a dye

needs to align perpendicular with respect to the substrate. However, these investigations are in a very initial stage, thus here only some tentative examples and preliminary results will be discussed. They will be continued in a future project.

In the hexagonal phase, the diffusion behaviour of the three TDI dyes was similar. All dyes diffuse in a highly structured manner, with similar diffusion coefficients. A tentative ranking of the diffusion coefficients is  $D_{\text{SW-TDI}} > D_{\text{AS-TDI}} > D_{\text{DIP-TDI}}$ . Moreover, polarization dependent measurements with the confocal setup showed that none of the dyes keeps a constant orientation while diffusing through the channels.

The diffusion behaviour in the lamellar phase differs strongly for the three different dyes. Whereas **AS-TDI** shows nearly exclusively doughnut patterns and some unstructured tracks on the surface, **SW-TDI** exhibits only some doughnut patterns and a high number of unstructured trajectories, of relatively fast molecules is observed. First experiments showed that these fast molecules can not be washed away from the surface. Therefore they must be in the bulk of the material. Contrary to **AS-TDI** and **SW-TDI**, the dye with two di-isopropyl-phenyl headgroups, **DIP-TDI**, did not show any doughnut patterns, but fast and unstructured diffusion. Like for the fast, unstructured molecules of **SW-TDI**, these molecules could not be washed away from the surface. In addition, some highly structured trajectories of **DIP-TDI** were observed in freshly prepared lamellar samples. The XRD of this sample was measured after the wide-field measurements, i.e. a few hours after the synthesis, and did show only one peak at the typical position of the pure lamellar phase. After about one day of ageing of the sample, only very few of these structured trajectories remained. One possible explanation is, that immediately after spin-coating a mixture of phases with a small amount of hexagonally arranged pores is present, which transforms within the first few minutes or hours into a purely lamellar structure. It is known from GISAXS measurements at a synchrotron source that the lamellar phase is build *via* an hexagonal phase<sup>0</sup>.

Interestingly, these structured trajectories show a large excess of forward steps and a higher diffusion coefficient than the molecules in the hexagonal phase of the pure samples or the phase mixture. This proves that there is no relation between the asymmetry of the molecule and the bias towards forward steps. Similar trajectories could be observed in one tentative example of **AS-TDI** in a sample synthesized with the intermediate recipe **B4**. In this sample doughnuts and highly structured trajectories with large diffusion coefficients coexisted. The XRD of this sample showed a large peak around  $2\theta = 1.45^\circ$  and a small peak at  $2\theta = 1.60^\circ$ , indicating the coexistence of the two phases. The structured trajectories show a significant excess of forward steps, as the samples of **B5** with **DIP-TDI**. Repeated experiments using recipe **B4**, however, showed

---

<sup>0</sup>personal communication by A. Zürner, Bein group, LMU Munich

mostly doughnuts and only sporadically some structured trajectories. Up to now, no satisfactory explanation could be found for the excess of forward steps in these structured trajectories, as for the unstructured diffusion in the lamellar phase. As a trend it was observed, that mostly samples synthesized with a high surfactant/silica ratio, showed this phenomenon, either in highly structured trajectories of gaussian shaped patterns or in the slow diffusion of the doughnuts.

These first preliminary results show already that even small structural changes at the end groups of the dye molecules can result in major changes of the behaviour of the dyes within the porous environment. Inducing favourable interactions of the hydrophobic tails of the template with the dye, which align the dye perpendicular to the silica planes, needs apparently the presence of hydrophobic alkyl tails in the dye molecule. Nonetheless, the asymmetric dye with only one alkyl chain showed much more orientation, than the analogous dye with four alkyl chains. This shows, that the host-guest or, more precisely, host-template-guest interactions cannot be explained by simple hydrophobic/hydrophilic interactions.

Though tentative, these results indicate that further investigations of the different dye molecules will provide a deeper understanding of the host-guest interactions within such mesoporous structures.



## 7.3 Pluronic Templated Films

Using Pluronic P123 as template, two different pore topologies of silica films were synthesized and investigated. The first recipe, **P1** (see Table 7.1), results in a hexagonal pore system, whereas the second recipe, **P2**, with higher surfactant/silica ratio yields a cubic pore structure. These structures were, similar to the Brij56-templated samples, synthesized on cleaned cover-slips and analysed using XRD and TEM. For the single-molecule studies on these materials, **AS-TDI** was used as fluorescent dye and incorporated into the pores during synthesis. Unless otherwise stated the single-molecule measurements in this section were done using the PentaMAX ICCD camera (see Section 3.3).

### 7.3.1 Characterisation of the Host

#### Recipe P1: Hexagonal Phase

Figure 7.18a shows the X-ray diffractogram of **P1** with the  $d(100)$  peak at  $2\theta = 1.025^\circ$ , which corresponds to a  $d$ -spacing of 8.6 nm of a hexagonal phase, and thus a pore-to-pore distance of  $a=10.0$  nm. The TEM plan-view image (Figure 7.18b) shows the hexagonal channels from top. Here, it is clearly visible that the channels are organised in domains with the long range order. As for the Brij-templated films, the hexagonally packed channels can be curved on a length scale of tens of nanometres, resulting in this fingerprint like structure of different domains.<sup>57</sup> The samples also exhibit a mosaic structure of domains having different in-plane orientations. Scanning the surface with an atomic force microscope shows distinct surface steps of about 10 – 11 nm. These steps have about the height of the pore-to-pore distance in the hexagonal system, like it was observed for the Brij-templated hexagonal sample **B2**.

#### Recipe P2: Cubic Phase

Figure 7.19a depicts the XRD of a sample synthesized with the **P2** recipe, showing a peak at  $2\theta = 0.96^\circ$ , i.e. a  $d$ -spacing of 9.2 nm. The plan-view TEM of this sample shows the cubic arrangement of spherical cavities (Figure 7.19b). The mosaic structure of domains, formed by a body centred cubic lattice (see Figure 2.2c), with coexistence of zones with [211] and [200] zone axes perpendicular to the substrate is visible. From grazing incidence X-ray diffraction (GISAXS) of non-calcined samples it is known that a one-dimensional contraction of  $\sim 15\%$  normal to the substrate surface occurs during

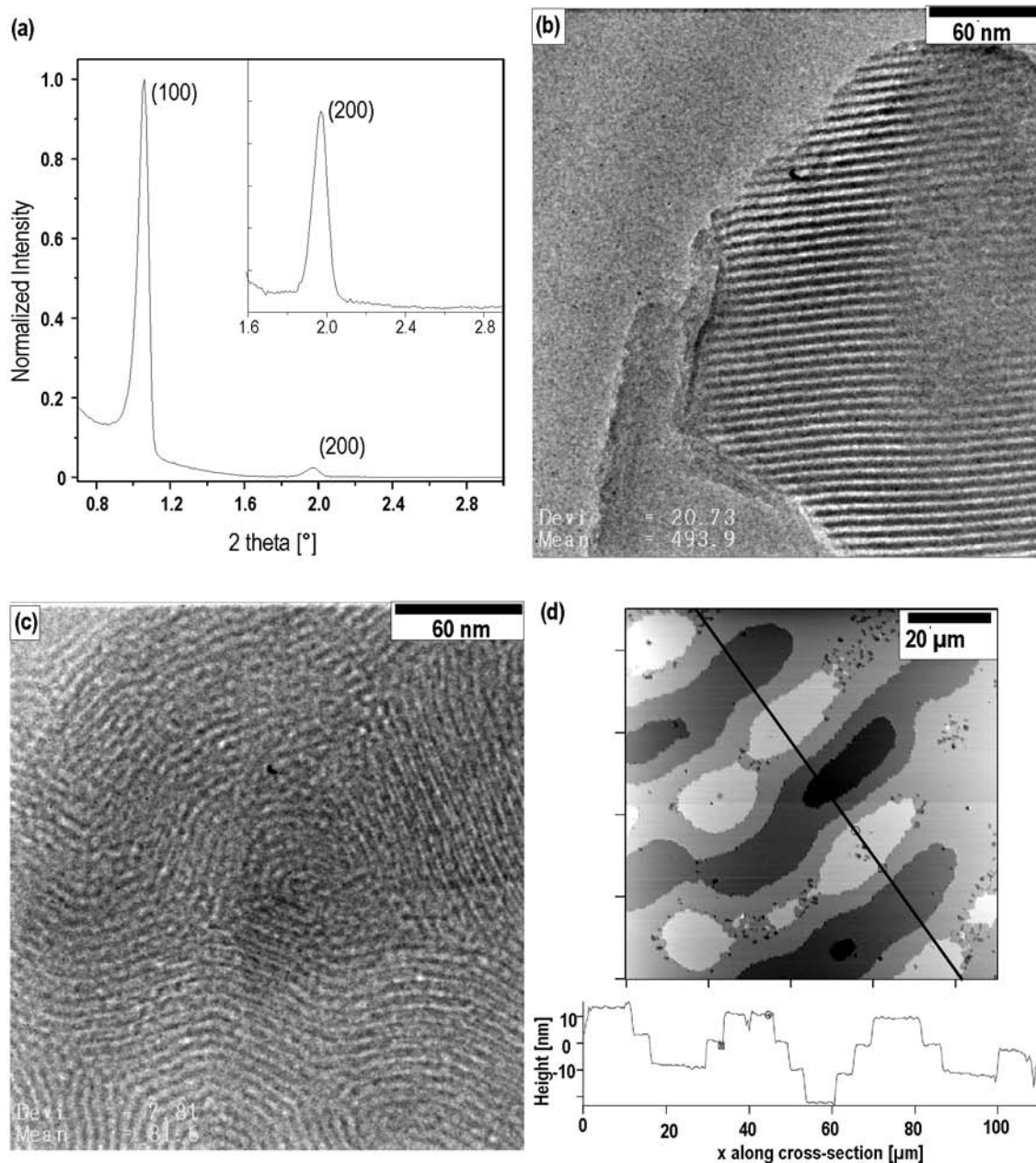


**Figure 7.18: XRD, TEM plan-view and AFM images of P1 (Hexagonal Phase).** (a) X-ray diffractograms of samples prepared using the recipe P1. (b) Plan-view TEM of a sample of P1, showing the parallel aligned channels of the hexagonal phase. (c) Another plan-view TEM of the hexagonal phase, representing the curvature and domain structure of the sample. (d) AFM image of the surface of a thin film synthesized in mica. Surface steps of 10 – 11 nm are visible in the cross-section along the black line. XRD and TEM courtesy of N. Petkov, Bein group, LMU Munich. Note that the TEM images were not measured from exactly the same samples than the single-molecule tracking, but from the same batch of samples.

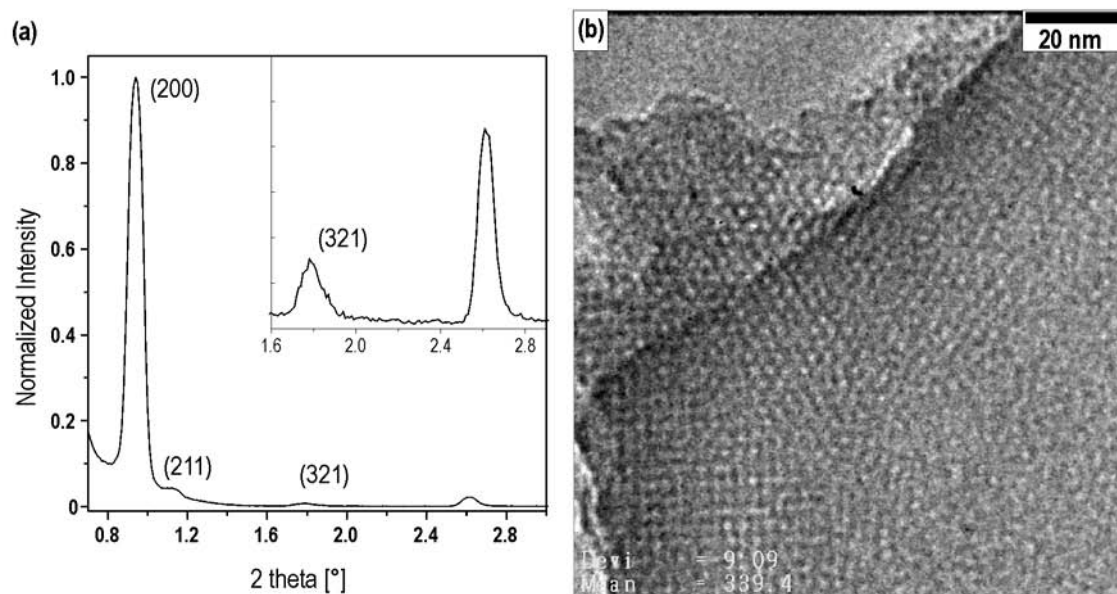


**Figure 7.19: XRD and TEM plan-view image of P2.** (a) X-ray diffractogrammes of samples prepared using the recipes **P2**. (b) TEM plan-view image of **P2**. The spherical cavities of a cubic ( $Im\bar{3}m$ ) phase are organised in different domains. Courtesy of N. Petkov, Bein group, LMU Munich.

the drying process of these samples. In as-synthesized samples the shrinkage normal to the substrate is typically smaller than for calcined samples. However, no GISAXS data have been measured for samples before calcination, thus the contraction after calcination can be taken as maximum value for the shrinkage of the as-synthesized films.

In addition, from  $N_2$ -sorption data of powder SBA-15 material (similar to the hexagonal thin films) the pore diameter is estimated to be  $\varnothing_{BJH} = 6.3 \text{ nm}$ .<sup>57</sup> As mentioned above, no  $N_2$ -sorption data could be gathered from the thin films.

### 7.3.2 Single-Molecule Trajectories in the Hexagonal Phase (P1)

In Figure 7.20 the overviews of all trajectories in two different movies from different samples synthesized using recipe **P1** are shown.

An immediate observation is that the diffusional behaviour is not homogeneous. Again, as previously seen in the Brij-templated films, different populations of molecules can be distinguished. There are faster moving molecules undergoing longer steps, that discover an area of several microns during their trajectories (population 3). These trajectories are unstructured and look like random motion, similar to population 3 in the

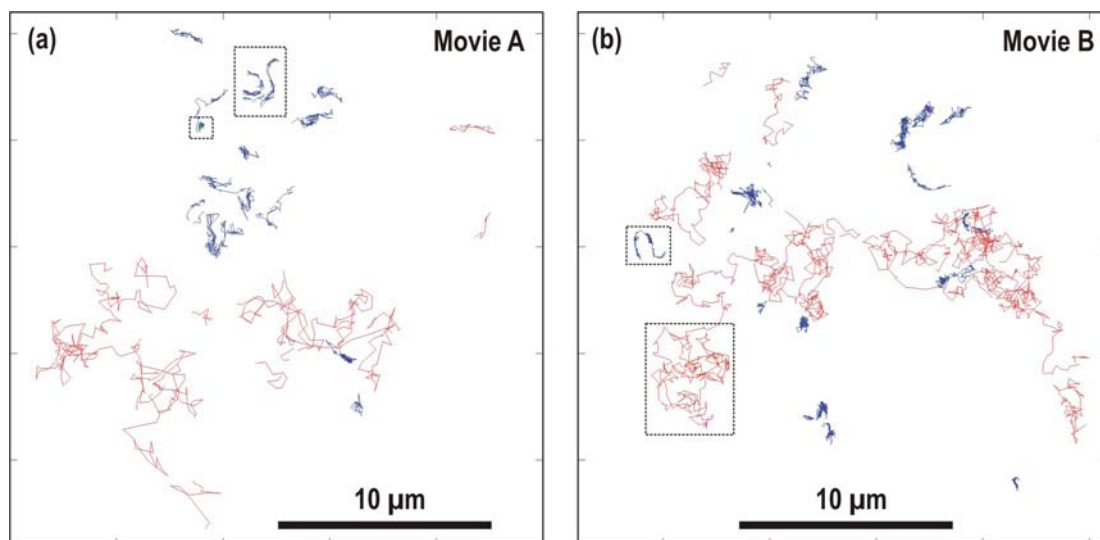


**Figure 7.20: Overview of all trajectories in two different wide-field movies of P1.** Different colours of the trajectories correspond to different mobilities of the molecules (see below). Population 1 molecules (immobile) shown in green, population 2 in blue (slow moving, structured trajectories) and population 3 (fast moving) in red. (a) 50 trajectories in 1000 images recorded with 70 ms per frame. (b) 1000 images recorded with 41 ms per frame. The trajectories marked by black rectangles are discussed in detail below (Figure 7.23 and 7.25).

Brij-templated films (see Section 7.2.2). These molecules could as well be removed by washing the surface of the samples with chloroform, therefore it is concluded that they were diffusing on the surface of the films. Other molecules do mainly shorter steps, remaining in areas restricted to about 2 – 3  $\mu\text{m}$  (population 2). In many cases the population 2 trajectories are highly structured, comparable to the molecules in the hexagonal phase of the Brij-templated films. Besides these two types of moving molecules also a few immobile ones (to within the positioning accuracy) can be observed (population 1).

### Separation of the different populations

As a criterion to distinguish between the different classes of molecules the median jump length in the individual trajectories was chosen, as described in Chapter 4. The threshold values were taken from the regions of the lowest slope in plots of the ranked median jump length (cf. Figure 7.21a, b), resulting in three different populations of molecules in the hexagonal thin films. They were selected for each movie separately, as the jump length is correlated with the temporal resolution of the movie. For movie A, depicted in Figure 7.20a, trajectories with a median  $< 70$  nm are classified as population 1, and  $> 210$  nm as population 3. Accordingly, jumps with a length  $< 70$  nm are considered as short and jumps  $> 210$  nm are long jumps. Owing to the higher temporal

resolution, the median step length in movie B (Figure 7.21b) is shorter than in movie A. Here the thresholds are set at  $< 50$  nm and  $> 180$  nm.

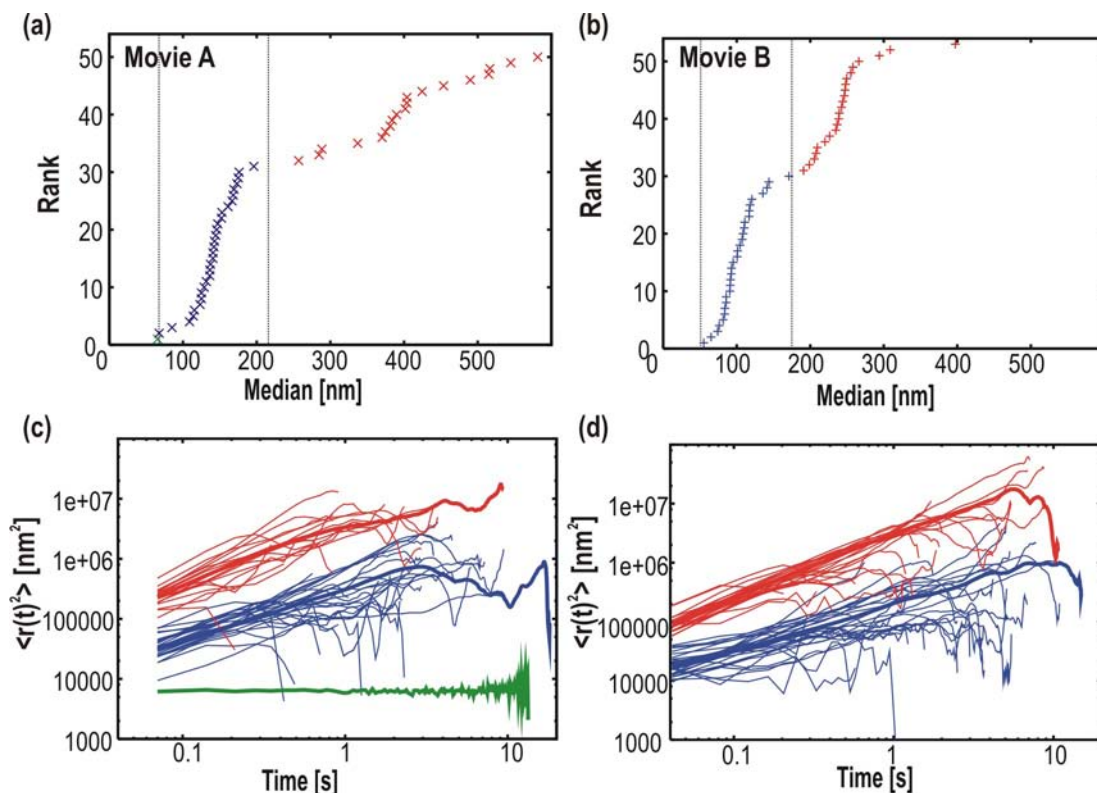


**Figure 7.21: Classification to different populations according to median step length and mean-square displacement.** (a) Movie A: Ranked median step length for all 50 trajectories. The thresholds to distinguish different populations are in the regions with the lowest slope, i.e. at 70 nm and 210 nm (vertical lines). (b) Ranked median step length in movie B. Owing to the higher frame rate, the steps are shorter than in (a). Thresholds are at 50 nm and 180 nm. (c) Mean-square displacements (MSD) of all individual trajectories in movie A as a function of time (double logarithmic plot). Population 1 molecules (immobile) are shown in green, population 2 in blue (slow moving, structured) and population 3 (fast moving, random diffusion on the surface) in red. Thick lines show the average values for the individual populations. (d) MSD plot for movie B, colour coding as in (c).

The existence of the different classes can also be visualised by plotting the mean-square displacement as a function of time for the individual trajectories. This is shown in Figure 7.21c and (d) in double logarithmic scale, thus different  $y$  axis intersects correspond to different diffusion coefficients. In Figure 7.21c clearly separated bundles of the individual MSD curves indicate the existence of three different classes of molecules. The thick lines correspond to the average value for each of the classes. Here the data of the two movies of Figure 7.20 are depicted, but the analyses of all movies in the hexagonal phase show curves, which are bundled in the same regions. For the fast moving molecules of population 3 the slope equals unity, as expected for random diffusion. Their diffusion coefficient is calculated according to the Equation for a 2D random walk (Equation 4.1.11). The average value for the bundle of red lines in (a) is  $D_{A:\text{population3}} =$

$(5.5 \pm 0.1) \times 10^{-1} \mu\text{m}^2 \text{s}^{-1}$ , and in (b):  $D_{\text{B:population3}} = (7.2 \pm 0.1) \times 10^{-1} \mu\text{m}^2 \text{s}^{-1}$ . The  $\langle r(t)^2 \rangle$  versus time for the slower moving molecules has a slope smaller than one. This might be assigned to spatial restrictions by the surrounding porous material. The respective diffusion coefficients, fitted by Equation 4.1.11 are  $D_{\text{A:population2}} = (7.8 \pm 0.1) \times 10^{-2} \mu\text{m}^2 \text{s}^{-1}$ , and in (b):  $D_{\text{B:population2}} = (4.1 \pm 0.1) \times 10^{-2} \mu\text{m}^2 \text{s}^{-1}$ . Averaged over the fits of the mean values in all analysed movies, the following diffusion coefficients are calculated:  $D_{\text{population2}} = 4 \times 10^{-2} \mu\text{m}^2 \text{s}^{-1}$  and  $D_{\text{population3}} = 3 \times 10^{-1} \mu\text{m}^2 \text{s}^{-1}$  for the mobile molecules. The diffusion coefficients between the molecules within the hexagonal pores and those on the surface differ thus by about an order of magnitude. Here, all lines, independent of the structure of the respective trajectories, were fitted according to 2D diffusion for comparison. However, it will be shown below, that for the structured molecules an analysis of the one-dimensional diffusion along the backbone of the trajectory is more precise.

Immobile molecules show horizontal lines between  $600 \text{ nm}^2$  and  $2200 \text{ nm}^2$ , i.e. they are confined to regions of about 23 nm to 45 nm. One example is shown by the green line in Figure 7.21c. These values are close to the positioning accuracy of the measurements.

### Angles between successive steps

The direction of successive steps, i.e. the distribution of angles in between steps, was analysed (see Section 4.2). The angular histogram for Movie B is shown in Figure 7.22a. By definition an angle of  $0^\circ$  is a step forward, the molecule keeps going in the same direction, backward steps correspond to angles of  $\pm 180^\circ$ , respectively (see Chapter 4.2).

For the immobile molecules a strong excess of backward steps is recorded due to the tracking artefact, which was explained in Chapter 4. The slower moving molecules, population 2, undergo more steps forward and backward and fewer steps perpendicular to the previous step. The molecules seem to follow a 'backbone' of the trajectories, as it would be expected for molecules enclosed into linear channels of a hexagonal pore system. Even though the movement of the fast molecules (population 3) appears to be fairly random, in about half of the trajectories a significant excess of forward steps is observed, causing the broad peak in the histogram around  $0^\circ$ . To investigate this phenomenon more closely, the percentage of forward (defined as  $|\text{angle}| = 0^\circ - 60^\circ$ ), intermediate ( $60^\circ - 120^\circ$ ) and backward ( $120^\circ - 180^\circ$ ) steps was calculated for each individual trajectory. A plot showing the percentage of forward, perpendicular and backward jumps (Figure 7.22b) – ranked with respect to the ratio of forward/backward jumps – indicates that this excess is visible for the population 3 molecules, whereas for the

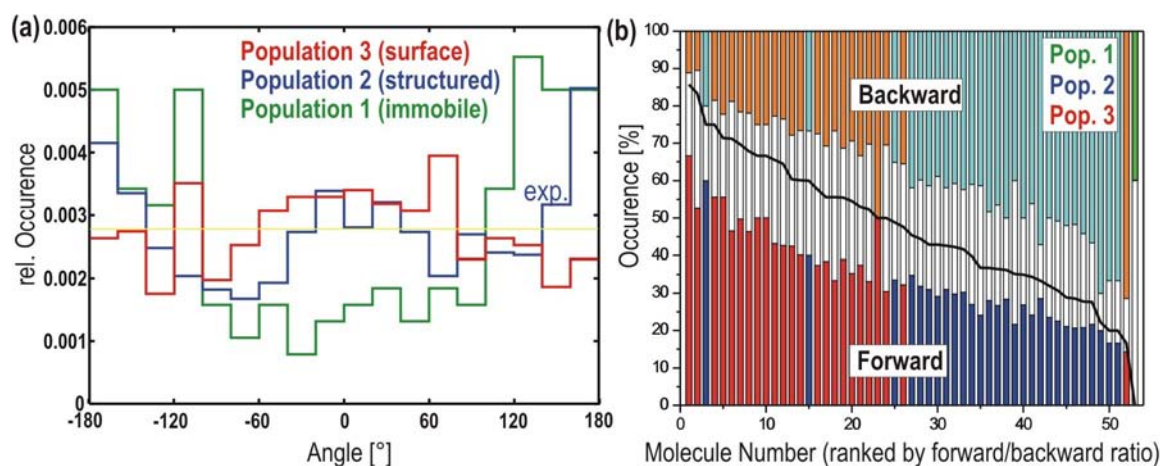


**Figure 7.22: Distribution of angles between successive steps.** Different colours corresponding to population 1, 2, 3, like in Figures 7.20, 7.21. (a) Histogram: Excess of forward steps for population 3; maximum of forward and backward steps and minimum for perpendicular steps for population 2. Strong excess of backward steps for immobile molecules (population 1), due to fitting artefact. (b) Percentage of forward, intermediate and backward steps. Ranked according to the ratio of forward/backward steps. For population 3 molecules a stronger excess of forward jumps is shown. Also for population 2 molecules a minimum of intermediate angles can be seen. Interestingly the classification into different populations can be found in this plot again.

population 2 molecules a small excess of backward steps is observed. It is striking that the separation of the individual classes in this plot is again very clear cut. Up to now, no plausible explanation for the excess of forward steps for surface diffusion has been found, as for the diffusion of the doughnuts in between the sheets of the Brij-templated lamellar phase (see Section 7.2.4). The small excess of backward steps for population 2 molecules originates probably from the high temporal resolution, which makes the step length in the range of the positioning accuracy and therefore the same tracking artefact as for the immobile molecules occurs.

### Individual, structured trajectories of population 2

In Figure 7.23a, b three exemplary population 2 trajectories showing a clear 'backbone' structure are depicted. The two molecules in Figure 7.23a appear one after the other in the same movie. The molecule showing the 'S-shaped' trajectory is present during 6.9 s between frame 64 and 162 of the movie and 14 s after it disappeared, the C-shaped trajectory starts in frame 323 and lasts 7.2 s until frame 426. As the samples are very diluted it is probable that the two trajectories close to each other shown in Figure 7.23a are from the same molecule, which blinks for 14 s. Panel (b) shows another trajectory from Movie B, showing a U-shaped structure. These molecules clearly follow the un-

derlying pore structure of the hexagonally arranged channels.

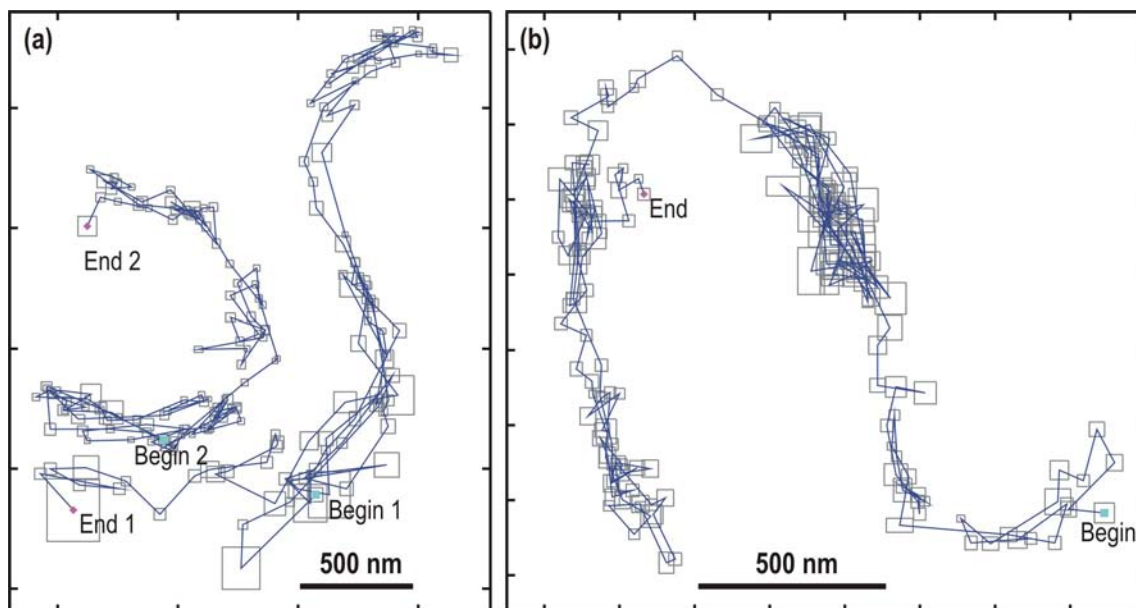


**Figure 7.23: Individual trajectories in the hexagonal phase.** (a) Two successive Trajectories, separated in time by 200 frames (14 s), at nearly the same position. Duration 99 and 104 frames, i.e. 6.9 s and 7.2 s, respectively. Time between frames: 70 ms. From Movie A, marked in the rectangular box in Figure 7.20a. (b) One individual Trajectory, following a U-shaped structure, in Movie B, marked in the rectangular box in Figure 7.20b. Temporal Resolution: 41 ms per frame, Duration 190 frames, i.e. 8 s. The grey boxes correspond to the tracking error of the individual points.

The angular distribution of these three trajectories has clear peaks at  $-180^\circ$ ,  $0^\circ$ ,  $180^\circ$ , corresponding to the movement along this backbone. This behaviour appears to be 1D, rather than 2D, therefore the diffusion has to be analysed along the backbone of the trajectory. The procedure is explained in Section 4.2. Figure 7.24a shows again the structure of the U-shaped trajectory in blue with the manually defined backbone points in red. The  $\langle r(t)^2 \rangle$  evolution with time is plotted in Figure 7.23b. Here, the red line corresponds to the values obtained by the averaging method of the backbone projected data and the blue line to the  $\langle r(t)^2 \rangle$  values obtained from the standard averaging method for different time lags of the two-dimensional trajectory. The kink at 1.2 s for the 2D MSD vs. time plot (blue) is not visible in the 1D MSD (red), as the analysis according to the backbone projection of the points is independent from the curvature of the trajectory. Whereas the blue line bends towards smaller values, the red line even appears to have a slope bigger than unity, the curve looks like a  $\langle r(t)^2 \rangle$  graph for diffusion with drift. This phenomenon is completely obscured in the blue curve from the standard  $\langle r(t)^2 \rangle$  calculation. Diffusion coefficients from fitting to the respective equation for 1D diffusion (Equation 4.1.9) are:  $D_{1D:backbone} = (2.7 \pm 0.1) \times 10^{-1} \mu\text{m}^2 \text{s}^{-1}$  and  $D_{1D:standard \text{ averaging}} = (1.8 \pm 0.1) \times 10^{-1} \mu\text{m}^2 \text{s}^{-1}$ .



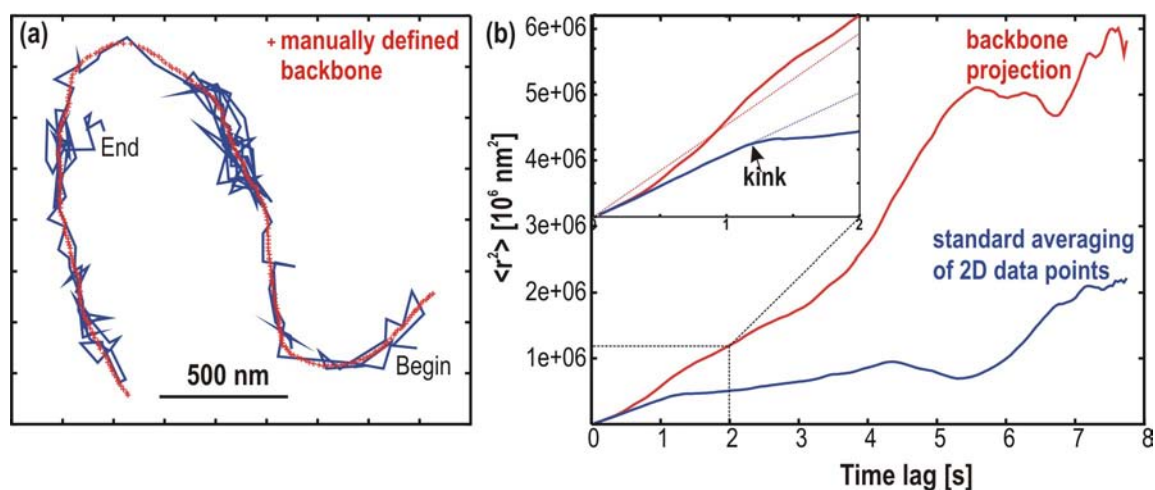


**Figure 7.24: Projection on the backbone of a structured trajectory.** (a) Trajectory and manually defined backbone (b) MSD plots for the 2D analysis and 1D backbone projection. The kink in the 2D plot at about 1.1 s originates from the strong curvature of the trajectory and therefore not visible in the 1D backbone projected analysis.

The same analysis was done for the two trajectories shown in Figure 7.23a. For the S-shaped trajectory a diffusion coefficient along the backbone of  $D_{1\text{D}:\text{backbone}} = (5.4 \pm 0.1) \times 10^{-1} \mu\text{m}^2 \text{s}^{-1}$  was calculated. In contrast, the diffusion coefficient for the C-shaped trajectory, which is probably from the same molecule, is  $D_{1\text{D}:\text{backbone}} = (1.2 \pm 0.1) \times 10^{-1} \mu\text{m}^2 \text{s}^{-1}$ , which is about a factor five smaller than that of the S-shaped trajectory. By the projection onto the backbone allowing to analyse the real 1D diffusion within the curved track, a bias towards smaller values due to the curvature of the pore can be excluded. Therefore this molecule must have explored two different environments, which have different influence on the diffusivity of the molecule. This shows again that not only different single molecules can be used to resolve inhomogeneities in the porous system, but also on single fluorescent molecule can be used as a reporter for various environments within a porous host.

### Immobile Molecules (population 1) and Surface Diffusion (population 3)

In Figure 7.25 one exemplary immobile molecule and one trajectory of a molecule diffusing on the surface is depicted, together with their cumulative distributions of angles between successive steps.

The immobile molecule in Figure 7.25a remains restricted to an area, which is in the range of the positioning accuracy. It is visible during 190 frames of the movie, corresponding to 13.3 s. Its cumulative distribution of angles shows a large excess of steps backward, due to the typical tracking artefact for immobile molecules described in

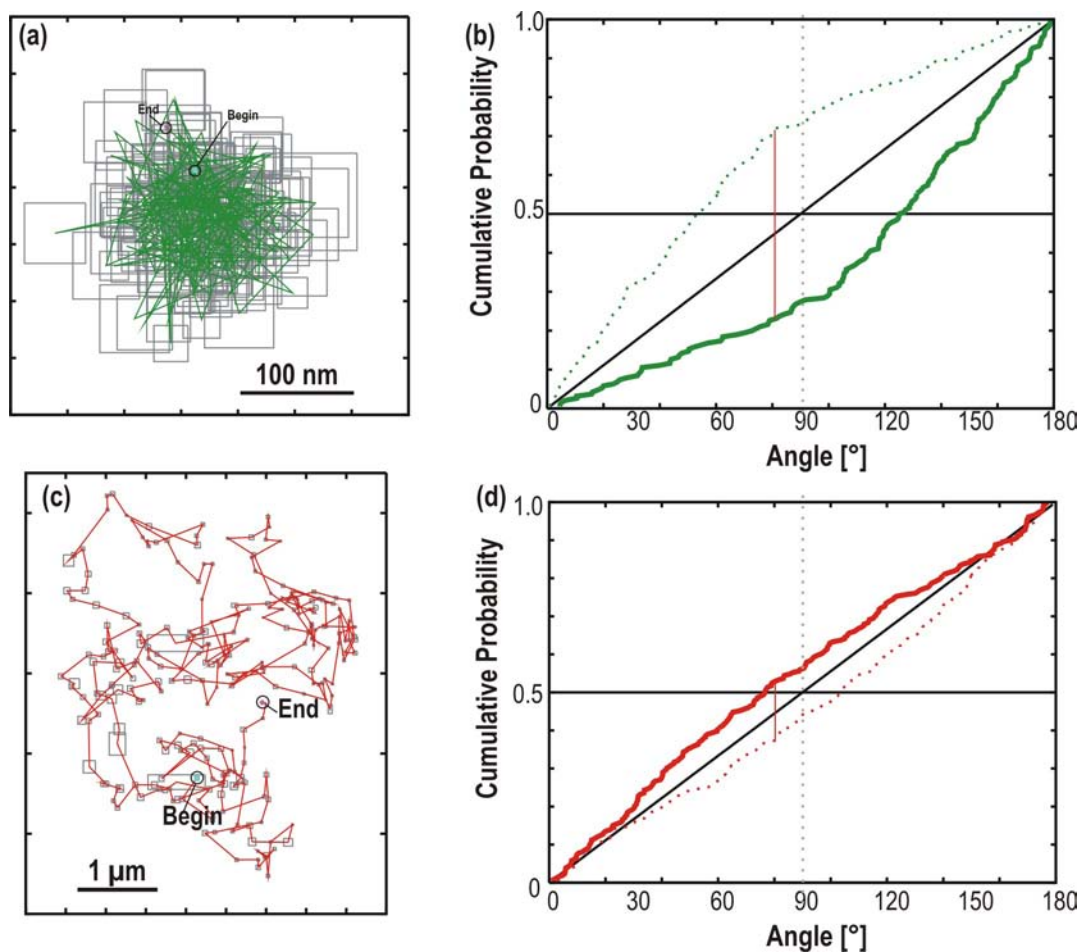


**Figure 7.25: Individual trajectories not related to the hexagonal pore system.** (a) Immobile Molecule (population 1). Temporal Resolution: 70 ms per frame. (b) Surface diffusion (population 3) in the hexagonal phase. Temporal Resolution: 41 ms per frame.

Chapter 4. The molecule on the surface, shown in Figure 7.25c lasts for 259 frames of the movie, i.e. for 10.6 s. The trajectory of this molecule has no specific structure, similar to the molecule moving on the surface of the Brij-templated thin film, shown in Figure 7.11c. However, in its angular distribution it shows a significant excess of forward jumps, visible in the cumulative distribution of angles in Panel (d). The probability that the difference between the cumulative distribution and its point mirrored inverse originates only from statistical noise, is 0.26 %, calculated by a Kolmogorov-Smirnov test. This observation agrees with the excess of forward jumps for population 3 molecules, that was shown above in Figure 7.22.

## 7.3.3 Single-Molecule Trajectories in the Cubic Phase (P2)

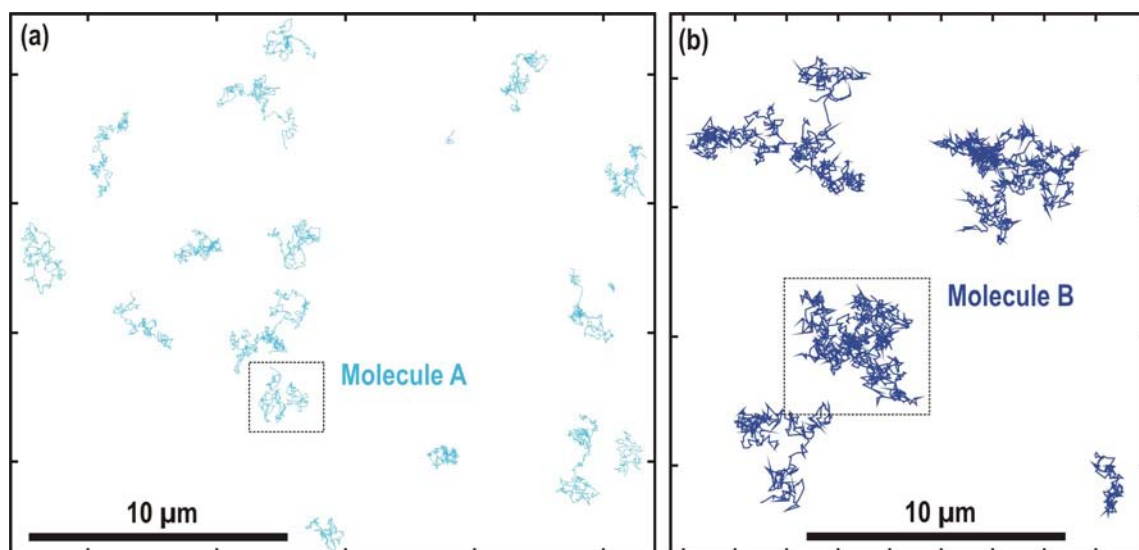


**Figure 7.26: Overview of all trajectories in two different wide-field movies of P2.** (a) Pale blue: Trajectories from 300 images recorded with 14 ms per frame (Andor iXon CCD). (b) Dark blue: Trajectories from 1000 images recorded with 42 ms per frame. (PentaMAX CCD)

In Figure 7.26 the overview of all trajectories in two samples of the cubic phase synthesized with recipe **P2** are shown. Panel (a) depicts in pale blue the trajectories from a movie acquired at 14 ms per frame using the Andor iXon EMCCD camera. On the right side on panel (b) all trajectories are shown from a movie that was taken from a cubic sample with the PentaMAX ICC camera (see Section 3.3 for details about the setup) at a lower temporal resolution, i.e. 42 ms per frame (dark blue traces). Note that the TDI concentration on the left panel was higher than on the right.

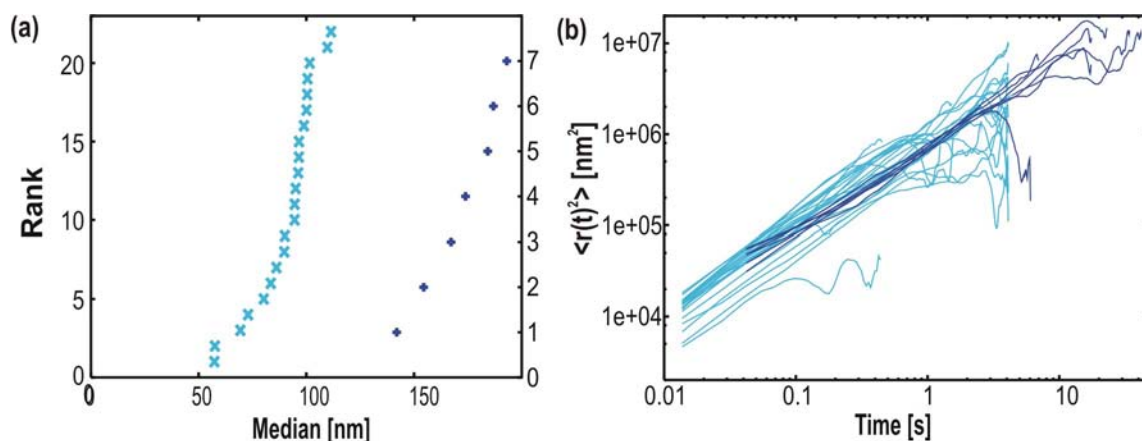


**Figure 7.27: Classification of the molecules according to median jumps and MSD.** (a) Ranked jump length median for the molecules in the two movies. The nearly vertical distribution indicates that only one class of molecules is present in the two samples. The steps in the movie with the slower framerate are longer. (b)  $\langle r(t)^2 \rangle$  against time for the two movies.

In both movies, most of the molecules are diffusing over areas of several micrometres. The diffusion appears to be much more homogeneous than in the hexagonal phase and the molecules do not seem to follow specific structures. The molecules cannot be removed by washing the surface of the samples with water or chloroform, therefore it can be concluded that the molecules diffuse in the interior of the thin film between the spherical micelles of the cubic phase, which are actually interconnected. This information about the connectivity of the micelles is not accessible by XRD or TEM. When plotting the ranked median jump length, only one main class of molecules, i.e. mostly moving and no or very few immobile, can be distinguished (see Figure 7.27a). This is also visible in the  $\langle r(t)^2 \rangle$  against time plot comparing the individual trajectories in one movie, depicted in Figure 7.27b. The average diffusion coefficients calculated according to random diffusion in 2D, Equation 4.1.9, are  $D_{\text{MovieA}} = 1.9 \times 10^{-1} \mu\text{m}^2 \text{s}^{-1}$  and  $D_{\text{MovieB}} = 1.6 \times 10^{-1} \mu\text{m}^2 \text{s}^{-1}$ .

### Individual Trajectories in cubic phase

The individual trajectories in the cubic phase do not show any specific structural features along which the molecules diffuse. At this temporal and spatial resolution the pathway from one spherical micelle to the neighbouring one cannot be resolved and the movement appears to be completely random in the 2D projection of the 3D diffusion. In addition, an analysis of the ranked  $\langle r(t)^2 \rangle$  for different time intervals (Figure 7.28c) demonstrates that only one type of diffusivity is present, because the ranked  $r^2$  are fitted nicely by mono-exponential decay functions. The diffusion coefficients derived from plotting the  $\langle r(t)^2 \rangle$  obtained by the mono-exponential fits against the time lag are for the two molecules  $D_{\text{MoleculeA}} = 2.8 \times 10^{-1} \mu\text{m}^2 \text{s}^{-1}$  and  $D_{\text{MoleculeB}} = 2.1 \times 10^{-1} \mu\text{m}^2 \text{s}^{-1}$  (Figure 7.28d).

Finally, the randomness of diffusion is underlined by plotting the histogram over the angles between successive steps for the two trajectories in Figure 7.29. The histogram shows a nearly flat distribution of angles between successive steps, as it would be expected for a random walk.

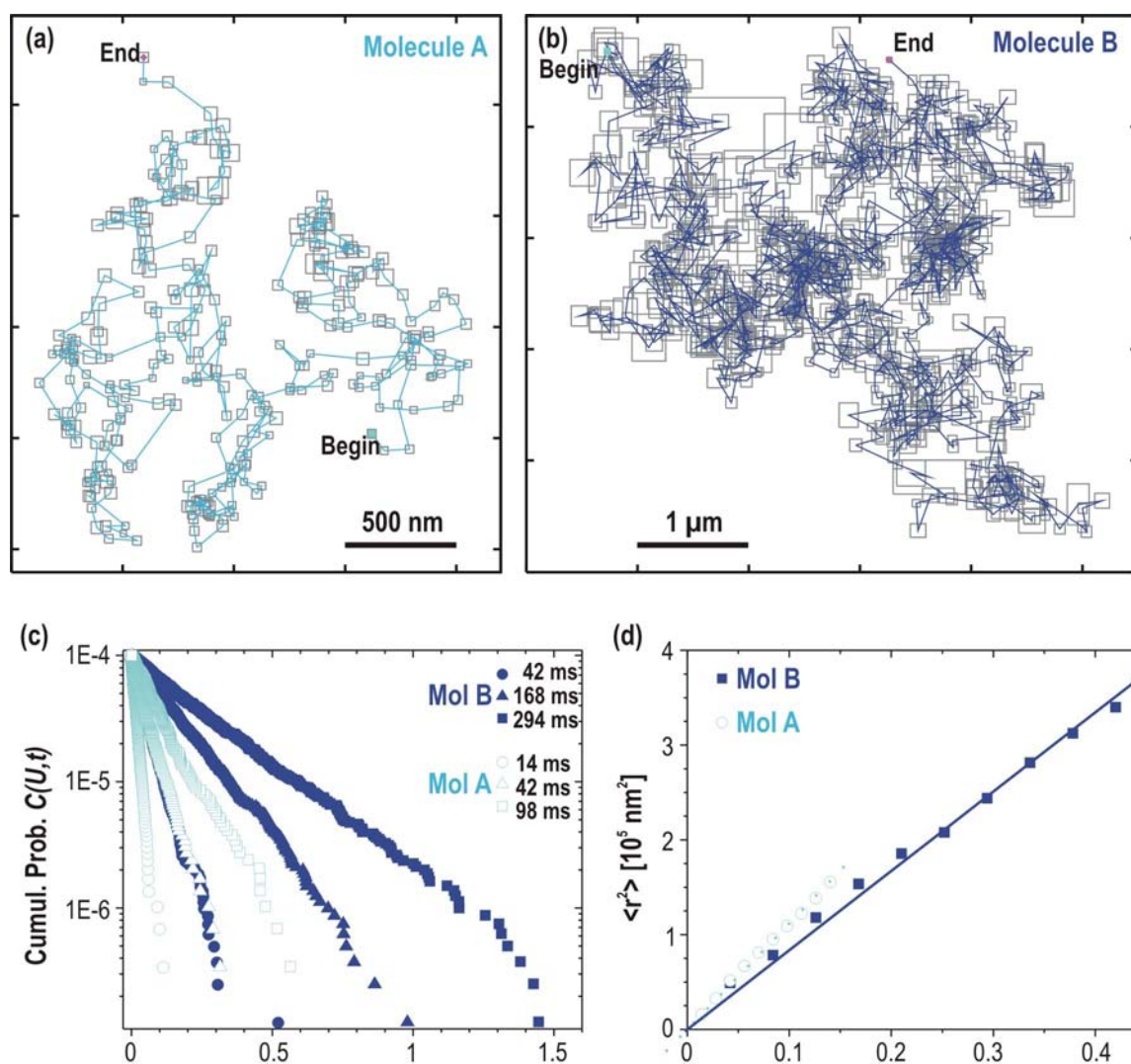


**Figure 7.28: Individual Trajectories in the cubic phase and mean-square displacement analysis.** The molecules in the cubic phase diffuse randomly, without following specific structural features. The grey boxes correspond to the positioning accuracy (one standard deviation of the fit). (a) Molecule A: Trajectory recorded at 14 ms per frame with the Andor iXon camera, marked in the rectangular box in Figure 7.26a. (b) Molecule B: Temporal Resolution (PentaMAX camera): 42 ms per frame, cf. Figure 7.26b. During this period the molecule blinked for 0.8 s, between frame 815 (End1) and 834 (Begin2). (c) Ranked squared step lengths of the two molecules in Figure 7.28 for three exemplary time lags and monoexponential fit to the data. Open, light blue symbols: Molecule A, Filled, dark blue symbols: Molecule B. (d) The plot of  $\langle r(t)^2 \rangle$  from the ranked data against time lag and linear fit gives diffusion coefficients of  $D_{\text{MoleculeA}} = 2.8 \times 10^{-1} \mu\text{m}^2 \text{s}^{-1}$  and  $D_{\text{MoleculeB}} = 2.1 \times 10^{-1} \mu\text{m}^2 \text{s}^{-1}$ .

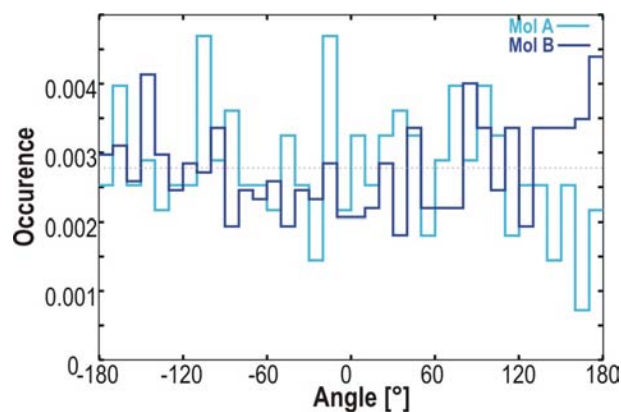


**Figure 7.29: Histogram of angles between successive steps.** The values for the angles are distributed evenly around the mean value (dotted line). Grey line: Distribution for Molecule A, Black line: Molecule B.

### 7.3.4 Comparison of Diffusion in the Hexagonal and the Cubic Phase

Figure 7.30 shows the  $\langle r(t)^2 \rangle$  against time for all molecules in movie B of the hexagonal phase and movie of the cubic phase. It is visible, that the diffusion coefficients in the cubic phase lie in between those of the two mobile populations in the hexagonal phase. The average values in the two phases are  $D_{\text{cubic}} = 1.6 \times 10^{-1} \mu\text{m}^2 \text{s}^{-1}$  and  $D_{\text{hexagonal:population2}} = (4.1 \pm 0.1) \times 10^{-2} \mu\text{m}^2 \text{s}^{-1}$   $D_{\text{hexagonal:population3}} = (7.2 \pm 0.1) \times 10^{-1} \mu\text{m}^2 \text{s}^{-1}$ .

Furthermore, the shape of the trajectories in the hexagonal phase reflects the structure of the porous system in which the molecules diffuse. In contrast, the diffusion in the

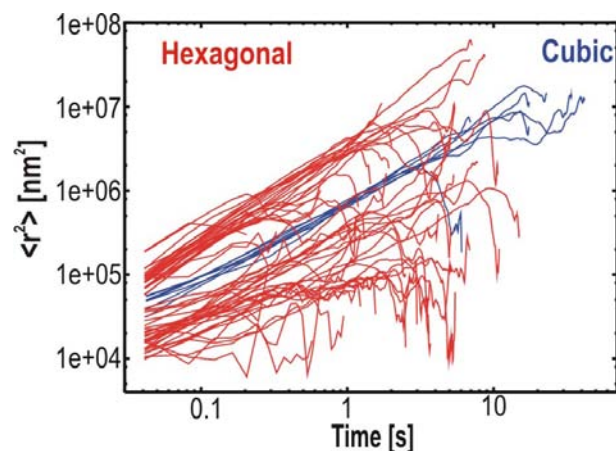


**Figure 7.30: Comparison of MSD in the two different Pluronic P123 templated phases.** Blue: Cubic phase (Movie B, Figure 7.20). Red: Hexagonal phase (populations 2 and 3; Movie B, Figure 7.26). The diffusion coefficient in the cubic phase lays in between the two mobile population of the hexagonal sample.

cubic phase appears to be random. No specific structural features of the host could be resolved in these trajectories. The shape of the trajectories resembles the shape of those on the surface of the hexagonal samples. However, their diffusion coefficient is about half as big.

## 7.4 Summary

In this chapter it was shown how tracking of single molecules with high spatial and temporal resolution, can be used to trace out the pore system of a mesoporous thin film. Whereas transmission electron microscopy (TEM) is restricted to small areas and very thin layers, using wide-field microscopy diffusion over an area of  $30\ \mu\text{m} \times 30\ \mu\text{m}$  or more can be investigated. Structured trajectories are seen, following the pores in the material for as much as five to ten microns. All trajectories in such a  $30\ \mu\text{m} \times 30\ \mu\text{m}$  region plotted together give a map of the arrangement of pores in this area. Moreover, based upon the structure of the trajectories, the diffusivities and the orientation of the molecules, dyes travelling on the external surface could be distinguished from those travelling inside the pore system, dyes that diffuse along horizontal channels of the hexagonal phase, and those that move much more slowly in lamellar galleries of the mesoporous material. It is even possible to observe the same single molecule migrating between one type of surrounding, e.g., hexagonal channel system, and another such as the lamellar phase. In addition, the structural heterogeneity of the channels is reflected by the complex modes of motion observed for single molecules within the hexagonal phase.

Furthermore, by using different templates, namely Brij 56 and Pluronic P123, for the synthesis of the mesoporous thin films, pore diameters of about 6 nm or 10 nm, respectively, could be obtained. It was found that the average diffusion coefficient in a hexagonal topology with smaller pores is  $D_{\text{Brijhex}} = 5.0 \times 10^{-3}\ \mu\text{m}^2\ \text{s}^{-1}$ , whereas the molecules in the larger pores have an average diffusion coefficient of  $D_{\text{Pluronichex}} = 4.1 \times 10^{-2}\ \mu\text{m}^2\ \text{s}^{-1}$ . Thus,  $D$  in the larger pores is about one order of magnitude higher than in the smaller pores. This difference results on the one hand from the difference in the pore diameter, on the other hand it is highly probable that the interactions of the dyes with the different templates, which remain in the pores of the as-synthesized films, have a strong influence on the diffusion dynamics.

First evidence that even small changes of the dye structure can result in completely different host-guest interactions, could be gained by incorporating three different terylene diimide (TDI) derivatives into the different topologies of Brij-templated films.

It was striking that the asymmetric dye developed favorable interactions with the template and was aligned perpendicular to the planes of the lamellar phase, whereas a symmetric dye with two diisopropyl phenyl head groups did not show any preferential orientation in between the planes. These measurements provide a basis for future research on the interactions of different dyes within the different porous host systems.

In summary, these data provide direct information about the topology, the intricate nanoscale connectivity and accessibility of the channels and the structural domains making up the porous sample.



# 8 Overview: Diffusion Measurements by SMT and other Methods

The aim of this chapter is to put the data obtained in this work into the context of diffusion measurements described in the literature. First, literature about the techniques used throughout this work, i.e. single-molecule microscopy and single particle tracking will be reviewed. Despite the promising applications in biological systems and thin polymer films, the number of studies using single-molecule tracking in porous host systems still remains fairly limited. In the second part of this chapter, the applications of single-molecule tracking to porous host systems, comparable to the materials investigated in this work, will be summarized. In addition an overview of different techniques to measure diffusion and other properties of guest molecules in porous systems will be given. An overview of the experimentally obtained diffusion coefficients in porous materials, including those determined in this work, is provided in Table 8.1 at the end.

## 8.1 Diffusion Measurements by Tracking of Single Fluorescent Molecules

The first experiments to measure the diffusion of single fluorophores at ambient conditions by videomicroscopy and subsequent tracking of the single-molecule signals were reported by Schmidt *et al.* in 1996.<sup>137</sup> Using a wide-field microscope, the authors followed the diffusion of phospholipid molecules labelled with one Rhodamine dye in a phospholipid membrane, with a temporal resolution down to 5 ms per frame and a positioning accuracy of 30 nm. Due to photobleaching of the dyes, trajectories of maximum 12 points could be collected. Averaging over 531 trajectories yielded a diffusion coefficient of  $D_{\text{SMT};\text{phospholipids}} = (1.4 \pm 0.13)\mu\text{m}^2 \text{s}^{-1}$ , which they compared to the value obtained from ensemble measurements by fluorescence recovery after photobleaching

(FRAP)  $D_{\text{FRAP:phospholipids}} = (0.77 \pm 0.13) \mu\text{m}^2 \text{s}^{-1}$ . The factor two between the values was assigned to the different length scales of the measurements: whereas single-molecule tracking is used to investigate diffusion on a scale of a few hundred nanometres, FRAP experiments cover areas of a few microns in diameter. The diffusion coefficients in the lipid membranes are at least one order of magnitude higher than the diffusion coefficients determined by single-molecule tracking within the porous host systems that were investigated in this work. They are, however, in the same range as the diffusion coefficients of molecules diffusing on the surface of the thin mesoporous films. This is a plausible result, as most probably the molecules on the surface are diffusing in a thin layer of liquid-crystal template, which is comparable in nature to a phospholipid membrane.

In a later study by the same group,<sup>98</sup> anomalous diffusion was revealed by single-molecule tracking experiments and successive data analysis using bi-exponential fits to the cumulative probability distributions of squared step lengths (cf. Chapter 4). In a fluid-supported phospholipid membrane a high mobility and a low mobility diffusion component were identified, with  $D_{\text{high mobility}} = 4.4 \mu\text{m}^2 \text{s}^{-1}$  and  $D_{\text{low mobility}} = 0.07 \mu\text{m}^2 \text{s}^{-1}$ . This reflects the results obtained previously in FRAP experiments, in which a second component has always been observed. This was commonly interpreted as an immobile fraction. However, from the experiments in Ref.,<sup>98</sup> it had to be inferred that this fraction appears to be mobile on a small length scale of at least 300 nm. Another work by this group<sup>143</sup> compared the diffusion in free standing films and in supported membranes, showing that the diffusion coefficient in the free standing films is about an order of magnitude higher than in the supported membranes. Furthermore, diffusion restricted to corrals of 140 nm in diameter was observed in polymer stabilized films.<sup>98</sup> In the present work, such corralled diffusion has been found in porous sol-gel matrices of **M3** (cf. Chapter 5).

Since these first tracking experiments on single fluorophores at room temperature by Schmidt *et al.*, single-molecule tracking has been applied to a huge number of biological systems. Here just a few exemplary studies shall be summarized. Soon after the first experiments in thin lipid membranes, Dickson *et al.* published a work on the behaviour of individual fluorescent molecules and individual singly labelled proteins in the water-filled pores of poly(acrylamide) (PAA) gels.<sup>167</sup> Using a total internal reflection (TIRF) microscope they could follow the single dye molecules as they moved within the gel structure in 3D. However, Cy5-labelled goat antibodies remained completely stationary in the PAA gels, presumably due to the too small pores of the gel matrices used. In the year 2000, Kubitscheck *et al.* presented for the first time single-molecule tracking of green-fluorescent protein molecules in the bulk of a glycerol matrix.<sup>121</sup> These measurements can be considered as preliminary tests for single molecule

experiments in the bulk of a biological environment. One year later, Seisenberger *et al.* in the Bräuchle group, managed to follow the infection pathway of a virus, labelled with a single fluorophore, into a living cell.<sup>83</sup> Using single particle tracking with a positioning accuracy of 40 nm they could show the repeated touching of the virus on the cell membrane prior to fast endocytosis. This inhomogeneous movement of the virus particles would not have been observable by any other means than single-molecule tracking. More recent single particle tracking studies in the Bräuchle group focus on the uptake of so-called artificial viruses into living cells.<sup>168,169</sup>

In 2003, Yildiz *et al.* achieved to follow the hand-over-hand walks of Myosin V molecular motors. Using TIRF microscopy and a highly sensitive CCD camera, they could accomplish Fluorescence Imaging with One-Nanometre Accuracy (FIONA). Recently, besides fluorescent dye molecules also other small species like gold- or semiconductor-nanoparticles are used for single particle tracking experiments, especially in biological systems. The group of Lounis presented in 2006 a method for tracking individual 5 nm gold nanoparticles on live cells.<sup>170</sup> It relied on the photothermal effect and the detection of the Laser Induced Scattering around a NanoAbsorber (LISNA) and the use of a triangulation procedure. As gold nanoparticles are not subjected to photobleaching, Single Nano-Particle Tracking (SNaPT) has the unique potential to record arbitrary long trajectories of membrane proteins using non-fluorescent nanometre sized labels. However, even though fairly small, the 5 nm particles would be still too big to fit in most of the porous systems that were investigated in this work. Furthermore, dye molecules can provide additional information about host-guest interactions, through their orientation or their spectra.

Another field in which single-molecule tracking has been extensively used, is the investigation of single-molecule diffusion close to interfaces. Schuster and von Borczyskowski published a number of papers focussed on the diffusion behaviour of single molecules, mostly Rhodamine 6G, in ultra-thin liquid films of e.g. tetrakis(2-ethylhexoxy)silane (TEHOS).<sup>132,171,172</sup> In Ref.<sup>132</sup> they presented an alternative method to determine the diffusion coefficient from single-molecule images. Here, the spot size of the single molecules is used to derive one individual diffusion coefficient per molecule and image of the movie. If a molecule is moving during the acquisition time of one movie frame its signal is a convolution of the point-spread-function (PSF), i.e. the microscope's transfer function yielding the typical diffraction limited spot, with an occupation frequency of certain positions during the exposure of the movie frame. The latter can be calculated from diffusion theory. Therefore, by fitting the elongated single-molecule signals with a 2D gaussian function, an individual diffusion coefficient for each molecule in every movie frame can be determined. This method is especially valuable, when the number of trajectory points per molecule is too low for a calcula-

tion of diffusion coefficients from averaging or ranking the squared step lengths. In the work presented in this thesis, a high number of very long trajectories with up to 1000 trajectory points were measured, therefore the averaging or ranking of the squared step lengths provides highly accurate diffusion data, which have a much higher significance than the data obtained with the method in Ref.<sup>132</sup>

The work on Rhodamine dyes in thin TEHOS films was continued by Schob and Cichos,<sup>173</sup> who built a surface forces apparatus combined with a fluorescence microscope to investigate the diffusion in confined liquids in detail using single-molecule tracking, here of Rhodamine B. They found the mean diffusion coefficient to be independent of the liquid film thickness, which was for all experiments below 300 nm, of  $D = 3 \mu\text{m}^2 \text{s}^{-1}$  and thus ten times smaller than the diffusion coefficient of Rhodamine B in bulk TEHOS.

Another interesting application of single-molecule tracking and single-molecule methods in general was developed by Roeffaers and Hofkens.<sup>174</sup> Using wide-field microscopy, they could observe the catalytic conversion of individual fluorescein ester molecules at specific locations of  $[\text{Li}^+ \text{Al}^{3+}]$  layered double hydroxide (LDH) catalysts, like the crystal faces or the basal plane. Furthermore, they could follow the translational diffusion of single product molecules diffusing randomly on specific LDH crystal surfaces by single particle tracking.

Last year, Werley and Moerner found by single-molecule microscopy three different populations of terrylene dye molecules incorporated into a thin spin-coated film of para-terphenyl.<sup>90</sup> Two spatially fixed populations that differed in the orientation of the transition dipole moments could be differentiated: One with the transition dipole moments, and thus the molecular long axis, perpendicular to the substrate with doughnut emission patterns (as reported previously by Pfab *et al.*<sup>128</sup>) and others having gaussian shaped patterns. Apart from the stationary molecules a, previously unreported, mobile fraction was detected, diffusing fairly linearly in areas of approximately  $3.5 \mu\text{m} \times 0.45 \mu\text{m}$  in size. These molecules explore the confinements of defect regions, that are generally long and thin, suggestive of cracks. The single-molecule trajectories provide information about the shape and the character of the crystal defects, information that is hard to obtain by other means.

## 8.2 Single-Molecule Experiments in Porous Hosts

The first single-molecule tracking experiments on mesoporous host systems were reported in 2002 by Seebacher *et al.*<sup>101</sup> in the Bräuchle group. Using a confocal laser scanning microscope the diffusion of single terrylene diimide molecules (AS-TDI, as used throughout this work) incorporated into mesoporous monoliths was followed. The mesoporous M41S silica monoliths with hexagonal arrangement of pores were synthesized using monododecyloctaethyleneglycol ether (OMO) as template, yielding pores of ca. 3 nm in diameter.<sup>175</sup> Due to the scanning technique the frame rate was as slow as 4 s per frame. The positioning accuracy was about 40 nm. Trajectories of up to 20 points were investigated and diffusion coefficients were calculated using the ranking method of squared displacements. At this temporal resolution only isotropic diffusion was found, with a diffusion coefficient of  $D_{av} = 3.72 \times 10^{-2} \mu\text{m}^2 \text{s}^{-1}$ . Apart from the mobile fraction a stationary fraction of 10% of all molecules was found to be immobile to within the positioning accuracy. In comparison, diffusion of AS-TDI in the pure liquid-crystal phase was found to be anisotropic, with a diffusion coefficient about two orders of magnitude higher than inside the bulk of the mesoporous host ( $D_{\text{liquid-crystal}} = 2.07 \mu\text{m}^2 \text{s}^{-1}$ ). This value is similar to the diffusion coefficients within the phospholipid membranes investigated by Schmidt *et al.* or on the surface of the mesoporous thin films in this work.

McCain *et al.* presented in 2003 single particle tracking of Rhodamine 6G in 450 nm thin dip-coated sol-gel films, that were synthesized without the use of a template, similar to the monolithic materials investigated in Chapter 5 of this thesis. Using wide-field microscopy, films of 300 frames in length with a temporal resolution of 0.779 s between frames (0.2 s exposure time plus 0.579 s readout time), yielding a total observation time of 234 s were collected. Five trajectories corresponding to four different regions of the film, with a maximum of 44 points in the longest trajectory and 115 track points all together, were investigated. By averaging the square displacements for different time lags for all trajectories a diffusion coefficient of  $D_{av} = (3 \pm 2) \times 10^{-2} \mu\text{m}^2 \text{s}^{-1}$  was determined, which is in the same order of magnitude as that determined here for **M3**. By fitting the histograms of the frequency of step size according to the probability density of step sizes, individual diffusion coefficients for the five trajectories were calculated between  $D_{\min} = (7 \pm 3) \times 10^{-3} \mu\text{m}^2 \text{s}^{-1}$  and  $D_{\max} = (7 \pm 2) \times 10^{-2} \mu\text{m}^2 \text{s}^{-1}$ . Using a statistical test (Fisher's F-test) they showed that the diffusion coefficients of two neighbouring molecules were significantly different and deduced that there are spatial heterogeneities within this sample; maybe the two neighbouring molecules were at different heights within the thin film and thus within different porous environments. In addition, similar to the observations in **M3** they report on a number of immobile molecules to within the positioning accuracy. However, as no porosity information

of the sol-gel samples was provided and the statistics from single-molecule tracking was poor, it remains difficult to directly compare their results with those presented in Chapter 5 of this work.

In the same year, Mahurin *et al.* published diffusion studies using fluorescence correlation spectroscopy (FCS) on the movement of Rhodamine 6G dissolved in methanol and loaded at very low concentrations into the pores of a commercially available mesoporous silica system. These materials had a disordered pore structure with an average mesopore diameter of 13 nm (calculated using the Barrett-Joyner-Halenda (BJH) method),<sup>176</sup> i.e. in between the mean mesopore diameter of **M3** and **M22**. The diffusion inside the material deviated from simple Brownian motion, and the correlation data could only be fitted either by a two-component diffusion model or diffusion plus adsorption. In the two-component model a population of 38% of the molecules with  $D_1=68.1 \mu\text{m}^2 \text{s}^{-1}$  and another population of 62% with  $D_2=4.84 \mu\text{m}^2 \text{s}^{-1}$  was found. However, the multicomponent diffusion model comprised of 80% free diffusion (with a diffusion coefficient of  $D_{\text{freediff}} = 48.9 \mu\text{m}^2 \text{s}^{-1}$ ) and 20% transient adsorption/desorption (desorption time of 67 ms) provides the best fit and the most plausible explanation of the correlation data, because even in a region where the dye diffused in the pure solvent close to the cover-slip interface a two-component model was needed to fit the data and the Rh6G dye has the opposite charge as the glass surface. However, through FCS measurements only it is not possible to resolve adsorption events of individual dye molecules. Compared with the data presented throughout this work it is striking that the diffusion coefficient determined by Mahurin *et al.* is at least one order of magnitude higher than the diffusion coefficients in either the sol-gel glasses or the mesoporous template-filled thin films. This might be explained by the fact, that ethylene glycol and also the template/ethanol/water inside the mesoporous thin films are much more viscous than methanol and also by the higher mean mesopore diameter of the materials used by Mahurin *et al.* .

In recent years, a number of publications on the behaviour of different single dye molecules within various porous hosts and polymer films was published by the group of Higgins at Kansas State University.<sup>177,178,179,180,181,182,183</sup> The most relevant investigations and findings will be summarized here. In one of the earlier studies,<sup>178</sup> Higgins *et al.* used the spectral shifts of individual dye molecules to compare the nanoscale properties of organically modified sol-gel-derived silicate thin films prepared from different silicate precursors without the use of a template. Similarly, microenvironmental acidity in thin sol-gel films was investigated through the spectral shifts of single pH sensitive dye molecules (dye: Carboxy SNARF-1). While these works provide insights into spectral jumps of single molecules, only Ref.<sup>177</sup> presents a brief analysis of tracking a small number of single molecules. Effects of ambient humidity on the emission

characteristics of Nile red in hydrophilic and hydrophobic films are reported by Hou *et al.*<sup>177</sup> Investigations of translational diffusion in silica hosts was reported in organically modified silicate (ORMOSIL) films.<sup>180</sup> Using FCS, the diffusion coefficients of free and silicate-bound Nile red were determined to be  $D_{\text{free}} = 3.9 \times 10^{-2} \mu\text{m}^2 \text{s}^{-1}$  and  $D_{\text{silica-bound}} = 1.6 \times 10^{-2} \mu\text{m}^2 \text{s}^{-1}$ , respectively. The unexpectedly rapid diffusion of silicate-bound Nile red is attributed to the presence of liquid-like silicate oligomers in the films. Comparison of the results derived from experimental and simulated time transients indicates film heterogeneity on sub-100-nm length scales that probably stem from the presence of inorganic- and organic-rich domains. In 2006, Fu *et al.*<sup>182</sup> presented diffusion measurements in templated mesoporous structures like those investigated in Chapters 6 and 7 in this thesis. The ionic surfactant cetyltrimethylammonium bromide (CTAB) was used as template, yielding a hexagonal pore system with a  $d$ -spacing of 3.5 nm. The spin-coated films were about 1  $\mu\text{m}$  thick. After calcination films were only 400 nm thick, and the mesopores in the films have collapsed and become somewhat disordered, exhibiting 2.4 nm periodicity. The dye Nile red is loaded into the films either prior to spin-coating or after calcination. FCS experiments showed that the dye is relatively mobile in as-synthesized films, whereas in dry, calcined films the dye molecules appear trapped at fixed locations and in rehydrated, calcined films they are mobile again. The determined diffusion coefficients are listed in Table 8.1 below. The time transients of the mobile molecules in the as-synthesized and the rehydrated calcined films provide evidence for frequent reversible adsorption of the dye to the silica surfaces. More thorough investigations of dye diffusion and surface interactions within mesoporous films are presented in a later study,<sup>183</sup> where three different dyes (Nile red, DiI and sulfonated perylene diimide), selected for their hydrophobicity and charge characteristics, are incorporated into similar, CTAB templated thin films. Again, FCS measurements were used to detect differences in the diffusion behaviour of the different dyes at various relative humidities in as-synthesized and calcined mesoporous films; the measured diffusion coefficients are summarized in Table 8.1. However, as mentioned above in Chapter 3, FCS data needs a suitable model for the interpretation of the time transients and it can only provide information about the general differences of the diffusivities of the single dye molecules. In order to get a detailed image of the diffusion pathways of single dye molecules through highly structured materials, like mesoporous thin films, single-molecule tracking is the method of choice.

Very recently, single-molecule measurements in the Bräuchle group by Jung *et al.* showed highly linear diffusion of single AS-TDI molecules within structured domains of CTAB templated thin films.<sup>112</sup> Furthermore, orientational and spectral information of the dyes inside the pores could be correlated.<sup>113</sup> We have recently submitted a manuscript on the detailed investigation of diffusion characteristics, including the diffusion coef-

ficients, with extremely high spatial resolution down to two nanometres allowing us to resolve the diffusion clearly in the individual channels. Like the measurements presented in this thesis, these investigations show the great advantage of single-molecule tracking over other means of measuring diffusion, like FCS. The trajectories yield the diffusion coefficients of the dyes within the porous host, but they also map out the structure of the host.

Thus, the present work gives for the first time a detailed picture of single-molecule diffusion within porous host systems. The high statistical significance of trajectories as long as 1000 data points provides an unprecedented insight into the structures, the pore accessibility and connectivity of the host systems. Furthermore, the molecules can be used as reporters for the local environment of the dyes within the host matrix. One must always be cautious comparing data on sol-gel materials between different authors, since small details in the synthesis may have important consequences for the final material, as may ageing. This thesis is to our knowledge the first time that single molecule tracking has been applied systematically to varied samples from the same sources, providing homogeneous sets of data on which to base comparisons.

Finally, the following table summarizes the different diffusion coefficients and particularities that were found in the various porous materials presented here. The first lines of the table show the results obtained throughout this work, presented in Chapters 5 to 7, and the second part of the table summarizes the findings of the various publications discussed in this chapter.



**Table 8.1: Diffusion coefficients of different dye molecules in various porous systems.** For abbreviations see appendix.

Source	System	Name	$D$ [ $\mu\text{m}^2/\text{s}$ ]	Method
<i>This work</i>				
Chapter 5	9A1 in sol-gel glass	<b>M3</b>	0.03	SMT
		<b>M22</b>	0.72	SMT
		<b>M22</b>	0.34	PFG NMR
	EG in sol-gel	<b>M3</b>	10	PFG NMR
		<b>M4</b>	13	PFG NMR
		<b>M22</b>	5	PFG NMR
Chapter 6	AS-TDI in ultrathin mesoporous films (template: Brij 56, d-spacing 6 nm)	<b>B6</b>	0.04	SMT (and TEM)
Chapter 7	AS-TDI in mesoporous thin films; template: Brij 56 (d-spacing 6 nm) template: Pluronic P123 (d-spacing 9 nm)	hex <b>B2</b>	$5.0 \times 10^{-3}$	SMT
		lam <b>B5</b>	$5.3 \times 10^{-5}$	SMT
		surface	0.2	SMT
		hex <b>P1</b>	0.04	SMT
		cub <b>P2</b>	0.18	SMT
		surface	0.3	SMT
<i>Literature</i>				
Seebacher 2002 <sup>101</sup>	AS-TDI in mesoporous monoliths (template OMO, pore $\varnothing$ ca. 3 nm) pure liquid-crystal	mob	0.0372	SMT (confocal)
		immob	$1.0 \times 10^{-4}$	
		hex	2.07	FCS
McCain 2003 <sup>91</sup>	Rhodamine in sol-gel films		0.03	SMT
Mahurin 2003 <sup>176</sup>	Rh6G in mesoporous glass (pore $\varnothing$ 13 nm)	38 %	68.1	FCS
		62 %	4.84	FCS
Fu 2006 <sup>182</sup>	Nile red in mesoporous films (template CTAB, d-spacing 3.5 nm)	as-synth	0.024	FCS
		calc(rehyd)	0.026	FCS
Ye 2007 <sup>183</sup>	different dyes in mesoporous films <sup>a</sup> template: CTAB (d-spacing 3.5 nm)	DiI (as-syn)	0.03	FCS
		DiI (calc)	0.031	FCS
		SPDI(calc)	0.040	FCS
		Nile red (as-syn)	0.027	FCS
		Nile red (calc)	0.029	FCS

<sup>a</sup>Measurements were done at various relative humidities. Here only those at 50% r.h. are listed, as they can be compared best to our data.



# List of Abbreviations

<b>1D</b>	one-dimensional
<b>2D</b>	two-dimensional
<b>3D</b>	three-dimensional
<b>BET</b>	Brunauer-Emmett-Teller
<b>BJH</b>	Barrett-Joyner-Halenda
<b>Brij 56</b>	Decaethylene glycol hexadecyl ether or Polyoxyethylene 10 cetyl ether
<b>CCD</b>	Charge coupled device
<b>CMC</b>	Critical micelle concentration
<b>CTAB</b>	Cetyltrimethylammonium bromide
<b>EISA</b>	Evaporation-induced self-assembly
<b>FCS</b>	Fluorescence correlation spectroscopy
<b>fps</b>	Frames per second
<b>GISAXS</b>	Grazing-incidence small-angle X-ray scattering
<b>HK</b>	Horvath-Kawazoe
<b>IUPAC</b>	International Union of Pure and Applied Chemistry
<b>MCM</b>	Mobil catalytic material
<b>MSD</b>	Mean-square displacement
<b>N.A.</b>	Numerical aperture
<b>NMR</b>	Nuclear magnetic resonance
<b>OD</b>	Optical density
<b>PFG NMR</b>	Pulsed-field gradient nuclear magnetic resonance
<b>PMMA</b>	Polymethyl methacrylat
<b>Pluronic P123</b>	Poly(ethylene oxide) <sub>20</sub> -poly(propylene oxide) <sub>70</sub> - poly(ethylene oxide) <sub>20</sub>
<b>PS</b>	Polystyrene
<b>rpm</b>	Rounds per minute
<b>SAXS</b>	Small-angle X-Ray scattering
<b>SBA</b>	Santa Barbara Acidic
<b>SMT</b>	Single-molecule tracking
<b>SNR</b>	Signal-to-noise ratio

<b>TDI</b>	Terrylene diimide
<b>TEM</b>	Transmission electron microscopy
<b>TEOS</b>	Tetraethyl orthosilicate
<b>TIRF</b>	Total internal reflection
<b>TMOS</b>	Tetramethyl orthosilicate
<b>XRD</b>	X-ray diffraction

# Bibliography

- [1] S. Fulford. Tom Paulin, Walking a Line, and Paul Klee. *The Cambridge Quarterly*, 31(1):57–75, 2002.
- [2] G. Binnig, H. Rohrer, Ch. Gerber, and E. Weibel. Tunneling through a controllable vacuum gap. *Appl. Phys. Lett.*, 40(2):178–180, 1981.
- [3] G. Binnig, H. Rohrer, Ch. Gerber, and E. Weibel. Surface Studies by Scanning Tunneling Microscopy. *Phys. Rev. Lett.*, 49(1):57–61, 1982.
- [4] G. Binnig, C. F. Quate, and Ch. Gerber. Atomic Force Microscope. *Phys. Rev. Lett.*, 56(9):930–933, 1986.
- [5] W. E. Moerner and L. Kador. Optical Detection and Spectroscopy of Single Molecules in a Solid. *Phys. Rev. Lett.*, 62(21):2535–2538, 1989.
- [6] M. Orrit and J. Bernard. Single Pentacene Molecules Detected by Fluorescence Excitation in a p-Terphenyl Crystal. *Phys. Rev. Lett.*, 65(21):2716–2719, 1990.
- [7] W. E. Moerner and M. Orrit. Illuminating Single Molecules in Condensed Matter. *Science*, 283(5408):1670–1676, 1999.
- [8] S. Nie and R. N. Zare. Optical Detection of Single Molecules. *Annu. Rev. Biophys. Biomol. Struct.*, 26:567–596, 1997.
- [9] J.S. Beck, J.C. Vartuli, W.J. Roth, M.E. Leonowicz, C.T. Kresge, K.D. Schmitt, C.T.-W. Chu, D.H. Olson, E.W. Sheppard, S.B. McCullen, J.B. Higgins, and J.L. Schlenker. A New Family of Mesoporous Molecular Sieves Prepared with Liquid Crystal Templates. *J. Am. Chem. Soc.*, 114(27):10834–10843, 1992.
- [10] C.T. Kresge, M.E. Leonowicz, W.J. Roth, C.E. Vartuli, and J.S. Beck. Ordered mesoporous molecular sieves synthesized by a liquid-crystal template mechanism. *Nature*, 359:710–712, 1992.
- [11] D. Zhao, J. Feng, Q. Huo, N. Melosh, G.H. Fredrickson, B.F. Chmelka, and G.D. Stucky. Triblock Copolymer Syntheses of Mesoporous Silica with Periodic 50 to 300 Angstrom Pores. *Science*, 279:548–552, Jan 1998.
- [12] M. Choi and R. Ryoo. Ordered nanoporous polymer-carbon composites. *Nat. Mater.*, 2(7):473–476, 2003.

- [13] D. Grosso, C. Boissière, B. Smarsly, T. Brezesinski, N. Pinna, P. A. Albouy, H. Amenitsch, M. Antonietti, and C. Sanchez. Periodically ordered nanoscale islands and mesoporous films composed of nanocrystalline multimetallic oxides. *Nat. Mater.*, 3:787–792, 2004.
- [14] J. Sun, D. Ma, H. Zhang, C. Wang, X. Bao, D.S. Su, A. Klein-Hoffmann, G. Weinberg, and S. Mann. Phase evolution in the alkane P123 water TEOS quadrupole component system: a feasible route to different complex mesostructured materials. *J. Mater. Chem.*, 16:1507–1510, 2006.
- [15] P.N. Trikalitis, K.K. Rangan, T. Bakas, and M.G. Kanatzidis. Varied pore organization in mesostructured semiconductors based on the  $[\text{SnSe}_4]^{4-}$  anion. *Nature*, 410:671–675, 2001.
- [16] D.E. De Vos, M. Dams, B.F. Sels, and P.A. Jacobs. Ordered Mesoporous and Microporous Molecular Sieves Functionalized with Transition Metal Complexes as Catalysts for Selective Organic Transformations. *Chem. Rev.*, 102(10):3615–3640, 2002.
- [17] S.J.L. Billinge, E.J. McKimmy, M. Shatnawi, H. Kim, V. Petkov, D. Wermeille, and T.J. Pinnavaia. Mercury Binding Sites in Thiol-Functionalized Mesostructured Silica. *J. Am. Chem. Soc.*, 127(23):8492–8498, 2005.
- [18] R. Ryoo, S.H. Joo, M. Kruk, and M. Jaroniec. Ordered Mesoporous Carbons. *Adv. Mater.*, 13(9):677–681, 2001.
- [19] C.-Y. Lai, B.G. Trewyn, D.M. Jeftinija, K. Jeftinija, S. Xu, S. Jeftinija, and V.S.-Y. Lin. A Mesoporous Silica Nanosphere-Based Carrier System with Chemically Removable CdS Nanoparticle Caps for Stimuli-Responsive Controlled Release of Neurotransmitters and Drug Molecules. *J. Am. Chem. Soc.*, 125(15):4451–4459, 2003.
- [20] I. Roy, T.Y. Ohulchanskyy, D.J. Bharali, H.E. Pudavar, R.A. Mistretta, N. Kaur, and P.N. Prasad. Optical tracking of organically modified silica nanoparticles as DNA carriers: A nonviral, nanomedicine approach for gene delivery. *Proc. Natl. Acad. Sci. U. S. A.*, 102(2):279–284, 2005.
- [21] P. C. Pandey, S. Upadhyay, and H. C. Pathak. A new glucose sensor based on encapsulated glucose oxidase within organically modified sol-gel glass. *Sens. Actuators, B*, 60(2-3):83–89, 1999.
- [22] Ö. Weiß, U. Wüstefeld, J. Loerke, F. Marlow, and F. Schüth. Host-Guest Interactions and Laser Activity in  $\text{AlPO}_4\text{-5}$ /Laser Dye Composites. *J. Solid State Chem.*, 167(2):302–309, 2002.
- [23] Renata Reisfeld. Lasers based on sol-gel technology. *J. Lumin.*, 72-74:7–8, 1997.

- [24] P. Yang, G. Wirnsberger, H.C. Huang, S.R. Cordero, M.D. McGehee, B. Scott, T. Deng, G.M. Whitesides, B.F. Chmelka, S.K. Buratto, and G.D. Stucky. Mirrorless Lasing from Mesostuctured Waveguides Patterned by Soft Lithography. *Science*, 287:465–467, 2000.
- [25] B. Darracq, F. Chaput, K. Lahlil, J.-P. Boilot, Y. Levy, V. Alain, L. Ventelon, and M. Blanchard-Desce. Novel photorefractive sol-gel materials. *Optical Materials*, 9(1-4):265–270, 1998.
- [26] N. Soggiu, H. Cardy, J. L. Habib Jiwan, I. Leray, J. Ph. Soumillion, and S. Lacombe. Organic sulfides photooxidation using sensitizers covalently grafted on silica: towards a more efficient and selective solar photochemistry. *J. Photochem. Photobiol., A*, 124:1–8, 1999.
- [27] P.B. Weisz. Diffusion and Chemical Transformation: An interdisciplinary excursion. *Science*, 179(4072):433–440, 1973.
- [28] Paul B. Weisz. Molecular Diffusion in Microporous Materials: Formalisms and Mechanisms. *Ind. Eng. Chem. Res.*, 34:2692–2699, 1995.
- [29] C. Jenny and P. Maddox. Supported polyolefin catalysts. *Current Opinion in Solid State and Materials Science*, 3:94–103, 1998.
- [30] D. Zhao, P. Yang, N. Melosh, J. Feng, B.F. Chmelka, and G.D. Stucky. Continuous Mesoporous Silica Films with Highly Ordered Large Pore Structures. *Adv. Mater.*, 10(16):1380–1385, 1998.
- [31] D. Grosso, F. Babonneau, P.-A. Albouy, H. Amenitsch, A. R. Balkenende, A. Brunet-Bruneau, and J. Rivory. An in Situ Study of Mesostuctured CTAB-Silica Film Formation during Dip Coating Using Time-Resolved SAXS and Interferometry Measurements. *Chem. Mater.*, 14(2):931–939, 2002.
- [32] P.C.A. Alberius, K.L. Frindell, R.C. Hayward, E.J. Kramer, G.D. Stucky, and B.F. Chmelka. General Predictive Syntheses of Cubic, Hexagonal, and Lamellar Silica and Titania Mesostuctured Thin Films. *Chem. Mater.*, 14(8):3284–3294, 2002.
- [33] D. H. Everett and L. K. Koopal. *Manual of Symbols and Terminology for Physicochemical Quantities and Units Appendix II: Definitions, Terminology and Symbols in Colloid and Surface Chemistry*. International Union of Pure and Applied Chemistry (IUPAC), 1971.
- [34] J.J. Ebelmen. Sur les produits de la decomposition des especes minerales de la famille des silicates. *Annales des Mines*, 7:3–66, 1845.
- [35] C. J. Brinker and G. W. Scherer. Sol → Gel → Glass: I. Gelation and Gel Structure. *J. Non-Cryst. Solids*, 70(3):301–322, 1985.

- [36] D. Avnir, S. Braun, O. Lev, and M. Ottolenghi. Enzymes and Other Proteins Entrapped in Sol-Gel Materials. *Chem. Mater.*, 6(10):1605–1614, 1994.
- [37] O. Lev, Z. Wu, S. Bharathi, V. Glezer, A. Modestov, J. Gun, L. Rabinovich, and S. Sampath. Sol-Gel Materials in Electrochemistry. *Chem. Mater.*, 9(11):2354–2375, 1997.
- [38] L.L. Hench and J.K. West. The Sol-Gel Process. *Chem. Rev.*, 90(1):33–72, 1990.
- [39] C. Burgdorff, H.-G. Löhmansröben, and R. Reisfeld. A perylene dye in sol-gel matrices: photophysical properties of N,N'-bis(2,5-di-tert-butylphenyl)-3,4:9,10-perylenebis(dicarboximide) in glasses and thin films. *Chem. Phys. Lett.*, 197(4-5):358–363, 1992.
- [40] R. Reisfeld and T. Saraidarov. Innovative materials based on sol-gel technology. *Optical Materials*, 28:64–70, 2006.
- [41] R. Reisfeld. Sol-gel technology for optoelectronic systems. Technical report, SPIE Newsroom-The International Society for Optical Engineering, 2006.
- [42] M.E. Raimondi and J.M. Seddon. Liquid crystal templating of porous materials. *Liq. Cryst.*, 26(3):305–339, 1999.
- [43] C.J. Brinker, Y. Lu, A. Sellinger, and H. Fan. Evaporation-Induced Self-Assembly: Nanostructures Made Easy. *Adv. Mater.*, 11(7):579–585, 1999.
- [44] H. Miyata and K. Kuroda. Preferred Alignment of Mesochannels in a Mesoporous Silica Film Grown on a Silicon (110) Surface. *J. Am. Chem. Soc.*, 121(33):7618–7624, 1999.
- [45] J.Y. Ying, C.P. Mehnert, and M.S. Wong. Synthese und Anwendungen von mit supramolekularen Templaten hergestellten mesoporösen Materialien. *Angew. Chem.*, 38:58–82, 1999.
- [46] G. Øye, J. Sjöblom, and M. Stöcker. Synthesis, characterization and potential applications of new materials in the mesoporous range. *Adv. Colloid Interface Sci.*, 89-90:439–466, 2001.
- [47] A. Monnier, F. Schüth, Q. Huo, D. Kumar, D. Margolese, R.S. Maxwell, G.D. Stucky, M. Krishnamurty, P. Petroff, A. Firouzi, M. Janicke, and B.F. Chmelka. Cooperative Formation of Inorganic-Organic Interfaces in the Synthesis of Silicate Mesostructures. *Science*, 261(5126):1299–1303, 1993.
- [48] Q. Huo, D.I. Margolese, U. Ciesla, D.G. Demuth, P. Feng, T.E. Gier, P. Sieger, A. Firouzi, B.F. Chmelka, F. Schüth, and G.D. Stucky. Organization of Organic Molecules with Inorganic Molecular Species into Nanocomposite Biphasic Arrays. *Chem. Mater.*, 6(8):1176–1191, 1994.



- [49] C.-Y. Chen, S.L. Burkett, H.-X. Li, and M.E. Davis. Studies on mesoporous materials II. Synthesis mechanism of MCM-41. *Microporous Materials*, 2(1):27–34, 1993.
- [50] S. Besson, T. Gacoin, C. Ricolleau, C. Jacquioud, and J.-P. Boilot. Phase diagram for mesoporous CTAB-silica films prepared under dynamic conditions. *J. Mater. Chem.*, 13:404–409, Nov 2003.
- [51] F. Cagnol, D. Grosso, G.J. de A. A. Soler-Illia, E.L. Crepaldi, F. Babonneau, H. Amenitsch, and C. Sanchez. Humidity-controlled mesostructuring in CTAB-templated silica thin film processing. The existence of a modulable steady state. *J. Mater. Chem.*, 13(1):61–66, 2003.
- [52] J.N. Israelachvili. *Intermolecular and Surface Forces*, pages 366–394. Academic Press (London), second edition, 1992.
- [53] Q. Huo, D.I. Margolese, and G.D. Stucky. Surfactant Control of Phases in the Synthesis of Mesoporous Silica-Based Materials. *Chem. Mater.*, 8(5):1147–1160, 1996.
- [54] M. Klotz, P.-A. Albouy, A. Ayril, C. Ménager, D. Grosso, A. Van der Lee, V. Cabuil, F. Babonneau, and C. Guizard. The True Structure of Hexagonal Mesophase-Templated Silica Films As Revealed by X-ray Scattering: Effects of Thermal Treatments and of Nanoparticle Seeding. *Chem. Mater.*, 12(6):1721–1728, 2000.
- [55] M. Noack, P. Kölsch, R. Schäfer, P. Toussaint, and J. Caro. Molekularsieb-Membranen für industrielle Anwendungen - Probleme, Fortschritte, Lösungen. *Chem. Ing. Tech.*, 73(8):958–967, 2001.
- [56] W.L. Bragg. Die Beugung kurzer elektromagnetischer Wellen durch einen Kristall. *Z. Anorg. Chem.*, 90:153–168, 1914.
- [57] N. Petkov. *Nanoporous hosts for the encapsulation of conductive nanostructured materials*. PhD thesis, LMU München, 2004.
- [58] Y. Sakamoto, M. Kaneda, O. Terasaki, D.Y. Zhao, J.M. Kim, G. Stucky, H.J. Shin, and R. Ryoo. Direct imaging of the pores and cages of three-dimensional mesoporous materials. *Nature*, 408:449–453, 2000.
- [59] O. Terasaki and T. Ohsuna. *Handbook of Zeolite Science and Technology*, pages 291–315. Marcel Dekker, Inc. NY, 2003.
- [60] S.N. Magonov and D.H. Reneker. Characterization of Polymer Surfaces with Atomic Force Microscopy. *Annu. Rev. Mater. Sci.*, 27:175–222, 1997.
- [61] T.R. Albrecht, P. Grütter, D. Horne, and D. Rugar. Frequency modulation detection using high-Q cantilevers for enhanced force microscope sensitivity. *J. Appl. Phys.*, 69(2):668–673, 1991.

- [62] Q. Zhong, D. Inniss, K. Kjoller, and V. B. Elings. Fractured polymer/silica fiber surface studied by tapping mode atomic force microscopy. *Surf. Sci. Lett.*, 290(1-2):L688–L692, 1993.
- [63] F. Rouquerol, J. Rouquerol, and K. Sing. *Adsorption by powders and porous solids*. Academic Press (London), 1999.
- [64] M. Kruk and M. Jaroniec. Gas Adsorption Characterization of Ordered Organic-Inorganic Nanocomposite Materials. *Chem. Mater.*, 13(10):3169–3183, 2001.
- [65] M. Jaroniec and R. Madey. *Physical adsorption on heterogeneous solids*. Elsevier Science Publishers (Amsterdam), 1988.
- [66] K. S. W. Sing, D. H. Everett, R. A. W. Haul, L. Moscou, R. A. Pierotti, J. Rouquerol, and T. Siemieniowska. Reporting Physisorption Data for Gas/Solid Systems with Special Reference to the Determination of Surface Area and Porosity. *Pure Appl. Chem.*, 57:603–619, 1985.
- [67] P. C. Ball and R. Evans. Temperature Dependence of Gas Adsorption on a Mesoporous Solid: Capillary Criticality and Hysteresis. *Langmuir*, 5(3):714–723, 1989.
- [68] S. Brunauer, P.H. Emmet, and E.J. Teller. Adsorption of Gases in Multimolecular Layers. *J. Am. Chem. Soc.*, 60:309–319, 1938.
- [69] I. Langmuir. The Constitution and Fundamental Properties of Solids and Liquids. Part I. Solids. *J. Am. Chem. Soc.*, 38(11):2221–2295, 1916.
- [70] E.P. Barrett, L.G. Joyner, and P.H. Halenda. The Determination of Pore Volume and Area Distributions in Porous Substances. I. Computations from Nitrogen Isotherms. *J. Am. Chem. Soc.*, 73:373–380, 1951.
- [71] A.V. Neimark, P.I. Ravikovitch, M. Grün, F. Schüth, and K.K. Unger. Pore Size Analysis of MCM-41 type of Adsorbents by Means of Nitrogen and Argon Adsorption. *J. Colloid Interface Sci.*, 207:159–169, 1998.
- [72] J. Kärger and W. Heink. The Propagator Representation of Molecular Transport in Microporous Crystallites. *Journal of Magnetic Resonance*, 51(1):1–7, 1983.
- [73] J. Kärger. The Benefit of Microscopic Measuring Techniques for Unveiling Structure-Mobility Relations in Molecular Diffusion under Confinement. *Diffusion-fundamentals online journal*, 1:5.1–5.170, 2005.
- [74] J. Kärger. The Random Walk of Understanding Diffusion. *Ind. Eng. Chem. Res.*, 41:3335–3340, 2002.
- [75] F. Stallmach, J. Kärger, C. Krause, M. Jeschke, and U. Oberhagemann. Evidence of Anisotropic Self-Diffusion of Guest Molecules in Nanoporous Materials of MCM-41 Type. *J. Am. Chem. Soc.*, 122:9237–9242, 2000.

- [76] Jörg Kärger, editor. *Leipzig, Einstein, Diffusion*. Leipziger Universitätsverlag, 2007.
- [77] J. Kärger and D. Freude. Stofftransport in mikro- und mesoporösen Materialien. *Chem. Ing. Tech.*, 73:1527–1527, 2001.
- [78] F. Stallmach and P. Galvosas. Spin Echo NMR Diffusion Studies. *Annu. Rep. NMR Spectrosc.*, 61:51–131, 2007.
- [79] Ph. Tamarat, A. Maali, B. Lounis, and M. Orrit. Ten Years of Single-Molecule Spectroscopy. *J. Phys. Chem. A*, 104(1):1–16, 2000.
- [80] W.E. Moerner. A Dozen Years of Single-Molecule Spectroscopy in Physics, Chemistry, and Biophysics. *J. Phys. Chem. B*, 106:910–927, 2002.
- [81] F. Kulzer and M. Orrit. Single-Molecule Optics. *Ann. Rev. Phys. Chem.*, 55:585–611, 2004.
- [82] S. Weiss. Fluorescence Spectroscopy of Single Biomolecules. *Science*, 283(5408):1676–1683, 1999.
- [83] G. Seisenberger, M.U. Ried, T. Endress, H. Büning, M. Hallek, and C. Bräuchle. Real-Time Single-Molecule Imaging of the Infection Pathway of an Adeno-Associated Virus. *Science*, 294:1929–1932, 2001.
- [84] A. Yildiz, J.N. Forkey, S.A. McKinney, T. Ha, Y.E. Goldman, and P.R. Selvin. Myosin V Walks Hand-Over-Hand: Single Fluorophore Imaging with 1.5-nm Localization. *Science*, 300(5628):2061–2065, 2003.
- [85] K. Shiroguchi and K. Kinosita (Jr.). Myosin V Walks by Lever Action and Brownian Motion. *Science*, 316(5828):1208–1212, 2007.
- [86] K. Kitamura, M. Tokunaga, A.H. Iwane, and T. Yanagida. A single myosin head moves along an actin filament with regular steps of 5.3 nanometres. *Nature*, 397:129–134, 1999.
- [87] K. Bacia, S.A. Kim, and P. Schwill. Fluorescence cross-correlation spectroscopy in living cells. *Nat. Methods*, 3:83–89, 2006.
- [88] S. Wörmke, S. Mackowski, T.H.P. Brotsudarmo, C. Jung, A. Zumbusch, M. Ehrl, H. Scheer, E. Hofmann, R.G. Hiller, and C. Bräuchle. Monitoring fluorescence of individual chromophores in peridinin-chlorophyll-protein complex using single molecule spectroscopy. *Biochim. Biophys. Acta, Bioenerg.*, 1767(7):956–964, 2007.
- [89] F. Schindler, J.M. Lupton, J. Müller, J. Feldmann, and U. Scherf. How single conjugated polymer molecules respond to electric fields. *Nat. Mater.*, 5(2):141–146, 2006.
- [90] C.A. Werley and W.E. Moerner. Single-Molecule Nanoprobes Explore Defects in Spin-Grown Crystals. *J. Phys. Chem. B*, 110(38):18939–18944, 2006.

- [91] K.S. McCain, D.C. Hanley, and J.M. Harris. Single-Molecule Fluorescence Trajectories for Investigating Molecular Transport in Thin Silica Sol-Gel Films. *Analytical Chemistry*, 75(17):4351–4359, 2003.
- [92] D.A. Vanden Bout, W.-T. Yip, D. Hu, D.-K. Fu, T.M. Swager, and P.F. Barbara. Discrete Intensity Jumps and Intramolecular Electronic Energy Transfer in the Spectroscopy of Single Conjugated Polymer Molecules. *Science*, 277(5329):1074–1077, 1997.
- [93] C. Hellriegel, J. Kirstein, C. Bräuchle, V. Latour, T. Pigot, R. Olivier, S. Lacombe, R. Brown, V. Guieu, C. Payraastre, A. Izquierdo, and Pierre Mocho. Diffusion of Single Streptocyanine Molecules in the Nanoporous Network of Sol-Gel Glasses. *J. Phys. Chem. B*, 108:14699–14709, 2004.
- [94] C Seebacher, C. Hellriegel, C. Bräuchle, M. Ganschow, and D. Wöhrle. Orientational Behavior of Single Molecules in Molecular Sieves: A Study of Oxazine Dyes in  $\text{AlPO}_4\text{-5}$  Crystals. *J. Phys. Chem. B*, 107(23):5445–5452, 2003.
- [95] J. Kirstein, B. Platschek, C. Jung, R. Brown, T. Bein, and C. Bräuchle. Exploration of nanostructured channel systems with single-molecule probes. *Nat. Mater.*, 5(4):303–310, 2007.
- [96] M.J. Saxton and K. Jacobson. Single-Particle Tracking: Applications to Membrane Dynamics. *Annu. Rev. Biophys. Biomol. Struct.*, 26:373–399, 1997.
- [97] H. Qian, M.P. Sheetz, and E.L. Elson. Single particle tracking. Analysis of diffusion and flow in two-dimensional systems. *Biophys. J.*, 60:910–921, 1991.
- [98] G.J. Schütz, H. Schindler, and Th. Schmidt. Single-Molecule Microscopy on Model Membranes Reveals Anomalous Diffusion. *Biophys. J.*, 73:1073–1080, 1997.
- [99] Th. Basché, S. Kummer, and C. Bräuchle. Direct spectroscopic observation of quantum jumps of a single molecule. *Nature*, 373:132–134, 1995.
- [100] F. Kulzer, S. Kummer, R. Matzke, C. Bräuchle, and T. Basché. Single-molecule optical switching of terrylene in p-terphenyl. *Nature*, 387:688–691, Jun 1997.
- [101] C. Seebacher, C. Hellriegel, F.-W. Deeg, C. Bräuchle, S. Altmaier, P. Behrens, and K. Müllen. Observation of Translational Diffusion of Single Terrylenediimide Molecules in a Mesoporous Molecular Sieve. *J. Phys. Chem. B*, 106:5591–5595, 2002.
- [102] W.E. Moerner and D.P. Fromm. Methods of single-molecule fluorescence spectroscopy and microscopy. *Rev. Sci. Instrum.*, 74(8):3597–3619, 2003.
- [103] F.O. Holtrup, G.R.J. Müller, H. Quante, S. De Feyter, F.C. De Schryver, and K. Müllen. Terrylenimides: new NIR Fluorescent Dyes. *Chem. Eur. J.*, 3(2):219–225, 1997.

- [104] F. Nolde, J. Qu, C. Kohl, N.G. Pschirer, E. Reuther, and K. Müllen. Synthesis and Modification of Terrylenediimides as High-Performance Fluorescent Dyes. *Chem. Eur. J.*, 11(13):3959–3967, 2005.
- [105] C. Jung, B.K. Müller, D.C. Lamb, F. Nolde, K. Müllen, and C. Bräuchle. A New Photostable Terrylene Diimide Dye for Applications in Single Molecule Studies and Membrane Labeling. *J. Am. Chem. Soc.*, 128(15):5283–5291, 2006.
- [106] R. Zondervan, F. Kulzer, S.B. Orlinskii, and M. Orrit. Photoblinking of Rhodamine 6G in Poly(vinyl alcohol): Radical Dark State Formed through the Triplet. *J. Phys. Chem. A*, 107(35):6770–6776, 2003.
- [107] W.P. Ambrose, P.M. Goodwin, J.C. Martin, and R.A. Keller. Single Molecule Detection and Photochemistry on a Surface Using Near-Field Optical Excitation. *Phys. Rev. Lett.*, 72(1):160–163, 1994.
- [108] D. Axelrod. Total Internal Reflection Fluorescence Microscopy in Cell Biology. *Meth. Enzy.*, 361:1–33, 2003.
- [109] T. Wazawa and M. Ueda. Total Internal Reflection Fluorescence Microscopy in Single Molecule Nanobioscience. *Adv. Biochem. Engin./Biotechnol.*, 95:77–106, 2005.
- [110] C. Seebacher. *Einzelmolekülspektroskopie von organischen Farbstoffmolekülen in porösen Festkörpern und Tieftemperaturspektroskopie an dem grün fluoreszierenden Protein*. PhD thesis, LMU München, 2002.
- [111] www.andor.com Andor Technology. *scientific camera solutions - catalog*, 2006.
- [112] C. Jung, C. Hellriegel, J. Michaelis, and C. Bräuchle. Single-Molecule Traffic in Mesoporous Materials: Translational, Orientational, and Spectral Dynamics. *Adv. Mater.*, 19(7):956–960, 2007.
- [113] C. Jung, C. Hellriegel, B. Platschek, D. Wöhrle, T. Bein, J. Michaelis, and C. Bräuchle. Simultaneous Measurement of Orientational and Spectral Dynamics of Single Molecules in Nanostructured Host-Guest Materials. *J. Am. Chem. Soc.*, 129:5570–5579, 2007.
- [114] R. Rigler, Ü. Mets, J. Widengren, and P. Kask. Fluorescence correlation spectroscopy with high count rate and low background: analysis of translational diffusion. *Eur. Biophys. J.*, 22(3):169–175, 1993.
- [115] M. Eigen and R. Rigler. Sorting single molecules: Application to diagnostics and evolutionary biotechnology. *Proc. Natl. Acad. Sci. U.S.A.*, 91(13):5740–5447, 1994.
- [116] P. Schwille, U. Haupts, S. Maiti, and W.W. Webb. Molecular Dynamics in Living Cells Observed by Fluorescence Correlation Spectroscopy with One- and Two-Photon Excitation. *Biophys. J.*, 77:2251–2265, 1999.

- [117] B.K. Müller, E. Zaychikov, C. Bräuchle, and D.C. Lamb. Pulsed Interleaved Excitation. *Biophys. J.*, 89(5):3508–3522, 2005.
- [118] J. Kirstein. Diffusionsmessungen auf Einzelmolekülbasis in nanoporösen M41S Molekularsieben und Modellierung der  $\text{AlPO}_4\text{-5}$  Struktur. Master's thesis, LMU München, 2002.
- [119] J. Enderlein, E. Toprak, and P.R. Selvin. Polarization effect on position accuracy of fluorophore localization. *Optics Express*, 14(18):8111–8120, 2006.
- [120] C. Hellriegel, J. Kirstein, and C. Bräuchle. Tracking of Single Molecules as a Powerful Method to Characterise Diffusivity of Organic Species in Mesoporous Materials. *New J. Phys.*, 7(23):1–14, 2005.
- [121] U. Kubitscheck, O. Kückmann, T. Kues, and R. Peters. Imaging and Tracking of Single GFP Molecules in Solution. *Biophys. J.*, 78(4):2170–2179, 2000.
- [122] C.M. Anderson, G.N. Georgiou, I.E. Morrison, G.V. Stevenson, and R.J. Cherry. Tracking of cell surface receptors by fluorescence digital imaging microscopy using a charge-coupled device camera. *J. Cell. Sci.*, 101(2):415–425, 1992.
- [123] M.K. Cheezum, W.F. Walker, and W.H. Guilford. Quantitative Comparison of Algorithms for Tracking Single Fluorescent Particles. *Biophys. J.*, 81:2378–2388, 2001.
- [124] R.M. Dickson, D.J. Norris, and W.E. Moerner. Simultaneous Imaging of Individual Molecules Aligned Both Parallel and Perpendicular to the Optic Axis. *Phys. Rev. Lett.*, 81(24):5322–5325, 1998.
- [125] A.P. Bartko and R.M. Dickson. Imaging Three-Dimensional Single Molecule Orientations. *J. Phys. Chem. B*, 103(51):11237–11241, 1999.
- [126] A.P. Bartko and R.M. Dickson. Three-Dimensional Orientations of Polymer-Bound Single Molecules. *J. Phys. Chem. B*, 103(16):3053–3056, 1999.
- [127] M. Böhmer and J. Enderlein. Orientation imaging of single molecules by wide-field epifluorescence microscopy. *J. Opt. Soc. Am. B*, 20(3):554, 2003.
- [128] R.J. Pfab, J. Zimmermann, C. Hettich, I. Gerhardt, A. Renn, and V. Sandoghdar. Aligned terrylene molecules in a spin-coated ultrathin crystalline film of p-terphenyl. *Chem. Phys. Lett.*, 387:490–495, 2004.
- [129] W. Lukosz and R.E. Kunz. Light emission by magnetic and electric dipoles close to a plane dielectric interface. II. Radiation patterns of perpendicular oriented dipoles. *J. Opt. Soc. Am.*, 67(12):1607–1615, 1977.
- [130] N. Bobroff. Position measurement with a resolution and noise-limited instrument. *Rev. Sci. Instrum.*, 57(6):1152–1157, 1986.

- [131] J. Schuster. *Untersuchung der Diffusion in dünnen Flüssigkeitsfilmen mit Methoden der Einzelmoleküldetektion*. PhD thesis, Fakultät für Naturwissenschaften der Technischen Universität Chemnitz, 2002.
- [132] J. Schuster, F. Cichos, and C. von Borczyskowski. Diffusion Measurements by Single-Molecule Spot-Size Analysis. *J. Phys. Chem. A*, 106(22):5403–5406, 2002.
- [133] T. Williams and C. Kelley. <http://www.gnuplot.info/>.
- [134] C. Eggeling, J. Widengren, R. Rigler, and C.A.M. Seidel. Photobleaching of Fluorescent Dyes under Conditions Used for Single-Molecule Detection: Evidence of Two-Step Photolysis. *Anal. Chem.*, 70(13):2651–2659, 1998.
- [135] A. Einstein. Über die von der molekularkinetischen Theorie der Wärme geforderte Bewegung von in ruhenden Flüssigkeiten suspendierten Teilchen. *Annalen der Physik*, 17:549–560, 1905.
- [136] H.C. Berg. *Random Walks in Biology*. Princeton University Press, 1983.
- [137] Th. Schmidt, G.J. Schütz, W. Baumgartner, H.J. Gruber, and H. Schindler. Imaging of single molecule diffusion. *Proc. Natl. Acad. Sci. U.S.A.*, 93:2926–2929, 1996.
- [138] J.-P. Bouchaud and A. Georges. Anomalous diffusion in disordered media: Statistical mechanisms, models and physical applications. *Physics Reports*, 195(4-5):127–293, 1990.
- [139] T.J. Feder, I. Brust-Mascher, J.P. Slattery, B. Baird, and W.W. Webb. Constrained diffusion or immobile fraction on cell surfaces: a new interpretation. *Biophys. J.*, 70(6):2767–2773, 1996.
- [140] A. Kusumi, Y. Sako, and M. Yamamoto. Confined Lateral Diffusion of Membrane Receptors as Studied by Single Particle Tracking (Nanovid Microscopy). Effects of Calcium-Induced Differentiation in Cultured Epithelial Cells. *Biophys. J.*, 65:2021–2040, 1993.
- [141] M. J. Saxton. Lateral diffusion in an archipelago. Single-particle diffusion. *Biophys. J.*, 64(6):1766–1780, 1993.
- [142] M.J. Saxton. Single-Particle Tracking: The Distribution of Diffusion Coefficients. *Biophys. J.*, 72:1744–1753, 1997.
- [143] A. Sonnleitner, G. J. Schütz, and Th. Schmidt. Free Brownian Motion of Individual Lipid Molecules in Biomembranes. *Biophys. J.*, 77:2368–2642, 1999.
- [144] J.R. Lakowicz. *Principles of Fluorescence Spectroscopy*. Springer, third edition, 1999.
- [145] W. H. Press, B. P. Flannery, S. A. Teukolsky, and W. T. Vetterling. *Numerical Recipes. The Art of Scientific Computing (Fortran Version)*. Cambridge University Press, Cambridge, U.K., 1992.

- [146] C.J. Brinker and G.W. Scherer. *Sol-Gel Science: The Physics and Chemistry of Sol-Gel Processing*. San Diego, 1990.
- [147] C. Cantau. *Nouveaux matériaux pour la photocatalyse dans le visible : de l'élaboration à la mise en oeuvre*. PhD thesis, Université de Pau et des pays de l'Adour (U.P.P.A), 2006.
- [148] V. Guieu, C. Payraastre, Y. Madaule, S. Garcia-Alonso, P.G. Lacroix, and K. Nakatani. Large Quadratic Nonlinear Optical Efficiencies in Pseudosymmetric Streptocyanine Dyes. *Chemistry of Materials*, 18(16):3674–3681, 2006.
- [149] V. Guieu, A. Izquierdo, S. Garcia-Alonso, C. André, Y. Madaule, and C. Payraastre. Fluorescent Streptocyanine Dyes: Synthesis and Photophysical Properties - Synthesis of a New Hemicarboxonium Salt. *Eur. J. Org. Chem.*, 5:804–810, 2007.
- [150] S. Brunauer, L.S. Deming, W.S. Deming, and E. Teller. On a Theory of the van der Waals Adsorption of Gases. *J. Am. Ceram. Soc.*, 62:1723, 1940.
- [151] G. Horvath and K. Kawazoe. Method for the calculation of effective pore size distribution in molecular sieve carbon. *J. Chem. Eng. Jpn.*, 16(6):470–475, 1983.
- [152] D. Montiel, H. Cang, and H. Yang. Quantitative characterization of changes in dynamical behaviour for single-particle tracking studies. *J. Phys. Chem. B*, 110:19762–19770, 2006.
- [153] H. Y. Carr and E. M. Purcell. Effects of Diffusion on Free Precession in Nuclear Magnetic Resonance Experiments. *Phys. Rev. E*, 94:630–638, 1954.
- [154] S. Meiboom and D. Gill. Modified Spin-Echo Method for Measuring Nuclear Relaxation Times. *Rev. Sci. Instr.*, 29:688–691, 1958.
- [155] S. Vasenkov, W. Böhlmann, P. Galvosas, O. Geier, H. Liu, and J. Kärger. PFG NMR study of diffusion in MFI-type zeolites: Evidence for the existence of intracrystalline transport barriers. *J. Phys. Chem. B*, 105:5922–5927, 2001.
- [156] S. Vasenkov and J. Kärger. Evidence for the existence of intracrystalline transport barriers in MFI-type zeolites: a model consistency check using MC simulations. *Microporous Mesoporous Mater.*, 55:139–145, 2002.
- [157] <http://webbook.nist.gov/chemistry/>.
- [158] J.B. Pedley, R.D. Naylor, and S.P. Kirby. *Thermochemical Data of Organic Compounds*. Chapman and Hall, New York, 1986.
- [159] Ö. Dag, G.A. Ozin, H. Yang, C. Reber, and G. Bussière. Photoluminescent Silicon Clusters in Oriented Hexagonal Mesoporous Silica Film. *Adv. Mater.*, 11(6):474–480, 1999.
- [160] Mark E. Davis. Ordered porous materials for emerging applications. *Nature*, 417:813–821, Jun 2002.



- [161] J. L. Shen, Y. L. Liu, Y. C. Lee, C. C. Yu, P. W. Cheng, and C. F. Cheng. Photoluminescence sites on MCM-48. *Microporous Mesoporous Mater.*, 64:135–143, 2003.
- [162] C. M. Yang, A. T. Cho, F. M. Pan, T. G. Tsai, and K. J. Chao. Spin-on Mesoporous Silica Films with Ultralow Dielectric Constants, Ordered Pore Structures, and Hydrophobic Surfaces. *Adv. Mater.*, 13:1099–1102, 2001.
- [163] Y. Wan and D. Zhao. On the Controllable Soft-Templating Approach to Mesoporous Silicates. *Chem. Rev.*, 107(7):2821–2860, 2007.
- [164] A. Zürner, J. Kirstein, M. Döblinger, C. Bräuchle, and T. Bein. Visualizing single-molecule diffusion in mesoporous materials. *submitted to Nature*.
- [165] T. Sen, G.J.T. Tiddy, J.L. Casci, and M.W. Anderson. Synthesis and Characterization of Hierarchically Ordered Porous Silica Materials. *Chem. Mater.*, 16(11):2044–2054, 2004.
- [166] B. Platschek. *Ordered Mesoporous Silica: Control of Morphology and Exploration with Single Molecules*. PhD thesis, Ludwig-Maximilians-Universität München, 2007.
- [167] R.M. Dickson, D.J. Norris, Y.-L. Tzeng, and W.E. Moerner. Three-Dimensional Imaging of Single Molecules Solvated in Pores of Poly(acrylamide) Gels. *Science*, 274(5289):966–968, 1996.
- [168] R. Bausinger, K. von Gersdorff, K. Braeckmans, M. Ogris, E. Wagner, C. Bräuchle, and A. Zumbusch. The Transport of Nanosized Gene Carriers Unraveled by Live-Cell Imaging. *Angew. Chem., Int. Ed.*, 45(10):1568–1572, 2006.
- [169] K. de Bruin, N. Ruthardt, K. von Gersdorff, R. Bausinger, E. Wagner, M. Ogris, and C. Bräuchle. Cellular Dynamics of EGF Receptor-Targeted Synthetic Viruses. *Mol. Ther.*, 15(7):1297–1305, 2007.
- [170] D. Lasne, G.A. Blab, S. Berciaud, M. Heine, L. Groc, D. Choquet, L. Cagnet, and B. Lounis. Single Nanoparticle Photothermal Tracking (SNaPT) of 5-nm Gold Beads in Live Cells. *Biophys. J.*, 91:4598–4604, 2006.
- [171] J. Schuster, F. Cichos, and Ch. von Borczyskowski. Anisotropic diffusion of single molecules in thin liquid films. *Eur. Phys. J. E*, 12(S1):75–80, 2003.
- [172] J. Schuster, F. Cichos, and C. von Borczyskowski. Diffusion in ultrathin liquid films. *Eur. Polym. J.*, 40(5):993–999, 2004.
- [173] A. Schob and F. Cichos. A Modified Surface Forces Apparatus for Single Molecule Tracking. *J. Phys. Chem. B*, 110(9):4354–4358, 2006.
- [174] M.B.J. Roeffaers, B.F. Sels, Hiroshi U. i, F.C. De Schryver, P.A. Jacobs, D.E. De Vos, and J. Hofkens. Spatially resolved observation of crystal-face-dependent catalysis by single turnover counting. *Nature*, 439:572–575, 2006.

- 
- [175] G.S. Attard, J.C. Glyde, and C.G. Göltner. Liquid-crystalline phases as templates for the synthesis of mesoporous silica. *Nature*, 378:366–368, 1995.
- [176] S.M. Mahurin, S. Dai, and M.D. Barnes. Probing the Diffusion of a Dilute Dye Solution in Mesoporous Glass with Fluorescence Correlation Spectroscopy. *J. Phys. Chem. B*, 107:13336–13340, 2003.
- [177] Y. Hou and D.A. Higgins. Single Molecule Studies of Dynamics in Polymer Thin Films and at Surfaces: Effect of Ambient Relative Humidity. *J. Phys. Chem. B*, 106(40):10306–10315, 2002.
- [178] D.A. Higgins, M.M. Collinson, G. Saroja, and A.M. Bardo. Single-Molecule Spectroscopic Studies of Nanoscale Heterogeneity in Organically Modified Silicate Thin Films. *Chem. Mater.*, 14(9):3734–3744, 2002.
- [179] Y. Fu, M.M. Collinson, and D.A. Higgins. Single-Molecule Spectroscopy Studies of Microenvironmental Acidity in Silicate Thin Films. *J. Am. Chem. Soc.*, 126(42):13838–13844, 2004.
- [180] S.A. Martin-Brown, Y. Fu, G. Saroja, M.M. Collinson, and D.A. Higgins. Single-Molecule Studies of Diffusion by Oligomer-Bound Dyes in Organically Modified Sol-Gel-Derived Silicate Films. *Anal. Chem.*, 77(2):486–494, 2005.
- [181] D.A. Higgins and M.M. Collinson. Gaining Insight into the Nanoscale Properties of Sol-Gel-Derived Silicate Thin Films by Single-Molecule Spectroscopy. *Langmuir*, 21(20):9023–9031, 2005.
- [182] Y. Fu, F. Ye, W.G. Sanders, M.M. Collinson, and D.A. Higgins. Single Molecule Spectroscopy Studies of Diffusion in Mesoporous Silica Thin Films. *J. Phys. Chem. B*, 110(18):9164–9170, 2006.
- [183] F. Ye, D.A. Higgins, and M.M. Collinson. Probing Chemical Interactions at the Single-Molecule Level in Mesoporous Silica Thin Films. *J. Phys. Chem. C*, 111:6772–6780, 2007.

# Acknowledgements

It is a pleasure to thank the many people who made this thesis possible:

- my two supervisors Prof. Christoph Bräuchle in Munich and Dr. Ross Brown in Pau.
- everybody from the Bräuchle group, especially Christophe Jung, Barbara Müller, Timo Lebold, Florian Feil, Julia Blechinger, Karla de Bruin, Stephan Wörmke, Peter Schwaderer, Alexandra Scherer, Moritz Ehrl and Silke Steger.
- my student assistants Yvonne Sörtl and Nina Rauhut
- all the people from the fine mechanics, electronics and glassblowing workshop
- the people from different groups, with whom I have been working, living or just having fun:
  - In Leipzig: Prof. Jörg Kärger and Bärbel Krause
  - In Munich: Prof. Thomas Bein, Barbara Platschek, Anderl Zürner, Nikolay Petkov, Markus Döblinger, Steffen Schmidt, Tina Reuther; Irmgard Frank and Michael Budde
  - In Pau: Patrice Bordat, Christophe Cantau, Virgnie Latour, Silvie Lacombe, Thierry Pigot, Pierro Mocho, Silvie Blanc, Jean-Pierre Campillo, Mohammadou Mérawa, Michel Rérat, Emilie Amzallag, Pierre-André Cazade, Jean-Michel Uhaldeborde, Cécile Brown
  - In Potsdam: Bernd Smarsly and Özlem Sel
  - In Toulouse: Valérie Guieu (now in Bordeaux) and Corinne Payrastré
- my parents, my brother and all my family
- my friends in Munich and all around the world.  
Above all , a special thanks goes to Moritz Ringler.

For financial support I thank:

Fonds of the chemical industry in the VCI (Verband der chemischen Industry), Elite-Network Bavaria and CeNS, SFB 486 of the German Research Foundation (DFG) and the French Ministry of Education and Research.



# List of Publications

Parts of this thesis have been published previously in somewhat modified form or are currently being prepared for publication:

- Chapter 5  
C. Hellriegel, J. Kirstein, C. Bräuchle, V. Latour, T. Pigot, R. Olivier, S. Lacombe, R. Brown, V. Guieu, C. Payraastre, A. Izquierdo, P. Mocho, Diffusion of Single Streptocyanine Molecules in the Nanoporous Network of Sol-Gel Glasses, *J. Phys. Chem. B*, **2004**, *108*, 14699-14709.
- Chapter 6  
A. Zürner\*, J. Kirstein\*, M. Döblinger, C. Bräuchle, T. Bein, Visualizing single-molecule diffusion in mesoporous materials, *Nature*, **2007**, *450*, 705-708.  
(\* A.Z. and J.K. contributed equally to this work).
- Chapter 7  
J. Kirstein, B. Platschek, C. Jung, R. Brown, T. Bein, C. Bräuchle, Exploration of nanostructured channel systems with single-molecule probes, *Nature Materials*, **2007**, *5* (4), 303-308.
- Parts of Chapters 5 and 7  
C. Hellriegel, J. Kirstein, C. Bräuchle, Tracking of Single Molecules as a Powerful Method to Characterise Diffusivity of Organic Species in Mesoporous Materials, *New Journal of Physics*, **2005**, *7*, 1-14.

The following publications are not included in this thesis:

- P. Bordat, J. Kirstein, P. Labeguerie, M. Merawa, R. Brown, Structure and Dynamics of AlPO<sub>4</sub>-5 and Other Aluminophosphates: Classical Molecular Dynamics and ab initio Calculations, *J. Phys. Chem. C*, **2007**, *111*, 10972-10981.
- C. Jung, J. Kirstein, B. Platschek, T. Bein, M. Budde, I. Frank, K. Müllen, J. Michaelis, C. Bräuchle, Diffusion of oriented single molecules with switchable mobility in networks of long unidimensional nanochannels, *J. Am. Chem. Soc.* (accepted for publication).



# Curriculum Vitae

## Persönliche Daten

---

**Name** Johanna Ursula Kirstein  
**Geburtsdatum** 04. August 1978  
**Geburtsort** München  
**Staatsangehörigkeit** deutsch

## Universitäre und schulische Ausbildung

---

Juli 2003 – Sept. 2007 **Ludwig-Maximilians-Universität (LMU) München und Université de Pau et des Pays de l'Adour (U.P.P.A.)**  
Doktorarbeit in physikalischer Chemie unter Doppelbetreuung (*cotutelle de thèse*) von Prof. Dr. C. Bräuchle (LMU München) und Dr. R. Brown (U.P.P.A., Frankreich)

1997 – 2002 **LMU München**  
Studium der Chemie  
Diplom: Dezember 2002, Vordiplom: November 1999

Juni – Dez. 2002 Diplomarbeit in physikalischer Chemie im Arbeitskreis von Prof. C. Bräuchle in Kooperation mit Dr. R. Brown

Sept. – Okt. 2001 **Université de Lausanne (Schweiz)**  
Aug. – Okt. 2000 **Imperial College London (Großbritannien)**

1988 – 1997 **Wilhelmsgymnasium München** (Abitur: Juni 1997)  
1984 – 1988 **Grundschule an der Gebelestrasse, München**

## Stipendien

---

seit Okt. 2004 Mitglied im internationalen Doktoranden-Kolleg Nano-Bio-Technologie (IDK NBT) des Elitenetzwerk Bayern

2004 – 2007 Mobilitätsstipendium zur *cotutelle de thèse* des französischen Forschungsministeriums (*Ministère de l'Enseignement supérieur et de la Recherche*)

Jan. 2004 – Dez. 2005 Chemifonds Stipendium des Verbandes der chemischen Industrie (VCI)

2000 und 2001 ERASMUS / SOCRATES Stipendium